Understanding the Chemistry of Acetohydroxamic Acid (AHA) in the Presence of Fe(III) in the Context of an Advanced PUREX Process

Suzanne Jones

BSc. Natural Sciences (Hons)

MSc. (By Research) Environmental Science (Dist)

Acknowledgements

This thesis is submitted in accordance with the requirements of

Lancaster University for the degree of Doctor of Philosophy

02/06/2023

Acknowledgements

Acknowledgements

Acknowledgements

Many people have offered their support and encouragement during the period of this research, without whom completion would not have been possible.

Firstly, I'd like to give thanks to my supervisor Professor Colin Boxall, not only for his guidance, support, and knowledge, but also for his enthusiasm for the research. I would also like to thank my second supervisor, Professor Fabrice Andrieux, and my industrial supervisor at the National Nuclear Laboratory, Dr Robin Taylor, for their support during this time. I would also like to acknowledge the EPSRC and Lloyd's Register Foundation, for the joint funding of this PhD studentship.

I would like to thank my research colleagues for their support, particularly Dr Richard Wilbraham for his help with some of the experimental work presented in this thesis and encouragement. Special thanks also goes to Mr Alexander Jackson for his kinetic modelling work, presented in Chapter 5 of this thesis, which was key in gaining understanding from some of the experimental data obtained.

Finally, I'd like to give my thanks to my friends and family who offered their support and encouragement when I needed it, and particularly my parents for supporting me in my life and academic studies. The most important person of all to the completion of this research was my husband, Dr Ashley Jones. I can't thank him enough for always being there to offer me love and encouragement when times were difficult and when my determination and resolve were low. Thank you also for rekindling my love of art during this period, and

finally, for the gift of our beautiful son, Caleb Jones. For my husband and my son, I dedicate the final push to completion.

Declaration

I, Suzanne Jones, hereby certify that this thesis and the research described in it is all my own work unless otherwise indicated and has not been submitted in any previous application for a higher degree. The work presented here was carried out at Lancaster University between *October 2014 and June 2023.*

Date..... Signature of candidate.....

Suzanne Jones

I, Professor Colin Boxall, hereby certify that the candidate has fulfilled the conditions of the resolution and regulations appropriate for the degree of Doctor of Philosophy at Lancaster University and that the candidate is qualified to submit this thesis in application for that degree.

Date..... Signature of supervisor.....

Professor Colin Boxall

Abstract

Since the 1950s, the majority of operating commercial nuclear fuel reprocessing plants, including those in the UK, France, Russia and Japan, have used the well-proven hydrometallurgical PUREX (plutonium uranium extraction) process, or a variant PUREX-based process to chemically separate uranium (U) and plutonium (Pu) from used nuclear fuel. However, enhancements to PUREX are needed for future fuel cycles to improve its proliferation resistance, its capability to handle higher burnup fuels and to minimize its waste arisings. A key objective within the development of an Advanced PUREX process is the effective control of the actinides U, neptunium (Np) and Pu within a single cycle flowsheet. Simple hydroxamic acids such as acetohydroxamic acid (AHA) have the ability to strip Pu(IV) and Np(IV) from tri-butyl phosphate into nitric acid and have thus been identified as suitable reagents for this purpose. Utilising this in an Advanced PUREX process will ultimately allow for the generation of a co-processed Pu/Np product and a high purity U product, addressing some of the shortcomings of traditional PUREX.

There are however a few key knowledge gaps that must be addressed before AHA can be implemented in such a process. Firstly, it is known that simple hydroxamic acids hydrolyse to hydroxylamine (NH_2OH) and the parent carboxylic acid in acidic media, the former product being known to react autocatalytically / explosively with nitric acid which is ubiquitous in reprocessing flowsheets. Whether the reaction mechanism or product distribution changes when the AHA is complexed to a metal ion is unclear. Additionally, observations that Pu(IV) is reduced to Pu(III) during complex hydrolysis have opened up the possibility of their use as replacements for U(IV)/N_2H_4 or NH_2OH in advanced

PUREX processes, but whether the reducing agent is the hydroxamate itself, or NH_2OH, is still in question.

To answer these questions, Fe(III) has been used as a non-active analogue to Pu(IV) and Np(IV), as it exhibits analogous complexation with AHA and whilst thermodynamically possible, redox chemistry mechanistically analogous to that of Pu(IV) is thought to be kinetically hindered at high hydrogen ion concentrations to the point where it can be ignored on the timescales of AHA hydrolysis. However, initial studies by Raman spectroscopy showed identical AHA hydrolysis products in the absence and presence of initial Fe(III), but with differing final yields. Further quantification techniques were then explored including a titrimetric method for hydroxylamine, UV-Vis spectroscopy for nitrous acid and Fe(II), and ion chromatography (IC) for multiple species, all of which suggested redox chemistry akin to Pu(IV).

A library of data to describe these systems has been gathered utilising a single column ion chromatography system to measure a number of key ions over time in nitric acid solutions of varying temperatures and initial Fe(III) and AHA concentrations. These key species include the acetate ion (CH_3COO^-) and protonated hydroxylamine (NH_3OH^+) from the hydrolysis of AHA, and the reduced form of the metal ion, Fe(II), which has been not previously been seen during hydrolysis of the Fe(III)-AHA complex. Our analysis therefore shows that the current definition of Fe(III) as a non-oxidizing metal ion with regards to AHA needs revising. Using CH_3COO^- ingrowth as a direct measure of AHA loss and assuming redox chemistry of Fe(III) mechanistically analogous to Pu(IV), these studies have additionally been combined with kinetic modelling in the software platform

gPROMS (General PROcess Modelling System), and have thus provided key insights into the nature of the reducing agent in these systems.

Abstract

Contents

List of Tables

List of Figures

List of Abbreviations and Acronyms

ABWR	Advanced Boiling Water Reactor
AERE	Atomic Energy Research Establishment
AFCs	Advanced Fuel Cycle
AFR	Away From Reactor
AGR	Advanced Gas-Cooled Reactor
AHA	Acetohydroxamic Acid
AR	At Reactor
An	Actinide element
BEPO	British Experimental Pile ‘0’
BHA	Benzohydroxamic Acid
BWR	Boiling Water Reactor
EURO-GANEX	European Group Actinide Extraction
FBR	Fast Breeder Reactor
Fe	Iron
FHA	Formohydroxamic Acid
FP	Fission Product
GDF	Geological Disposal Facility
GIF	Generation IV International Forum
GLEEP	Graphite Low Energy Experimental Pile
gPROMS	General PROcess Modelling System
HAN	Hydroxylamine Nitrate
HLW	High-Level Waste
HPLC	High Performance Liquid Chromatography
IC	Ion Chromatography
Ln	Lanthanide element
LOD	Limit of Detection
LOQ	Limit of Quantification
LWR	Light Water Reactors

MA	Minor Actinide
MOx	Mixed Oxide
MSR	Molten Salt Reactor
NNL	National Nuclear Laboratory
Np	Neptunium
OK	Odourless Kerosene
Pu	Plutonium
PUREX	Plutonium Uranium Redox Extraction
PWR	Pressurized Water Reactor
P&T	Partitioning and Transmutation
QRS	Quantitative Raman Spectroscopy
RSD	Relative Standard Deviation
R&D	Research and Development
SACSESS	Safety of Actinide Separation Processes
SADT	Self-accelerating decomposition temperature
SCE	Saturated calomel electrode
SERS	Surface-enhanced Raman Spectroscopy
SFR	Sodium-cooled Fast Reactor
SHE	Standard Hydrogen Electrode
SNF	Spent Nuclear Fuel
SIT	Specific Ion Interaction
TBP	Tri-Butyl Phosphate
THORP	Thermal Oxide Reprocessing Plant
TRU	Transuranic
U	Uranium
UKAEA	United Kingdom Atomic Energy Authority
UO_x	Uranium Oxide
UREX	Uranium Extraction
UV-Vis	Ultraviolet-Visible
VHTR	Very High Temperature Reactor

XHA	Simple hydroxamic acid

List of Symbols

A	Pre-exponential Factor	κ	Conductivity
A_λ	Absorbance at wavelength λ	l	Path length
A_sF	Asymmetry factor	L	hydroxamate anion
β_n	Stability constant	M	mol dm^{-3}
β_n'	Conditional stability constant	$r.t.p$	Room temperature & pressure
c	Concentration of sample	R	Universal gas constant
D	Distribution coefficient	R^2	Correlation coefficient
E	Redox potential	T	Temperature
E^o	Standard redox potential	t	Time
E_a	Activation energy	$t_{1/2}$	Half life
E_B/A	Binding energy per nucleon	t_0	Dead time
eV	Electron volts	t_R	Retention Time
ε	Extinction coefficient	t_R'	Net Retention Time
F	Faradays constant	tHM	Tonnes of heavy metal
h	Plank's constant	wt%	Weight percentage
HL	hydroxamic acid	z	Ionic Charge
I	Ionic Strength	Λ_m	Molar conductivity
J	Joules	λ	Wavelength
k	Kinetic rate constant	$\Delta H^\#$	Enthalpy of activation
k_B	Boltzmann's constant	ΔH^0	Enthalpy of formation
K	Kelvin	$\Delta S^\#$	Entropy of activation
K_n	Equilibrium constant	ΔS^0	Entropy of formation
K_d	Dissociation constant	σ	Cross section

CHAPTER 1

Introduction

1 Introduction

1.1 Research Motivation and Objectives

Historically, the commercial hydrometallurgical PUREX (Plutonium Uranium Redox EXtraction) process has been successfully used to chemically separate uranium (U) and plutonium (Pu) from used nuclear fuel. Once separated, U and Pu can be recycled as new uranium oxide (UOx) or mixed oxide (MOx) fuels for re-use in current and future reactors. The remaining highly radioactive liquid containing, amongst other things, fission products (FPs) such as short-lived Cesium-137 and Strontium-90 and long lived Iodine-129 and Technicium-99, and minor actinides (mainly neptunium (Np), americium and curium) is vitrified into glass for immobilisation of the radionuclides and stored pending geological disposal as high-level waste (HLW).

There is a significant international research effort with regards to enhancement of PUREX that meet the requirements of future fuel cycles, especially with regards to:

- The prevention of the formation of a pure Pu stream and thereby preventing the use of the recovered plutonium in weapons manufacture and enhancing the proliferation resistance of the process.
- Its process safety – especially with respect to explosion risks under maloperations from the possible occurrence of autocatalytic reactions of the reductant hydroxylamine with nitric acid, and the removal of U(IV)/hydrazine as a reductant.

- Its management of the highly radiotoxic minor actinides (MAs) to be compatible with the design of future aqueous flowsheets that will aim to recycle the elements as fuel materials to be burnt within a reactor, rather than being ultimately sent to disposal.
- Simplification of the process into a single cycle flowsheet compatible with centrifugal contactors, leading to a reduction waste arisings, and overall plant footprint, complexity and associated costs.

With these requirements in mind, an Advanced PUREX process, under a range of different names, is currently being developed in the UK, US and EU, amongst others. To address some of the short-comings of traditional PUREX, the National Nuclear Laboratory (NNL) is developing a process centred around the use of hydroxamic acids as selective complexants for the tetravalent actinides Pu(IV) and Np(IV). The design of the process will ultimately result in the generation of a high purity bulk uranium product and a co-processed U/Pu product, with Np also remaining with the latter.

Much work has already been done on the study of actinide-HA systems of relevance to Advanced PUREX. However, key science and technology gaps remain. Firstly, it is well known that hydroxamate ligands undergo hydrolysis under acid conditions to generate hydroxylamine and the corresponding carboxylic acid. Whilst this hydrolytic instability is beneficial in terms of the downstream decomposition of the ligand, it must be understood in any process flowsheet. Whether the mechanism and ultimate products of the hydrolysis are affected by complexation of the hydroxamic acid with the Pu(IV) or Np(IV) ions is as yet unresolved.

Further, the hydroxamates are redox active; for example, Pu(IV) undergoes reduction to Pu(III) in the presence of hydrolysing hydroxamates. This redox behaviour opens up the possibility of their use in an Advanced PUREX process as replacements for U(IV)/N_2H_4 or hydroxylamine used in current reprocessing flowsheets. However, the nature of the reductant is unclear, being potentially the hydroxamate itself, its hydrolysis products hydroxylamine, or some other, as yet unidentified, agent. From a process safety point of view, there are also key uncertainties about the possible (explosive) reaction between hydroxamate-derived hydroxylamine and HNO_3.

This thesis aims to address these knowledge gaps via a study of the hydrolysis of AHA in the presence of Fe(III) which, like Np(IV), is currently defined as a complexing but non-oxidising metal ion with regards to AHA. Whereas Np(IV)-AHA speciation in nitric acid is complicated by the formation of competing nitrate complexes, this is not the case with Fe(III), thus allowing analysis of the hydrolysis of the Fe(III)-AHA complex(es).

An ingrowth of Pu(III) is observed during the associated Pu(IV)-AHA complex hydrolysis as a result of redox reactions of Pu(IV) with NH_2OH and/or AHA, which complicate the study of the hydrolysis reaction in this system. Whilst mechanistically similar reactions are known to be thermodynamically feasible with Fe(III), they have not been observed in these systems to date and are thought to be absent due to kinetic hinderance, pertaining to the definition of Fe(III) as non-oxidising in these systems.

This thesis will aim to answer these questions and is structured in the following way. After summarising the motivation behind the research and aims of the project in

Chapter 1 (this Chapter), Chapter 2 will then discuss introduce the concept of the nuclear fuel cycle, the different types of fuel cycle including the closed fuel cycle with aqueous reprocessing via the current PUREX process, the options for advanced fuel cycles and the use of AHA in Advanced PUREX process, and finally, the chemistry of AHA in acidic media, and in the presence of metal ions that must be understood before its implementation.

Chapter 3 will then describe the materials and experimental methods used in this thesis for analysis of the various species of interest in the Fe(III)/AHA/HNO_3 system, with the aim to fill in the knowledge gaps relating to the complex hydrolysis that will ultimately inform the Pu(IV)-AHA system. Chapter 4 will then present the results of the various analyses and discuss the implications, including Raman spectroscopy for identity of hydrolysis products, a titrimetric method for quantification of hydroxylamine, Ultraviolet-Visible (UV-Vis) absorption spectroscopy for nitrous acid and Fe(II) measurements, and ion chromatography (IC) for real-time quantification of multiple species.

Chapter 5 will discuss the development of a revised full kinetic model of this system based on the experimental results by ion chromatography presented in Chapter 4. The experimental work presented here showed that the current knowledge of the Fe(III)-AHA system is incomplete, and incorporation of redox chemistry akin to that observed in the Pu(IV)-AHA system was required. The chemical theory and analysis work behind the model development is the work of this thesis. The modelling work itself described in this Chapter was performed by Mr Alexander Jackson.

Finally, Chapter 6 summarises the conclusions drawn from the work presented here and suggests possible future work from it.

CHAPTER 2

Background

2 Background

2.1 Nuclear Power

Nuclear power plants harness the energy released from the disintegration of an unstable atomic nucleus [1], a process termed nuclear fission. Fission involves the splitting of the atomic nucleus of a radioactive element into two (occasionally three) individual nuclei [2], which in turn creates heat that is used to boil water and create steam, and the steam is used to turn a turbine that drives generators that produce electricity. Ernest Rutherford, widely accepted as a pioneer for the study of radiation, first observed the great energy emerging from samples of uranium, thorium, and other radioactive substances, and hinted at an enormous reservoir of energy locked inside their atoms [3].

Whilst there are many different types of nuclear reactors, they can all be defined as ‘apparatus in which a nuclear fission chain reaction can be initiated, sustained and controlled for generating heat or the production of useful radiation’ [2]. Four things happen in a typical fission reactor core:

- A uranium atom is hit by neutrons and splits, producing heat, fission products & fast neutrons
- Fast neutrons are slowed by the moderator to form thermal neutrons
- ^{238}U, the majority uranium isotope, is hit by and absorbs thermal neutrons to form ^{239}U initially, but decaying quickly to the relatively stable ^{239}Pu isotope

- ^{235}U, the minority uranium isotope, typically enriched to ~2.5-5 wt% in metal oxide-based fuels, is hit by and absorbs thermal neutron and then splits, giving heat, fission products & fast neutrons

To understand the role of these processes in the generation of nuclear power, a knowledge of nuclear fission and its wider place within what is termed the nuclear fuel cycle, is required. Fission and the fuel cycle are the subject of the next two sections.

2.1.1 Nuclear Fission

A key milestone in the field of nuclear and elementary particle physics was the discovery of the neutron by James Chadwick in 1932 [4], a crucial factor in our understanding of the atomic nucleus and the mechanism of nuclear fission. Neutrons exhibit different energies, ranging from being in thermal equilibrium with their surroundings (0.0253 eV at 293 K) to beyond 1 MeV in nuclear energy applications [5], and thus are termed accordingly. In the context of conventional nuclear power generation, low energy thermal neutrons are required to drive the fission process.

As mentioned previously, nuclear fission is a reaction involving the splitting of an atomic nucleus into smaller fragments and can take place in certain unstable heavy nuclei after capture of a neutron. An important measure of nuclear stability is the binding energy per nucleon, E_B/A, which is shown in Figure 2.1 as a function of the atomic mass number, or number of nucleons, for all known elements [6]. The higher the value of E_B/A, the more stable nuclide. The most stable nuclide with the greatest E_B/A is that of $^{56}_{26}Fe$. Below this, unstable lighter nuclei can undergo a process called

nuclear fusion to give heavier, more stable nuclei (higher E_B/A), whereas above this, nuclear fission of unstable heavy nuclei will give lighter, more stable nuclei (higher E_B/A). The latter can occur either by spontaneous fission, typically of the even-number transuranic isotopes such as ^{252}Cf, ^{244}Cm, ^{240}Pu and ^{238}U, or stimulated fission associated with operating reactors, as in the case of ^{235}U and ^{239}Pu [2, 5].

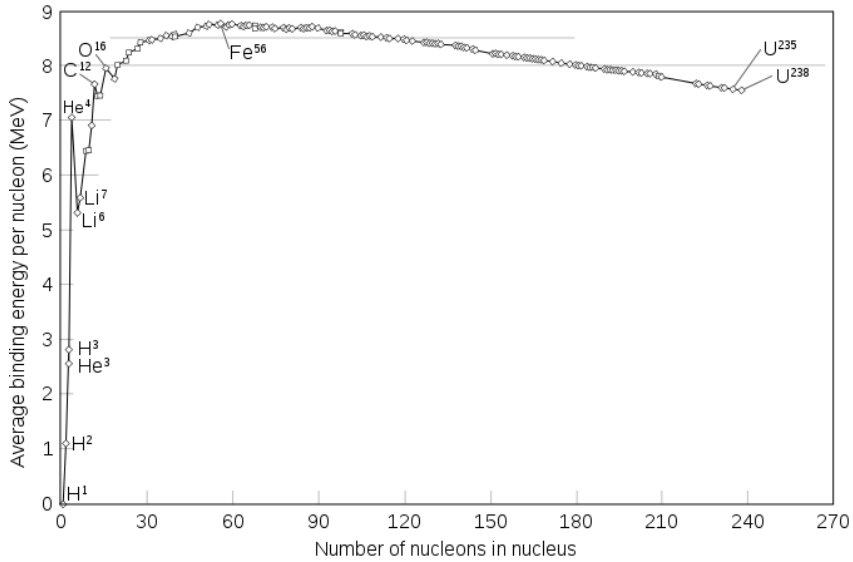

Figure 2.1: Binding energy per nucleon as a function of atomic mass number, or number of nucleons, for ^{2}H through to ^{252}Cf. Source: [Wikimedia Commons].

The fission of heavy elements was first experimentally demonstrated by Hahn and Strassmann in 1939 [7]. They bombarded a uranium compound with neutrons to create elements of much smaller weight and atomic charge. This ‘splitting’ of the atom was subsequently named fission by Meitner and Frisch [8], due to the process being an analogy to the division of a fluid sphere. The first publication on the physics and mechanism of the nuclear fission reaction was published by Bohr and Wheeler in September 1939 [9], who pointed out that fission is more likely to occur with ^{235}U than ^{238}U.

In its very nature, radioactive decay is a stochastic or 'random' process. Fission concerns the probability of a neutron interacting with a given nucleus, termed the cross section, which is given the mathematical symbol σ and is measured in barns, where a barn is 10^{-24} cm^2 [2]. Depending on the specific nuclide in question and the incident neutron energy, several types of interaction are often possible, and thus an attempt is made to divide up the total probability into partial cross sections for each interaction. Figure 2.2 shows the cross-section of neutron-induced fission for the isotopes of ^{235}U, ^{238}U and ^{239}Pu [10]. It can be thought of as an area surrounding the nucleus within which a neutron must enter to induce the interaction in question.

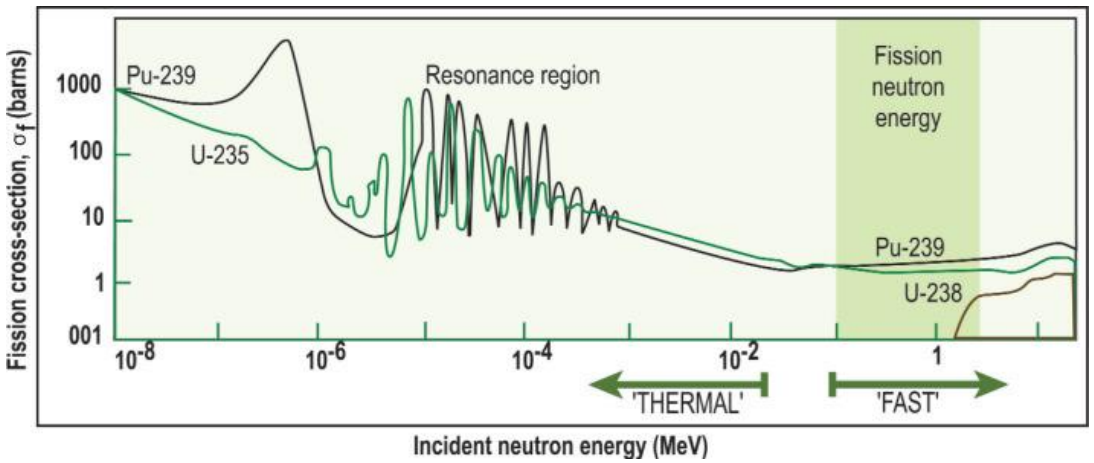

Figure 2.2: Neutron cross sections for the fission of Uranium and Plutonium [10] (reproduced with permission from source [10], copyright 2007 Elsevier).

As can be seen in Figure 2.2, values of the neutron cross section for ^{235}U are greater at the lower energies of thermal neutrons, making the chain reaction easier to sustain in this region. To reduce the incident neutron energies, a material known as a moderator is thus included in reactor designs. The most common thermal reactors worldwide are light water reactors (LWRs), either pressurised water reactors (PWRs) or boiling water reactors (BWRs), which are fuelled by the fissile isotope ^{235}U and incorporate water

as a moderator, slowing the initially fast (> 0.5 MeV) neutrons produced by the fission reaction [11]. The general fission reaction of ^{235}U occurring in a reactor core is given by Eq. 2.1. ^{235}U initially absorbs a neutron to produce ^{236}U, which then splits into two unequal fragments, releasing a large amount (~200MeV) of energy and typically 2-4 neutrons, 1 of which must trigger another fission to sustain a chain reaction [12].

$$^{235}U + n \rightarrow {}^{236}U \rightarrow fission\ fragments + xn + \sim 200MeV \tag{2.1}$$

The only naturally occurring thermally fissile isotope is ^{235}U, which makes up only 0.7% of natural uranium. Other fissile isotopes such as ^{239}Pu and ^{241}Pu, can be produced artificially in a reactor via a series of beta particle emissions and neutron capture events, from the isotopes ^{238}U and ^{240}Pu respectively [9], termed fertile isotopes. This concept is for example utilised in the design of breeder reactors, which would use fissile ^{239}Pu as the core, and use the neutrons leaked from the core to breed further ^{239}Pu from a fertile ^{238}U blanket that surrounds it as described by Eq. 2.2 [13].

$$^{238}U + n \rightarrow {}^{239}U \xrightarrow{\beta^-,\ 23.5m} {}^{239}Np \xrightarrow{\beta^-,\ 2.4d} {}^{239}Pu \tag{2.2}$$

As mentioned previously, the nuclear fission reaction occurring in the core of a nuclear reactor forms just part of something termed the nuclear fuel cycle, which is described in the following section.

2.2 The Nuclear Fuel Cycle

The collective processes and operations involved in the manufacture of nuclear fuel, its irradiation in nuclear reactors, and the storage, reprocessing or final disposal of spent nuclear fuel (SNF), are described as the nuclear fuel cycle. This is illustrated in Figure 2.3 [14].

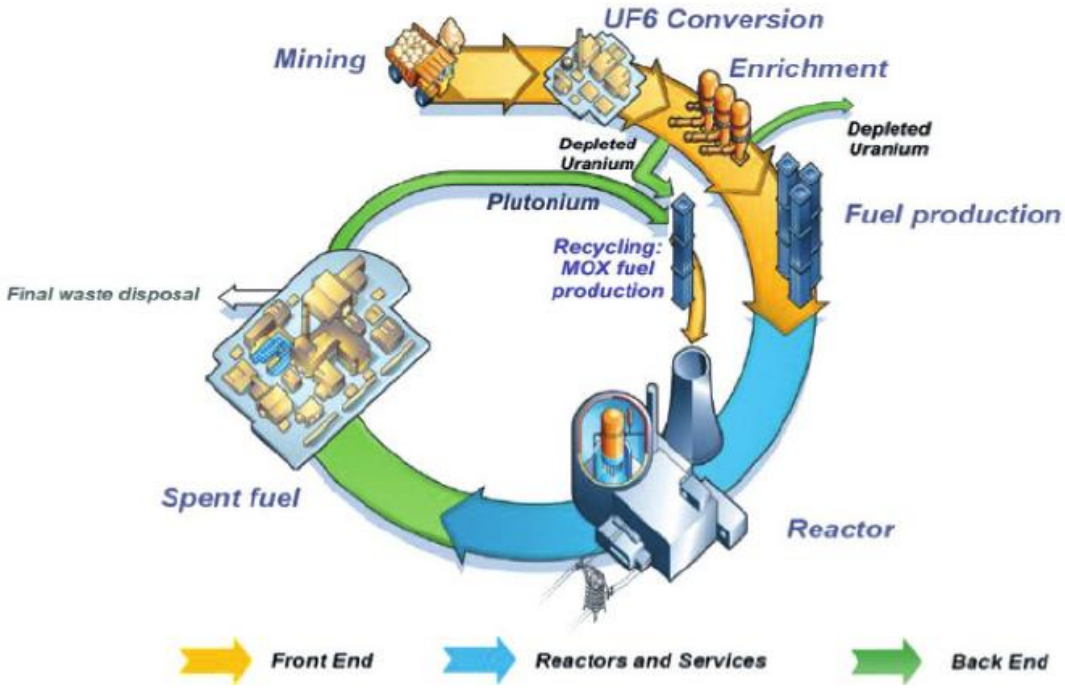

Figure 2.3: The nuclear fuel cycle (reproduced from open access source, reference [14]).

From Figure 2.3 it can be seen that the nuclear fuel cycle is subdivided into three main stages:

(i) The front-end, which involves the nuclear fuel manufacture;

(ii) Reactors and Services, which involves the processes involved in the operation of a nuclear reactor and the generation of energy, including the

in-reactor irradiation of the fuel, inducing the fission of fissile isotopes and the release of heat;

(iii) and the back-end, which begins with the discharge of nuclear fuel from the reactor and ends in either reprocessing/recycle or geological disposal.

Stages (i) and (ii) are beyond the scope of this thesis whose focus is very much on the back-end, stage (iii). However, it is useful to briefly discuss the evolution and future of reactor technology, especially in the UK as this informs the direction that developments and advances that stage (iii) technologies may take over the next 50 years. Thus, the next section will briefly review the timeline of reactor evolution in the UK, before moving on to a detailed discussion of back-end in subsequent sections.

2.2.1 Reactor Technology and its evolution

To describe the evolution of reactor technology, a classification system of reactor designs by generation has been adopted, encompassing all commercial nuclear power reactors currently in use today, those now defunct, and new designs under development. This is illustrated in Figure 2.4, which shows the time ranges corresponding to the first deployment of each generation of reactor design [15].

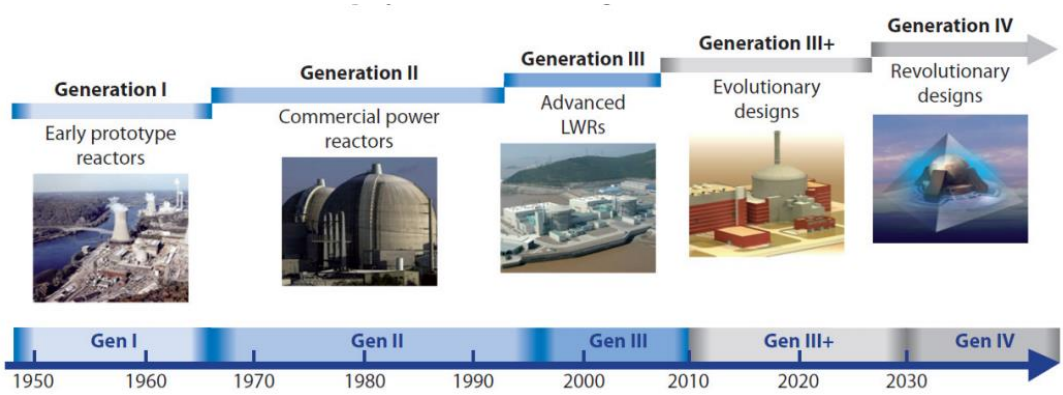

Figure 2.4: Nuclear Technology Roadmap (reproduced with permission from source [15], copyright 2014 OECD. Original source of material: GIF (2002), "A Technology Roadmap for Generation IV Nuclear Energy Systems", «Sodium-cooled Fast Reactor (SFR) » https://www.gen-4.org/.gif/jcms/c_40481/technology-roadmap.)

The reactor types can be summarised as follows:

- Generation I: The earliest prototype reactors, designed and commissioned in the late 1950s and early 1960s. The power output is usually small by the standards of the reactor generations that followed and most of these have now reached the end of their functional life.
- Generation II: The majority of the operating reactors worldwide fall into this category, including the PWR and BWR designs in the US and France, and the advanced gas-cooled reactors (AGRs) in the UK [16]. In comparison to Generation I, these reactors have a larger power generation capacity and utilise oxide-based fuels capable of higher burn-up for sustained operation.
- Generation III: Designed as direct follow-ons from Generation II. This includes the advanced LWRs such as the Sizewell B PWR in the United Kingdom, and the advanced boiling water reactors (ABWR) in Japan, with improved operational life expectancy and reductions in core damage frequency.

- Generation III+: This is a sub generation of designs that are an evolutionary development of Gen III reactors incorporating extra passive safety features. Otherwise known as passive cooling, these are design feature that do not require active controls or operator intervention to shut down the plant safely in the event of an emergency [17].
- Generation IV (Gen IV): Gen IV reactor technologies encompass design concepts that offer significant advantages over Gen III and III+ that would be expected to be deployed commercially in approximately 30-40 years – including very high temperature thermal reactors (VHTR), molten salt reactors (MSR) and fast reactors. The emphasis with Gen IV systems is that such a design uses fuel more efficiently, produces less waste, is economically competitive and compliant with high standards of safety and proliferation resistance.

Having briefly described the reactor classification system, the next section will describe the evolution of nuclear reactors specifically in the UK.

2.2.2 Nuclear Energy in the UK

The UK's first nuclear reactors, termed atomic piles at the time, were experimental piles built at the Atomic Energy Research Establishment (AERE) at Harwell, Oxfordshire, built to enable scientists to determine the most effective design, materials and construction methods to be used in later piles. This began with the air-cooled graphite moderated GLEEP (Graphite Low Energy Experimental Pile), which commenced operation in 1946 as the first working reactor in Western Europe, and was

followed in 1947 by the commissioning of the 6 MWth British Experimental Pile ‘0’ (BEPO) reactor on the same site [18]. This reactor demonstrated the viability of nuclear power reactors prior to the construction of the Windscale Piles at Sellafield completed in 1951.

The UK’s first nuclear reactors were built following the Second World War, initially under the nuclear weapons programme, until 1953, when President Eisenhower addressed the United Nations and called for international co-operation in the development of nuclear technology for peaceful purposes. The UK Atomic Energy Authority (UKAEA) was then set up in 1954 to take control of this program, and the small-scale commercial Magnox nuclear power station opened and commenced operation at Calder Hall near Sellafield in 1956 [19]. These first gas-cooled reactors were also used to produce plutonium for the weapons programme in addition to electricity. Over the next 15 years, the original design was scaled up and 10 additional stations comprising 26 reactor units started operation [20]. The Magnox reactors were followed later by the Advanced Gas-Cooled Reactors (AGRs), totalling 7 plants, which opened between 1976 and 1988. The UKs nuclear installed capacity peaked at 12.7 GW in 1995 with the opening of the UKs only Pressurised Water Reactor (PWR), Sizewell B, pushing nuclears share of supply to a peak of 26.9% by 1997 [21].

In 2017, nuclear energy contributed to 19% of the UKs electricity. There are currently 15 operational reactors operated by EDF Energy, consisting of 14 AGRs and 1 PWR, and with a total generating capacity of 9.5 GWe. All but one are scheduled to be retired by 2023-2030, with the only exception being Sizewell B, which began operations in 1995 and is scheduled for decommissioning in 2035 [22]. The UK is currently formally

considering four different Pressurised Water Reactor (PWR) designs for new nuclear build. These are: 1) the Framatome EPR (originally the Areva European Pressurised Reactor, 2 units currently under construction as Hinckley Point C), 2) Westinghouse's AP1000 (considered for the now-abandoned Moorside development, 3) Hitachi-GE's Advanced Boiling Water Reactor (ABWR, to be sited at Wylfa), and 4) the Chinese Hualong HPR1000 (currently under assessment for construction at Bradwell B).

2.2.3 Back End

The fate of the irradiated fuel once it is removed from the reactor, otherwise known as spent nuclear fuel (SNF), defines the nature of the fuel cycle being implemented. There are two general types of nuclear fuel cycle defined as follows:

- Open Fuel Cycle: – also referred to as a once-through fuel cycle, whereby SNF is disposed of directly and sent straight to final waste disposal in a geological repository.
- Closed Fuel Cycle: - whereby SNF is reprocessed to extract the uranium and plutonium it contains for reuse in new fuel. For complete closure of the fuel cycle commercial implementation of technologies for the partitioning and transmutation (P&T) of plutonium and the minor actinides (MAs) in fast neutron reactors is required to fully utilise all the reusable material, extracting 50 - 100 times more energy from the originally mined uranium than reactors currently in operation today [23]. Development work for these Gen IV reactors is however still on-going.

In some countries currently, such as France, a partially closed fuel cycle is in operation. This is where SNF is reprocessed once for the extraction of uranium and plutonium, which are reused in MOX fuel (mixed oxide fuel) in existing thermal neutron reactors. The spent MOX fuel is then stored, pending future reprocessing in fast neutron reactors, whilst the remaining processed uranium can be re-enriched and re-used in fuel. This approach improves the overall utilisation of the original mined uranium resource by approximately 20% compared to an open fuel cycle [23].

The type of back-end fuel cycle deployed is a matter of national policy with some countries adopting an open, some a partially closed and some a fully closed fuel cycle. For example, Korea, the United States and the United Kingdom (since November 2018) currently operate a once-through, or open fuel cycle. Whilst Korea is currently implementing a “wait and see” policy with regards to SNF management, they have a development plan for a closed fuel cycle with the construction of a pyroprocessing (dry, high-temperature recycling) demonstration facility by 2025 together with an advanced prototype sodium-cooled fast reactor (SFR) plant by 2028. [24]. The UK is currently investing in research and development (R&D) in numerous aspects of the fuel cycle, including both aqueous reprocessing and pyroprocessing technologies. It is assumed long-term that it will operate a fully closed fuel cycle including fast reactors and recycle of at least uranium and plutonium from LWRs to fuel the first of these reactors before fast reactor recycling is available [25]. The US policy however still considers an open cycle with final geological disposal, but there is ongoing investment in R&D around advanced reactors and waste management with the aim to support existing reactors fleet and evaluate options for advanced fuel cycles in 2030 [26].

France and Japan are currently reprocessing towards closed fuel cycles, which France has implemented from the beginning of their nuclear programme in the 1980s with reprocessing and MOx fuel fabrication activities at the La Hague and Marcoule sites. France is focusing currently on multi-recycling of plutonium-based mixed oxide fuels in the mid-term, with the generation IV SFR as the current reference option for the long-term [27]. Japan is prioritising R&D on pyroprocessing and P&T for full closure of the full cycle, with plans for construction of a Transmutation Experimental Facility (TEF) [24]. Some strategies countries are adopting are summarised in Table 2.1 below.

Table 2.1: Summary of fuel cycles currently adopted by some countries and considered for future use.

Country	Active reprocessing plants	Fuel cycle	Future fuel cycle policy
Japan	Rokkasho (currently in test phase)	Closed	Closed. R&D focussed on fast reactors, pyroprocessing and P&T.
France	UP2.400, UP3 and UP2.800 at La Hague	Closed	Closed. Focus on multi-recycling of Pu-based MOx fuels.
India	Trombay, Tarapur-I, Tarapur-II, Kalpakkam	Closed	Closed. Plans for diversifying from uranium to thorium cycle with thermal breeder reactors.
UK	None	Open	Full closure of fuel cycle including fast reactors and reprocessing.
US	None	Open	No decision yet. R&D around advanced fuel cycles ongoing.
Korea	None	Open	Closed. Plans for SFR fleet with pyroprocessing.

Having described the types of fuel cycles, the following sections will describe the back-end processes that define each, beginning with geological disposal of SNF in a repository, the final step in an open fuel cycle (UKs current option).

2.2.4 Geological disposal

Once the fuel has reached its designed burnup level it must be removed from the reactor, but due to its high level of radioactivity, SNF generates large amounts of heat. Whether destined for reprocessing or final geological disposal, SNF is initially stored in At-Reactor (AR) pools for an interim period of time, typically 90 – 180 days [28], to allow the majority of the short lived 'hot' isotopes to decay away. After this initial storage period, the fuel is transferred to Away From Reactor (AFR) storage facilities, which can be wet (pools) or dry (dry silos or containers) in design [29]. Figure 2.5 shows an example of the former, the spent fuel AFR interim storage ponds at the Thermal Oxide Reprocessing Plant (THORP) at Sellafield in the UK [30]. Whilst the reprocessing activities at THORP, which are described in the next section in more detail, have now ceased, the facility will be used to store SNF until the 2070s [31].

Figure 2.5: Receipt of spent fuel and interim storage at THORP [30] (reproduced with permission from reference [30], copyright 2015 Sellafield Ltd.).

Figure 2.6 shows the contents of 1 tonne of a typical spent fuel from a PWR after a 10 year cooling period in interim storage. Spent UO_2 fuel from a typical LWR contains; 94-95% uranium (< 1% ^{235}U), approximately 1% plutonium consisting of over 50% ^{239}Pu and the isotopes ^{238}Pu, ^{240}Pu, ^{241}Pu and ^{242}Pu making up the rest, between 3 and

5% fission products (FPs) and approximately 0.1-0.2% minor actinides [32]. The MAs consist of neptunium primarily as ^{237}Np with a half-life ($t_{1/2}$) of 2.14×10^6 years, and various isotopes of americium and curium. Only a few elements; plutonium, neptunium, americium, curium and some long-lived FPs such as iodine and technetium ($t_{1/2}$ = 15.7×10^6 and 0.21×10^6 years respectively) at concentration levels of grams per tonne, contribute to the major hazard from SNF [33]. However, due to the hazards they present to life forms when released to the environment, their disposal requires isolation from the biosphere in stable deep geological formations for long periods of time [34]. The required size of a geological repository (not yet available), and siting, thus presents significant challenges.

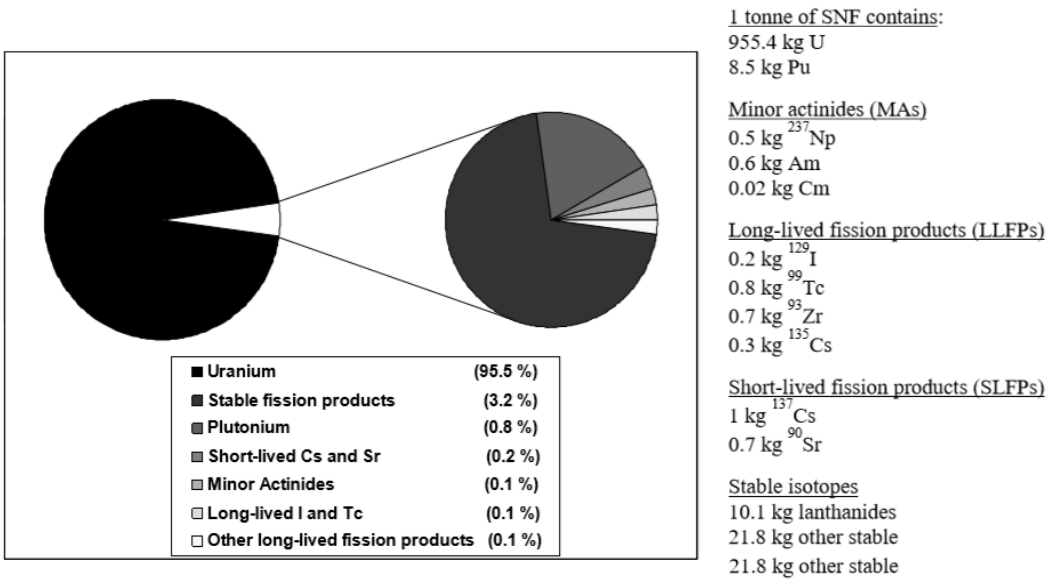

Figure 2.6: Composition of SNF for a standard PWR with UO_2 fuel, 33 GWd/t burn-up, 10-year cooling period [33] (reproduced with permission from reference [33], copyright 2006 OECD).

At the end of 2016, approximately 58,000 tHM (tonnes of heavy metal) of spent fuel was stored in the EU [35]. Figure 2.7 shows the timescales for decay of the total radiotoxicity of spent PWR fuel and the fuel and the contributing components. The

radiotoxicity associated with the raw materials used for fabrication of 1 tonne of enriched uranium, including all uranium isotopes and their radioactive progenies, is indicated as a reference level on Figure 2.7 as “Uranium Ore”. SNF only reaches this level after periods of more than 100,000 years [34]. The first 100 years of this period is dominated by the FPs, which decrease to the natural reference level in about 300 years. The actinides, mainly plutonium and americium, dominate the long-term radiotoxicity. Between approximately 100-1000 years after discharge, the radiotoxicity is dominated by ^{241}Am, the radioactive daughter of ^{241}Pu which has a level approximately 300 times that of natural ore. After this time, the main contributors become ^{240}Pu, followed by ^{239}Pu and finally long-lived FPs descended from ^{241}Am.

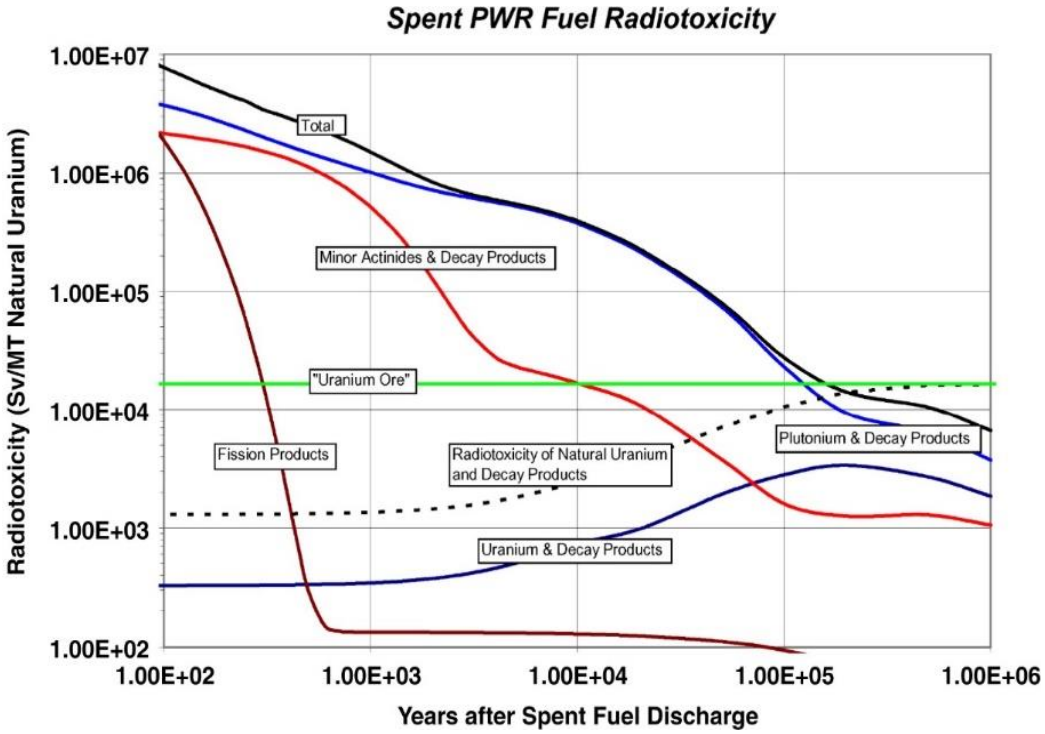

Figure 2.7: Radiotoxicity of SNF [34] (reproduced with permission from reference [34], copyright 2011 Elsevier).

The overall aim of any geological disposal facility (GDF) for final disposal of waste is that the radioactivity remains isolated and contained from the biosphere until it has

decayed to the safe reference level. Whilst the specific design of a GDF will vary, they all adopt a philosophy whereby several barriers are in place, known as the engineered barrier system (EDS). These barriers comprise those directly around the specific waste form itself for immobilisation of the radionuclides, and those provided by the disposal facility they are ultimately stored in which, for example, might be a specially-excavated, grout-lined vault [36]. The geological structure selected for siting of the GDF needs to be deep, inaccessible and stable for long timescales.

Having discussed geologic disposal in an open cycle as UK's currently favoured option, Section 2.2.5 will now discuss the closed fuel cycle with reprocessing as the UK's historically favoured option and proposed option of the future.

2.2.5 Nuclear Fuel Reprocessing

Nuclear fuel reprocessing is the process by which uranium and plutonium are separated and purified from SNF and subsequently converted into a new uranium oxide (UOx) or MOx [37]. Until recently, the THORP facility had been reprocessing spent fuel from oxide fuel reactors (e.g. AGRs, PWRs and BWRs) for over forty years, and spent uranium metal-based fuel from the UK's first generation of Magnox reactors, was reprocessed at the Magnox reprocessing plant at the same site [38].

In the UK there have been several geopolitical reasons for reprocessing SNF over the last 50 years. Historically, reprocessing was primarily used to contribute to both national energy and security programmes by recovering the unused fissile Pu and fertile U contained post-burnup in the fuel elements, which comprise ~95% of SNF.

The added benefit of reprocessing was the reduction of waste volumes and radioactivity, thus lowering the burden on a GDF. The separation of pure uranium and plutonium however, also raise concerns over the proliferation of nuclear material, amongst other factors. The following section will discuss in more detail the PUREX process, which is the only commercially available technology for spent fuel recycling.

2.2.6 The UK PUREX Process

Between its opening in the 1990's to the ceasing of operations in November 2018, THORP at Sellafield in the UK has used the Plutonium Uranium Extraction (PUREX) process to reprocess 9331 tonnes of used nuclear fuel from nine countries around the world [39]. The industrial reprocessing flowsheets still in operation today were originally developed for the production of pure weapons grade plutonium and thus have very high separation efficiency and product qualification requirements in regards to the purity of the produced uranium and plutonium [40].

The key stages of the THORP reprocessing plant are shown in Figure 2.8 [41], including the initial stages to prepare the fuel for the PUREX process and a summary of the extraction process itself. Prior to extraction, spent fuel is first chopped and dissolved in hot (about 100^{o}C) nitric acid. The undissolved fuel cladding and insoluble fission products are then removed from the solution of SNF and nitric acid, vitrified and disposed of as high-level waste (HLW). The dissolution of the fuel also liberates volatile radioactive gases which are scrubbed and purified. The resultant SNF liquor is then conditioned to adjust the pH in preparation for reprocessing by the PUREX extraction process [32].

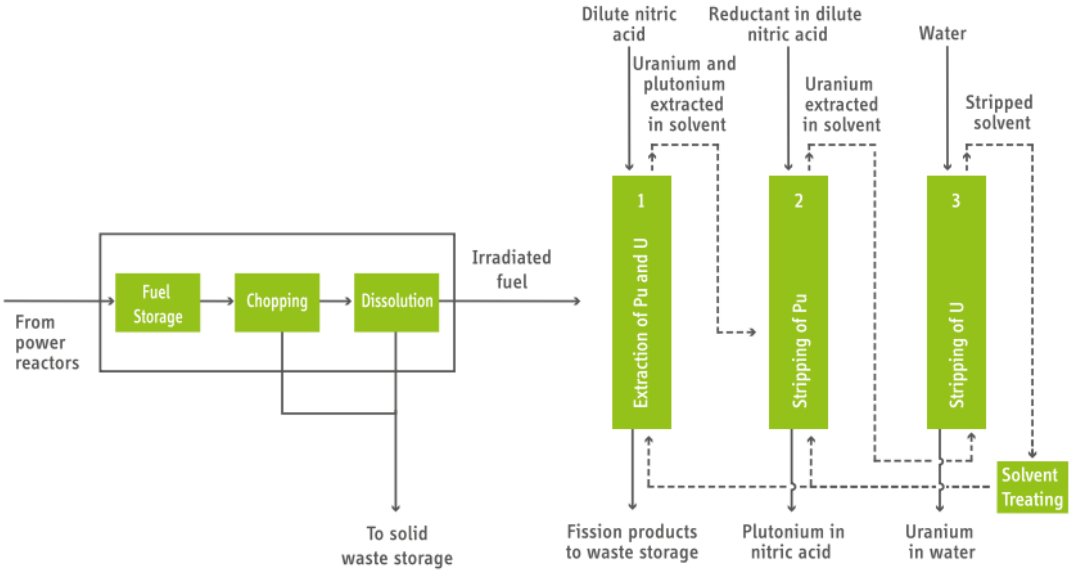

Figure 2.8: Key stages in a reprocessing plant (reproduced from open access source, reference [41]).

PUREX is a 3-cycle liquid-liquid solvent extraction process that produces high purity separate U and Pu product streams as the end product [24], utilizing tri-butyl phosphate (TBP) as the organic solvent and nitric acid as the salting agent. This process is classed as a heterogeneous recycle process, meaning it involves the separate management and recycle of the Pu and MAs, in comparison to a homogeneous recycle process which would involve a grouped recycling. A detailed description of each cycle in this process is provided in the following paragraphs.

In the first cycle, U(VI) present as UO_2^{2+} and Pu(IV) are separated from the fission products and minor actinides via multiple liquid-liquid extractions using TBP, typically 30% diluted in odourless kerosene (OK). The Pu(IV) and U(VI) cations form neutral nitrate complexes in the aqueous phase that are selectively complexed by TBP and extracted into the organic phase via Eqs. 2.3 and 2.4, whereas fission product cations generally do not form nitrate complexes under these conditions and are not

extracted. The structures of TBP, and the complexes formed with UO_2^{2+} and Pu(IV) ions are shown in Figure 2.9 below.

$$Pu^{4+} + 4NO_3^- + 2TBP \rightleftharpoons Pu(NO_3)_4.2TBP \quad (2.3)$$

$$UO_2^{2+} + 2NO_3^- + 2TBP \rightleftharpoons UO_2(NO_3)_2.2TBP \quad (2.4)$$

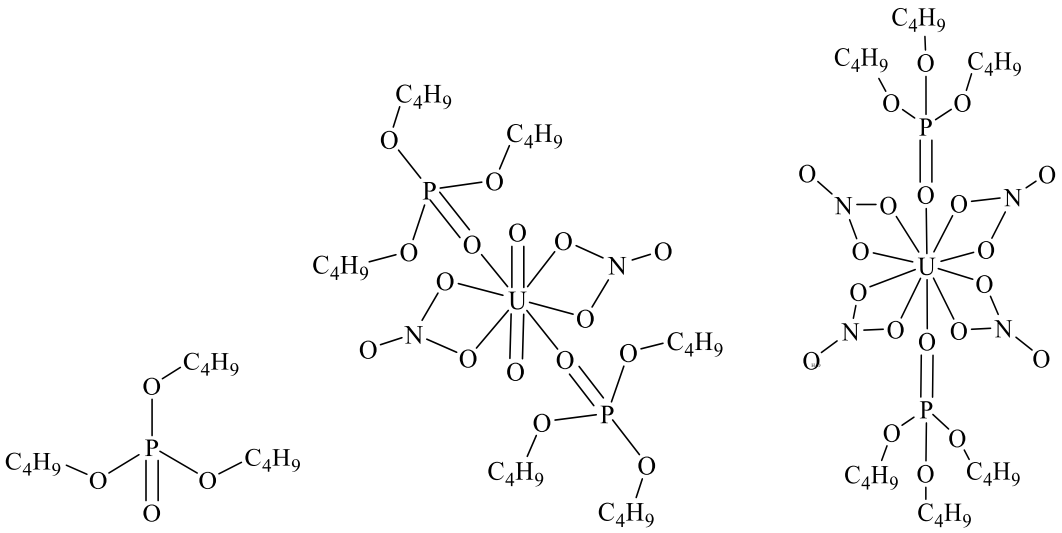

Figure 2.9: From left to right: Chemical structures of TBP, $Pu(NO_3)_4.2TBP$ and $UO_2(NO_3)_2.2TBP$.

Whilst TBP is an effective extractant for Pu(IV) and U(VI), it is too dense and viscous to use pure. A diluent is therefore used to reduce the density and viscosity of the organic phase, improving the physical characteristics to enhance the phase separation kinetics [32]. Due to the required formation of the nitrate complexes, extraction of Pu(IV) and U(VI) is also a function of nitrate concentration, known as the salting effect, thus the concentration of HNO_3 is strictly controlled. This initial stage of the PUREX process uses strongly acidic ~3M HNO_3 to drive, *via* Le Chatelier's principle, lipophilic U(VI)-TBP-nitrate and Pu(IV)-TBP-nitrate complex formation and thus the extraction of Pu(IV) and U(VI) into the organic phase. After extraction, the remaining

nitric acid stream, which now contains only highly active fission products/minor actinides, is then routed for vitrification and subsequent geological disposal.

In the second cycle, U is separated from Pu via a reductive stripping process. A reductant, such as uranium nitrate (U^{4+}) stabilised with hydrazine, is added to the organic phase to reduce Pu(IV) to Pu(III) by Eq. 2.5 [37]. The stabilizer for U(IV) prevents the occurrence of the autocatalytic oxidation of U(IV) by NO_2^- [42]. Due to the change in the oxidation state of Pu to an odd charge state via Eq. 2.5, the TBP releases the Pu(III) back into a newly added clean aqueous phase, while the mixture of U(IV) as U^{4+} and U(VI) as UO_2^{2+} remains complexed in the organic phase by TBP.

$$2Pu^{4+} + U^{4+} + 2H_2O \rightleftharpoons 2Pu^{3+} + UO_2^{2+} + 4H^+ \quad (2.5)$$

The final cycle is comprised of two subsidiary cycles – the uranium purification (UP) cycle and the plutonium purification (PP) cycle. In the UP cycle, the loaded TBP/OK/U phase is re-contacted with dilute (~0.1M) nitric acid to reverse, again via Le Chatelier's principle, the complexing reaction of U(VI) with TBP described by Eq. 2.4. This results in a slow back extraction of the U(VI) as UO_2^{2+} from the organic phase into the dilute acid aqueous phase. This resulting aqueous phase is then concentrated by evaporation before being sent for product finishing. Here the uranium nitrate left after evaporation of the HNO_3 from the aqueous stream is first calcined to a powder form of UO_3, before subsequent pelletization and reduction in close to pure hydrogen to form the final fuel form UO_2 [43].

In the PP cycle, the Pu(III) requires stabilising in the aqueous phase because nitric acid can easily re-oxidise Pu(III) back to Pu(IV) via a series of reactions autocatalyzed by

nitrous acid (Eqs. 2.6 and 2.7). A nitrous acid scavenger, such as hydrazine, is therefore added into the separation column during this cycle (Eqs. 2.8 and 2.9) [37].

$$Pu^{3+} + HNO_2 + H^+ \rightarrow Pu^{4+} + NO + H_2O \quad (2.6)$$

$$2NO + HNO_3 + H_2O \rightarrow 3HNO_2 \quad (2.7)$$

$$N_2H_4 + HNO_2 \rightarrow NH_3 + 2H_2O \quad (2.8)$$

$$NH_3 + HNO_2 \rightarrow N_2 + N_2O + H_2O \quad (2.9)$$

The plutonium nitrate product is then concentrated by an evaporation process similar to the uranium nitrate product, before being precipitated via an oxalate precipitation process and calcined to a powder form of PuO_2 for reuse in fuel [43].

Whilst the PUREX process described in this section is an established and mature technology, significant improvements to the process are required to optimise it for future Advanced Fuel Cycles (AFCs). The concept of an AFC will be described in the next section, followed by a discussion of some reprocessing flowsheets under development.

2.3 Gen IV Advanced Fuel Cycles

2.3.1 Key Challenges for Advanced Reprocessing Schemes

There has been a growing international interest in future Advanced fuel cycles, and based around the basic alternatives of an open, partially closed or fully closed cycle, a

variety of different scenarios have been proposed. The Generation IV International Forum (GIF) defines four key areas in its *Technology Roadmap* [15] for advancement in nuclear energy going through to Gen IV fuel cycles. These are; 1) sustainability, 2) safety and reliability, 3) economic competitiveness, and 4) proliferation resistance and physical protection.

Improving the overall sustainability of nuclear energy involves enhancements for more effective natural resource utilisation and reduction in the volume and long-term radioactivity of high level waste, whilst maintaining energy costs to an economically viable level [44]. There are number of variations on AFCs, but in order to meet the sustainability goal, most scenarios aim to include a full recycling and burnup of all the transuranic (TRU) actinide elements [37]. Partitioning and Transmutation (P&T) involves separation of the FPs from the actinide elements (Partitioning), and removal of the latter from a reactor irradiation (Transmutation).

It is anticipated that the well-established PUREX process will play an important role in upcoming and advanced future nuclear fuel cycles. There are however three major challenges, namely; i) modification of the process to be compatible with the recycle of the MAs (Np, Am, Cm), ii) the design of aqueous flowsheets with the ability to handle very high burn-up fuels greater Pu content, and iii) enhancing proliferation resistance by avoiding production of a pure Pu stream. With these requirements in mind, some options for AFCs include (but are not limited to) the Advanced PUREX process being developed by National Nuclear Laboratory (NNL), and the European Grouped Actinide Extraction (EURO-GANEX) process. These will be described in more detail in the following sections.

2.3.2 The Advanced PUREX Process

While the PUREX process has been used successfully to reprocess irradiated fuel for the last 40 years, many enhancements are needed for incorporation into AFCs. A major objective is the full control of the actinides U, Np and Pu within a single solvent extraction cycle that is flexible to a wide range of feeds, whereby the process meets high product specifications on the U streams and offers increased proliferation resistance on the Pu streams [37]. The use of a single cycle flowsheet compatible with centrifugal contactors would consequently lead to a reduction in plant size, complexity and waste volumes [45]. Centrifugal contractors off several advantages over currently used mixer settlers and extraction columns including; 1) high compactness (low capital and operating costs), 2) short residence time (less solvent degradation and reduction in solvent waste volume), 3) excellent phase separation, 4) high mass-transfer efficiency, and 5) high safety with respect to criticality [46].

The NNL have been developing such an Advanced PUREX process centred around the use of acetohydroxamic acid (AHA), whereby Pu(IV) and Np(IV) are co-separated by the formation of strong hydrophilic complexes with AHA and Np(VI) is stripped from U(VI) via a rapid reduction by AHA to Np(V) [47]. A simple schematic of the process is illustrated in Figure 2.10.

After the initial U/Pu separation stage, conducted as per the conventional PUREX process using 30% TBP/OK solvent, Np(IV) is then effectively rejected from the solvent phase by contacting with a low acidity aqueous nitric acid phase, containing the hydroxamic acid. The hydroxamic acid selectively complexes tetravalent over

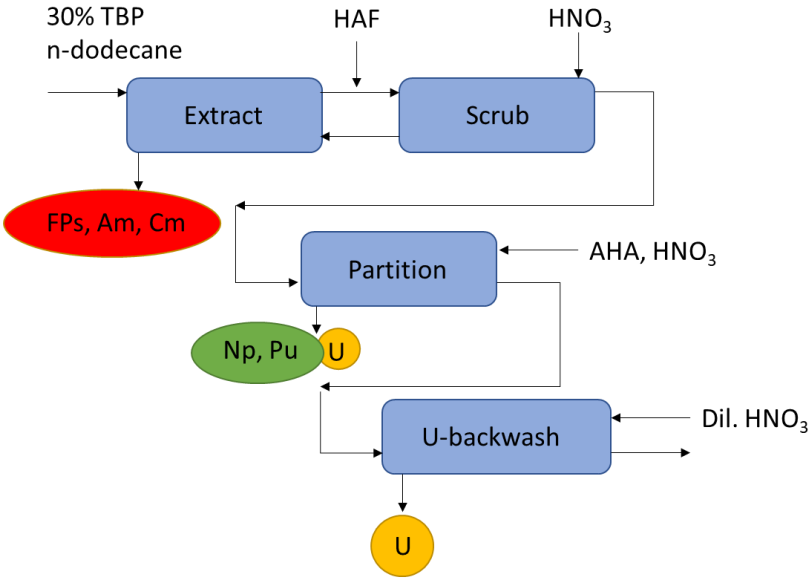

Figure 2.10: The single cycle Advanced PUREX process suitable for Gen IV fuel reprocessing.

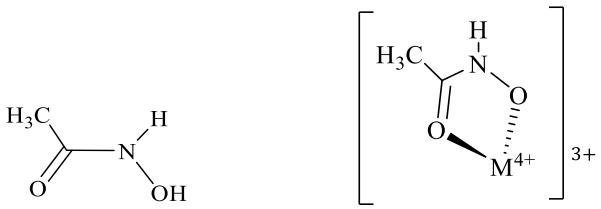

Figure 2.11: The structure of acetohydroxamic acid (left) and the principal complex formed in low acidity HNO_3 with a metal ion M^{4+}, where M^{4+} is Pu(IV) or Np(IV) (right).

hexavalent actinides in nitric acid, and thus complexes Np(IV) and Pu(IV), stripping them to the aqueous phase, whilst U(VI) is unaffected and remains in the organic solvent phase. In this way, the co-extraction of Np(IV) and Pu(IV) is achieved, avoiding a pure Pu stream and thus increasing the proliferation resistance of the process. The structure of AHA and the principal complex it forms in low acidity HNO_3 with Pu(IV) or Np(IV) is shown in Figure 2.11. Flowsheet trials at laboratory scale have demonstrated high actinide recoveries and decontamination factors on products

for active feeds up to 40 wt.% Pu [37] comparable with the requirements for Advanced flowsheets as stated by Birkett *et al*. and summarised in Table 2.2 [37].

Table 2.2: Key objectives within the design of an Advanced PUREX process for LWR and/or fast breeder reactor (FBR) fuel reprocessing.

Objective	How to meet it
Reduced costs	Reduction in plant footprint and size by the development of a single cycle flowsheet compatible with centrifugal contractors.
Reduction in waste arisings and environmental impact	Use of a single cycle flowsheet with fewer streams and lower volumes, and use of decomposable organic (CHON) reagents.
Reduced impact on geological repositories	Reduce heat loading in GDF via minor actinide separation processes.
Increased proliferation resistance	Avoid the separation of pure Pu by co-processing and integration with fuel fabrication.
Greater flexibility	Ability to processes much higher burnup MOx fuels within the flowsheet.
Enhanced process safety	Removal of U(IV)/hydrazine as a reductant and replacement with AHA.

Fuels reprocessed currently are generally oxide fuels with 1% or less Pu by mass, whereas a much higher Pu content, possibly tens of percent, is envisaged for future, higher burnup fuels. There are significant drawbacks with the use of U(IV)/hydrazine used for the reductive stripping of Pu in the current PUREX process, and many of which are exacerbated with increased Pu content fuels, thus replacement of this step by a complexation with AHA offers significant advantages in process safety. Other advantages of complexation include fast kinetics and relative temperature insensitivity compared to redox reactions, and additionally, AHA itself is a salt-free organic reagent that decomposes in nitric acid – so offering a convenient disposal route. These aspects

relating to the chemistry of hydroxamic acids will be described further in subsequent sections.

Extraction of not only U and Pu, but also Np, also reduces the radiotoxicity and heat load in the final HLW and thus the burden on any GDF. The extraction of other MAs and some FPs would reduce this further, and there are several modifications of this process under development for this purpose. One of these is the EURO-GANEX process described in the next section.

2.3.3 The EURO-GANEX Process

There are many advanced actinide management options under development worldwide, which are either based on a heterogeneous or homogeneous recycling concept. One of the aqueous flowsheets being developed by The Safety of Actinide Separation Processes (SACSESS) programme is the European Grouped Actinide Extraction (EURO-GANEX) process. This is an example of the latter concept, which involves the grouped recycling of all actinides (including Pu and the MAs) in a single stream [40]. The flowsheet for the GANEX process is a 2-cycle flowsheet, broadly similar to the Advanced PUREX flowsheet but employing different solvents, also improves proliferation resistance by eliminating the production of a pure plutonium stream [48]. The flowsheet for the overall GANEX process is shown in Figure 2.12.

The concept assumes that the heavy metal content of the dissolved SNF solution is initially reduced via a uranium extraction process (GANEX-1) which extracts U from the FPs, actinides and lanthanides, followed by subsequent separation on the highly

active aqueous stream for full recovery of the transuranic actinides (Np, Pu, Am, Cm) via the EURO-GANEX process [47].

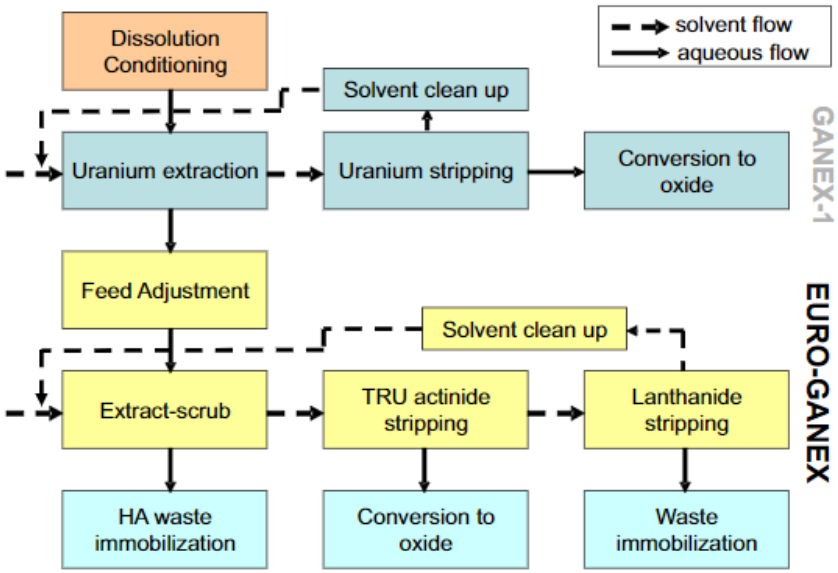

Figure 2.12: Flowsheet for the overall GANEX process (reproduced from open access source, reference [47]).

In the first, GANEX-1, cycle the feed is contacted with 1M N,N-di-2-ethylhexyl-isobutyramide (DEHiBA) dissolved in odourless kerosene, which selectively extracts the uranium and some actinide species and FPs, particularly neptunium and technetium, into the organic phase. A scrub or solvent clean up section then follows in which the solvent is contacted with hydrazine to re-extract technetium and neptunium back to the aqueous phase.

The 2nd cycle comprises a TRU Extraction and Scrub and TRU Back Extraction. The latter can be further divided into three sub-sections: i) Actinide Strip 1 in which the FPs are separated from the actinides and lanthanides, followed by ii) Actinide Strip 2, and iii) Lanthanide Strip. This cycle forms three output streams overall [49]. A number of reagents are utilised in these steps but an aqueous stream consisting of 0.5M nitric

acid, 0.55M bis-triazinyl pyridine (BTP) and 1M AHA is added between the Actinide Strip 2 and Lanthanide Strip sections for stripping the actinides from the lanthanides.

The overall goal to allow for complete closure of the fuel cycle is via elimination of 99.9% of the actinide elements from the reprocessing of SNF using P&T strategies, which would reduce the radioactivity of HLW by a factor of up to 100,000 [38], and thus the burden on a GDF. R&D on flowsheet development and optimisation is still ongoing but flowsheet demonstrations of the EURO-GANEX process so far have been highly successful, achieving almost complete recovery of Pu, Np and Am, and less than 0.1% lanthanide impurities in the actinide product and vice versa [50].

Both the options for AFCs described here include the use of AHA as a complexant for the co-extraction of Pu and Np. The remaining sections of this Chapter will therefore discuss the behaviour and important chemistry of hydroxamic acids in relation to the GANEX and, especially, Advanced PUREX processes and modifications thereof.

2.4 The Chemistry of Hydroxamic Acids

Simple hydroxamic acids (XHAs) such as formo- and acetohydroxamic acid (FHA and AHA) are hydrophilic, organic acids with the general structure RCONHOH. Figure 2.11 shows the structure of AHA for which R=CH_3. XHAs are structurally related to carboxylic acids, but with a much weaker dissociation [51], illustrated by the respective pKa values of 4.74 for acetic acid and 9.2 for AHA. They have several characteristics that identify them as suitable reagents for use in a GANEX and,

especially, an Advanced PUREX process. Their small organic backbone ensures a low solubility in TBP solvents, and they have the advantage of being salt-free, containing only C, H, O and N, meaning that they decompose in high temperature and/or highly acidic solutions to form NO_2 and CO_2 gases, thus not significantly adding to the aqueous waste [52].

They have been shown to reduce important actinides [53], for example, studies have shown the rapid reduction of Np(VI) by FHA [54] and by AHA [55] to inextractable Np(V) for separation from U. In strongly acidic media, Np(V) undergoes a disproportionation reaction to form Np(VI) and Np(IV) [56] which, coupled with the reduction of Np(V), could offer a potential route for the complete conversion to Np(IV), as the former of which would be reduced back to Np(V) and disproportionate once more. With tetravalent actinides such as Np(IV) and Pu(IV), hydroxamic acids form stable complexes while not affecting uranium extraction behaviour. This complexation behaviour with certain metal ions, which makes them suitable candidates for use in an Advanced PUREX process, will be described in the next section.

2.4.1 Complexation with Metal Ions

Hydroxamic acids are weak acids that act as O-O donor bidentate ligands with high affinities for hard cations with high charge densities such as Fe(III), Pu(IV) and Np(IV), with which they form strong 5-membered chelate rings [57]. While related to carboxylic acids, their metal chelates are generally much stronger. They have many applications including use as enzyme inhibitors, soil enhancers, spectrophotometric

reagents for the determination of metal ions, and uses in drug delivery systems and ion exchange applications among others [58]. They are also utilised by fungi in naturally occurring biomolecules called siderophores, which employ a hydroxamate group for sequestration of Fe from soils [59].

The complexation of a metal ion (*M*) and a monovalent ligand (*L*) is described by Eq. 2.10, where *z* is the charge of the metal ion and *n* is the number of interacting ligands [60]. The equilibrium constant for the formation of a complex with *n* number of ligands (K_n) is related to the stability constant (β_n) of that complex in solution by Eq. 2.11, where the {} braces denote the molar activity; the effective concentration of a species in solution. For systems where the activity of species is unknown and these true stability constants cannot be calculated, the conditional stability constants (β_n') can be determined from the molar concentration of each species by Eq. 2.12.

$$M_{(aq)}^{z+} + nL_{(aq)}^{-} \overset{K_n}{\rightleftharpoons} ML_n^{(z-n)+}{}_{(aq)} \tag{2.10}$$

$$\beta_n = K_1 \cdot K_1 \cdot \ldots \cdot K_n = \frac{\left\{ML_n^{(z-n)+}\right\}}{\left\{M^{z+}\right\}\{L^{-}\}^n} \tag{2.11}$$

$$\beta_n' = \frac{[ML_n^{(z-n)+}]}{[M^{z+}][L^{-}]^n} \tag{2.12}$$

XHAs preferentially complex tetravalent ions such as Pu(IV) and Np(IV), as can be observed in Table 2.3 in the form of higher stability constants for AHA complexes with these ions over U(VI) and others. AHA generally does not form strong complexes with actinides of other oxidation states, particularly the tri- and pentavalent oxidation states. Via a concept known as the actinide contraction, the ionic radii of the actinides in the same oxidation state systematically decreases along the series with the increase

in atomic number [65]. This is because the increase in the nuclear charge subsequently leads to a more effective attraction of the outer electron shell. The effect of a smaller radius is an increase in cationic charge density, and therefore greater attraction for the ligand and more rapid complex formation. Actinide ions therefore show an increase in the stability constants in line with an increase of effective cationic charge [66].

Table 2.3: Stability constants for the 1:1 to 1:5 complexes with AHA. [a] determined at 298K. [b] determined at 295K.

Reference	Metal ion	$\log \beta_1$	$\log \beta_2$	$\log \beta_3$	$\log \beta_4$	$\log \beta_5$
[57]	Fe(III)	10.94	20.68	28.26		
[61]	Fe(III)	11.00[a]	20.93[a]	28.75[a]		
[62]	Pu(III)	5.77[b]	11.66[b]	14.83[b]	15.84[b]	
[63]	Pu(IV)	14.2	24.1	32.2		
[64]	Np(IV)	12.83	22.96	31.00	36.17	39.33
[64]	U(IV)	12.25	22.24	30.11	34.36	36.80
[64]	U(VI)	7.94	14.11			

The complexation of these hydroxamic acids with certain metal ions is well understood. A less understood but important issue that must be addressed before XHAs can be employed in the implementation of an Advanced PUREX process, is their hydrolytic instability in acidic media that ultimately leads to their decomposition [67], particularly in the presence of these metal ions. This will be discussed in the following sections.

2.4.2 Acid-catalysed Hydrolysis of Free AHA

The acid catalysed hydrolysis of hydroxamic acids to form NH_2OH and the parent carboxylic acid (Eq. 2.13) is well known. The structure of the former product, NH_2OH, and its protonation in acidic media is shown in Figure 2.13. Although this hydrolytic instability is beneficial in terms of the downstream decomposition and removal / disposal of the ligand, it must be understood and controlled in any process flowsheet.

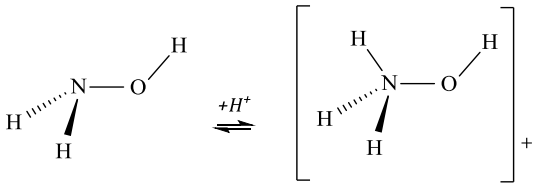

Figure 2.13: The structure of hydroxylamine in neutral (left) and acidic (right) media.

$$XHA + H_2O + H^+ \xrightarrow{k_0} RCOOH + NH_3OH^+ \qquad (2.13)$$

The established mechanism in the low to moderate acidity range is based on a collection of studies on both natural siderophores [68] and free hydroxamic acids in acidic media [67, 69, 70]. Consequently, it is widely accepted to be an addition-elimination reaction mechanism similar to that of amide hydrolysis; a multi-step associative bimolecular mechanism involving the formation of a tetrahedral intermediate. Mollin and Kucerova [71] first suggested the framework for the mechanism of the hydrolysis of hydroxamic acids. Further studies by Ghosh [67] on benzohydroxamic acid (BHA) and its derivatives provided a more detailed mechanism, that has been widely used to describe the behaviour of hydroxamic acids in general. This mechanism is shown in Figure 2.14.

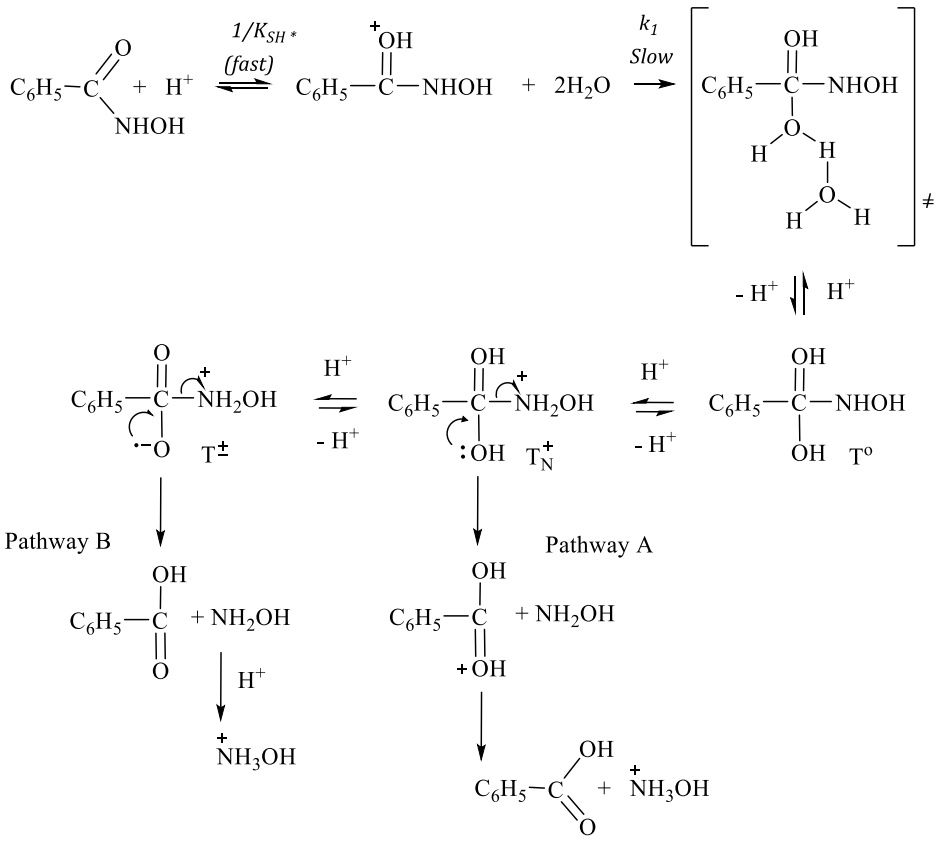

Figure 2.14: Mechanism for the acid-catalysed hydrolysis of BHA. Redrawn from reference [67].

The steps include: (i) a rapid pre-equilibrium protonation of the hydroxamic acid, (ii) the attack of water on the carbonyl group resulting in a neutral tetrahedral intermediate (T^O), and (iii) the recreation of the carbonyl group and the loss of the leaving group NH_2OH [67]. Step (iii) can happen in two ways. In highly acidic media which can support the formation of a protonated ester (T_N^+), hydroxylamine is lost directly (Pathway A). In low to moderately acidic media, it's more likely that the loss of an OH proton will give the zwitterion ($T^{\pm}$) which readily loses NH_2OH to give the corresponding acid by Pathway B [72].

The first study on the kinetics of the acid-catalysed hydrolysis of unsubstituted hydroxamic acids in aqueous solution was performed by Berndt and Fuller [73], who reported a linear increase of rate with increasing acid concentration for BHA over a low acidity range (0.1 - 0.58 mol dm^{-3} hydrochloric acid (HCl) equivalent to a pH of 0.26-0.79). Subsequent studies on unsubstituted hydroxamic acids have shown that a hydrolytic rate maximum exists at higher acidities, above which there is a decrease in the rate of XHA hydrolysis [67]. The overall rate acidity profile is therefore a bell-shaped curve, with the maximum thought to correspond to complete conversion of the substrate into the conjugate acid via Eq. 2.14. For simple hydroxamic acids such as FHA and AHA, this rate maximum falls in the range of acidities that are commonly accessed in reprocessing scenarios.

$$XHA + H^+ \rightarrow XHAH^+ \tag{2.14}$$

Studies on the hydrolysis of simple hydroxamic acids in the context of the PUREX process are commonly performed in the presence of the PUREX acid, HNO_3. In low to moderately acidic media, the kinetics for the acid catalysed hydrolysis of FHA [74] and AHA [69, 74-76] in HNO_3 have been found to follow second order kinetics in accordance with Eq. 2.15. In this equation, k_0 is the second order rate constant for the reaction as described, and k_0' is the corresponding pseudo first-order rate constant (i.e. incorporating $[H^+]$ in its definition). Due to the bell-shaped nature of the dependence of the rate of reaction on proton concentration, Eq. 2.15 is only valid up to 3 mol dm^{-3} HNO_3 ($pH \geq -0.48$), and when $[HNO_3] > [XHA]$.

$$-\frac{d[XHA]}{dt} = k_0'[XHA], \qquad \text{where } k_0' = k_0[H^+] \tag{2.15}$$

The kinetic rate constant for free AHA hydrolysis, k_0, has been determined by several authors using indirect measurements. Via analysis of UV-Vis spectra of Fe(III) bound to AHA in the form of the mono-complex, which has a maximum absorbance at 498nm, the remaining free AHA can be calculated. Using this method, Andrieux and co-workers [77] reported a value of $k_0 = 1.84\times10^{-5}$ $dm^3\cdot mol^{-1}\cdot s^{-1}$ at all pH > -0.5 in comparison to previously reported values of 3.42×10^{-5} and 2.5×10^{-5} $dm^3\cdot mol^{-1}\cdot s^{-1}$ by Taylor *et al.* [78] and Chung and Lee [69] respectively, using the same spectrophotometric based method. More recently, Quantitative Raman Spectroscopy (QRS) has also been utilised as a direct method for determining the kinetics of AHA hydrolysis, with these authors reporting a similar value of $k_0 = 2.53\times10^{-5}$ $dm^3\cdot mol^{-1}\cdot s^{-1}$ at 298K [79].

Having discussed the hydrolysis of free XHAs in acidic solution, a discussion of the less understood hydrolysis of XHAs when bound to a metal ion is required, particularly with regards to Np and Pu that undergo co-separation from U and transfer across the aqueous-organic interface a result of complexation by AHA within the Advanced PUREX process.

2.4.3 Acid-catalysed Hydrolysis of Complexed AHA

As mentioned previously, hydroxamic acids are ligands with high affinities for hard cations with high charge densities such as Fe(III), Pu(IV) and Np(IV). They are also redox active, with the onset potential for AHA oxidation determined on a gold

electrode as +0.62V vs. saturated calomel electrode (SCE) at pH 1 [74]. Fe(III) acts similar to tetravalent actinides, chemically speaking, and is therefore often used as a useful non-active analogue to Np(IV) and Pu(IV). To date, Fe(III) and Np(IV) have been characterized as metal ions that complex with but do not oxidize the ligand [80], whereas Pu(IV) does oxidize the ligand (see Section 2.4.3.3). These definitions are based on the observation that the AHA hydrolysis product NH_2OH, reduces Pu(IV) but not Fe(III) [81] and the suggestion that AHA itself may reduce Pu(IV) ions during complex hydrolysis [82].

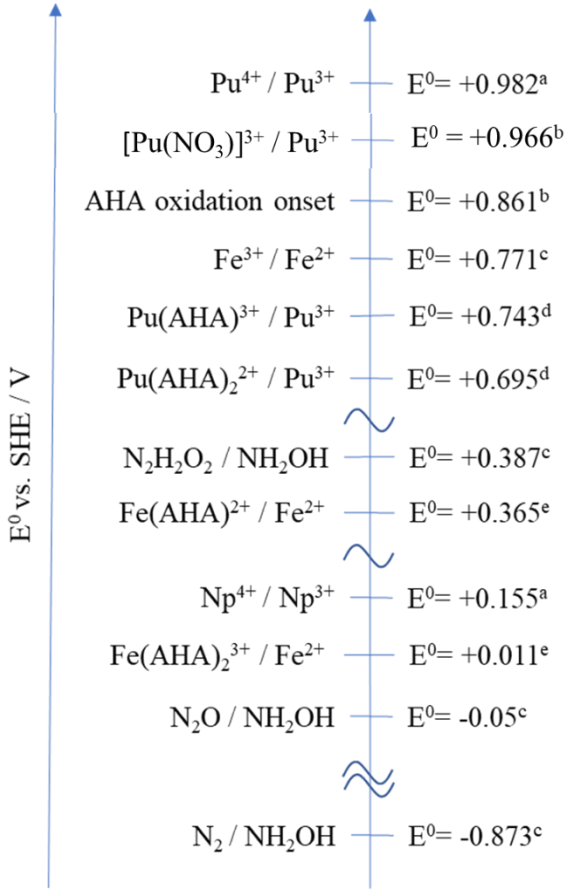

Figure 2.15: Schematic diagram showing formal redox potentials E^0 in volts (V) vs. standard hydrogen electrode (SHE). [a][Lemire, 2001], [b][Carrot et al., 2008], [c][Bard et al., 1985], [d][Andrieux et al., unpublished], [e]calculated in this thesis.

Figure 2.15 shows some standard redox potentials vs. standard hydrogen electrode (SHE), both experimentally determined and calculated values, for several redox couples relevant to these systems. Looking specifically at the free metal ion couples, observation of this figure shows that the reduction of Pu(IV) is thermodynamically possible by either AHA or it's hydrolysis product NH_2OH. In the case of Np(IV) and Fe(III), the reduction by NH_2OH is thought to be thermodynamically possible but kinetically hindered; in contrast, reduction of Np(IV) or Fe(III) ions by AHA is thermodynamically impossible.

Formal potentials for the reduction of $Pu(AHA)^{3+}$ and $Pu(AHA)_2^{2+}$ are calculated from electrochemical measurements obtained by Carrott *et al*. [74]. Whilst the authors suggested that thermodynamically, hydroxylamine should reduce Pu(IV)-AHA complexes, they did not observe this experimentally, and suggested that steric factors were likely resulting in kinetic hinderance. Similar theoretical potentials for the $Fe(AHA)^{2+}/Fe^{2+}$ and $Fe(AHA)_2^{3+}/Fe^{2+}$ couples have additionally been calculated in this thesis and will be described in Chapter 5.

Having introduced the three primary metal ions of interest with regards to AHA/HNO_3 systems, the following sections will now discuss the speciation and complex hydrolysis kinetics of each of the systems in more detail, beginning with Fe(III).

2.4.3.1 The Fe(III)-AHA system

Study of the hydrolysis of metal-AHA systems in HNO_3 or other acidic media, requires knowledge of the complex speciation. Analogous to Np(IV) and Pu(IV), Fe(III) is

known to form mono-, bis- and tris-hydroxamato complexes with AHA by the following equilibria (Eqs. 2.16 - 2.18), where *HL* = hydroxamic acid and *L* = hydroxamate anion. The structure of the three complexes is shown in Figure 2.16. From preliminary investigations by stopped flow spectroscopy in the presence of excess Fe(III), Taylor *et al.* [64] suggested the complexation kinetics of the mono-complex were rapid, but these are complicated in the presence of excess AHA and [H^+] by the equilibria for the 1:2 and 1:3 complexes.

$$HL + Fe^{3+} \overset{K_1}{\rightleftharpoons} FeL^{2+} + H^+ \qquad K_1 = 62.46 \tag{2.16}$$

$$HL + FeL^{2+} \overset{K_2}{\rightleftharpoons} FeL_2^{+} + H^+ \qquad K_2 = 2.81 \tag{2.17}$$

$$HL + FeL_2^{+} \overset{K_3}{\rightleftharpoons} FeL_3 + H^+ \qquad K_3 = 1.58 \times 10^{-2} \tag{2.18}$$

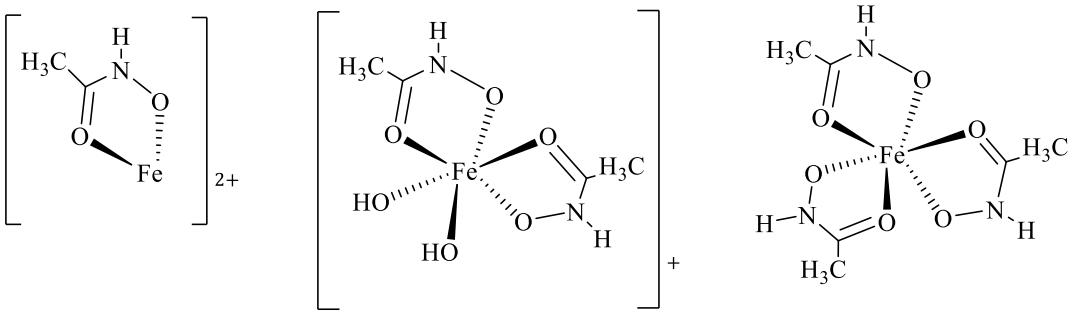

Figure 2.16: From left to right: Chemical structure of the mono-, bis- and tris-acetohydroxamatoiron(III) complexes, formation of which is described by Eqs. 2.16 – 2.18.

Andrieux *et al.* [77] performed a kinetic study on hydrolysis in Fe(III)-AHA systems in HNO_3 at 293K; using UV-Vis spectroscopy to follow the mono-complex hydrolysis, given by Eq. 2.19, via its maximum absorbance at 498nm, and calculating the free AHA remaining. Using their data obtained for the acid-catalysed hydrolysis of Fe(III)-complexed AHA, these authors developed a kinetic model for the hydrolysis of XHAs

in the presence of a complexing but non-oxidising metal ion (Fe(III) and Np(IV)). These authors reported on hydrolysis kinetics from experiments conducted at a constant AHA:Fe(III) ratio of 1.6:1 where mono-complex dominates, at 298K and over a range of pH values. From this low temperature study, they concluded equivalent pseudo-first order kinetics for the complex, via Eq. 2.20, and a mechanism analogous to that of free AHA. Their reported value for k_1 = 1.02×10^{-4} dm^3·mol^{-1}·s^{-1} was greater than the analogous k_0 parameter, except pH < -0.5 where they obtained a negative value of k_1. They attributed this to a change in mechanism due to the complete conversion of AHA into its conjugate acid AHAH$^+$.

$$FeL^{2+} + H_2O + H^+ \overset{k_1}{\rightarrow} Fe^{3+} + RCOOH + NH_3OH^+ \tag{2.19}$$

$$-\frac{d[FeL^{2+}]}{dt} = k_1'[FeL^{2+}], \qquad \text{where } k_1' = k_1[H^+]^{m=1} \tag{2.20}$$

Following this initial study, the same authors then reported on the temperature dependant speciation of Fe(III)-AHA complexes in acidic media and determined values for the complex equilibrium constants K_1 - K_3 at 293-323K, each under conditions where the concentrations of other complexes were thought to be minimal, in a pH range of 0.2-0.93 ([acid] = 0.1-0.65 mol dm^{-3}) [57]. The equilibrium constants shown in Eqs. 2.16 - 2.18 are those they reported at 293K. Using their published temperature dependent speciation data to determine conditions where the mono-complex dominated, they produced a further publication on the kinetics of the hydrolysis of Fe(III)-complexed AHA at low pH (pH = 1.02) and elevated temperatures up to 333K. They found $k_1 > k_0$ for at all temperature considered, and thus concluded that complexed AHA is more susceptible to hydrolysis than free AHA.

The Arrhenius relationship for a rate constant *k* is shown in Eq. 2.21, where *R* is the Gas constant, and T is temperature.

$$k = Ae^{\frac{-E_a}{RT}} \tag{2.21}$$

From a collection of studies in the literature, the Arrhenius factor (*A*) and activation energy (E_a) for the acid-catalysed hydrolysis of free AHA has been shown to be approximately 4×10^9 $dm^3 \cdot mol^{-1} \cdot s^{-1}$ and 80 $kJ \cdot mol^{-1}$ respectively, see Table 2.4. Taylor and co-workers [78] provided one of the first studies on the acid-catalysed hydrolysis of the Fe(III)-complexed AHA and, whilst they didn't specifically quote their value, they stated that E_a for the hydrolysis of the ligand in the complex was approximately 30 $kJ \cdot mol^{-1}$ lower than that of their previously determined value of E_a = 79.9 $kJ.mol^{-1}$ for the free ligand hydrolysis. More recently, Andrieux *et al.* [83] have determined *A* and E_a for the hydrolysis of the complexed ligand to be 2.44×10^{11} $dm^3 \cdot mol^{-1} \cdot s^{-1}$ and 89.6 $kJ \cdot mol^{-1}$ respectively, also shown in Table 2.4. These values correspond to an increase with respect to the free ligand of approximately 2 orders of magnitude in *A* and 10 $kJ \cdot mol^{-1}$ in E_a.

Table 2.4: Activation parameters for the acid-catalysed hydrolysis of free and Fe(III)-complexed AHA.

Ref.	Metal ion	$[HNO_3]$ / M	T / K	*A* / dm^3 mol^{-1} s^{-1}	E_a / kJ mol^{-1}	$\Delta H^{\neq}$ / kJ mol^{-1}	$\Delta S^{\neq}$ / $J.K^{-1}$ mol^{-1}
[78], [74]	-	0.5–3	298	3.22×10^9	79.9	-	-
[69]	-	1 – 3	298-318	4.64×10^9	81.4	-	-
[84]	-	1.5 - 2.5	298-313	-	76.27	73.68	-79.24
[83]	-	0.1	293-333	4.24×10^9	80.1	77.2	-70.3
[84]	Fe(III)	0.1	293-333	2.44×10^{11}	89.6	87.0	-35.7

The enthalpy ($\Delta H^{\#}$) and entropy ($\Delta S^{\#}$) of activation for the hydrolysis processes can be obtained from a collection of temperature dependent rate parameters using the linear form of Eyring's equation (Eq. 2.22), where h is Planck's constant and k_B is Boltzmann's constant.

$$\ln\frac{k}{T} = -\frac{\Delta H^{\#}}{RT} + \ln\frac{k_B}{h} + \frac{\Delta S^{\#}}{R} \tag{2.22}$$

Andrieux *et al.* [83] reported values for $\Delta H^{\#}$ of 77.2 kJ·mol^{-1} and 87.0 kJ·mol^{-1} and values for $\Delta S^{\#}$ of -70.3 J·mol^{-1}·K^{-1} and -35.7 J·mol^{-1}·K^{-1} for the free and complexed ligand hydrolysis respectively, which compare well with previously reported values, see Table 2.4. These authors correlated the differences in the $\Delta H^{\#}$ values for the free and complexed AHA hydrolysis, which is the major component associated with bond breaking in the transition state, with quantum mechanical modelling to suggest a subtly different mechanism. Illustrated in Figure 2.17, they proposed a difference in the initial protonation step, with the bound ligand protonating on the nitrogen rather than the carbonyl oxygen, producing a transition state with a lower degree of order as indicated by the entropy of activation.

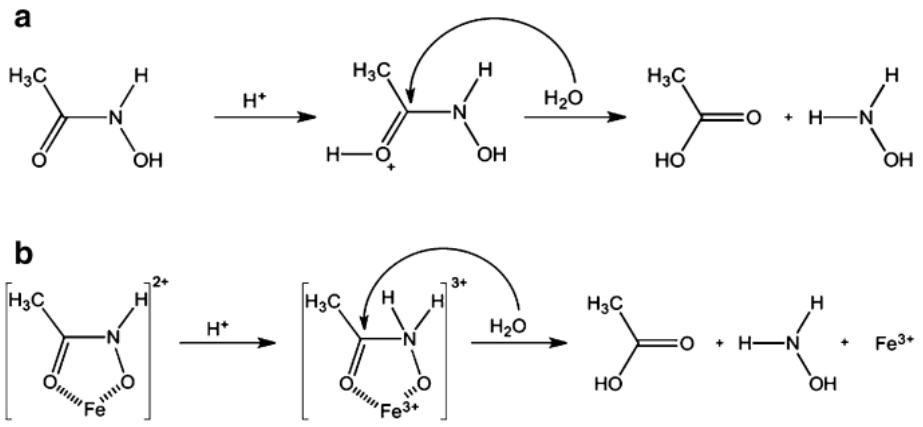

Figure 2.17: Proposed mechanism for the acid-catalysed hydrolysis of; a) free AHA and b) Fe(III)-complexed AHA [83] (reproduced with permission from reference [83], copyright 2014 Springer Nature).

The Fe(III)-AHA system is considered a useful non-active actinide analogue for studying the hydrolysis of both free and metal-complexed AHA, as other interfering complexation or redox reactions that must be considered with regards to Np(IV) and Pu(III) are thought to be absent. Kinetic analysis of the Fe(III)-AHA system can therefore provide a basis for study of the Np(IV)-AHA system, which is described in the next section, and finally the Pu(IV)-AHA system.

2.4.3.2 The Np(IV)-AHA system

While Fe(III) and Np(IV) are both defined as complexing but non-oxidizing with regards to AHA, Np(IV) has additional complications over Fe(III) due to the formation of weak Np(IV) mono- and di-nitrate complexes, which limit the availability of Np(IV) for complexation with AHA [85]. Taylor *et al.* [86] first determined stability constants at 295K of $\log \beta_1 = 12.83$, $\log \beta_2 = 22.96$ and $\log \beta_3 = 30.06$ for the mono-, bis- and tris- Np(IV)-AHA complexes respectively in non-complexing perchlorate media at a constant ionic strength (I) of 2.0 mol dm^{-3}. Those for the equivalent Np(V)-complexes

were found to be significantly lower, with $\log \beta_1 = 4.83$ for the mono-complex [86], and thus β_1 differing by eight orders of magnitude compared to that for Np(IV).

These authors later performed some studies on the hydrolysis of Np(IV)-XHA complexes at [HNO_3] of 0.79 mol dm^{-3} – 1.30 mol dm^{-3} (0.10 > pH > -0.11). Whilst they observed pseudo first-order kinetics analogous to that of free XHA when the concentration of the metal was approximately equal to that of *XHA*, an S-shaped or exponential decay was observed when [metal] « [*XHA*] [64]. In the latter case, an induction period was observed, where the concentration of the complex remained initially constant, which had not been observed for the hydrolysis of free FHA or Fe(III)-complexed AHA. They attributed this to an immediate re-complexation of the free metal ions produced from the complex hydrolysis while free XHA remained, and the removal of the complex was only observed once the free XHA was fully hydrolysed.

Later, Andrieux *et al.* [80] studied hydrolysis kinetics of the 1:1 Np(IV)-FHA complex in HNO_3. By using previously published speciation data and interpretation of Np(IV) absorption spectra in the presence of AHA and FHA, they first identified conditions under which the 1:1 Np(IV)-FHA complex was the dominant species, and obtained spectrophotometric Np(IV)-FHA hydrolysis data under these conditions. They applied their kinetic model developed previously for hydrolysis of XHAs in the presence of a complexing but non-oxidising metal ion to this data, but with a slight modification; the formation of weak nitrate complexes was taken into account by the incorporation of a modified K_1' for nitrate-complexing actinide(IV) species via Eq. 2.23, where K_d is the dissociation constant for the weak nitrate complex.

$$K_1' = -\frac{K_1}{1 + ([NO_3^-]_T/K_d)} \quad (2.23)$$

In agreement with Taylor *et al.* [64], these authors also observed an induction period. They attributed this to a high equilibrium constant for the 1:1 Np(IV)-FHA complex (estimated in their study to be K_1 = 2754), meaning that the complex will be present at a significant concentration for a longer period before it breaks down at the lower ligand concentrations. Using this approach, they estimated the parameter k_1' to be less than k_0', obtaining values of k_1'= 7.9×10^{-6} s^{-1} and 1.3×10^{-5} s^{-1} at 0.79 and 1.3 mol dm^{-3} HNO_3 respectively, thus concluding that complexation protects the ligand from hydrolysis at 0.1 > pH > -0.1. The authors explain this by assuming an analogous mechanism to that of the Fe(III)-AHA system; in the initial rate-determining step, the 3+ charge on the NpL^{3+} complex in the makes the interaction with a proton more unfavourable compared to the same interaction with the FeL^{2+} complex.

$$HL + Np^{4+} \overset{K_1}{\rightleftharpoons} NpL^{3+} + H^+ \qquad K_1 = 5370 \quad (2.24)$$

$$HL + NpL^{3+} \overset{K_2}{\rightleftharpoons} NpL_2^{2+} + H^+ \qquad K_2 = 10.71 \quad (2.25)$$

$$HL + NpL_2^{2+} \overset{K_3}{\rightleftharpoons} NpL_3^{+} + H^+ \qquad K_3 = 1.0 \times 10^{-2} \quad (2.26)$$

$$Np^{4+} + OH^- \overset{K_{1,OH}}{\rightleftharpoons} NpOH^{3+} \qquad \log_{10} K_{1,OH}^0 = 1.23 \quad (2.27)$$

$$Np^{4+} + NO_3^- \overset{\beta_{1,OH}}{\rightleftharpoons} Np(NO_3)^{3+} \qquad \log_{10} \beta_{1,NO_3}^0 = 1.79 \quad (2.28)$$

$$Np^{4+} + 2NO_3^- \overset{\beta_{2,OH}}{\rightleftharpoons} Np(NO_3)_3^{2+} \qquad \log_{10} \beta_{2,NO_3}^0 = 2.29 \quad (2.29)$$

More recently, Edwards *et al.* [58] have performed a full kinetic analysis on the Np(IV)-AHA system in HNO_3, including the mono- and bishydroxamato-complex

hydrolysis, and the formation of the mono- and bisnitrato-Np(IV) complexes, and the Np(IV)-OH complex. Their values for Np(IV)-AHA complex equilibrium constants $K_1 - K_3$, given in Eqs. 2.24 – 2.26 above, are reported at 295K and 1 mol dm^{-3} HNO_3. Based off stability constants for the complex formation reported by Sinkov [86], these authors used Specific Ion Interaction (SIT) theory to calculate values at the conditions specific to their study, incorporating the AHA dissociation constant in their calculations. Additionally, the authors used SIT theory for the calculation of conditional stability constants for the $NpOH^{3+}$ and mono- and bisnitrato-Np(IV) complexes as shown in Eqs. 2.27 – 2.29. Their values for $\log_{10} \beta^0_{1,NO_3}$ = 1.79 ± 0.14 and $\Delta\varepsilon_{1,NO_3}$ = 0.13 ± 0.03) kg·mol^{-1} compare favourably with the values of $\log_{10} \beta^0_{1,NO_3}$ = 1.90 ± 0.15 and $\Delta\varepsilon_{1,NO_3}$ = -(0.09 ± 0.05) kg·mol^{-1} reported in a critical review by Lemire [87]. In the absence of AHA, these authors reported that the $NpOH^{3+}$ concentration is negligible at [HNO_3] > 0.50 mol dm^{-3}, and the nitrate complexes dominate at [HNO_3] > ∼0.30 mol dm^{-3}, particularly the $Np(NO_3)^{3+}$ complex which quickly rises to a maximum value at [HNO_3] = ∼1 mol dm^{-3}. Through their modelling of kinetic data at pH = 0, and they reported hydrolysis rate parameters for the mono- and bis-hydroxamato complexes of $k_1 = 3.5\times10^{-5} \pm 2.5\times10^{-5}$ $dm^3\cdot mol^{-1}\cdot s^{-1}$ and $k_2 = 1.9\times10^{-3} \pm 1.3\times10^{-3}$ $dm^3\cdot mol^{-1}\cdot s^{-1}$ respectively at 298K. In contrast to the Np(IV)-FHA system, they found $k_2 > k_1 > k_0$, indicating that complexation of Np(IV) with AHA increases the rate of ligand hydrolysis. With this trend being the same as that observed in the Fe(III)-AHA system , a similar mechanism was suggested to operate, with the carbonyl carbon in the transition state being more susceptible to nucleophilic attack due to the electron withdrawing effect of the Np(IV) centre.

In comparison to the Fe(III)-AHA system, further knowledge of the speciation is required with Np(IV), not only with AHA, but also with nitrate ions from the acidic media itself. It is still currently considered possible however to study the complex hydrolysis reactions so long as the speciation is known. Further interfering reactions however can occur in the case of the Pu(IV)-AHA system, which is discussed in the next section.

2.4.3.3 The Pu(IV)-AHA system

In comparison to those containing the non-oxidizing metal ions Fe(III) or Np(IV), acidic solutions of AHA containing Pu(IV) show another added complexity in the form of the reduction of Pu(IV) to Pu(III) during the associated complex hydrolysis. While this has been known for many years, the complexity and conditions in the reaction system have made identification of the specific redox reactions difficult [51]. By following the growth of the Pu(III) absorption band at 908nm, Carrot *et al.* [74] showed the slow reduction of AHA-complexed Pu(IV) to free Pu(III) ions to be characterized by a variable induction period where no Pu(III) is seen, followed by a near zero-order growth in Pu(III). These authors suggested a mechanism for this whereby Pu(IV) is initially strongly stabilized as the hydroxamate complex, while excess free AHA is being continuously depleted by hydrolysis. At a critical point, the complex then starts to dissociate and releases a reducible form of Pu(IV) (as free Pu(IV) or $PuNO_3^{3+}$), and the Pu(IV) is then rapidly reduced by either the AHA itself, or NH_2OH.

With their model previously developed for the hydrolysis of XHAs in the presence of non-oxidizing metal ions (Fe(III) and Np(IV)), Andrieux *et al.* [82] then reviewed data on the hydrolysis of XHAs in the presence of Pu(IV) ions, following Pu(III) ingrowth under conditions of a large excess of XHA to Pu(IV) in 1M HNO_3 at 291K. Under these conditions the authors thought that redox processes could potentially be neglected and they could adopt the approach whereby nitrate and AHA are expected to competitively complex Pu(IV) but the concentration of AHA was not so high as to allow the formation of nitrate-AHA cross complexes [88]. The speciation of the system considered was therefore described by Eqs. 2.30 – 2.34 below.

$$HL + Pu^{4+} \overset{K_1}{\rightleftharpoons} PuL^{3+} + H^+ \qquad K_1 = 14{,}516 \qquad (2.30)$$

$$HL + PuL^{3+} \overset{K_2}{\rightleftharpoons} PuL_2^{2+} + H^+ \qquad K_2 = 0.562 \qquad (2.31)$$

$$HL + PuL_2^{2+} \overset{K_3}{\rightleftharpoons} PuL_3^{+} + H^+ \qquad K_3 = 1.2 \times 10^{-2} \qquad (2.32)$$

$$Pu^{4+} + NO_3^- \overset{K_{1,NO_3}}{\rightleftharpoons} Pu(NO_3)^{3+} \qquad K_{1,NO_3} = 3.23 \qquad (2.33)$$

$$Pu(NO_3)^{3+} + NO_3^- \overset{K_{2,NO_3}}{\rightleftharpoons} Pu(NO_3)_3^{2+} \qquad K_{2,NO_3} = 3.47 \qquad (2.34)$$

Using previously published values of K_{1,NO_3} or K_{2,NO_3} (reported for I = 2.0 mol dm^{-3}) [81], and stability constants for the formation of Pu(IV)-AHA complexes.[63], these authors calculated the equilibrium constants shown in Eqs. 2.30 – 2.32 for the formation of the Pu(IV)-AHA complexes under their experimental conditions. Based on the extremely high calculated value of K_1 compared to that of K_2, K_3, K_{1,NO_3} or K_{2,NO_3}, they suggested that the chemistry of the Pu(IV)-AHA system would likely be dominated by the monohydroxamato complex rather than the higher complexes or the

nitrato-complexes, even in the presence of a large excess of hydroxamic acid. Calculation of speciation diagrams with a 24-fold excess of AHA showed this to be true for -0.8 < pH <1.3, with the bishydroxamato complex only present at non-negligible amounts at pH > 0.5. Under these conditions, they found the formation of the nitrato-complexes, primarily as the bisnitrato complex, only at pH < -0.8, the formation of which was accounted for the by use of an analogous K_1' parameter as used for the Np(IV)-AHA system [80].

From the described kinetic analysis, Andrieux *et al*. [82] reported a rate parameter for the hydrolysis of the bound ligand of $k_1' = k_1[H^+] = 1.45\times10^{-3}\ s^{-1}$, which is two orders of magnitude larger than that obtained for the free AHA hydrolysis of $k_0' = k_0[H^+] = 1.47\times10^{-5}\ s^{-1}$. They suggested that, as for Fe(III) and Np(IV)-complexed AHA, complex formation with Pu(IV) increases the rate of hydrolysis and that the higher the co-ordination number, the faster the hydrolysis of the ligand proceeds.

Having discussed the speciation and hydrolysis of AHA in the presence of metal ions, the final sections will describe the chemistry of the AHA hydrolysis product, hydroxylamine. This is important to understand for two reasons; i) under high acid, high temperature conditions, hydroxylamine can react autocatalytically / explosively with nitric acid, which is ubiquitous in reprocessing flowsheets, and ii) the nature of the reducing agent for the reduction of free Pu(IV) ions in the presence of AHA is still unclear, potentially being the hydroxamic acid itself, or hydroxylamine. The known chemistry of hydroxylamine with regards to its reaction with HNO_3 and metal ions will therefore be described in the following sections.

2.5 The Chemistry of Hydroxylamine

2.5.1 Instability in Nitric Acid

Hydroxylamine is oxidised by both nitrous and nitric acid. For the more familiar reaction of hydroxylamine with nitrous acid, the kinetics and mechanism have been investigated in some detail, with the reaction having been found to occur readily in aqueous solution at room temperature according to Eq. 2.35 [89].

$$NH_3OH^+ + HNO_2 \xrightarrow{k_{HNO_2}} N_2O + H_3O^+ + H_2O \qquad (2.35)$$

Values for the rate parameter, k_{HNO_2}, have been published by a number of authors [90-92] from measurements made in both nitric and perchloric acid media at I = 0.1 – 6.0 mol dm^{-3} and temperatures of 273 – 323K. Barney [90] reports an increase in the rate constant from 10.0 ±0.8M^{-2}sec^{-1} – 35.6 ± 1.0M^{-2}s^{-1} in the range of 303 – 323K in HNO_3 media at I = 2.00, and observed rate constants in the range of 8.27 – 11.14 M^{-2}s^{-1} for H^+ concentrations of 0.3 – 1.89M at 298K in HNO_3 media at I = 2.00. Rate constants of 13.1 – 24.2 M^{-1}s^{-1} have been reported in 2-6M $HClO_4$ at 298K. Measurements at 298K in HNO_3 media have shown that at higher ionic strengths of 4M, the rate constant increases with increasing acid concentration until it reaches a maximum of approximately 30 M^{-1}s^{-1} between 0.5 and 1.0 M H^+, after which it decreases [91].

However, hydroxylamine can also be oxidised by HNO_3 to form nitrous acid (HNO_2) via Eq. 2.36 and subsequently dinitrogen monoxide (N_2O) via Eq. 2.35, in proportions that vary with the reaction conditions. From their experiments of varying initial

[HNO_2] and [NH_3OH^+] at 25°C and 3 mol dm^{-3} H^+, Bennett *et al*. [91] observed the products of the above mentioned reaction of hydroxylamine with HNO_3 to be HNO_2, N_2O, and additionally N_2 from a reaction of HNO_2 with hyponitrous acid, the yields of which were all dependent on the initial NH_3OH^+ and HNO_2.

$$NH_3OH^+ + 2HNO_3 \rightarrow 3HNO_2 + H_3O^+ \quad (2.36)$$

When investigating the oxidation of hydroxylamine by HNO_3, Pembridge and Stedman [92] found aqueous solutions of hydroxylammonium nitrate (HAN) to be stable at room temperature, but to react autocatalytically by Eq. 2.36 when heated with excess HNO_3. Specifically, they found the reaction to be characterized by an induction period followed by the rapid autocatalytic process – suggesting that the main reaction product, HNO_2, acts as a catalyst for the HAN/nitric acid reaction described by Eq. 2.36. Gowland and Stedman [93] later studied this further, producing boundary conditions for the decomposition of hydroxylamine in nitric acid (Figure 2.18) by plotting the yield nitrous acid, $Y = ([HNO_2]_\infty - [HNO_2]_0)/[NH_3OH^+]_0$ against $[NH_3OH^+]_0$ and extrapolating to $Y = 0$. Nitric acid solutions of HAN are stable in the region of low [HNO_3] and T, where the nitrous acid scavenging reaction (Eq. 2.35) dominates over the reaction that produces it (Eq. 2.36) [94], so inhibiting any autocatalytic effect that the nitrous may have on the latter process.

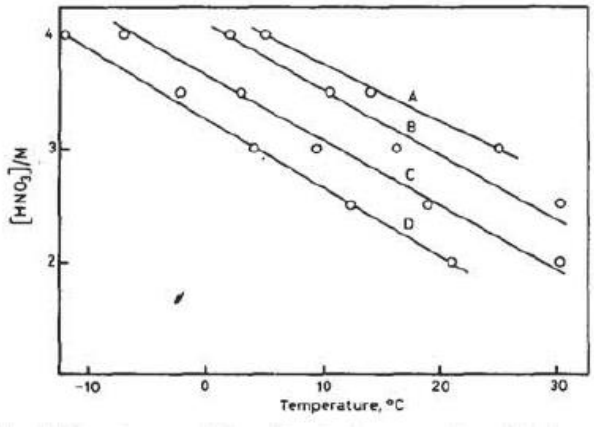

Figure 2.18: Boundary conditions for the decomposition of NH_3OH^+ in nitric acid with (A) $[NH_3OH^+]/M$ =0.05. (B) 0.02. (C) 0.01. (D) 0.005. Solutions of HAN in nitric acid are stable below the lines and unstable above them [93] (reproduced with permission from source [93], copyright 1981 Elsevier).

From their investigations, these authors found the HNO_2 scavenging reaction to follow simple second order kinetics (Eq. 2.37) at low hydroxylamine (<0.01 mol dm^{-3}), and fixed HNO_3 concentrations in the range 3 - 8 mol dm^{-3}.

$$-\frac{d[HNO_2]}{dt} = k_{HNO_2}[HNO_2][NH_3OH^+] \qquad where\ k_{HNO_2} = k[H^+] \qquad (2.37)$$

The reaction rate constant, k_{HNO_2}, varied only slightly in this range, but when HNO_3 fell below 3 mol dm^{-3} a "critical" concentration was reached and k_{HNO_2} fell sharply to zero [94]. Bennett *et a1.* [91] then later studied the reaction in solutions of constant ionic strength $LiNO_3$ + HNO_3, providing a more quantitative treatment of k_{HNO2} using calculated values of the hydrogen ion activity a_{H^+}. This is shown in Eq. 2.38 below, where *c*, *d* and *f* are constants. Under the conditions studied by these authors, a_{H^+} was calculated to be almost proportional to the molar concentration of nitric acid, equivalent to $[H^+]$.

$$k_{HNO_2} = \frac{c(a_{H^+})}{1 + d(a_{H^+}) + f(a_{H^+})^2} \qquad (2.38)$$

The mechanism proposed by Pembridge and Stedman [92] to describe the observed autocatalytic appearance of HNO_2 from the oxidation of hydroxylamine by HNO_3 is given by Eqs. 2.39 – 2.43.

$$HNO_2 + H^+ + NO_3^- \rightleftharpoons N_2O_4 + H_2O \qquad \textit{Rate-determining step} \qquad (2.39)$$

$$N_2O_4 + NH_2OH \rightarrow HNO + N_2O_3 \qquad (2.40)$$

$$N_2O_4 + HNO \rightarrow HNO_2 + N_2O_3 \qquad (2.41)$$

$$N_2O_3 + H_2O \rightarrow 2HNO_2 \qquad \textit{Fast} \qquad (2.42)$$

$$NH_3OH^+ \rightleftharpoons NH_2OH + H^+ \qquad (2.43)$$

The nitrate ion is a weak nucleophile and therefore the initial rate of formation of N_2O_4, which controls the rate of N_2O_3 and subsequently rate of HNO_2 regeneration, is slow. When the concentration of NH_2OH is sufficiently great to capture every molecule of N_2O_4 by Eqs. 2.40 and 2.41, the rate of HNO_2 generation is controlled by this slow N_2O_4 generation, which is independent of $[NH_3OH^+]$. When $[NH_3OH^+]$ falls, the rate of HNO_2 scavenging decreases much more quickly, and the system crosses the boundary conditions where Eq. 2.36 dominates, resulting in the generation of HNO_2 and promotion of the autocatalysis.

These reactions that result in the destruction of NH_2OH are therefore important to be understood in terms of process safety for any advanced reprocessing flowsheet involving the use of AHA. Finally, the next section will discuss the capability of NH_2OH as a potential reducing agent in the case of Pu(IV) in the presence of AHA, and the analogous reduction of Fe(III).

2.5.2 Redox Reactions with Metal Ions

Along with other one-equivalent metal ion oxidants such as Fe(III), Pu(IV) can undergo a reduction reaction with hydroxylamine. The reaction of Pu(IV) with hydroxylamine nitrate (HAN) in nitric acid media was first studied by G. Scott Barney [95] and found to follow one of two pathways (Eqs. 2.44 and 2.45) with a variable stoichiometry that depends on the initial ratio $R = [Pu(IV)]_0/[NH_3OH^+]_0$.

$$2NH_3OH^+ + 4Pu^{4+} \rightarrow 4Pu^{3+} + N_2O + H_2O + 6H^+ \qquad \text{when R > 1} \qquad (2.44)$$

$$2NH_3OH^+ + 2Pu^{4+} \rightarrow 2Pu^{3+} + N_2 + 2H_2O + 4H^+ \qquad \text{when R < 1} \qquad (2.45)$$

These authors varied the HNO_3 concentration in the range of 1.5 - 2.5 mol dm^{-3}, while keeping the total ionic strength constant at I = 2.5 by the addition of sodium perchlorate. From their experimental studies under conditions of excess HAN, these authors suggested a mechanism described by Eqs. 2.46 and 2.47 and rate equation described by Eq. 2.48 for the more likely one-equivalent reduction of Pu(IV). The overall reaction is thought to follow a two-step process whereby; 1) the reduction reaction forms an unstable radical, and rapidly approaches equilibrium with the reverse reaction (Eq. 2.46), and 2) the slow dimerization of this radical then becomes the final rate-controlling step (Eq. 2.47).

$$Pu^{4+} + NH_2OH \rightleftharpoons Pu^{3+} + NH_2O^* + H_2O \qquad (2.46)$$

$$2NH_2O^* \rightarrow N_2 + 2H_2O \qquad (2.47)$$

$$\frac{-d[Pu(IV)]}{dt} = k' \frac{[Pu(IV)]^2[NH_2OH^+]^2}{[Pu(III)]^2[H^+]^4(K_d + NO_3^-)^2} \qquad (2.48)$$

The (K_d + [NO_3^-]) term in the denominator of Eq. 2.48 relates to the formation of the single $(Pu(IV)NO_3)^{3+}$ complex, with a dissociation constant K_d, although higher Pu(IV)-nitrate complexes are known to form [96]. An independent study by Koltununov and Zhuravleva [97] gave results at 303K that agreed reasonably well with the rate law above. These authors had also used a large excess of hydroxylamine, with HAN/Pu ratios of 40, but maintained a constant [NO_3^-] of 3 mol dm^{-3} by the addition of sodium nitrate while varying the [HNO_3] from 0.985 - 2.8 mol dm^{-3}. Their derived kinetic relationship thus differed by the absence of any nitrate dependence.

A later report by Yarbro *et al.* [98] noted that, while the original kinetic relationship was good at the high HAN/Pu ratios, it was poor at the low HAN/Pu ratios more typical to that found in reprocessing plants. These authors thus chose to conduct experiments at a constant HAN/Pu ratio of 2 while varying the [HNO_3] and [NO_3^-] from 2.4 to 7.0 mol dm^{-3}. Rather than define a kinetic expression in terms of concentrations, they defined an expression in terms of a fractional conversion, $X = 1 - \left(N_A/N_{A_0}\right)$, where N_{A_0} is the initial number of moles of reactant A, and N_A is the number of moles at time t, which they fit to Pu(III) ingrowth data. These authors said they obtained good fits but suggested that their model could be improved to include the kinetics of HAN oxidation by nitric acid and re-oxidation of Pu(III) by nitrous acid at a minimum.

Similarly, the reduction of Fe(III) by HAN has been studied by Bengtsson and co-workers [99], who found the reaction to occur by analogous pathways depending on the initial metal/HAN ratio. They reported an analogous rate equation for the one-equivalent reduction of Fe(III) to Fe(II) to that of Pu(IV) to Pu(III), with the exception of no (K_d + [NO_3^-]) term due to the absence of nitrate complex formation. In contrast

to the reduction of Pu(IV) where the rapid 2:1 stoichiometry is seen when R >1, these authors found that the formation of purely N_2O via this pathway only occurred if the initial [Fe(III)] was in at least five- to 10-fold excess to the initial HAN. In an intermediate region, they suggest that a mixture of N_2 and N_2O should be obtained from the two competing pathways. These authors suggest a mechanism for this whereby the Fe(III) can participate in two steps of the oxidation of HAN by Eqs. 2.49 and 2.50.

$$Fe^{3+} + NH_2OH \overset{\beta_1'}{\rightleftharpoons} Fe(NH_2OH)^{3+} \leftrightarrow Fe^{2+} + NH_2O^* + H^+ \quad (2.49)$$

$$Fe^{3+} + NH_2O^* \rightarrow Fe^{2+} + HNO + H^+ \quad (2.50)$$

$$2HNO \rightarrow N_2O + H_2O \quad (2.51)$$

$$\frac{-d[Fe(III)]}{dt} = B' \frac{[Fe(III)]^2[NH_2OH^+]}{([Fe(II)][H^+]^2 + C'[Fe(II)][H^+])} \quad (2.52)$$

For the 1:1 stoichiometry pathway, the dimerization of the NH_2O^* radical is the rate-determining step as before, but for the 2:1 stoichiometry this radical reacts further with Fe(III) to produce HNO, the dimerization of which becomes the rate-determining step (Eq. 2.51).

The rate equation suggested for the two-equivalent reduction is described by Eq. 2.52, where *B'* and *C'* are lumped parameters consisting of multiple rate constants and β_1' is the stability constant for the $Fe(NH_2OH)^{3+}$ precursor complex. They note however the difficulty in obtaining an empirical rate law for this process due to the slower kinetics of the Fe(III) reduction compared to Pu(IV) and the required boiling of the solution to obtain a purely 2:1 stoichiometry.

To summarise the discussions of primary importance in this Chapter, the concept of the nuclear fuel cycle has been introduced, along with the Advanced PUREX process for future fuel reprocessing and where this process fits in the wider fuel cycle. Simple hydroxamic acids are considered suitable candidates for use in this process, however key knowledge gaps remain with regards to the chemistry of AHA in the presence of metal ions, which must be addressed before implementation of AHA in any advanced reprocessing flowsheet. This thesis, focussed on the study of Fe(III)-AHA systems as a non-active analogue to Np(IV) and Pu(IV), will therefore aim to address two key questions; i) is there any change in the products of AHA hydrolysis when the hydroxamic acid is complexed to a metal ion, and ii) what is the nature of the reducing agent responsible for the observed ingrowth of Pu(III) during the associated Pu(IV)-AHA hydrolysis.

CHAPTER 3

Experimental Methods

3 Experimental Methods

All experiments were carried out at Lancaster University in the UTGARD (Uranium / Thorium beta-Gamma Active R&D Lab) and wet chemical laboratories. UTGARD is a government-funded facility established for the study of spent nuclear fuel recycle and waste management as part of the EPSRC (Engineering and Physical Sciences Research Council) supported NNUF (National Nuclear Users Facility) initiative. This laboratory housed the Metrohm 930 Compact single column IC Flex system, and the Horiba XploRA ONE^{TM} Raman spectrometer and the Shimadzu UV-2600 UV-Vis spectrophotometer, all of which are described in the relevant sections below.

3.1 Reagents

All chemicals reagents used were AnalaR grade or higher and supplied by Sigma Aldrich (Gillingham, Dorset, UK). All water used was ultrapure doubly de-ionized water supplied by a Direct-Q 3 UV Millipore water purification system (Millipore, Watford, UK) to a resistivity of 18.2 MΩ·cm. AHA was stored in a conventional refrigerator at 4^{o}C to avoid decomposition.

3.2 Calculation of Fe(AHA) speciation

For all experiments involving Fe(III) and AHA, speciation diagrams were constructed prior to use in order to determine appropriate experimental conditions. Speciation

diagrams were constructed using temperature dependent equilibrium constants calculated by Andrieux *et al.* [57]. This approach was previously used by these authors in a study whereby they defined a kinetic model of the Fe(III)-AHA system [77], and an analogous approach has been used recently by the same authors for the modelling of Np(IV)-AHA data [58].

Equilibrium constants, K_1, K_2 and K_3, calculated by Andrieux *et al.* [57] for the formation of the mono-, bis- and tris- FeAHA complexes respectively are shown in Eqs. 3.1 – 3.3.

$$K_1 = \frac{[H^+][FeL^{2+}]}{[Fe^{3+}][HL]} = e^{\frac{6783.7}{T} - 19.0} \quad (3.1)$$

$$K_2 = \frac{[H^+][FeL_2^+]}{[FeL^{2+}][HL]} = e^{\frac{2055.6}{T} - 6.0} \quad (3.2)$$

$$K_3 = \frac{[H^+][FeL_3]}{[FeL_2^+][HL]} = e^{\frac{2374.3}{T} + 0.3} \quad (3.3)$$

The concentration of individual Fe(III)-containing species can be calculated using K_1, K_2 and K_3, and the total concentrations of Fe(III)-nitrate ($Fe(NO_3)_3$) and AHA added.

For convenience, the symbol γ is also used in these equations, which is an expression relating $[H^+]$ and [AHA] as detailed in Eq. 3.8, where Fe_T and L_T are the total concentrations of ferric ions (initially added as $Fe(NO_3)_3$) and AHA added respectively.

$$[Fe^{3+}] = \frac{Fe_T}{1 + K_1\gamma + K_2K_1\gamma^2 + K_3K_2K_1\gamma^3} \quad (3.4)$$

$$[FeL^{2+}] = \frac{K_1\gamma Fe_T}{1 + K_1\gamma + K_2K_1\gamma^2 + K_3K_2K_1\gamma^3} \quad (3.5)$$

$$[FeL_2^{+}] = \frac{K_2K_1\gamma^2 Fe_T}{1 + K_1\gamma + K_2K_1\gamma^2 + K_3K_2K_1\gamma^3} \quad (3.6)$$

$$[FeL_3] = \frac{K_3K_2K_1\gamma^3 Fe_T}{1 + K_1\gamma + K_2K_1\gamma^2 + K_3K_2K_1\gamma^3} \quad (3.7)$$

$$\gamma = \frac{[HL]}{[H^+]} = \frac{[NO_3^-]}{[H^+]} + \frac{L_T}{[H^+]} - 1 \quad (3.8)$$

Using the approach described here, speciation diagrams were constructed to inform decisions on the initial conditions used for the experiments that will be reported on in this thesis. These are shown in Figure 3.1 to Figure 3.3. Several analytical techniques were used for identification and quantification of various important species during or after completion of the hydrolysis of free and Fe(III)-complexed AHA, all of which will be described in this Chapter, beginning with Raman spectroscopy.

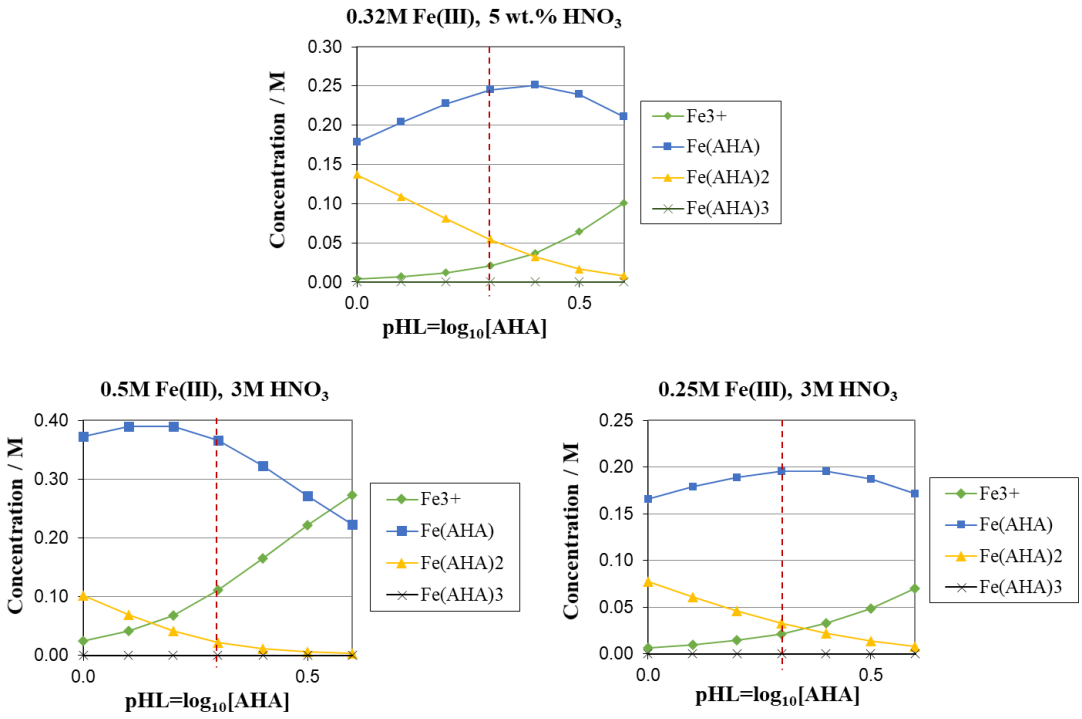

Figure 3.1: Speciation diagrams for the Fe(III) AHA system at 298K, showing concentrations of Fe^{3+}, FeL^{2+}, FeL_2^{+} and FeL_3 as a function of total AHA concentration (expressed as pHL = $-\log_{10}[HL]$), for HNO_3 and initial Fe(III) concentrations used in Raman studies. pHL = 0.3 (0.5 mol dm^{-3} AHA) is marked.

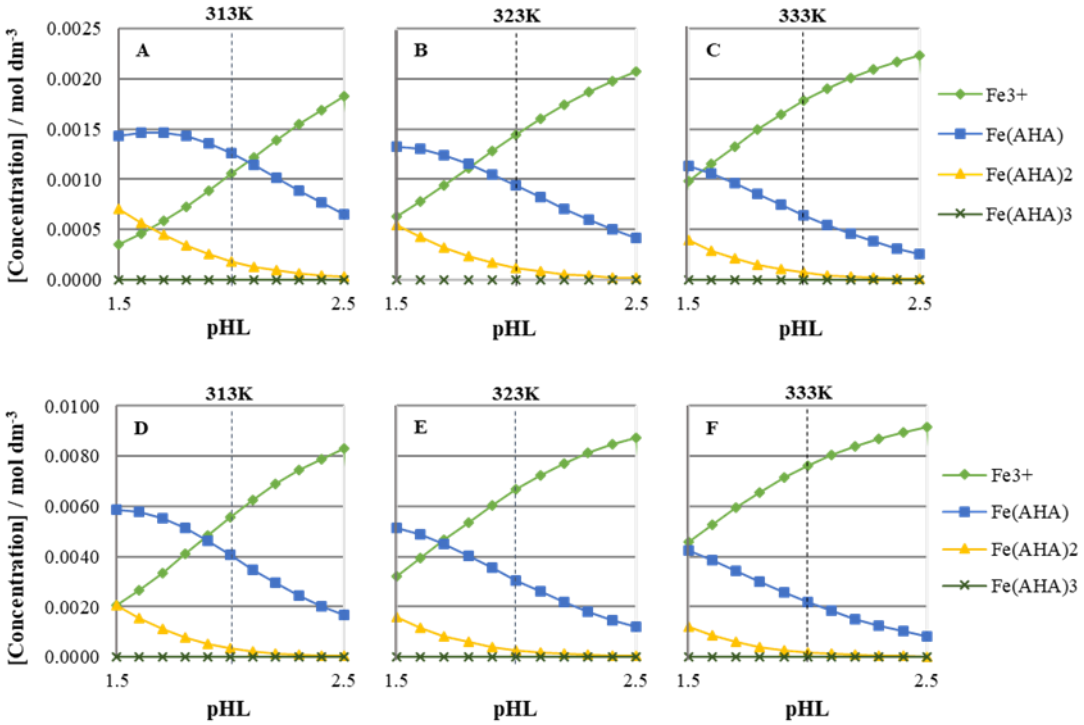

Figure 3.2: Speciation diagrams used in IC studies for the Fe(III) AHA system at 313K, 323K and 333K, showing concentrations of Fe^{3+}, FeL^{2+}, FeL_2^{+} and FeL_3 as a function of total AHA concentration (expressed as pHL = $-\log_{10}$[HL]), for $[HNO_3]$ = 0.1 mol dm^{-3} and initial [Fe(III)] = 2.5 mmol dm^{-3} (A-C) and 10 mmol dm^{-3} (D-F). pHL = 2 (10 mmol dm^{-3} AHA) is marked.

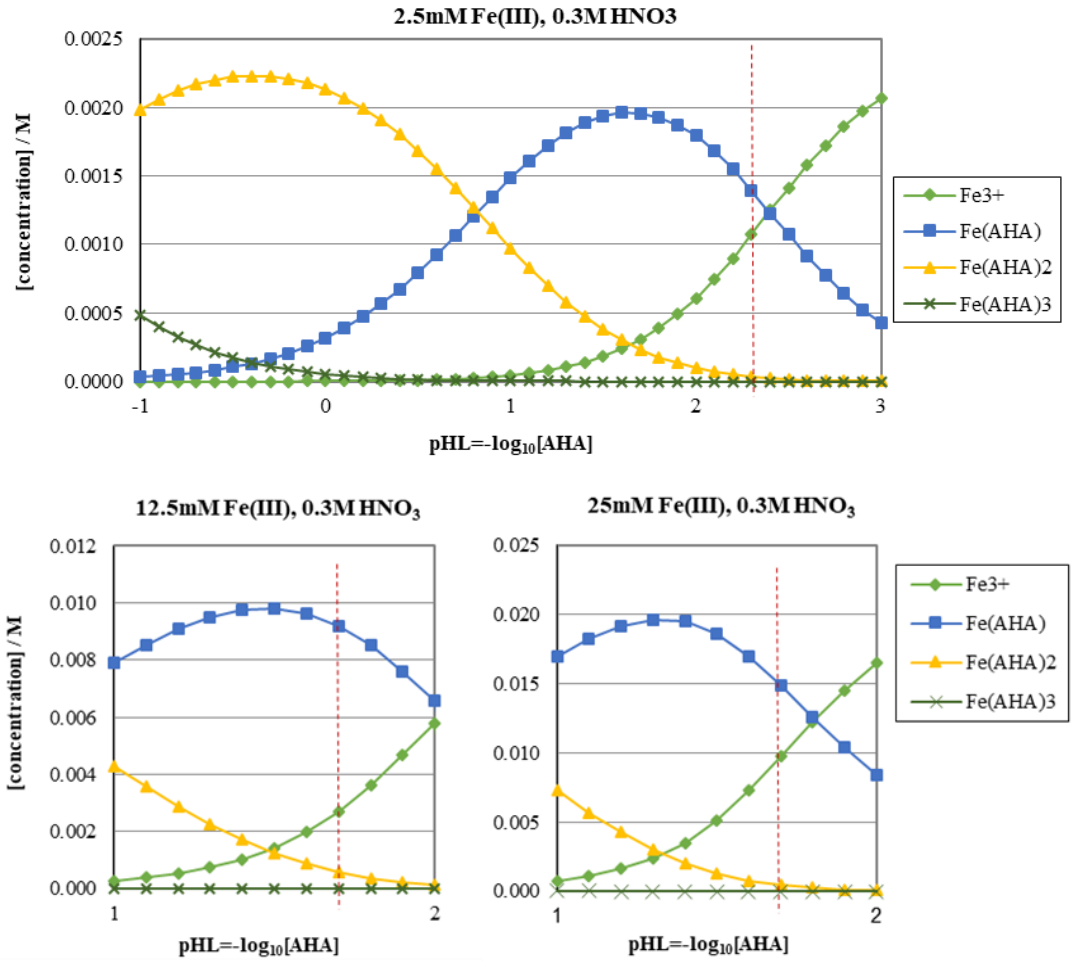

Figure 3.3: Speciation diagrams used in titrimetric studies for the Fe^{3+} .AHA system for $[HNO_3]$ = 0.3 mol dm^{-3} at 298K, showing the concentrations of Fe^{3+}, $[Fe(AHA)]^{2+}$, $[Fe(AHA)_2]^{+}$ and $Fe(AHA)_3$ as a function of total AHA concentration (expressed as pHL = $-\log_{10}[AHA]$). Total [Fe(III)] is equal to 2.5 mmol dm^{-3} (top), 12.5 mmol dm^{-3} (bottom left) and 25mmol dm^{-3}(bottom right). The concentration of AHA used for the experiments performed at each initial concentration of Fe(III) are marked by the red dotted lines.

3.3 Identification of AHA Hydrolysis Products by Raman Spectroscopy

Raman spectroscopy was utilised to identify the products of AHA hydrolysis in the absence and presence of Fe(III), at both ambient and elevated temperatures. The overall aim of these experiments was to investigate whether the mechanism of AHA

hydrolysis and subsequent product distribution changes when AHA is complexed with a metal ion. Two different instruments and methods were investigated, which are described in sections 3.3.2 and 3.3.3. Before describing the methods used, the theory behind the technique will be discussed.

3.3.1 Optical Spectroscopy

Optical spectroscopy is a technique that uses the interaction of a physical object with electromagnetic radiation in the form of light, to give information about the properties of that object. The nature of the interaction gives rise to numerous classifications of spectroscopy, including resonance, absorption, emission, elastic scattering (reflection), and inelastic scattering [100]. Raman spectroscopy looks at Raman, or inelastic scattered light.

3.3.1.1 Raman Spectroscopy

The first paper on Raman spectroscopy was published by its inventor from who it gets its name, C.V. Raman, along with K.S. Krishnan in 1928 [101]. Raman spectroscopy looks at scattered light, which occurs when incident light interacts with molecular vibrations, and can reveal the chemical and structural composition of a sample. Illuminating a sample with a monochromatic light source, such as a laser, is the first step in creating a Raman spectrum. The majority of the scattered light remains unchanged in energy from that of the incident radiation, via a very short-lived elastic scattering process known as Rayleigh scattering. A very small fraction of it however, approximately 1 in 10^7 photons, gains or loses energy and is inelastically or Raman

scattered [102]. This produces a Raman shift, which is the difference between the energy of the incident photon absorbed and the scattered photon emitted. This change in energy depends on the vibrational frequency of the atoms within the molecule that the photon interacts with.

When a photon interacts with a molecule, it polarises the electron cloud and can induce a short-lived transition to a “virtual” energy state, as shown in Figure 3.4. When relaxation occurs in an inelastic manner, a molecule releases a different quantity of energy to that of the incident photon. There are two types of Raman scattering; Stokes and anti-Stokes scattering [103]. Stokes shifted Raman bands are more intense than anti-Stokes bands because they arise due to transitions from lower to higher energy vibrational levels in the molecules electronic ground state and are therefore the bands measured in conventional Raman spectroscopy [104].

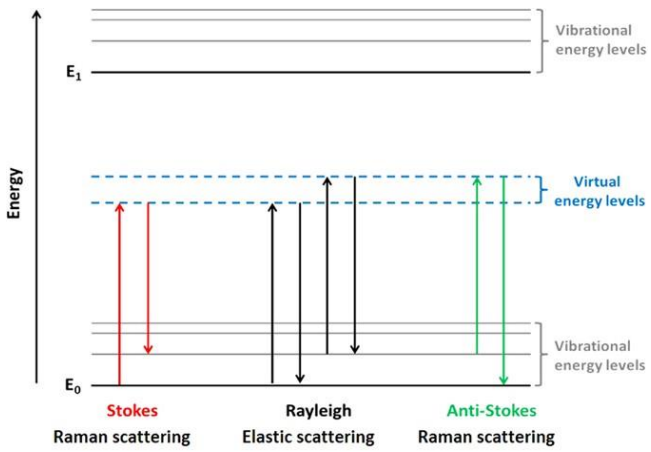

Figure 3.4: "Jablonski" style diagram of energetic transitions involved in Raman and Rayleigh scattering [103] (reproduced from open access source, reference [103]).

The small intensity of Raman signals from molecules can be significantly improved by a phenomenon known as the surface-enhanced Raman scattering (SERS) effect, a

result of the electromagnetic and chemical enhancements between metal structures and molecules in close proximity. First observed by Fleischmann *et al*. in 1974, it was suggested this effect could enhance the Raman signal by a factor of 10^6 [105]. There has been significant research into the area in the over 40 years since its discovery and enhancement factors up to 10^8 or even larger have been observed for molecules adsorbed onto corrugated metal surfaces such as silver or gold nanoparticles (NPs) [106]. It is now widely accepted that the enhancement is largely electromagnetic in nature, occurring primarily as a result of surface plasmon excitations i.e. charge density waves in the metal oscillating in phase with the incoming radiation field [107]. It can also be thought of as a dipole field coupling between dipoles in both the metal particles and the molecule, simultaneously excited by the incident electromagnetic field. The enhancement is particularly strong when metals are illuminated with light in resonance with the surface plasmon frequency.

3.3.2 Surface-Enhanced Raman Spectroscopy (SERS) Studies

Surface-enhanced Raman spectroscopy (SERS) studies were performed using a Voyage Confocal Microscope (B&WTek, USA) Raman spectrometer equipped with a 785nm laser focused through a 20x objective lens.

A SERS methodology was chosen in order to allow analysis of small volume liquid samples in a microscope system that is typically geometrically optimised for the analysis of small solid samples. A 2µl drop of analyte solution was pipetted onto a highly polished gold disk deposited onto quartz crystal (Maxtek AT-cut, 1 in. diameter gold crystal, INFICON) in order to give a SERS enhancement of the analyte signal

[108]. Once the droplet was placed on the gold surface, the objective lens was focused onto the centre of the added droplet and spectra covering the wavelength range of 200 - 3000 cm^{-1} were taken using an acquisition time of 40 seconds with 2 accumulations. Due to the observation of variations in peak intensities between consecutive samples described in section 3.3.2.1, spectra of 3 separate 2µl droplets were obtained for each sample. Using this method, solutions of 0.5 mol dm^{-3} AHA in 5 %wt. (1.1 mol dm^{-3}) HNO_3 in the absence and presence of 0.32 mol dm^{-3} $Fe(NO_3)_3$, were left to hydrolyse at laboratory temperature and analysed pre- and post-hydrolysis.

3.3.2.1 Method development using an epoxy well

During consecutive spectral acquisition, significant variation was often observed in some of the peak intensities, particularly that of the main ν_s(N-O) stretching mode in the spectra of HNO_3 at 1044 cm^{-1}. This variation was observed regardless of whether the laser power was set at 50% or 70%, and whether the spectra were acquired from a single or from multiple droplets. It was hypothesised that, depending on the exact location that the laser hit, the curvature of the droplet placed on the gold surface might affect the intensity of the peaks obtained.

With the aim to obtain a more consistent result between samples for the intensity of this peak, a small epoxy well was thus created on the gold surface, which could hold a 10µl aliquot of the sample. It was hoped that having a larger volume and a more uniform surface for the laser to aim at would reduce the amount of variation.

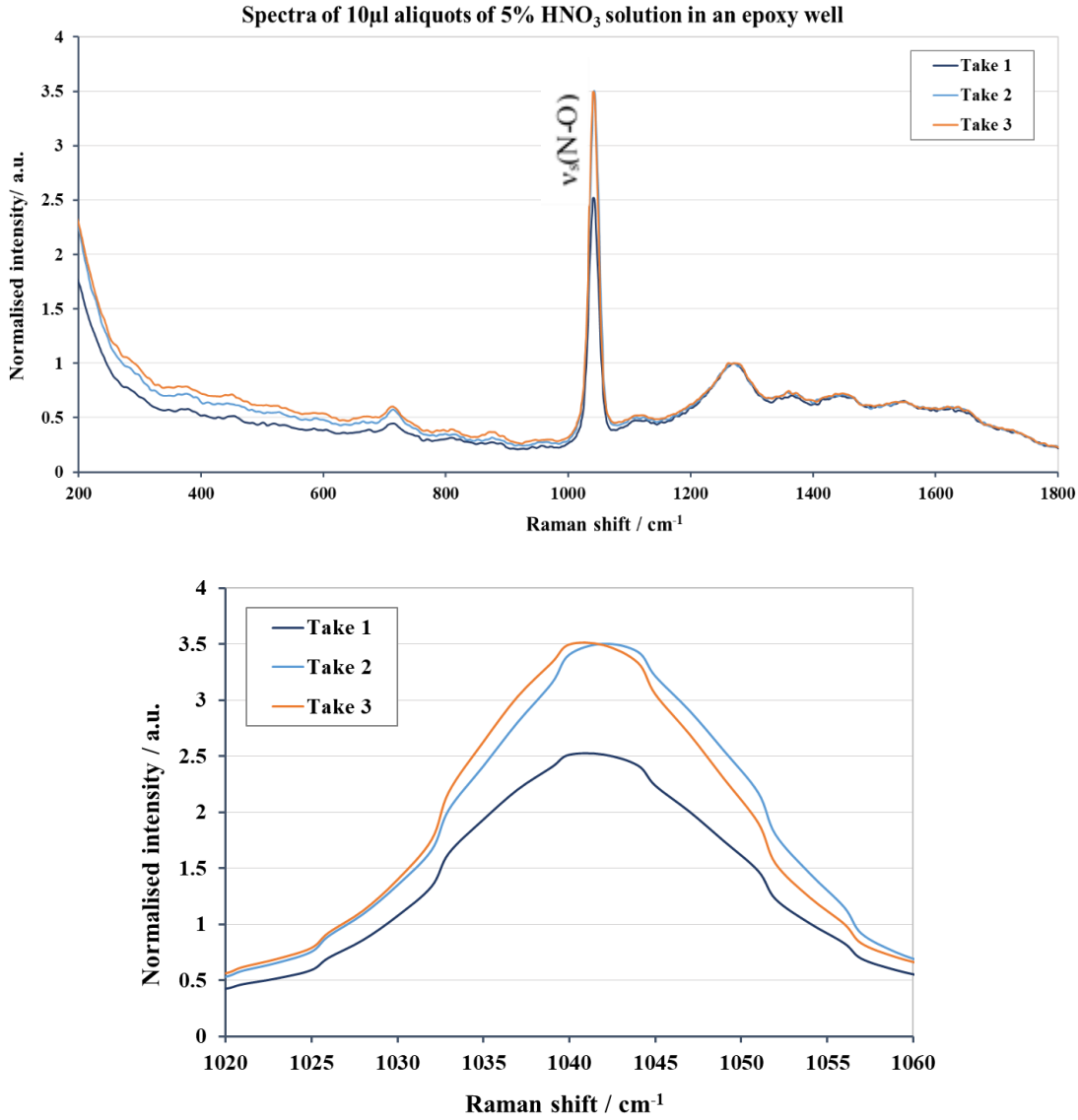

Figure 3.5: Spectra taken of 3 separate 10ul aliquots of 5% HNO_3 in the epoxy well on the gold surface. Intensity is normalised to the primary gold peak at 1270 cm^{-1}.

Figure 3.5 shows the spectra taken of 3 separate droplets using this method. It can be seen that a large variation was still observed in the intensity of the primary ν_s(N-O) stretching mode of HNO_3 at 1044 cm^{-1}. These reproducibility issues could be due to scatter at the meniscus surface or focus misalignment causing out of plane background shifts. The use of an epoxy well was therefore not continued in subsequent SERS

studies using this system, and further studies were done utilising a Raman spectrometer equipped with a solution cell setup as described in the next section.

3.3.3 Raman Spectroscopy Using a Solution Cell

Following on from the SERS study, further experiments were performed using a Horiba XploRA ONE^{TM} (Horiba Scientific, UK) Raman spectrometer fitted with a 532nm wavelength laser and a solution adapter, within which samples were housed in a 3ml cuvette. The use of a solution cell was expected to have several advantages over the previous SERS method including; i) the allowance for a larger volume of sample which would be more representative of the bulk solution than the 2µl drop, and ii) improvements in peak resolution due to the absence of the effects from the gold background in the region specifically of 1100-1800 cm^{-1}. The possible occurrence of fluorescence around the use of Fe in some of the samples was considered as water-based iron nanoparticles show fluorescence emissions at about 590 nm [109]. The 532nm laser, whilst therefore having a higher chance of fluorescence in comparison to the 758nm laser used in the SERS method, has some advantages including a higher Raman scattering efficiency and both a reduction in the required scan time and improved signal to noise ratio. The Labspec program was used to collect the spectra within a 3 second acquisition time with multiple accumulations, and an internal intensity correction (ICS HORIBA) was used to correct the intensities from the Electron Multiplying CCD detector.

This setup was used to analyse samples of 0.5 mol dm^{-3} AHA in 3 mol dm^{-3} HNO_3 in the absence and presence of 0.25 mol dm^{-3} and 0.5 mol dm^{-3} Fe(III), pre and post-

hydrolysis at 333K. Based on speciation diagrams constructed prior, these concentrations were chosen to increase the proportion of AHA complexed as the mono-complex in the systems studied. Drawn from the speciation diagrams shown in Figure 3.1 in section 3.2, the speciation data is shown in Table 3.1.

Table 3.1: Speciation data for the systems studied by Raman spectroscopy. Concentrations in units of mol dm^{-3}. The initial added concentration of Fe(III) is defined as Fe_T.

[Fe_T]	**[HNO_3]**	**Fe:AHA ratio**	**1:1 complex**		**2:1 complex**		**3:1 complex**	
			[]	**% of all complexes**	**[]**	**% of all complexes**	**[]**	**% of all complexes**
0.32	1.1	1:1.6	0.245	81.85	0.054	18.14	4.36×10^{-5}	0.015
0.25	3	1:2	0.195	85.58	0.033	14.41	2.01×10^{-5}	8.81×10^{-3}
0.5	3	1:1	0.366	94.20	0.023	5.80	1.04×10^{-6}	1.30×10^{-3}

After the identification of the AHA hydrolysis products by Raman spectroscopy, the following sections 3.4 - 3.7 will describe the various methods used for the quantification of other key species studied / quantified in the work presented here including acetic acid, nitrous acid, hydroxylamine and Fe(II), both during and after completion of AHA hydrolysis.

3.4 Real-time Quantification of Acetate by Ion Chromatography

Ion chromatography (IC) has been used to measure ingrowth of the acetate ion during the acid-catalysed hydrolysis of both free and complexed AHA. In so doing, it has provided a novel and convenient method for studying the kinetics of this process. Kinetic analysis of the hydrolysis of AHA has most commonly been achieved through

observing the disappearance of the Fe(III)-AHA complex by UV-Vis spectroscopy, with subsequent spectral deconvolution [45, 69, 77]. However, as will be seen, one of the products of the hydrolysis of AHA, hydroxylamine, may reduce Fe(III) to Fe(II). Given that the complexation constant for the latter with AHA is substantially smaller than the former, the Fe-AHA complex will dissociate as a result of this reduction – so providing a second means, additional to that provided by simple hydrolysis of the AHA ligand, by which the absorbance of the Fe(III)-AHA complex may be seen to decrease as a function of time. Deconvoluting these two effects in order to extract the effect of AHA hydrolysis alone on the time dependence of the absorbance of the Fe(III)-AHA complex is non-trivial; indeed, if the effect of the hydroxylamine-driven reductive dissociation of the complex is not explicitly accounted for, it may be concluded that the AHA on-complex is hydrolysing faster than it actually is. Thus a method is needed for following of the hydrolysis of the AHA where the analyte studied interacts neither with the complex or the products of the hydrolysis of the complex. Studying the time dependence of the evolution of the hydrolysis product acetic acid provides just such a method. The acetic acid product of the hydrolysis of AHA however is considered silent once generated, and its' concentration thus provides a direct measurement for the total AHA lost in the system, requiring no assumptions or manipulations of the data. Before describing the method used, a discussion of the theory of chromatography will be presented.

3.4.1 Theory of Ion Chromatography

Chromatography is a physicochemical method for separating mixtures of substances based on repeated distribution between a stationary phase and a mobile phase [110, 111]. Ion chromatography is a term that was first introduced in 1975 by Small, Stevens and Bauman when they combined conductivity detection with a chemical reduction in conductivity [112]. Today the term encompasses all high-performance liquid chromatography (HPLC) methods to determine inorganic or organic ions. [111]

Ion chromatography techniques can be classed as suppressed or non-suppressed methods, in relation to the use of chemical suppression. A direct or non-suppressed method employs salts of organic acids in low concentrations on low capacity ion exchangers to achieve a sufficiently low background conductivity that can be suppressed by electronic means. To achieve a lower background conductivity, suppressed systems employ both electrically and chemical suppression to reduce the background conductivity resulting from the mobile phase composition [111].

Ions are identified by their conductivity, which is defined as the ability of electrolyte solutions in an electric field applied between two electrodes to transport current by ion migration [111]. The conductivity κ, is an intrinsic property of the solution, which is dependent on the specific conductivity of every ion in solution and linearly dependent on the concentration c in "solutions of infinite dilution". The conductivity of the solution is normally expressed in terms of the molar conductivity Λ_m, expressed in units of $S.cm^2.cm^{-1}$ [113].

$$\Lambda_m = \frac{\kappa}{c} \tag{3.9}$$

During the chromatographic separation of a mixture of species, each species forms a distribution equilibrium between the stationary and mobile phases as it passes through the column. This is described by a distribution coefficient *D*, which is defined as the ratio of the concentrations of a particular species *X*, between the stationary phases ($[X]_S$) and the mobile phases ($[X]_M$). Species in a mixture can only be separated successfully when their distribution coefficients are sufficiently different [110]. Species with larger values of *D* are retained more strongly on the column and will elute from the column later.

$$D = \frac{[X]_S}{[X]_M} \tag{3.10}$$

The output after a chromatographic separation with conductivity detection is an elution curve of conductivity against time, termed a chromatogram. It has several important characteristics [114], illustrated in Figure 3.6, [115] including;

- Dead time t_0 – the time needed for the mobile phase to flow through the system.
- Retention time t_R – the time needed for the concentration maximum of a particular injected species to reach the end of the separation system.
- Net retention time t'_R– corresponds to the actual time of a species on the migration path. $t'_R = t_R - t_0$

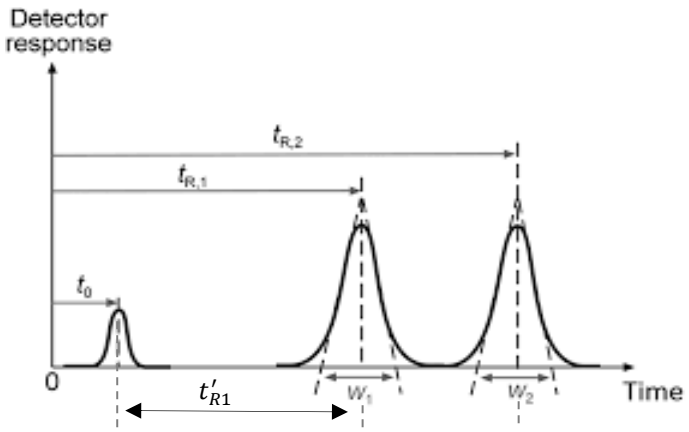

Figure 3.6: General chromatogram characteristics [115] (reproduced with permission from reference [115], copyright 2015 John Wiley and Sons)

3.4.2 Experimental equipment setup

The equipment consisted of a Metrohm 919 Ion Chromatography Autosampler, a Metrohm Dosino Unit, and a Metrohm 930 Compact single column IC Flex system coupled with a suppressor unit, a Metrohm IC Conductivity Detector and MagicNET data analysis software (Metrohm UK Ltd., UK). The Autosampler was required during instrument calibration and the Dosino Unit utilized for automated sample uptake during experimental runs. A 0.25µl injection loop was fitted to allow for an 80-fold dilution of the sample compared to the standard 20µl loop that was initially supplied with the instrument. Figure 3.7 shows the IC system configuration used.

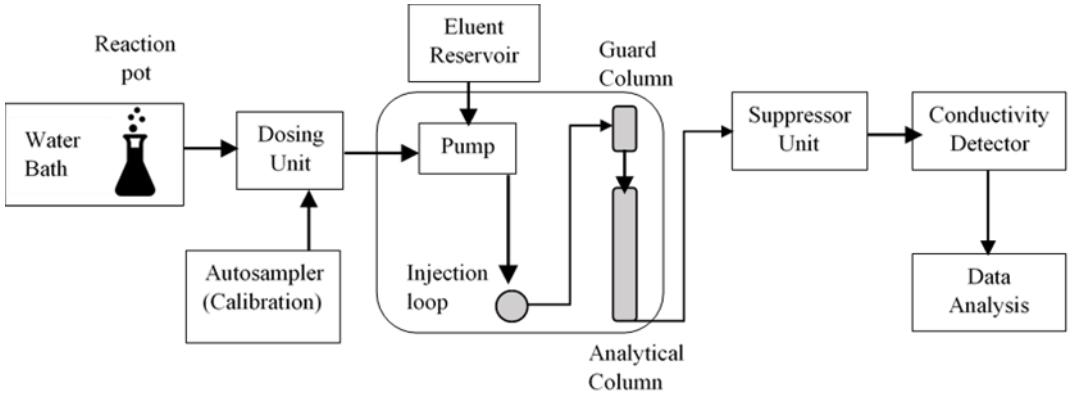

Figure 3.7: Ion chromatography system setup for anion analysis.

For anion analysis, a Metrosep A Supp 5 – 150/4.0 anion separation column was used with a Metrohm RP 2 guard column to protect the column from Fe precipitates. This guard column was also used in all subsequent IC analyses but was of greatest importance in anion analysis due to the use of a basic eluent. The anion column was used with its standard eluent of 2.5 mmol·dm^{-3} sodium carbonate (Na_2CO_3) / 1.0 mmol·dm^{-3} sodium hydrogen carbonate ($NaHCO_3$), pumped though the system at a rate of 0.7 ml·min^{-1}. Standard anion eluents have a relatively high salt content, and thus high conductivity compared to the sample ions present at a much lower concentration. The conductivity of the eluate must therefore be reduced considerably after contact with the column, in order to detect differences in the conductivity of the eluate due to the sample ions. This is done by continuous flow through a membrane suppressor where the eluate is contacted with a solution of 0.1 mol·dm^{-3} oxalic acid ($C_2H_2O_4$) / 0.1 mol·dm^{-3} H_2SO_4. This allows the cations of the eluent (in this case Na^+) are replaced by H^+ from the acidic suppressor solution, thus converting the eluent to a weak carbonic acid (H_2CO_3) or water and subsequently decreasing the background conductivity. An added benefit of suppression is that the association of the analyte

anions with the highly conductive hydronium ion also increases the sample ion signals, and thus the sensitivity of the analysis [113].

It is important to degas the eluent prior to use because gas bubbles in the eluent can cause baseline fluctuations and interfere with ion peaks in the chromatogram, and to help protect the high-pressure pump, which can transport liquids but not gases. Oxygen bubbles in the eluent and suppressor solution were therefore removed by purging both with less soluble nitrogen gas for approximately 30 minutes whilst continuously stirring. To put the IC system into operation, it was then allowed to equilibrate by running the degassed eluent and suppressor solution through the system at the desired rate for approximately 30-40 minutes, or until the baseline in the chromatogram had settled.

3.4.3 Calibration Procedure

A calibration in ion chromatography is a relationship function calculated by the software of peak area as a function of the concentration of known external standards provided by the user. Calibrations were performed using the relative standard deviation (*RSD*) method in the software (as described in Appendix A). A total of 3-5 acetate standards in 0.1 $mol \cdot dm^{-3}$ HNO_3 that covered the range of possible concentrations, were prepared from 100 ml stock solutions of 1 $mol \cdot dm^{-3}$ HNO_3 and 100 $mmol \cdot dm^{-3}$ sodium acetate (CH_3COONa). Standards were prepared in 25ml volumetric flasks, by taking aliquots of the stock solutions and diluting with de-ionised water. A 5 ml aliquot of each prepared standard was then transferred to an 11 ml sample tube positioned on the autosampler. The Dosino was programmed to take up 3 ml of a sample for each

measurement; enough to fully flush the tubing that ran into this device from the sampling needle on the autosampler and thus provide accurate measurements of simultaneous samples back-to-back without the need to flush the line after each sample. From this 3 ml aliquot only 0.25 µl was injected into the column for analysis. A method and sampling table was set up using the MagicNET software, and the sampling interval in the method set to 0 minutes so each standard was sampled immediately after the previous was complete.

All the calibration curves produced are shown in Figure 3.8, and the values for RSD and R^2 values obtained for each calibration function are shown in Table 3.2. The calibration functions are all non-linear, as is expected in ion chromatography with suppressed conduction detection due to the influence of the autoprotolysis of water at low concentrations up to 1 µmol dm^{-3} and to the incomplete dissociation of weak acid analytes such as acetic acid [116]. A single calibration was initially utilised for multiple experiments, and separate calibrations for each experiment thereafter based on large and unexpected variations seen amongst cation analyses (see section 3.6.2.2). Very little variation was found however in any of the acetate calibrations performed throughout the entire range of experiments, this allowing for the experiments performed on the same calibration method to remain valid with accurate quantification.

Table 3.2: Equation, RSD and R^2 values for each acetate calibration performed. In the equations, A is the peak area in units of $\mu S.cm^{-1}.min$, and Q is the injected concentration of CH_3COO^- in $mmol{\cdot}dm^{-3}$.

Calibration	Equation	RSD / %	R^2	Experiments
Anions_0.1M HNO_3 – reaction pot	$A = 0.0787 \times Q - 9.192\times10^{-4} \times Q^2$	0.663	1.000	All 333K Free AHA, 323K 1:4 Fe:AHA, 323K
Anions_method_template_2	$A = 0.0785 \times Q - 3.814\times10^{-4} \times Q^2$	0.375	1.000	1:1 Fe:AHA, 323K
Anions_method_template_3	$A = 0.0797 \times Q - 2.334\times10^{-4} \times Q^2$	0.289	1.000	Free AHA, 313K
Anions_method_template_4	$A = 0.0775 \times Q - 2.157\times10^{-4} \times Q^2$	0.834	1.000	1:4 Fe:AHA, 313K
Anions_method_template_6	$A = 0.0734 \times Q - 2.491\times10^{-3} \times Q^2$	1.489	1.000	1:1 Fe:AHA, 313K

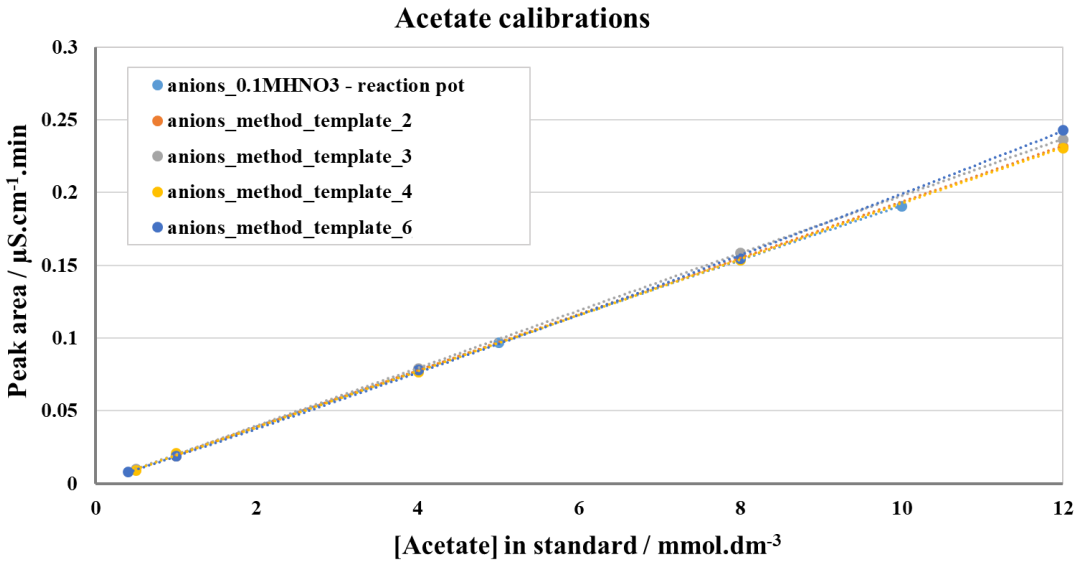

Figure 3.8: Calibration curves of acetate concentration [$mmol{\cdot}dm^{-3}$] against peak area [$\mu S\ cm^{-1}$]. Vertical error bars are shown as the %RSD values for the respective calibration curves as written in Table 3.2, but are too small to be visible on the plots.

An example chromatogram produced from a 1 mmol dm^{-3} standard of $NaCH_3COO$ and $NaNO_2$ (see section 3.5.1) in aqueous solution is shown in Figure 3.9. Analyte peaks showed the expected Gaussian shape, with a small amount of asymmetric tailing as is usually found in any analysis in practice. These variations from the ideal peak are

quantified by the asymmetry factor, A_sF. The ideal Gaussian peak has a value of $A_sF = 1$, and variations of $A_sF > 1$ and $A_sF < 1$ are known as tailing and fronting respectively. The aim is for $0.9 < A_sF < 1.1$, although a trouble-free evaluation of peak area should be achieved if $A_sF \leq 2.5$ [111]. A_sF factors were largely within the range or only slightly outside it, and all were < 2.5.

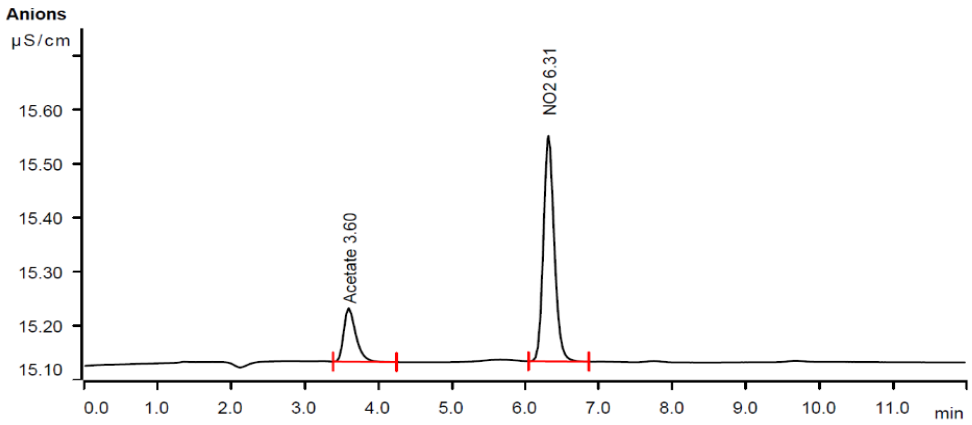

Figure 3.9: Example of a chromatogram of 1 mmol dm^{-3} injected acetate and nitrite ions, prepared as their respective sodium salts in aqueous solution.

Due to the high concentration of NO_3^- from the fully dissociated HNO_3 media, a very intense peak for nitrate appears at ~9 min for standards in 0.1 mol dm^{-3} HNO_3. Whilst the peak intensity for NO_3^- was far greater than that of acetate or NO_2^- (described in section 3.5.1), the position of the peak was sufficiently far from these to have no effect on the shape of the peak or their determination.

3.4.4 Experimental procedure

For an initial concentration of 10 mmol·dm^{-3} AHA, its' hydrolysis in 0.1 mol·dm^{-3} HNO_3 (pH1) was followed in the presence of i) no initial Fe(III), ii) 2.5 mmol·dm^{-3}

Fe(III), and iii) 10 mmol·dm^{-3} Fe(III). These systems were studied at a range of temperatures including 333K, 323K, and 313K. Speciation diagrams for the initial conditions involving Fe(III), constructed as described in section 3.2, are shown in Figure 3.2. From these, calculated quantities of free and complexed Fe(III) and AHA shown in Table 3.3. For each set of initial conditions, the ingrowth of the anions acetate (CH_3COO^-, from the hydrolysis of AHA) and nitrite (NO_2^-, from the potential reaction of the AHA hydrolysis product hydroxylamine with nitric acid), and cations NH_3OH^+ (from the protonation of the AHA hydrolysis product hydroxylamine) and Fe(II) (from the potential reduction of both AHA-complexed and non-complexed Fe(III) by hydroxylamine) were followed. Due to equipment limitations, three separate analyses were required for i) the anionic species, ii) protonated hydroxylamine, and iii) Fe(II). The analysis for NO_2^-, NH_3OH^+ and Fe(II) are described in sections 3.5.1, 3.6.2 and 3.7.2 respectively.

Table 3.3: Speciation for 10 mmol dm^{-3} initial AHA and 0.1 mol dm^{-3} HNO_3, for varying total iron concentrations (Fe_T) and temperatures. All concentrations (shown in []) are in mmol dm^{-3}.

Diagram	[free HL]	1:1 complex		2:1 complex		free Fe(III)		Free HL:Fe(III)
		[]	% of all complexes	[]	% of all complexes	[]	% of Fe_T	
A	8.37	1.26	87.27	0.184	12.27	1.05	42.0	7.97:1
B	8.83	0.937	88.80	0.118	11.20	1.44	57.6	6.13:1
C	9.21	0.645	90.15	0.070	9.85	1.78	71.2	5.17:1
D	5.23	4.06	91.87	0.359	8.13	5.59	55.9	0.94:1
E	6.39	3.06	91.80	0.273	8.20	6.67	66.7	0.96:1
F	7.43	2.19	92.02	0.189	7.98	7.62	76.2	0.93:1

For an experimental run, a solution of 2.5 mmol·dm^{-3} or 10 mmol·dm^{-3} $Fe(NO_3)_3$ in 0.1 mol·dm^{-3} HNO_3 was prepared and transferred to a 250 ml or 500 ml conical flask, depending on the length of the experimental run and therefore the volume of solution

required. This flask was covered with parafilm and left to equilibrate at the desired temperature in a covered water bath. The eluent was left to run through at a continuous rate for the duration of the entire experimental run, therefore the eluent usage was high. For the experiments at 323K and 333K, a 2L standard anion eluent was sufficient, whereas a single experiment at 313K required 5L of eluent. A method was created in the MagicNET software, with a sampling interval of 15, 20, or 60 minutes for experiments performed at 333K, 323K or 313K respectively. Once the solution reached equilibrium at the desired temperature, the required amount of AHA was added in solid form to the conical flask, and the solution well mixed and sealed with parafilm. Lastly, the tubing running from the autosampler needle to the Dosino was disconnected from the autosampler, submerged in the reaction mixture and the experimental run started. The first sample measurement was taken to be 4 minutes, to allow for addition of AHA, IC-system start up and sample aspiration time.

Acetate was the earliest eluting ion of all the species studied by IC, observed at approximately 3.6 minutes compared to 5-6 minutes for NO_2^-, NH_3OH^+ and Fe(II), with a complete chromatogram taking 11 minutes to obtain. These times are all however very short on the timescale of a complete hydrolysis run, which ranged from approximately 14 hours for the quickest run at 333K to over 90 hours for the longest run at 313K. At induvial ion elution times of < 1% of the total hydrolysis time, no further significant hydrolysis will therefore occur during the running of this analysis. This is even less of a concern with anion analysis, as the use of a basic eluent will cease the hydrolysis reaction on contact with the sample.

3.5 Techniques for Analysis of Nitrous Acid

3.5.1 Real-time Quantification of Nitrite by Ion Chromatography

Nitrous acid may be produced from the reaction of the AHA hydrolysis product, hydroxylamine, with nitric acid. Thus, as an additional analyte in the IC anion analysis procedure, the concentration of nitrite (NO_2^-) was also measured for the same systems during the course of free and complexed AHA hydrolysis. In was hoped that this analysis would provide some insight into the role of nitrous acid (HNO_2) in these systems, which is known to interfere via several chemical reactions, including its reaction with hydroxylamine nitrate (HAN) in acidic media [91], and its role in various interactions with Fe(III)/Fe(II) in HNO_3 [94, 117].

3.5.1.1 Calibration Procedure

The system setup and calibration procedure for the NO_2^- ion was the same as described for acetate analysis in section 3.4 as both of these anions were analysed simultaneously. The instrument was calibrated using 3-5 standards of $NaNO_2$ in 0.1 mol·dm^{-3} HNO_3, prepared from 100 ml stock solutions of 100 mmol dm^{-3} $NaNO_2$ and 1 mol dm^{-3} HNO_3. All the calibration curves produced are shown in Figure 3.10, and the values for RSD and R^2 values obtained for each calibration function in Table 3.4.

Table 3.4: RSD and R^2 values for each NO_2^- calibration performed. In the equations, A is the peak area in units of $\mu S.cm^{-1}.min$, and Q is the injected concentration of NO_2^- in $mmol{\cdot}dm^{-3}$.

Calibration method	Equation	RSD / %	R^2	Experiments
Anions_0.1M HNO3 – reaction pot	$A = 0.2983 \times Q - 1.306\times10^{-3} \times Q^2$	0.663	1.000	All 333K Free AHA, 323K 1:4 Fe:AHA, 323K
Anions_method_template_2	$A = 0.2553 \times Q + 2.762 \times10^{-3} \times Q^2$	1.142	1.000	1:1 Fe:AHA, 323K
Anions_method_template_3	$A = 0.2532 \times Q + 9.912 \times10^{-3} \times Q^2$	1.517	1.000	Free AHA, 313K
Anions_method_template_4	$A = 0.2340 \times Q + 7.505 \times10^{-3} \times Q^2$	2.438	0.999	1:4 Fe:AHA, 313K
Anions_method_template_6	$A = 0.2950 \times Q - 1.394 \times10^{-1} \times Q^2$	3.030	1.000	1:1Fe:AHA, 313K

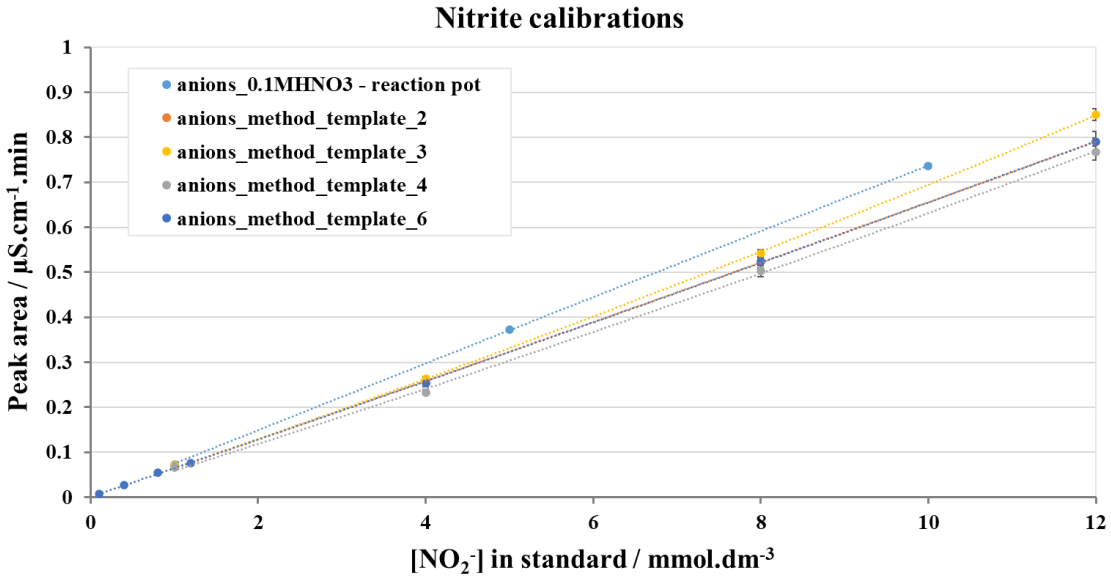

Figure 3.10: Calibration curves of nitrite concentration [$mmol{\cdot}dm^{-3}$] against peak area [$\mu S\ cm^{-1}$]. Vertical error bars are shown as the %RSD values for the respective calibration curves as written in Table 3.4.

On contact with the suppressor solution the NO_2^- ion is converted to the weak acid HNO_2, thus the curves are all non-linear for the same reasons as described for the acetate ion in section 3.4.3. Slightly more variation was found in the calibration curves at the higher concentrations of nitrite than found for acetate, which is likely due to the instability of HNO_2/NO_2^- in HNO_3 subsequently leading to a slow deterioration in

standard concentrations between preparation and sampling. Most calibrations were performed using standards in the range of 1 – 12 mmol dm^{-3} analogous to the acetate standard concentrations, but the final calibration also included standards at concentrations of less than 1 mmol dm^{-3} as any nitrite found in prior experiments was present in samples at concentrations on the order of µmol dm^{-3}.

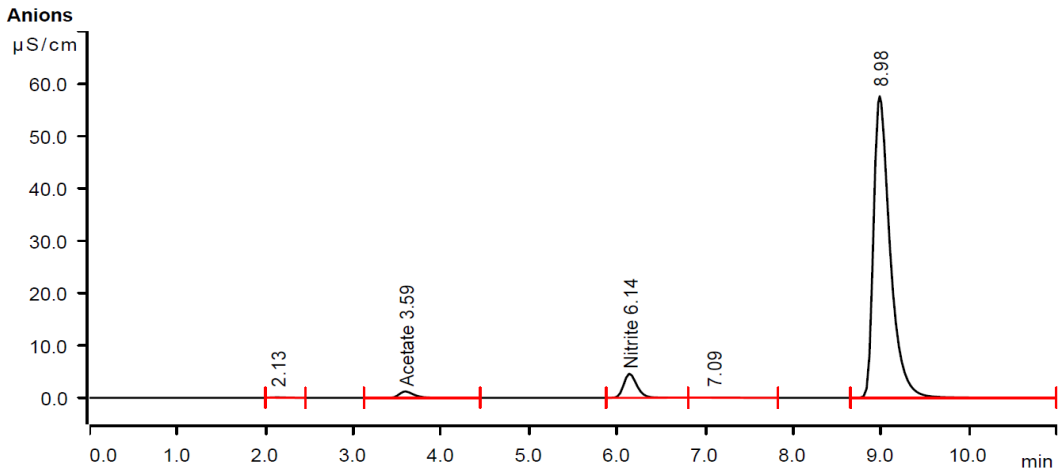

Figure 3.11: Example chromatogram of a 12 mmol dm^{-3} acetate and nitrite standard in 0.1 mol dm^{-3} HNO_3.

Figure 3.11 shows an example chromatogram of 12 mmol dm^{-3} $NaCH_3COO$ and $NaNO_2$ in 0.1 mol dm^{-3} HNO_3. Whilst significantly smaller than the unassigned NO_3^- peak at 8.98 minutes in this chromatogram and thus less visible over the entire conductivty range of the seperation, the same asymmetric Gaussian peaks found in aqueous solution are still obtained for the analytes in HNO_3. This chromatogram illustrates the comparitively greater peak areas produced by the nitrite ions and therefore the possibility of quantifying lower concentrations of nitrite than acetate.

3.5.2 Quantification of nitrous acid by the Shinn Method

With the aim of helping to inform the findings of the IC experiments described previously, a colorimetric Ultraviolet-Visible spectroscopic method for nitrite determination was used to determine intrinsic concentrations of HNO_2 present in HNO_3 as a function of temperature, and the rate of its decomposition at high temperatures. This technique was useful for quantification of small HNO_2/NO_2^- concentrations on the order of μmol dm^{-3}.

3.5.2.1 Theory of UV-Vis Spectroscopy

Similar to Raman spectroscopy described in section 3.3.1.1, Ultraviolet-Visible (*UV-Vis)* spectroscopy is a form of optical spectroscopy, but under the classification of electronic absorption spectroscopy. UV-Vis spectroscopy is associated with the absorption of visible and ultraviolet (100-800nm) radiation as photons, resulting in the excitation of electrons, in atoms and molecules, from lower to higher energy levels. Energy levels of matter are defined as quantized, meaning that only photons with the precise amount of energy equal to the difference between two energy levels, can cause electron transitions from one level to another and will be absorbed. Absorption of a photon and subsequent excitation of an electron to a higher electronic state, illustrated in the Jablonski diagram in Figure 3.12 by the straight line pointing up, is a very fast transition on the order of 10^{-15} seconds [118]. Once excited, an electron can dissipate the energy in a number of ways. This can include vibrational relaxation, another fast process (between 10^{-14} and 10^{-11} seconds), or emission of a photon, in a slow process

(on the order of 10^{-9} to 10^{-7} seconds) termed fluorescence. These are also illustrated in Figure 3.12.

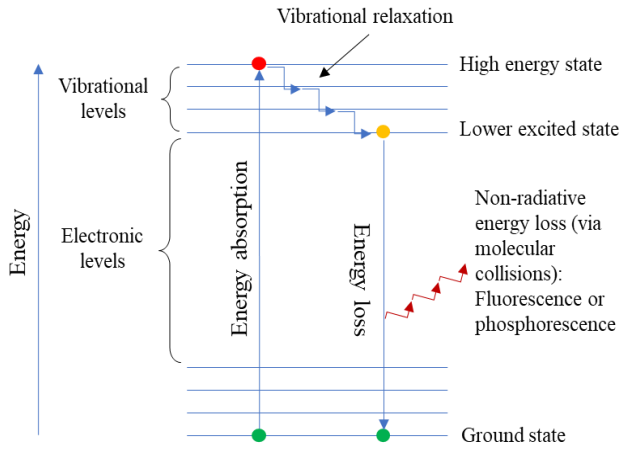

Figure 3.12: Jablonski diagram showing electronic and vibrational energy levels associated with spectroscopy.

The intensity of the absorption is dependent on the amount of substance and is related to the transmittance (*T*); the more radiation of a particular frequency (measured by wavelength, λ, in nm) is absorbed, the less is transmitted. Values of *T* lie between 0 and 1, but transmittance is often represented experimentally as a percentage [119]. The transmittance is equal to the ratio of the transmitted radiation (*I*) to that of the incident (or incoming) radiation (I_0) and is related to the absorbance (A_λ) by Eq. 3.11. In a spectrophotometer, the sample is contained in a solution cell of known dimensions. The Beer-Lambert Law (Eq. 3.12) is used to relate the absorbance to the sample concentration (*c*), and the distance travelled by the radiation through the cell, or path length (*l*), where ε is the molar extinction coefficient of the sample.

$$A_\lambda = -log\frac{I}{I_0} \tag{3.11}$$

$$A_\lambda = -log\frac{I}{I_0} = \varepsilon \times c \times l \qquad \text{Beer-Lambert Law} \tag{3.12}$$

3.5.2.2 Experimental procedure

The concentration of HNO_2/free NO_2^- was determined using a modified version of the Shinn method [120]. In this method, the addition of an acidic solution of sulfanilamide to a sample ensures that free NO_2^- is present as HNO_2, which can then react with sulfanilamide to form an azide intermediate. This azide intermediate then undergoes coupling with N-(1-naphthyl)ethylenediamine dihydrochloride which yields a purple azo dye, as shown in Figure 3.13 [121].

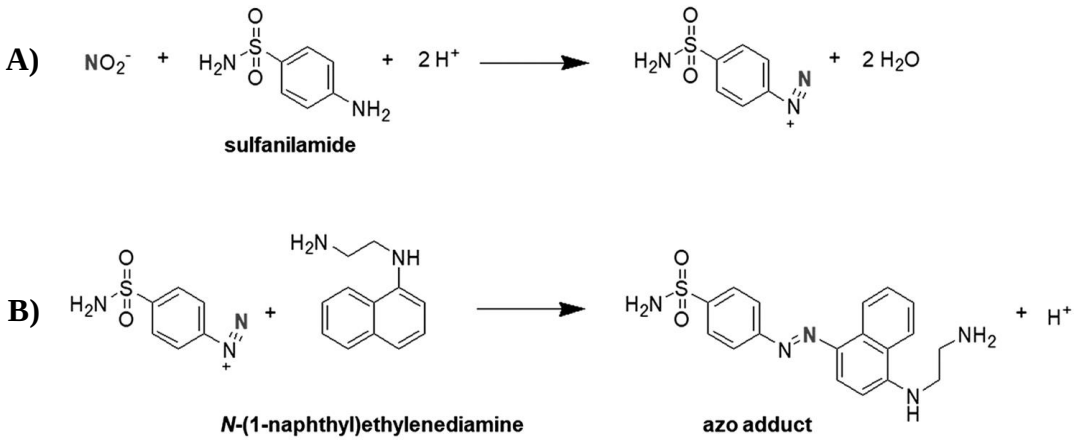

Figure 3.13: Reactions of a) sulfanilamide with nitrous acid to form an azide intermediate, and b) reaction of the azide intermediate with N-(1-naphthyl)ethylenediamine to form the azo dye [121] (reproduced with permission from reference [121], copyright 2018 RSC Publishing).

A Shimadzu UV-2600 UV-Vis spectrophotometer (Shimadzu UK Ltd., Milton Keynes, UK) was used to record spectra in the range 300 - 750nm. A freshly made 100 ml stock solution of 2 mmol·dm^{-3} $NaNO_2$ was prepared and the instrument calibrated using standards of $NaNO_2$ between 5 and 50 μmol·dm^{-3}, prepared by taking aliquots of the stock as shown in Table 3.5 and diluting to 50 ml with deionised water. The two

reagents used in this method were made up as follows; 1) 1 g of sulfanilamide in 100 mL hydrochloric acid (1.2 mol·dm^{-3}), and 2) 0.1 g of N-(1-naphthyl)ethylenediamine dihydrochloride added to 100 mL deionised water.

Table 3.5: Preparation of 5 - 50 µmol dm^{-3} nitrite standard solutions for calibration from the initial 2 mmol dm^{-3} stock solution.

Volume of stock added	Dilution	Concentration of standard / µmol·dm^{-3}	Concentration after addition of Shinn reagents / µmol·dm^{-3}
125µl	1:400	0.005	4.81
250µl	1:200	0.01	9.62
500µl	1:100	0.02	19.2
1.25ml	1:40	0.05	48.1

To prepare a standard for measurement, 1 mL of sulfanilamide solution was added to 50 ml of standard and left for a few minutes, after which 1 mL of the N-(1-Naphthyl)ethylenediamine dihydrochloride solution was added, forming the azo-dye that is purple in colour with maximum colour intensity at 543nm being achieved after about 10 minutes [122]. The intensity of the colour of the azo dye measured by UV-Vis spectroscopy is directly proportional to the concentration of nitrous acid present in the solution. The spectrophotometer was baselined using a mixture of deionised water with the addition of the Shinn reagents, and the absorbance measurements at 543nm as a function of concentration, shown in Figure 3.14, used to produce the calibration curve in Figure 3.15. Observation of Figure 3.15 shows that the trend line for the calibration plot passes close to, but not through the origin. This was attributed to nitrite impurities in the reagents or in the distilled water by Bendschneider and Robinson [123], since they found that neither reagent produced absorption an 543nm when added alone to distilled water.

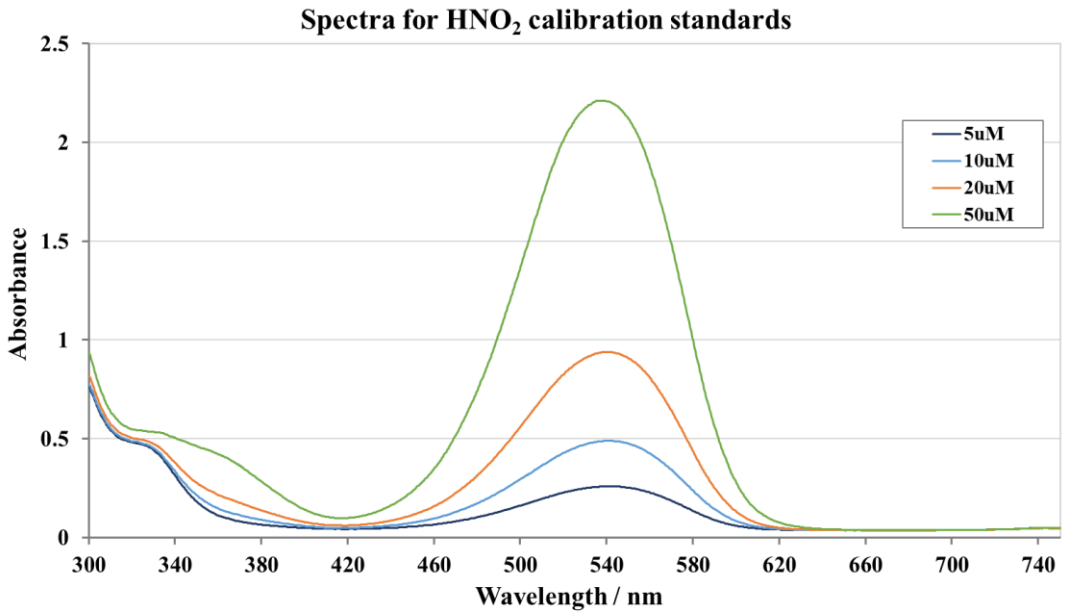

Figure 3.14: UV-Vis electronic absorption spectra of HNO_2 standards from 5 - 50 µmol dm^{-3}.

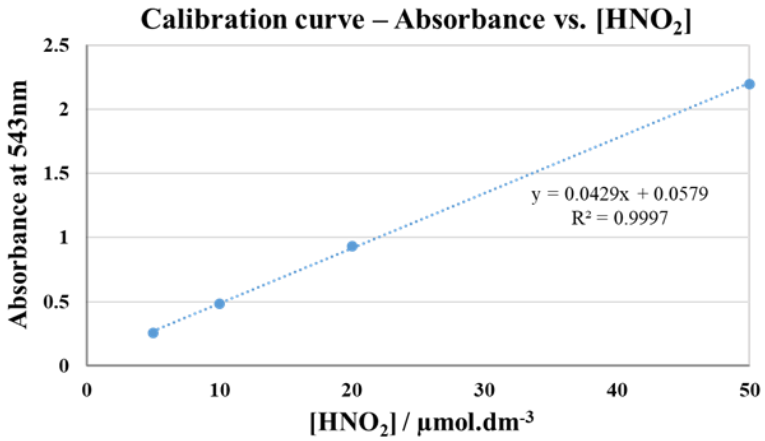

Figure 3.15: Calibration curve for the maximum absorbance at 543nm against [HNO_2], with [HNO_2] in units of µmol dm^{-3}.

This method was then used to measure i) residual HNO_2 in 0.1 mol·dm^{-3} HNO_3 as a function of temperature in the range 313 – 333K, and ii) the rate of decomposition of 100 µmol·dm^{-3} HNO_2 in 0.1 mol·dm^{-3} HNO_3 at the higher temperatures of 323K and 333K. For these measurements, the spectrometer was baselined with a 5 ml aliquot of a solution of 0.1 mol·dm^{-3} HNO_3 equilibrated at the desired temperature, with 0.1 ml

of each Shinn reagent added. To prepare a sample for measurement, 0.1 mL of sulfanilamide solution was added to 5 ml of solution and left for a few minutes, after which 0.1 mL of the N-(1-Naphthyl)ethylenediamine dihydrochloride solution was added and the sample measured after 10 minutes. In this way, the ratio of sample to Shinn reagents was kept constant and the sample concentrations were within the calibration range.

3.6 Techniques for Analysis of Hydroxylamine

Having described methods for the quantification of the ingrowth of the acetic acid product over the course of AHA hydrolysis, the following sections will describe methods for the quantification of the hydrolysis product hydroxylamine. Two methods have been used for this purpose; i) a titrimetric method for measuring the concentration of NH_2OH following both free and complexed AHA hydrolysis in media of varying acidity, and ii) an IC method for quantifying the ingrowth of the protonated NH_3OH^+ ion in the same systems described in section 3.4.4.

3.6.1 Quantification by Redox Titration

3.6.1.1 Oxidation of hydroxylamine with bromine monochloride

The concentration of NH_2OH produced from both free and Fe(III)-complexed AHA was determined via its' oxidation reaction with potassium bromate ($KBrO_3$), followed by iodometric titration with sodium thiosulphate ($Na_2S_2O_3$), as described in Vogel's

textbook of Quantitative Chemical Analysis [124]. A standard 0.02 mol dm^{-3} $KBrO_3$ solution was prepared by drying some finely powdered $KBrO_3$ for 1-2 hours at 120°C and allowing to cool in a closed vessel in a desiccator. Once dry, 3.34g of this was dissolved in 1L of deionized water before being stored ready for use. For preparation of 0.1 mol·dm^{-3} $Na_2S_2O_3$, 1L of deionized water was boiled for 10-15 minutes before being allowed to cool to room temperature, 15.811g $Na_2S_2O_3$ added to it, and the solution stirred until the solid had dissolved. The pH of the solution was measured, and 0.1g·L^{-1} (100mg) of Na_2CO_3 added to it if needed to adjust the pH to between 9 and 10. The final solution was transferred to a clean glass 1L bottle and made up to the mark before being stored in a dark place to avoid deterioration.

To perform the titration, an excess of 0.02 mol·dm^{-3} $KBrO_3$ (approximately 30 ml) along with 10ml of 5 mol·dm^{-3} HCl and 0.25-0.3g KBr, was initially added to an aliquot of the NH_2OH containing solution in a glass stopped bottle, sealed and left for 15 minutes. This allows the bromate to react with NH_2OH (Eq. 3.13) and the excess bromate to react with bromide (produced by Eq. 3.13 and added initially in excess) to create bromine (Br_2) via Eq. 3.14. After 15 minutes the solution was transferred to an Erlenmeyer flask, and 5 ml of freshly prepared 10% potassium iodide (KI) was added to provide excess iodide that produces iodine (I_2) via Eq. 3.15, and the solution immediately titrated with 0.1 mol·dm^{-3} $Na_2S_2O_3$ until it was a pale yellow colour. This process removes most of the liberated iodine via Eq. 3.16. A 3 ml aliquot of starch indicator was added just before the end and a back-titration performed to the disappearance of the blue colour. The indicator is added at the end because the insolubility of the blue starch-iodine complex may prevent some of the iodine reacting

with the titrant. The amount of NH_2OH in solution is then back calculated from the volume of titrant used (shown in Appendix A).

$$BrO_3^- + NH_2OH \xrightarrow{HCL} Br^- + NO_3^- + H^+ + H_2O \quad (3.13)$$

$$BrO_3^- + 5Br^- + 6H^+ \rightarrow 3Br_2 + 3H_2O \quad (3.14)$$

$$2I^- + Br_2 \rightarrow I_2 + 2Br^- \quad (3.15)$$

$$I_2 + 2Na_2S_2O_3 \rightarrow 2NaI + Na_2S_4O_6 \quad (3.16)$$

3.6.1.2 Standardisation of the $Na_2S_2O_3$ titrant

The $Na_2S_2O_3$ titrant was standardised prior to use and any remaining titrant was re-standardised weekly to confirm the stability of the solution. For this procedure 20 ml of 0.02 mol·dm^{-3} $KBrO_3$ was accurately measured into a conical flask, and into this was introduced 2-3g of KI and 5 ml of 3 mol·dm^{-3} sulphuric acid (H_2SO_4). This solution was then immediately titrated with 0.1 mol·dm^{-3} $Na_2S_2O_3$ until it was a pale yellow colour, at which point 3 ml of starch indicator was added, and the solution titrated once more until the disappearance of the blue colour. The reactions occurring during this procedure are shown in Eqs. 3.17 & 3.18 below. The concentration of the $Na_2S_4O_6$ solution can then be back calculated (see Appendix A).

$$BrO_3^- + 6I^- + 6H^+ \rightarrow Br^- + 3I_2 + 3H_2O \quad (3.17)$$

$$I_2 + 2Na_2S_2O_3 \rightarrow 2NaI + Na_2S_4O_6 \quad (3.18)$$

3.6.1.3 Experimental conditions

Conditions of low pH and high temperature were chosen for these experiments to ensure rapid hydrolysis of AHA and resultant product formation. In order to determine experimental conditions where the mono-acetohydroxamatoiron(III) complex ($[Fe(AHA)]^{2+}$) dominates, speciation diagrams in 0.3 mol·dm^{-3} HNO_3 media were created using the equations outlined in section 3.2, at Fe(III) concentrations ranging from 0.0025 – 1 mol·dm^{-3} and AHA concentrations from 0.01 mol dm^{-3} – 10 mol dm^{-3}. From these, conditions of 4 mmol·dm^{-3} AHA, 2.5 mmol·dm^{-3} Fe(III) and 0.3 mol·dm^{-3} HNO_3 were chosen for the preliminary studies. In later revised studies, the concentration of AHA was increased to 20 mmol dm^{-3} to reduce the errors in measurements, and Fe(III) added in the same 1:1.6 ratio of Fe(III):AHA, and additionally in a ratio of 1.25:1 for studies of the hydrolysis under conditions of excess Fe(III). Calculated from speciation diagrams shown in Figure 3.3 in section 3.2, the speciation data for the three sets of initial conditions is shown in Table 3.6 below.

Table 3.6: Speciation data for the Fe^{3+} AHA system for $[HNO_3]$ = 0.3 mol dm^{-3} at 298K. All concentrations (shown in []) are in mmol dm^{-3}.

[Fe_T]	**[AHA]**	**1:1 complex**		**2:1 complex**		**3:1 complex**	
		[]	**% of all complexes**	**[]**	**% of all complexes**	**[]**	**% of all complexes**
2.5	4	1.23	98.18	0.023	1.82	1.53×10^{-6}	1.22×10^{-4}
12.5	20	9.21	94.01	0.586	5.99	1.35×10^{-4}	1.38×10^{-3}
25	20	1.79	99.86	2.58×10^{-3}	0.14	1.35×10^{-8}	7.52×10^{-7}

A series of experiments were also conducted in other acidic media to remove the effect of NO_3^-, including several performed in the same molarity H_2SO_4 and perchloric acid ($HClO_4$), with Fe(III) added as ferric sulphate ($Fe_2(SO_4)_3$) and ferric perchlorate

($Fe(ClO_4)_3$) respectively. For the range of experiments performed in different acidic media, the speciation was assumed to be analogous to that in HNO_3.

Finally, experiments were performed in $HClO_4$ under an inert N_2 atmosphere to avoid; i) through use of perchlorate, the possibility of hydroxylamine reacting with HNO_3/HNO_2, and ii) through use of an inert atmosphere, the possibility that any amount of Fe(III) that might be reduced by NH_2OH could be re-oxidised back to Fe(III) and further react with NH_2OH. In a fume hood, all glassware was initially degassed prior to use by purging with N_2 gas. A 50 ml stock solution of 50 $mmol \cdot dm^{-3}$ $Fe(ClO_4)_3$ acidified in 0.6 $mol \cdot dm^{-3}$ $HClO_4$, and a 50 ml solution of 40 $mmol \cdot dm^{-3}$ AHA were prepared. N_2 gas was then bubbled through each of the solutions for 20 minutes at a rate of approximately 0.5 L hr^{-1}. By mixing aliquots of the two purged stock solutions in a 1:1 ratio, solutions of 20 $mmol \cdot dm^{-3}$ AHA in 0.3 $mol \cdot dm^{-3}$ $HClO_4$ in the presence of 25 $mmol \cdot dm^{-3}$ Fe(III) perchlorate where prepared in 10ml volumetric flasks, stoppered and sealed with parafilm. Two of these were placed in the oven and left to hydrolyse at 333K for 24 hours and one was placed in positive pressure glove box and left to hydrolyse for 2 weeks. Once hydrolysis was complete, all solutions required for the titration procedure were degassed prior to use and the titration performed on the benchtop.

3.6.2 Real-time Quantification by Ion Chromatography

Following the measurements of NH_2OH taken on completion of AHA hydrolysis, a method was needed for understanding its evolution throughout the reaction in real-time. With the knowledge that NH_2OH was likely to be present as a protonated form

in acidic media, the previously described IC system was utilised to quantify the NH_3OH^+ ion over the course of free and complexed AHA hydrolysis under the same initial conditions as described in section 3.4.4.

3.6.2.1 Equipment setup

The equipment setup for the analysis of cationic NH_3OH^+ necessarily differs from that for the analysis of anionic CH_3COO^- and NO_2^- (described in sections 3.4 and 3.5.1) by the nature of the separation column and the absence of a chemical suppression system between the column and the detector. The equipment setup is shown in Figure 3.16. The Metrohm RP 2 guard column used for anion analysis previously was utilised, along with a standard Metrosep C 4 - 150/4.0 cation column and the standard eluent composition of 1.7 mmol·dm^{-3} HNO_3 / 0.7 mmol·dm^{-3} 2,4-Pyridinedicarboxylic acid (PDCA) eluent / 0.05 mmol·dm^{-3} crown ether, pumped at a rate of 0.9 ml·min^{-1}.

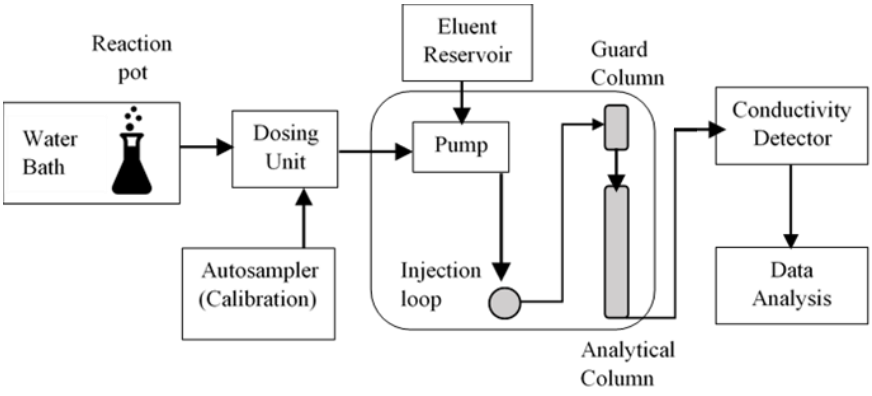

Figure 3.16: Ion chromatography system configuration for cation analysis.

In comparison to anion analysis, the quantification of cations by ion chromatography is usually performed by a direct (unsuppressed) method and as a result is often a less

sensitive technique. The background conductivity is relatively large in comparison to the measuring signal, thus very high demands are placed on the conductivity detector in direct ion chromatography to compensate for this. In these types of analysis involving electronic suppression of the background, the consistency of the background conductivity is thus of key importance. Degassing of the eluent prior to use is even more important to reduce the risk of bubbles that can damage the high-pressure pump, cause baseline fluctuations and interfere with ion peaks in the chromatogram. This was done for at least 30 minutes by purging with nitrogen gas whilst stirring.

3.6.2.2 Calibration and experimental procedure

For calibration of the instrument, a total of 3-5 standards of hydroxylamine hydrochloride ($NH_2OH.HCl$) in 0.1 mol·dm^{-3} HNO_3 were prepared from 100ml stock solutions of 1 mol·dm^{-3} HNO_3 and 100 mmol·dm^{-3} $NH_2OH.HCl$, and the calibration was performed in the same way as described in section 3.4.2.

An example chromatogram of a 4 mmol dm^{-3} standard of $NH_2OH.HCl$ in 0.1 mol dm^{-3} HNO_3 is shown in Figure 3.17. The background conductivity of the slightly acidic eluent was approximately 715 µS cm^{-1} and cations produce a lowering of this conductivity on reaching the detector and thus a negative peak in the chromatogram. Applying changes in the software to baseline the chromatogram and reverse the y-axis provides ease of visualisation.

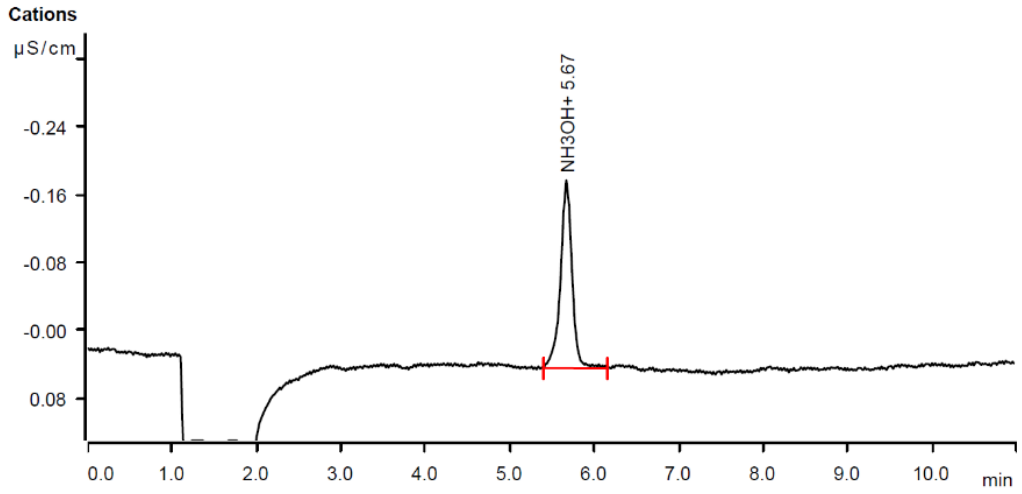

Figure 3.17: Example chromatogram of 4 mmol dm^{-3} $NH_2OH.HCl$ in 0.1 mol dm^{-3} HNO_3, with baseline correction and a reversed y-axis.

All the calibration curves used in experiments are shown in Figure 3.18, and the values for RSD and correlation coefficients (R^2) for each calibration function are shown in Table 3.7.

Table 3.7: Equations, RSD and R^2 values for each NH_3OH^+ calibration shown. In the equations, A is the peak area in units of $\mu S.cm^{-1}.min$, and Q is the injected concentration of NH_3OH^+.

Calibration	Equation	RSD / %	R^2	Experiments
Cations_method_template	A = 0.0377 × Q	1.338	0.999	1:4 Fe:AHA, 323K
Cations_method_template_2	A = 0.0313 × Q	1.564	0.999	Free AHA, 323K
Cations_method_template_3	A = 0.0548 × Q	2.933	0.999	1:1 Fe:AHA, 323K
Cations_2_method_template_2	A = 0.0677× Q	4.391	0.999	All 333K
Cation_2_method_template_3	A = 0.0504× Q	5.826	0.999	1:4 Fe:AHA, 313K
Cations_2_method_template_4	A = 0.0452× Q	6.278	0.998	Free AHA, 313K
Cation_2_method_template_7	A = 0.0438× Q	5.992	0.998	1:1 Fe:AHA, 313K, first 72 hrs
Cation_2_method_template_6	A = 0.0306× Q	4.234	0.999	1:1 Fe:AHA, 313K, final 24 hrs

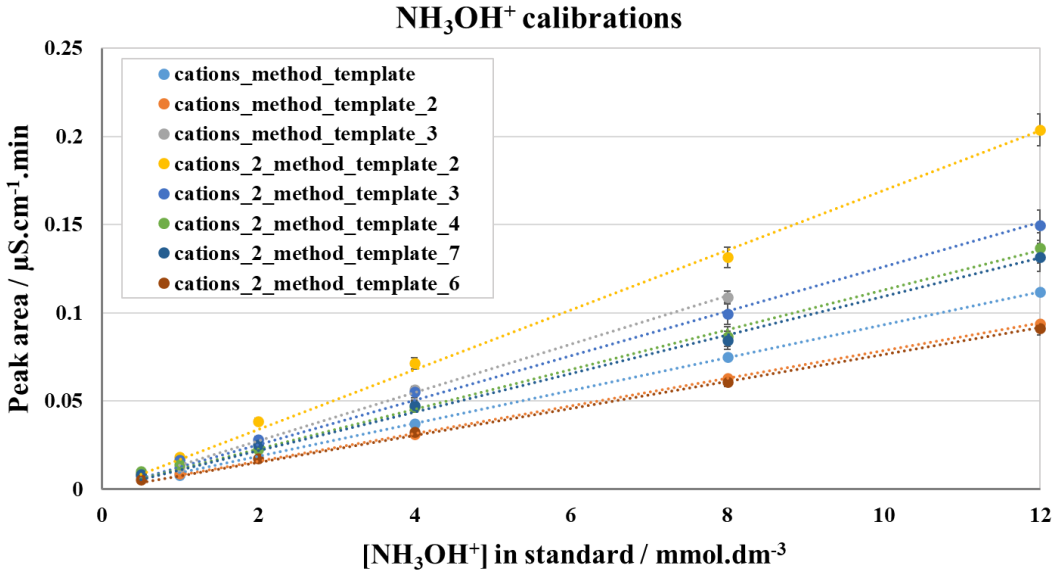

Figure 3.18: Calibration curves of NH_3OH^+ concentration in units of mmol·dm^{-3} against peak area in µS cm^{-1}. Vertical error bars are shown as the %RSD values for the respective calibration curves as written in Table 3.7.

Inspection of Figure 3.18 shows two key differences between the range of calibration functions for NH_3OH^+ compared to those of both anions, namely i) the calibration functions are linear for analysis of NH_3OH^+ by unsuppressed conductivity detection, and ii) significant variation is seen throughout the range of calibration functions. As with the anion analysis previously, all experiments at 333K were initially performed using different eluents but analysed by a single calibration. However further calibrations for NH_3OH^+ showed a much greater sensitivity to the exact composition of the eluent, and thus the experiments at 333K were repeated. Only a single calibration on 5L eluent was required, as this volume proved sufficient for running all three of the experiments immediately after one another. In this case, the system was rinsed thoroughly between each experiment, re-equilibrated, and 3 check standards were run through the column prior to running the next experiment in order to confirm the validity of the calibration.

The experimental procedure was the same as described for anions, with the exception of the final experiment performed at 313K with an initial Fe(III):AHA ratio of 1:1. In this case, the length of the run required more than a single 5L of eluent. Two eluents were therefore prepared and separately calibrated prior to experimental setup, and changed over during the experimental run. Whilst short on the time scale of the experimental run, this caused a pause in data collection during the run whilst the system was rinsed, re-equilibrated to remove air bubbles created by this change, and put back into operation.

3.7 Techniques for Analysis of Fe(II)

Based on previous work conducted by Andrieux *et al*. [77, 83] Fe(III) was initially assumed to be a non-oxidising metal ion with regards to AHA and hydroxylamine due to thermodynamic hindrances, an assumption which has allowed many authors to perform kinetic analysis of AHA hydrolysis via a colorimetric analysis of the Fe(III)-AHA mono-complex. To investigate whether this assumption holds true or if it may require some revision, two different techniques were utilised to quantify any Fe(II) present from the reduction of Fe(III) in solution during or after completion of hydrolysis.

3.7.1 Quantification by UV-Vis Spectroscopy

Solutions of AHA hydrolysed in the presence of Fe(III) were analysed for Fe(II) content via UV-Vis spectroscopy. Fe(II) reacts with 1,10-phenanthroline to form an

orange-red complex $[(C_{12}H_8N_2)_3Fe]^{2+}$, the colour intensity of which is independent of the acidity in the pH range 2-9, and is stable for long periods [124]. The complex has a maximum absorbance at 511nm which can be used to determine the amount of Fe(II) in a sample.

$$Fe^{2+} + 3Phen \rightarrow Fe(Phen)_3^{2+} \tag{3.19}$$

3.7.1.1 Experimental Procedure

Aqueous stock solutions of 100 ml of 0.25% 1,10-phenanthroline, and 10% hydroxylamine chloride (NH_3OHCl) were prepared by dissolving the required mass in deionised water. A buffer solution of pH 4.1 was prepared by the addition of 2.6 ml of a 0.1 mol·dm^{-3} sodium hydroxide (NaOH) solution to 100 ml of 0.1 mol·dm^{-3} potassium hydrogen phthalate (KHP). Ammonium iron(II) sulphate hexahydrate ($(NH_4)_2Fe(SO_4)_2{\cdot}6H_2O$) was used to create a 1000ppm stock and 100ppm working solution for calibration purposes.

Standards between 1 – 6 ppm Fe(II) were prepared by the addition of aliquots of the $(NH_4)_2Fe(SO_4)_2{\cdot}6H_2O$ working solution to a 50ml volumetric flask, followed by 4 ml of 1,10-phenanthroline, before being buffered with KHP to a pH of 3.9 and diluted to 50ml. A Shimadzu UV-2600 UV-Vis spectrophotometer (Shimadzu UK Ltd., Milton Keynes, UK) was used to record spectra at 0.2nm increments over the wavelength range of 320 - 600nm. Figure 3.19 shows the spectra recorded for each of the 5 standards and the calibration curve produced for the maximum absorbance at 511nm against standard Fe(II) concentration is shown in Figure 3.20.

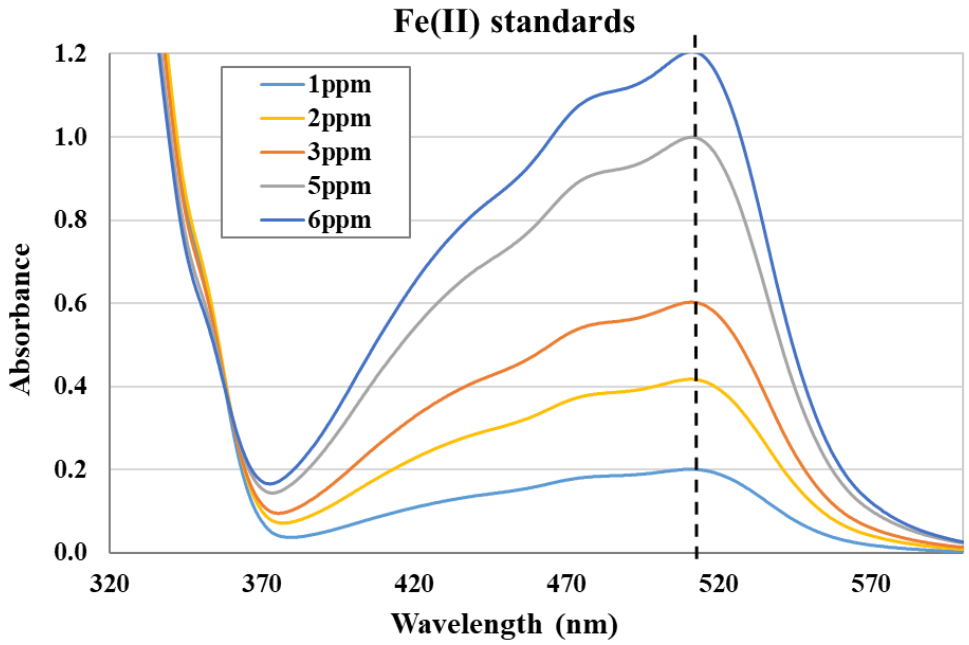

Figure 3.19: UV-Vis electronic absorption spectra recorded for Fe(II) standards in the range of 1 - 6 ppm using a reference solution of de-ionised water.

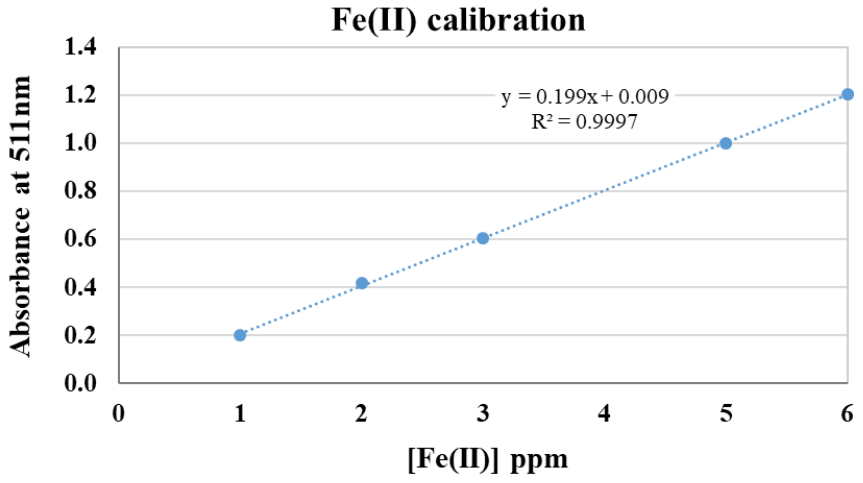

Figure 3.20: Calibration curve produced from the maximum absorbance of the Fe(II)-phenanthroline complex at 511nm against standard Fe(II) concentration in ppm.

It has been reported that the chromophoric complexes formed by 1-10-phenanthroline and high concentrations of Fe(III) could increase the absorbance of samples at 511nm and thus interfere with the Fe(II) determination in this method. Zhu *et al*. [125] noted

the error reached 22.6% when the concentration of Fe(III) was 16 times more than that of Fe(II) and more than 50% when Fe(III) was not complexed and Fe(II) was less than 1% of the total iron. Whilst Fe(III) was not expected in large excess, the presence of Fe(III) on the determination of Fe(II) via it's absorbance at 511nm was therefore tested. Using the 3 ppm Fe(II) standard, Fe(III) was added as its' sulphate salt in concentrations of 1, 3 and 10 ppm, to give ratios of Fe(III):Fe(II) of 0.33, 1, and 3.33. Figure 3.21 shows the spectra of the 3 ppm Fe(II) standard with additional Fe(III). At these concentrations the Fe(III) had no effect on the determination of Fe(II), and the intensity of the peak at 511 nm remained constant within experimental errors showing a variation of only 0.17%.

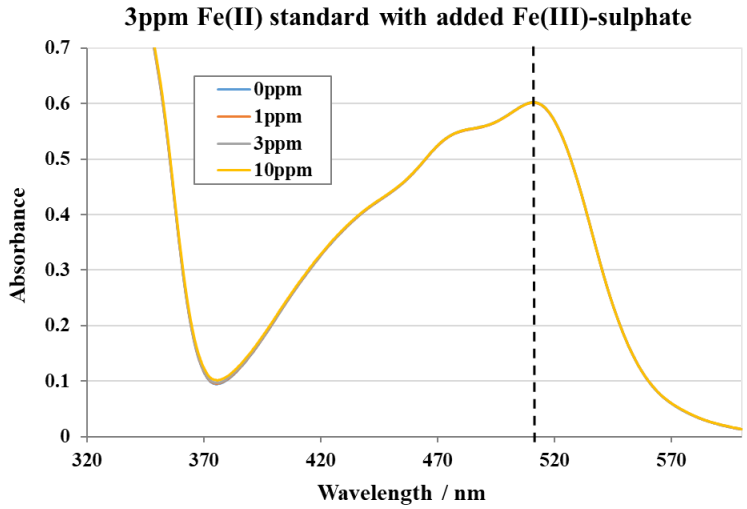

Figure 3.21: UV-Vis electronic absorption spectra of the 3ppm Fe(II) standard, and the same standard with Fe(III) added as it's sulphate salt in concentrations of 1, 3 and 10ppm.

For sample measurement, 0.2 ml of sample was added to a 50ml volumetric flask, followed by 4 ml of 1,10-phenanthroline, before being buffered with KHP to a pH of 3.9 and diluted to 50ml. This provided a 250-fold dilution of the samples to place them

within the calibration range. Separate spectra for 1.2 mmol dm^{-3} $HClO_4$ and HNO_3 were taken separately, using a water reference, and subtracted from the sample spectra.

3.7.2 Real-time Quantification by Ion Chromatography

Following the measurements of Fe(II) taken on completion of AHA hydrolysis, a method was needed for understanding its evolution throughout the process in real-time. For this purpose, the previously described IC system was utilised for quantification of the ingrowth of Fe(II) ion over the course of complexed AHA hydrolysis, under the same initial conditions as described in section 3.4.4. Additional experiments were also performed to investigate the ingrowth of Fe(II) from the reduction of Fe(III) by NH_2OH in solutions of varying Fe(III):NH_2OH initial ratios.

3.7.2.1 Equipment setup

The same equipment setup for measuring cationic Fe(II) was used in both types of experiments, which differs from that for the measurement of cationic NH_3OH^+ (described in section 3.6.2.1) only by the nature of the separation column. The Metrohm RP 2 guard column was used with a Nucleosil 5SA - 125/4.0 cation column, and the columns' standard eluent composition of 4.0 mmol·dm^{-3} tartaric acid / 0.5 mmol·dm^{-3} citric acid / 3.0 mmol·dm^{-3} ethylenediamine / 5% Acetone, pumped at a rate of 1.5 ml·min^{-1}.

3.7.2.2 Calibration and experimental procedure

Calibration of the instrument was performed in the same way for both sets of experiments. A total of 3-5 standards of $(NH_4)_2Fe(SO_4)_2$ in 0.1 mol·dm^{-3} HNO_3 were prepared from 100 ml stock solutions of 100 mmol·dm^{-3} $(NH_4)_2Fe(SO_4)_2$ and 1 mol·dm^{-3} HNO_3, and the calibration was performed in the same way as described in section 3.4.2. All the calibration curves procedure shown in Figure 3.22, and the values for RSD and R^2 for each of calibration functions are shown in Table 3.8. Little variation was seen in the calibration curves.

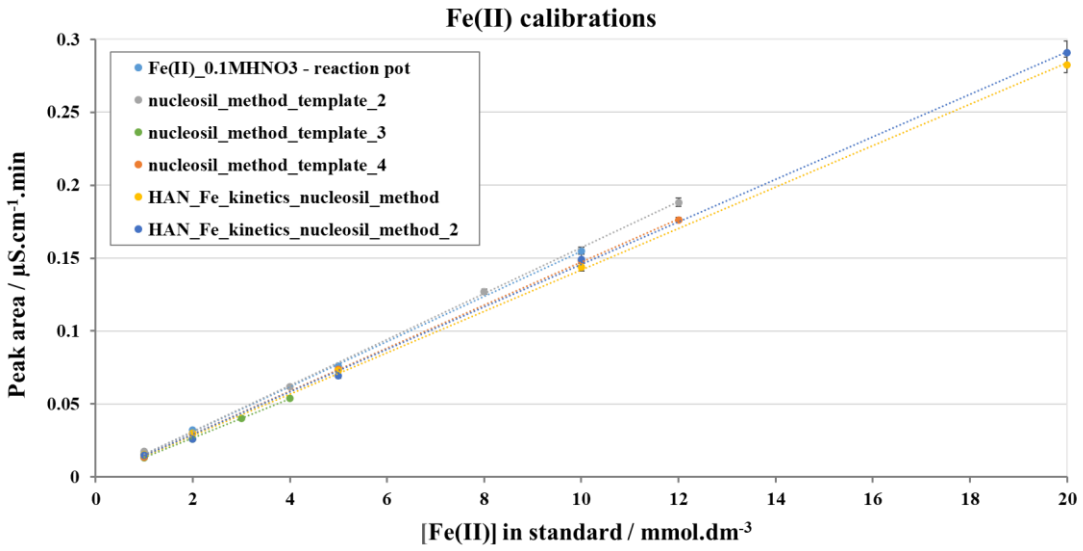

Figure 3.22: Calibration curves of Fe^{2+} concentration [mmol·dm^{-3}] against peak area [µS.cm^{-1}.min]. Vertical error bars are shown as the %RSD values for the respective calibration curves as written in Table 3.8. For calibrations used in AHA hydrolysis experiments, the maximum [Fe(II)] varies from 4 to 12 mmol dm-3 dependent upon whether the initial [Fe(III)], and thus theoretical maximum [Fe(II)], was 2.5 or 10 mmol dm^{-3} in the relevant experimental run. Calibrations relating to the second set of experiments, i.e. investigating the reduction of Fe(III) by NH_2OH in solutions of varying Fe(III):NH_2OH initial ratios, were performed up to a theoretical maximum [Fe(II)] measurement of 20 mmol dm^{-3}.

Table 3.8: RSD and R^2 values for each Fe^{2+} calibration performed. In the equations, A is the peak area in units of $\mu S.cm^{-1}.min$, and Q is the injected concentration of Fe^{2+} in $mmol \cdot dm^{-3}$.

Calibration	Equation	RSD / %	R^2	Experiments
Fe(II)_0.1MHNO3 – reaction pot	A = 0.0617 × Q	1.568	1.000	All 333K 1:4 Fe:AHA, 323K
Nucleosil_method_template_2	A = 0.0629 × Q	1.539	1.000	1:1 Fe:AHA 323K
Nucleosil_method_template_3	A = 0.0537 × Q	1.451	1.000	4:1 Fe:AHA, 313K
Nucleosil_method_template_4	A = 0.0590 × Q	0.931	1.000	1:1 Fe:AHA, 313K
HAN_Fe_kinetics_nucleosil_method	A = 0.0568 × Q	1.907	1.000	Fe:HAN > 1
HAN_Fe_kinetics_nucleosil_method_2	A = 0.0583 × Q	2.761	1.000	Fe:HAN = 1

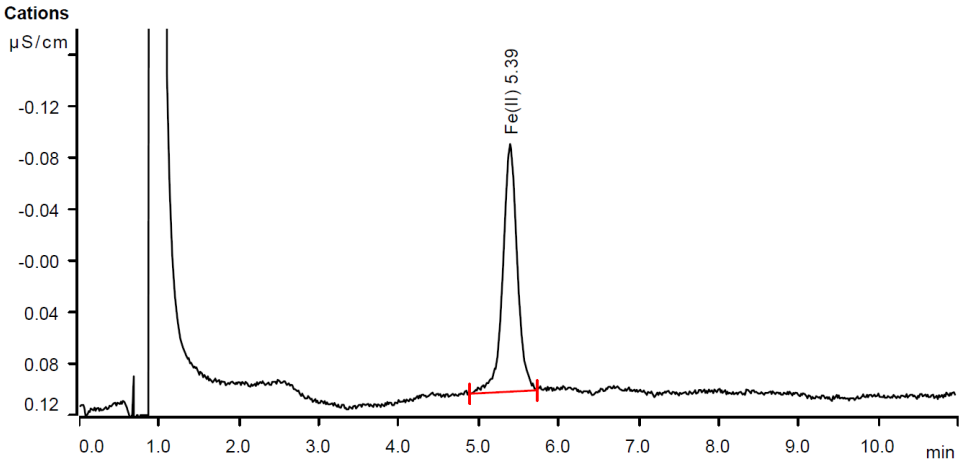

Figure 3.23: Example chromatogram of 3 mmol dm^{-3} standard of Fe(II) in 0.1 mol dm^{-3} HNO_3, with baseline correction and a reversed y-axis.

An example chromatogram of a 3 mmol dm^{-3} standard of Fe(II) in 0.1 mol dm^{-3} HNO_3 is shown in Figure 3.23. Analogous to the analysis of NH_3OH^+, the same changes in the software were applied to baseline the chromatogram and reverse the y-axis due to the production of a negative peak. The background conductivity of the eluent was lower than that used in NH_3OH^+ analysis at approximately 500 µS cm^{-1}, but chromatogram showed higher baseline noise. Continuous stirring of the eluent is advised due to the volatility of acetone, however due to the higher background noise

from a significantly greater flowrate of eluent required for this analysis compared to previous ones, and the higher risk of air bubbles, the eluent was not stirred.

The experimental procedure for the AHA hydrolysis studies was the same as described for anions previously. With the flowrate of the eluent being higher than the previous cation analysis for NH_3OH^+ and over double that required for anion analysis, very high demands were placed on the high-pressure pump, For this reason, along with the volume of eluent required, the duration of this analysis for most experiments was shorter. In the case of the final experimental run at 313K with an initial Fe(III) concentration of 10 mmol dm^{-3}, the eluent was changed half way through by following the same procedure as described for the analysis of NH_3OH^+ in this same experiment.

3.7.2.3 Studies on the reduction of Fe(III) by HAN

The reduction of Pu(IV) by NH_2OH is well-known, with the reaction occurring by one of two pathways that depends on the initial ratio R = Pu(IV)/NH_2OH [95], with a 2:1 stoichiometry followed when R > 1 and a 1:1 stoichiometry followed when R < 1. For the less thermodynamically feasible reduction of Fe(III) by HAN, Bengtsson *et al*. [99] suggested that the 2:1 reaction stoichiometry could only occur at high temperatures and/or high Fe(III):HAN ratios where Fe(III) was in at least 5 – 10 fold excess. This was considered likely at the start of some experiments at elevated temperatures, therefore the reduction of Fe(III) by HAN was followed over a range of Fe(III):HAN ratios, under conditions of 0.1 mol dm^{-3} HNO_3 and 323K. The ratios considered are shown in Table 3.9.

Table 3.9: Initial ratios of Fe(III):NH_2OH investigated for the reduction of Fe(III) by NH_2OH in 0.1 mol dm^{-3} HNO_3 at 323K, with the dominant reaction stoichiometry expected and theoretical maximum Fe(II) concentration possible for the case where a single stoichiometry occurrs.

Fe(III) / mmol dm^{-3}	HAN / mmol dm^{-3}	Ratio Fe(III):HAN	Sulfamic acid / mmol dm^{-3}	Dominant stoichiometry expected	Maximum theoretical Fe(II) / mmol dm^{-3}
10	10	1:1	-	1:1	10
50	10	2:1	-	1:1	20
20	10	5:1	-	2:1	20
50	5	10:1	-	2:1	10
50	5	10:1	25	2:1	10

Solutions of 20 – 50 mmol dm^{-3} $Fe(NO_3)_3$ acidified in 0.1 mol dm^{-3} HNO_3 were prepared, transferred to a 250 ml conical flask sealed with parafilm, and left to equilibrate in a water bath at 323K. The MagicNET software was used to create a sample table and method, with a sampling interval of 10 minutes. Once the solution reached equilibrium at the desired temperature, the required amount of hydroxylamine was added in solid form as $NH_2OH.HCl$ to the conical flask, and the solution well mixed and resealed with parafilm. In one experiment, sulfamic acid was added in solid form along with the hydroxylamine. Lastly, the other end of the tubing running from the Dosino was submerged in the reaction mixture and the experimental run started. The first sample measurement was taken to be 4 minutes, to allow for addition of $NH_2OH.HCl$, IC-system start up and sample aspiration time.

CHAPTER 4

Results and Discussion

4 Results and Discussion

As stated at the end of Chapter 2, this thesis is focussed on the study of Fe(III)-AHA systems as a non-active analogue to Np(IV) and Pu(IV), and aims to address two key questions:

i) is there any change in the products of AHA hydrolysis when the hydroxamic acid is complexed to a metal ion, and

ii) what is the nature of the reducing agent responsible for the observed ingrowth of Pu(III) during the associated Pu(IV)-AHA hydrolysis.

This Chapter begins by seeking to address question (i).

4.1 Identification of Hydrolysis Products by Raman Spectroscopy

Raman spectroscopy was first utilised to confirm the identity of the products of the acid-catalysed hydrolysis of AHA, and determine whether there are any changes to the product distribution from the hydrolysis of Fe(III)-complexed AHA in comparison to that of free AHA. The results of studies performed using two separate instruments, a 785 nm SERS and a 532 nm solution cell Raman microscope, are discussed in the following sections.

4.1.1 Surface-Enhanced Raman Spectroscopy (SERS) Studies

4.1.1.1 Identification of hydrolysis products from standards

Stock solutions of AHA and the hydrolysis product acetic acid (CH_3COOH) were created at a concentration of 0.538 mol dm^{-3}. From these, 200 µl standard solutions of 0.5 mol dm^{-3} were further prepared by taking 186 µl of each stock and diluting with either 14 µl of de-ionized water or 70 wt.% HNO_3 for either aqueous experiments or and those acidified in 5 wt.% HNO_3 respectively. For the hydrolysis product hydroxylamine, a 0.538 mol dm^{-3} stock solution was prepared from a 50 wt.% NH_2OH solution and a 200 µl standard solution of 0.5 mol dm^{-3} NH_2OH was created by taking a 186 µl aliquot of the stock and diluting with 14 µl of de-ionized water, 5 wt.% HCl or 5% HNO_3. 20 µl aliquots of each standard solution were loaded onto gold substrates for SERS analysis as described in Section 3.3.2.

In order to determine a suitable laser power for obtaining appropriate peak intensities whilst avoiding localised heating of the sample, a scoping study of AHA standards was initially carried out using different laser powers. Figure 4.1B shows the spectra of the AHA standards, where the laser power was adjusted by addition of a neutral density filter of 0.5 and 0.79, i.e. 50 % and 79 % laser power respectively. A spectrum of the gold background is shown in Figure 4.1A for reference.

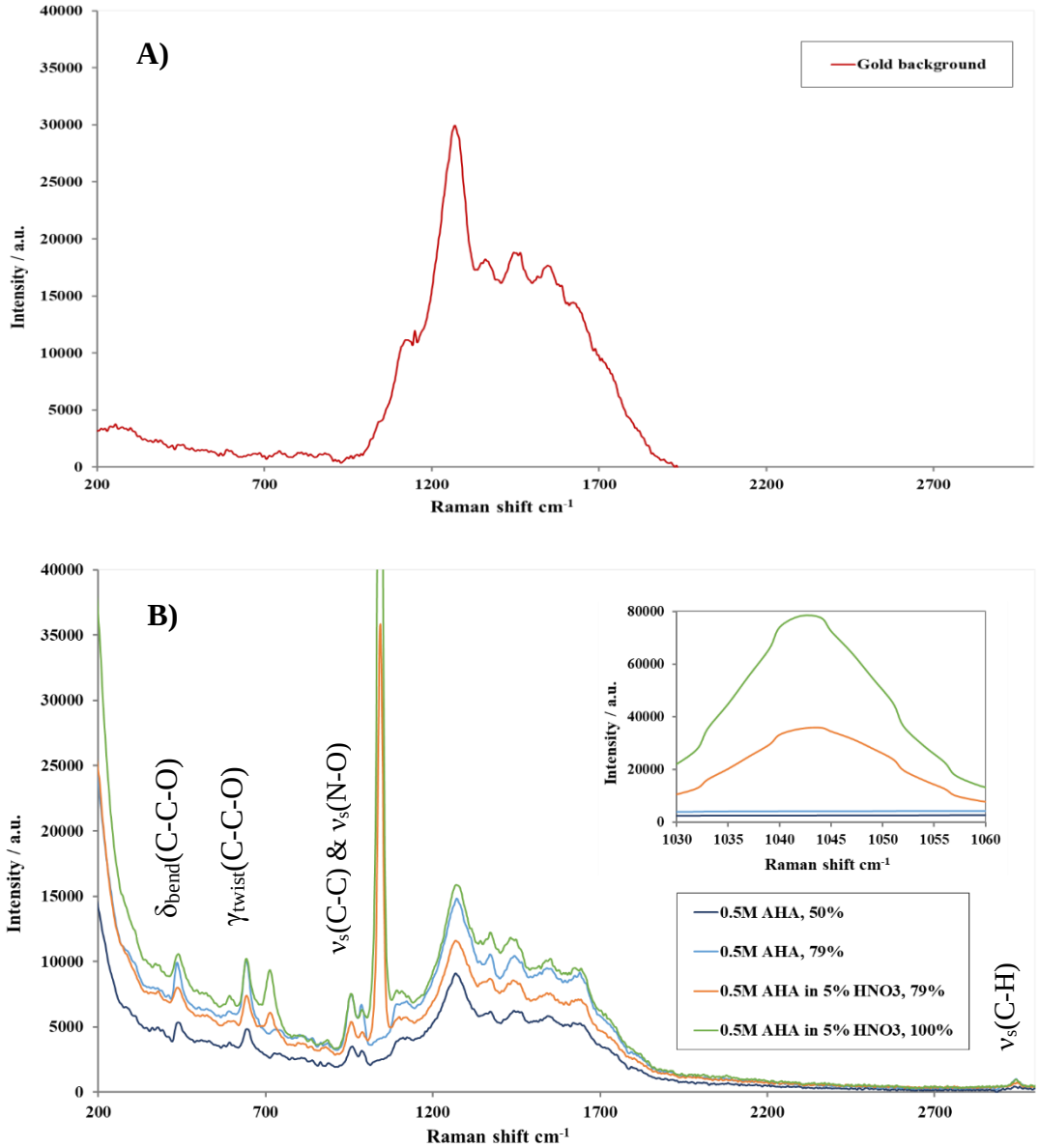

Figure 4.1: A) Spectrum of gold background. B) Spectra of 0.5 mol dm^{-3} AHA in de-ionized water and 5% wt. HNO_3, taken with varying laser powers of 50%, 79% and 100%.

From Figure 4.1A it can be seen that the gold substrate background dominates the spectral region between 1100 – 1800 cm^{-1}. For the Raman spectrum in Figure 4.1B of AHA in de-ionized water (irrespective of laser power), the bands at 436 cm^{-1} and 643 cm^{-1} are assigned to the δ_{bend}(C-C-O) in plane bend and γ_{twist}(C-C-O) out of plane bend, whilst the doublet peak at 957 cm^{-1} and 987 cm^{-1} corresponds to the ν_s(C-C) stretching

and ν_s(N-O) stretching modes respectively [79]. A minor band is also seen for AHA at 2947 cm^{-1} that is assigned to the ν_s(C-H) stretching mode. For the spectra in 5% wt. HNO_3 (again irrespective of laser power); i) The above assigned AHA peaks shift to a higher wavenumber by 1-2 cm^{-1} and ii) a new very intense peak at 1044 cm^{-1} appears. Both spectral differences can be attributed to the presence of HNO_3, in the former weak electrostatic attractions between NO_3^- and AHA causing a wavenumber shift and in the latter to the ν_s(N-O) stretching mode [126].

Considering now the effect of laser power and returning to the Raman spectra of AHA diluted using de-ionized water in Figure 4.1B, the higher laser power of 79% produced higher intensity peaks and better signal to noise compared to 50% laser power. Interestingly, using 79% laser power on a sample of AHA diluted in 5% wt. HNO_3 produced a spectrum with peaks that were well defined, but comparatively lower in intensity than for AHA diluted in de-ionized water. For comparison, a further spectrum of AHA in 5% HNO_3 taken with 100 % laser power was also acquired (Figure 4.1). Whilst the mode intensities relating to AHA are seen to increase further in this spectrum, the ν_s(N-O) stretching mode for HNO_3 at 1044 cm^{-1} also increases further to the point where it oversaturates the detector. The 79 % setting was thus chosen for analysing subsequent samples.

Consideration next of the hydrolysis products of AHA, starting with CH_3COOH, Figure 4.2 shows the spectra of 0.5 mol dm^{-3} CH_3COOH in de-ionised water and 5 % HNO_3 media at the chosen laser power of 79%. The main band for CH_3COOH at 886 cm^{-1} is assigned to the ν_s(C-C) stretching mode, based on Raman assignments of acetic acid published by Nakabayashi *et al.*[127]. This band is more intense than those of

AHA in Figure 4.1 and does not significantly decrease in intensity in 5% HNO_3. However, and as per the previously described AHA bands, addition of 5% HNO_3 does result in a similar shift in the 886 cm^{-1} peak to a higher wavenumber by 1-2 cm^{-1}. Similar to AHA, CH_3COOH also shows a minor band centred at 2943 cm^{-1} that is assigned to the ν_s(C-H) stretching mode.

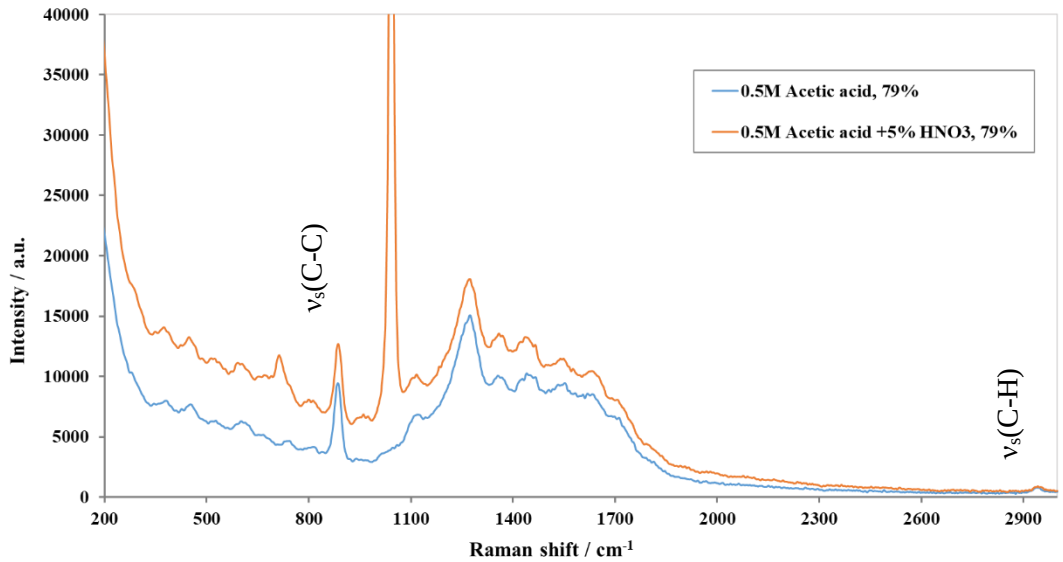

Figure 4.2: Spectra of solutions of 0.5 mol dm^{-3} acetic acid standard in de-ionized water, and a standard in 5% HNO_3 using the chosen laser power of 79%.

Finally, considering the second AHA hydrolysis product hydroxylamine, spectra were taken using the optimum laser power determined above of 79%. Figure 4.3 shows data acquired from the wavenumber range 200 – 2000 cm^{-1}, with spectral intensities normalised to the major peak of the gold background at 1270 cm^{-1}. No further significant peaks were observed at wavenumbers above 2000 cm^{-1}, and so this part of the spectrum has been accordingly omitted.

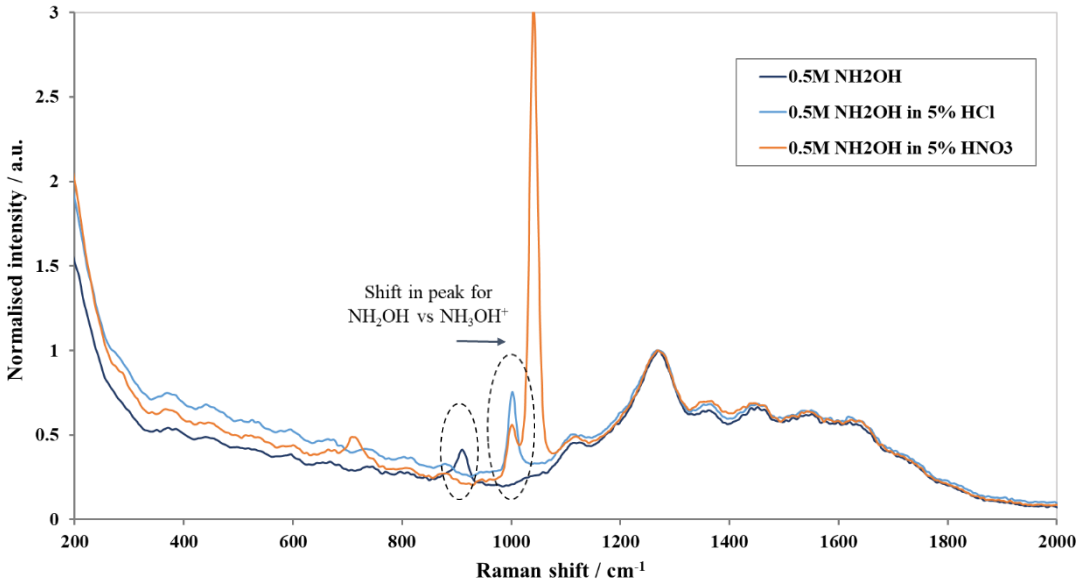

Figure 4.3: Spectra of aqueous and acidified solutions of hydroxylamine showing the shift in the peak position from 910 cm^{-1} for NH_2OH to 1002 cm^{-1} for NH_3OH^+. Spectra are normalised to the gold peak at 1270 cm^{-1}.

The Raman band at 910 cm^{-1} in the spectrum of hydroxylamine in deionised water is assigned to the primary ν_s(N-O) stretch according to the same assignment of the band at ~912 cm^{-1} for solid hydroxylamine reported by Nightingale and Wagner [128]. However, in acidic solutions of 5% HCl or 5% HNO_3, this peak shifts to 1002 cm^{-1}. Such a shift of ~90 cm^{-1} (from 912 cm^{-1} to 1002 cm^{-1}) could be due to the protonation of NH_2OH to NH_3OH^+ based on the Raman spectra of hydroxylamine hydrochloride ($NH_3OH.Cl$) crystals reported by Krishnan *et al*. [129], with these authors suggesting the primary ν_s(N-O) stretch for a single $NH_3OH.Cl$ crystal is found at 1004 cm^{-1}. The pKa of hydroxylamine is 5.96 [130]. Whilst not measured here, the pH of deionized water is ~5.7 [131], meaning the degree of protonation in deionised water would be minimal compared to that in acidic media. Solutions of hydroxylamine hydrochloride (HAH) and hydroxylamine nitrate (HAN) are very similar, with both containing the hydroxylammonium cation and differing only with respect to their counter-anion;

therefore Krishnan's work can be exported to HAN. In HAH, an additional hydrogen resides on the nitrogen of hydroxylamine and thus a new N-H bond is created. As for HAH, hydrogen atoms in HAN are involved in hydrogen bonding [132], which is noted by Krishnan *et al.* [129] to very much influence the observed N-H and O-H stretching vibrations in NH_3OHCl. The same behaviour is assumed for HAN, therefore it is likely that the new N-H hydrogen bond results in the observed shift of the ν_s(N-O) stretch seen here. We would expect to see peaks relating to the NH_3 rocking and deformation modes in the region of approximately 1100-1650 cm^{-1} [129, 133], however the gold background signal swamps any peaks that might be otherwise observed in this region. The band at 714 cm^{-1} in the spectrum of NH_2OH in HNO_3 solution can be assigned to the deformation of NO_3^-, $\delta_{bend}(NO_3^-)$ [134].

Whilst the AHA hydrolysis product CH_3COOH is expected to be stable in HNO_3, the instability of HAN in HNO_3 is well-known, a reaction occurring between the two in acidic media as shown in Eq. 4.1, autocatalyzed by the HNO_2 product [93]. The result would be a lower concentration of NH_3OH^+ and therefore a less intensity ν_s(N-O) stretch than would be expected from AHA hydrolysis.

$$NH_3OH^+ + 2HNO_3 \rightarrow 3HNO_2 + H_3O^+ \quad (4.1)$$

As can be seen in Figure 4.3, the ν_s(N-O) stretch for NH_3OH^+ at 1002 cm^{-1} resides on the edge of the ν_s(N-O) stretch for HNO_3 at 1044 cm^{-1} and thus is partially convoluted, resulting in potential difficulties in separated observation of NH_3OH^+, particularly if its concentration diminishes significantly.

Prior to commencing hydrolysis studies, a final set of standards were therefore taken in order to identify the position of the nitrite (NO_2^-) peak, as the production of HNO_2 via Eq. 4.1 would be expected to be rapid and pronounced if the autocatalytic decomposition of HAN were to occur under the conditions of the AHA hydrolysis experiments described later in section 4.1.1.2. In order to attempt to measure NO_2^- in HNO_3 solutions, excess nitrite was added to a 5% HNO_3 solution in the form of sodium nitrite ($NaNO_2$); nitrate-free HNO_2 was also prepared from the reaction of $NaNO_2$ and HCl as a control via Eq. 4.2. Nitrous acid is a weak acid that can both weakly dissociate (pKa = 3.14 [113]) and undergoes disproportionation to HNO_3 and NO via Eq. 4.3 and 4.4 below. Spectra were therefore taken immediately due to its' inherent instability, the results of which are shown in Figure 4.4.

$$NaNO_2 + HCl \Leftrightarrow NaCl + HNO_2 \quad (4.2)$$

$$HNO_2 \Leftrightarrow H^+ + NO_2^- \quad (4.3)$$

$$3HNO_2 \rightarrow HNO_3 + 2NO + H_2O \quad (4.4)$$

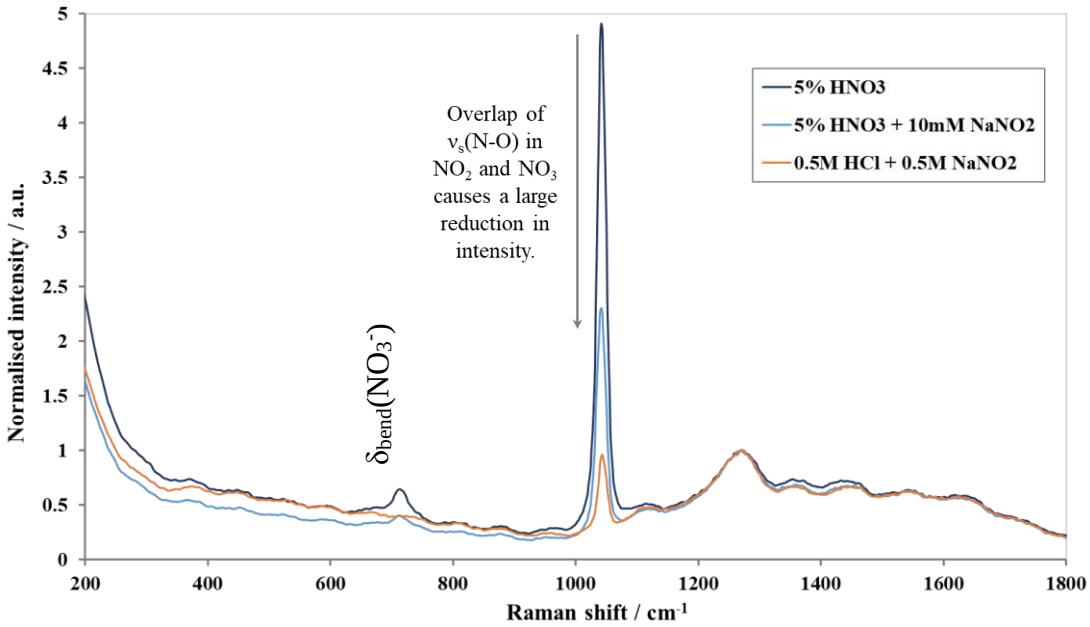

Figure 4.4: Spectra showing the overlap of the main ν_s(N-O) stretch for NO_3 and NO_2. Spectra are normalised to the major peak of the gold background at 1270 cm^{-1}.

From the spectra in Figure 4.4 of pure HNO_2 produced from the reaction of $NaNO_2$ and HCl, it can be seen that the primary ν_s(N-O) stretch in HNO_2 overlaps with the analogous stretch in HNO_3, appearing at 1044 cm^{-1} in HNO_3 and 1045 cm^{-1} in HNO_2, and differing only in relative intensity. There are no other minor HNO_2 or HNO_3 peaks in the spectrum, with the exception of the peak appearing at 714 cm^{-1} in both of the HNO_3 solutions can be assigned to the deformation of NO_3^-, $\delta_{bend}(NO_3^-)$ [134]. Turning now to the addition of $NaNO_2$ to HNO_3, the addition of 10 mmol dm^{-3} $NaNO_2$ to HNO_3 did not shift the position of the ν_s(N-O) stretch but causes a significant reduction in peak intensity. At least in part, this could be a result of the formation of N_2O_4 from the interaction of HNO_3 and HNO_2 as shown by Eq. 4.5 below [135].

$$N_2O_4 + H_2O \rightleftharpoons HNO_2 + H^+ + NO_3^- \quad (4.5)$$

4.1.1.2 Hydrolysis studies

Prior to their hydrolysis at room temperature and pressure (r.t.p), initial spectra were taken of the solutions of 0.5 mol dm^{-3} AHA in 5 %wt. HNO_3 in the absence and presence of 0.32 mol dm^{-3} $Fe(III)(NO_3)_3$. This corresponds to an AHA:Fe ratio of 1.6:1 equivalent to the ratio used in a study by Andriuex *et al* [77], where the mono-complex dominates, as shown previously in speciation diagrams in section 3.2. Further increasing the ratio of AHA:Fe would result in formation of a greater proportion of higher complexes. Figure 4.5 illustrates this by comparing the spectra of the initial solutions studied along with a solution of 0.5 mol dm^{-3} AHA in 5 %wt. HNO_3 in the presence of 0.15 mol dm^{-3} Fe(III), corresponding to an AHA:Fe ratio of 3.3:1 where a greater proportion of the higher, bis-complex will be present.

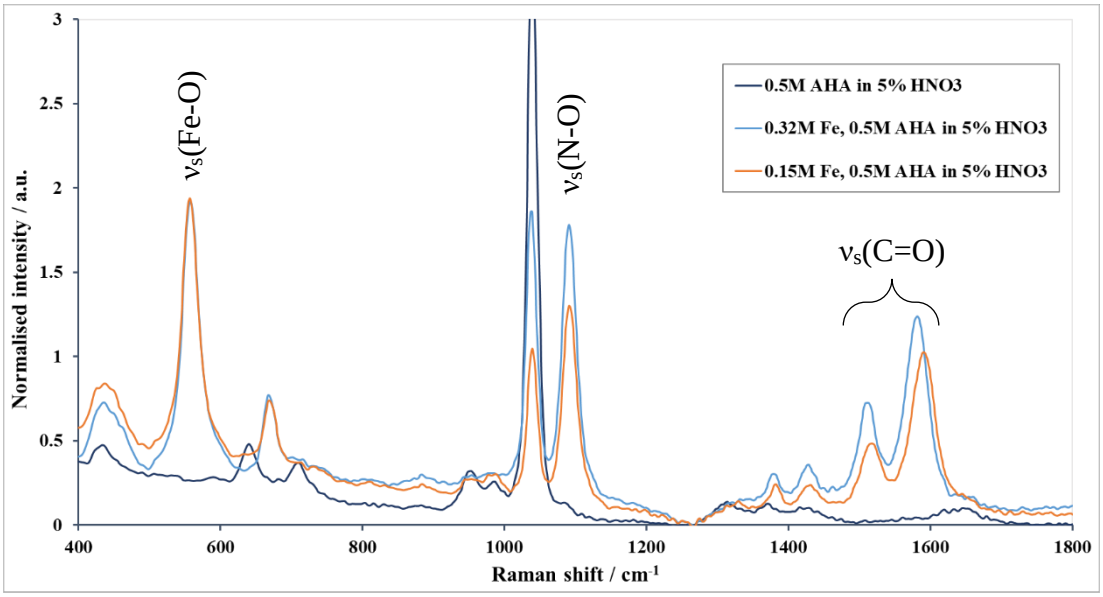

Figure 4.5: Spectra of 0.5 mol dm^{-3} AHA in 5 %wt. HNO_3 compared to that with a) 0.32 mol dm^{-3} Fe(III) present, where the mono-complex is dominant and b) 0.15 mol dm^{-3} Fe(III) initially present, where the bis-complex is present in significant concentrations.

Absent from the spectra of AHA in 5 wt.% HNO_3, the two spectra for Fe(III)-complexed AHA shows several intense peaks that are in general agreement with experimental and theoretical Raman studies by Hope *et al*, Edwards *et al* and Cozar *et al* of Cu and Fe complexes with AHA and hydroxamate-based siderophores [136-138]. The band at 557 cm^{-1} is assigned to the νs(Fe-O) stretch, based on Raman spectra of Cu-AHA complexes [136] and the νs(Fe-O_2) stretch in oxyhemoglobin, the frequency of which is influenced by direct hydrogen bonding interactions between the bound oxygen and neighbouring residues [139]. Based on theoretical calculations of the $Fe(AHA)_3$ complex by Edwards *et al* [137], the intense band at 1091 cm^{-1} is assigned to the ν_s(N-O) stretching band which is strongly coupled to the $\delta(CH_3)$ bend, and enhanced relative to free AHA due to the involvement of the NO group in the Fe(III) complex. The observed peaks at 1511 and 1591 cm^{-1} include contributions from the ν_s(C=O) stretching bands [137, 138], which, on increasing the AHA:Fe ratio from 1.6:1 to 3.3:1 and thus increasing the proportion of the bis-complex, show a small shift to higher wavenumbers. This is consistent with a decreased residual positive charge at the Fe(III) centre in the bis-complex relative to the mono-complex [140].

Following the complete hydrolysis of an acidified solution of 0.5 mol dm^{-3} AHA in the absence and presence of 0.32 mol dm^{-3} Fe(III), the final spectra obtained are shown in Figure 4.6. Due to differences in rates of hydrolysis, spectra shown are those after 5 days in the case of free AHA, and 3 weeks for the Fe(III)-complexed AHA solution. After 5 days, free AHA had fully hydrolysed in 5 %wt HNO_3, whereas this was not the case for the complexed AHA. For the latter, the peaks for the ν_s(C-C) stretching band of acetic acid and ν_s(N-O) stretching band of hydroxylamine at 886 cm^{-1} and

1002 cm^{-1} respectively were growing in slowly at this time, but the complex peaks were still prominent, disappearing only after 3 weeks. This qualitatively indicates that complexation may protect the ligand against acid hydrolysis – contradicting the earlier findings of Andrieux *et al*. that complexation with Fe(III) accelerates ligand hydrolysis [77]. Resolving this conflict is a major theme of this Chapter. All spectra in Figure 4.6 have been normalised to the gold peak, with subsequent subtraction of the gold background.

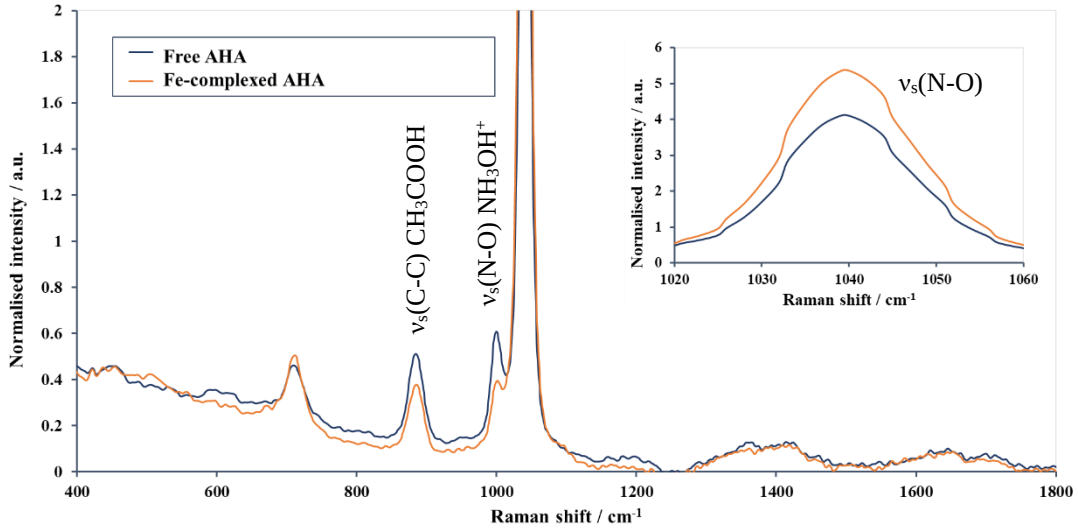

Figure 4.6: Comparison of final spectra taken after hydrolysis of 0.5 mol dm^{-3} AHA in 5 wt.% HNO_3 at r.t.p, in the absence and presence of 0.32 mol dm^{-3} Fe(III). Intensity is normalised to the main gold peak, with the gold background subtracted. Three separate spectra were taken for each sample for reliability, but only a single representative one is shown for each solution.

Examination of Figure 4.6 shows that, along with those at 710 cm^{-1} and 1040 cm^{-1} relating to HNO_3, the only peaks observed are those of the expected products, acetic acid and hydroxylammonium ion at 886 cm^{-1} and 1002 cm^{-1} respectively. While the intensity of the ν_s(C-C) stretching band assigned to acetic acid is very similar in both spectra, the lower intensity of the ν_s(N-O) stretching band for hydroxylamine in the presence of Fe(III) suggests a lower overall yield of this product from the complexed

AHA hydrolysis compared to free AHA hydrolysis and we shall return to this point later. Slight differences are also seen in the intensity of the $\delta_{bend}(NO_3^-)$ and ν_s(N-O) stretching bands in HNO_3, however the variation in the intensity of this peak found whilst acquiring standard spectra showed this to be unreliable. There is no change in the position of this peak in the final spectra of free and Fe(III)-complexed AHA. Overall, observation of the spectra suggests that the products of AHA hydrolysis remain the same when complexed to Fe(III).

The described SERS study relied on aiming a 532 nm laser at a 20 µl liquid drop on the gold surface. It was thought that the resulting peak intensities in the final spectra might be influenced by i) the exact location of the laser on the convex surface of the droplet, and ii) evaporation of the droplet by the laser. This method was therefore compared to another; using an instrument with a 785 nm laser equipped with a solution cell that could hold up to 3 ml of sample, with the expectation that less variation would be found between consecutive spectra. In these studies, described in section 4.1.2, the concentration of HNO_3 was additionally increased to 3 mol dm^{-3} to decrease the timescale required for complete hydrolysis.

4.1.2 Raman Spectroscopy Using a Solution Cell

4.1.2.1 Peak identification from standards

Standard 10ml solutions of the expected hydrolysis products acetic acid and NH_3OH^+ were prepared in concentrations of 0.5 mol dm^{-3}, with NH_3OH^+ prepared in 5 wt.% HCl solution. Two standards of 0.5 mol dm^{-3} AHA were prepared, one in deionised

water and one acidified in 3 mol dm^{-3} HNO_3. A spectrum of 3 mol dm^{-3} HNO_3 was also taken for comparison. Table 4.1 shows the peak assignments for all the spectra obtained using this 532 nm laser instrument setup in comparison to those obtained from the previous 785 nm instrument and SERS method. All the major peaks identified previously using the 785 nm laser system are seen, with the majority showing a minor shift to higher wavenumbers (1-2 cm^{-1}) when using the 532 nm system and solution cell setup. This latter observation may be due to variances in the calibration and spectral resolution of the two instruments used.

Table 4.1: Peak assignments for the two different instruments used. In general, peaks were shifted slightly to the right using the 785 nm laser and liquid drop method compared with the 532 nm and solution cell setup. Bands are assigned based on references[79] and [127-129] (see relevant text of sections 4.1.1.1 and 4.1.2.1).

Spectral Peak / cm^{-1}		**Assignment**	**Species**
785nm laser	**532nm laser**		
Not observed	458	δ_{bend}(C-C-O) in plane bend	Acetic acid
Not observed	626	γ_{twist}(C-C-O) out of plane bend	Acetic acid
886	892	ν_s(C-C) stretching band	Acetic acid
Not observed	1643, 1709	ν_s(C=O) stretching bands	Acetic acid
2947	2948	ν_s(C-H) stretching band	Acetic acid
1002	1005	ν_s(N-O) stretching band	Hydroxylamine
436	443	δ_{bend}(C-C-O) in plane bend	AHA
643	648	γ_{twist}(C-C-O) out of plane bend	AHA
957	962	ν_s(C-C) stretching band	AHA
987	990	ν_s(N-O) stretching band	AHA
Not observed	1319	ν_s(C-N) stretching band	AHA
Not observed	1378	δ_{bend}(C-N-H) in plane bend	AHA
2943	2947	ν_s(C-H) stretching band	AHA

All standard spectra, shown in Figure 4.7, are baseline corrected and normalised to the primary ν_s(N-O) stretching band in HNO_3 found at 1048 cm^{-1} using this instrument.

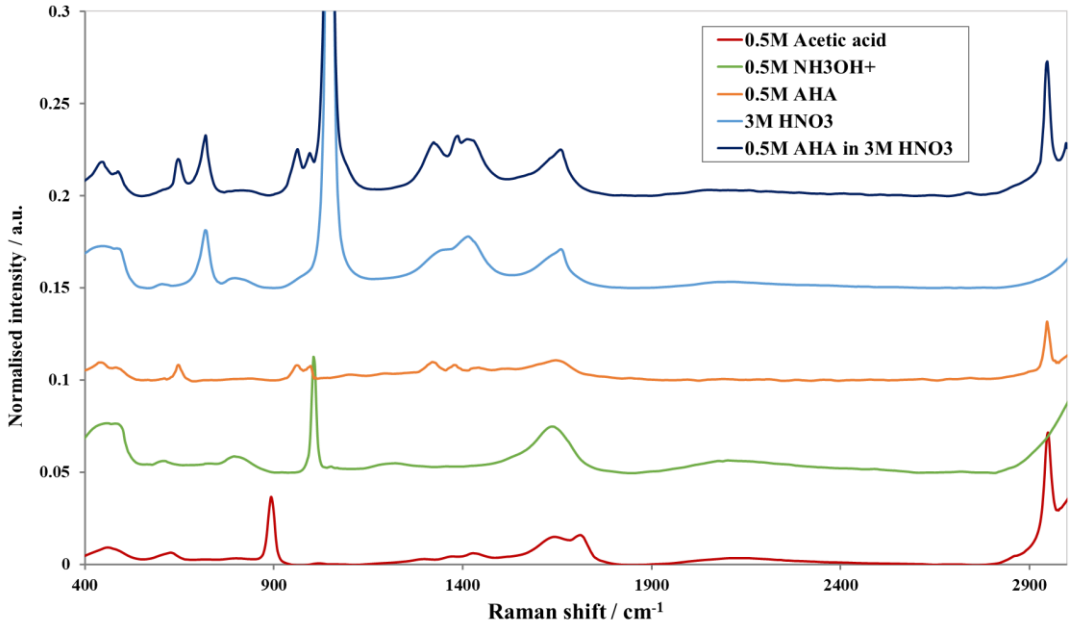

Figure 4.7: Spectra of the expected hydrolysis products acetic acid and NH_3OH^+(bottom), AHA in aqueous solution, in 3 mol dm^{-3} HNO_3, and AHA in 3 mol dm^{-3} HNO_3 (top) and Spectra are baseline corrected and normalised to the primary ν_s(N-O) stretch in HNO_3.

Considering first the spectrum of acetic acid, the intensity of the peak at 2948 cm^{-1} assigned to ν_s(C-H) stretching is seen to increase significantly using the 532 nm system. Additionally, two low frequency bands not seen under 785 nm laser excitation at Raman shifts of 458 cm^{-1} and 626 cm^{-1} are found when using the 532 nm laser system. Such bands are analogous to those seen at similar frequencies in AHA and consequently assigned to the δ_{bend}(C-C-O) in plane bend and γ_{twist}(C-C-O) out of plane bend [79]. Previously masked by the gold background signal, medium intensity bands at 1643 and 1709 cm^{-1} are also now visible in the 532 nm data of Figure 4.7. Such bands are assigned to the ν_s(C=O) stretching band in acetic acid for strongly and

weakly hydrogen bonded C=O groups respectively, based on published Raman data on liquid acetic acid [127].

Considering now the spectrum of NH_3OH^+, Figure 4.7 shows a single defined peak at 1005 cm^{-1}, which is assigned to the ν_s(N-O) stretching band [79]. The standard shown is in 5% HCl rather than HNO_3 for ease of observation of this stretch, as it was shown in the previous SERS study that it resides on the edge of the same more intense stretch for HNO_3. The only other features of the hydroxylamine spectrum in Figure 4.7 are broad bands centred around 450 and 1650 cm^{-1} which arise from O-H stretches in aqueous HCl [141].

Finally, turning now to the spectrum of AHA in Figure 4.7, the ν_s(C-H) stretching band observed at 2948 cm^{-1} in the spectra of AHA increases significantly under 532 nm laser excitation as was also observed for CH_3COOH. Previously masked by the gold background signal, previously unobserved peaks are now additionally seen at 1319 and 1378 cm^{-1}, which can be assigned to the ν_s(C-N) stretching band and δ_{bend}(C-N-H) in plane bend respectively, based on typical amide band assignment tables [79].

A spectra of 3M HNO_3 in the absence and presence of 0.5M AHA are also shown. Whilst difficult to view in Figure 4.7, the addition of HNO_3 to AHA causes a slight negative shift and reduction in intensity of the ν_s(N-O) stretching band in AHA at 990 cm^{-1}. These effects are likely due to a partial convolution of the assigned ν_s(N-O) stretching band in the AHA spectrum by the analogous but much more intense vibration in HNO_3 at 1044 cm^{-1}.

For the same reasons as described for the 785 nm SERS studies in section 4.1.1.1, the position and relative intensity of the primary ν_s(N-O) stretching bands for HNO_2 and HNO_3 were also investigated using the 532 nm laser and solution cell setup. The results of this analysis are shown in Figure 4.8.

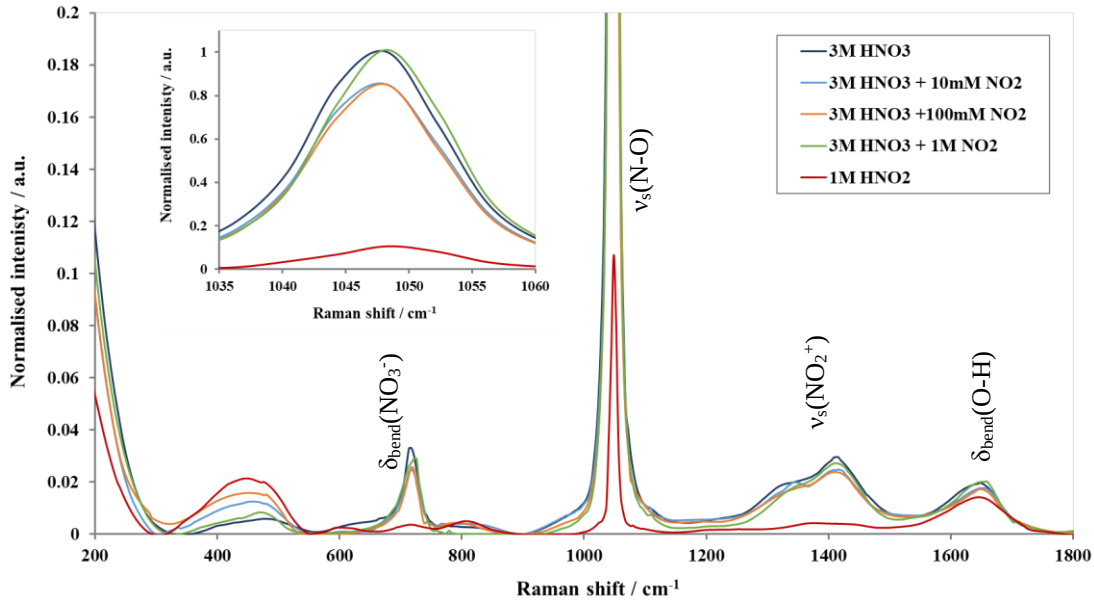

Figure 4.8: Spectra of 1 mol dm^{-3} HNO_2, 3 mol dm^{-3} HNO_3 and 3 mol dm^{-3} HNO_3 with 0.01 – 1 mol dm^{-3} NO_2 added as $NaNO_2$. Spectra are normalised to the primary ν_s(N-O) stretching band at 1048cm^{-1} of pure HNO_3.

As can be seen from Figure 4.8, the ν_s(N-O) stretches overlap at 1048 cm^{-1}. The absence of a gold background shows additional medium and low intensity bands in the spectra of 1 mol dm^{-3} HNO_2, including a broad band centred at 1644 cm^{-1} which is assigned to the stretching vibrations of the NO_2 group [126], overlapping with the δ_{bend}(O-H) bend [79]. In all spectra containing 3 mol dm^{-3} HNO_3 the medium intensity band at 717 cm^{-1} assigned to the $\delta_{bend}(NO_3^-)$ in plane bend is seen, a band at 1415 cm^{-1} is assigned to the stretching vibrations of the NO_2^+ group in HNO_3 [126].

4.1.2.2 Hydrolysis studies

4.1.2.2.1 Decomposition at r.t.p.

After identification of AHA hydrolysis products by Raman spectroscopy, the hydrolysis of 0.5 mol dm^{-3} AHA in 3 mol dm^{-3} HNO_3 was followed at r.t.p. over a 24 hour period, with spectra taken at 20 minute intervals for the first hour, and every hour thereafter. All spectra were normalised to the ν_s(N-O) stretching band for HNO_3. Observation of Figure 4.9 shows the expected decrease in the intensity of the peaks at 648 cm^{-1} and 962 cm^{-1} corresponding to the γ_{twist}(C-C-O) bend and ν_s(C-C) stretching band for AHA respectively, and an ingrowth of the ν_s(C-C) stretching band at 892 cm^{-1} assigned to CH_3COOH. Interestingly, the ν_s(N-O) stretching band for NH_3OH^+ at 1005 cm^{-1} was seen to increase in intensity over the first 7 hours, before falling slightly thereafter, likely as a result of its' instability in HNO_3 [93].

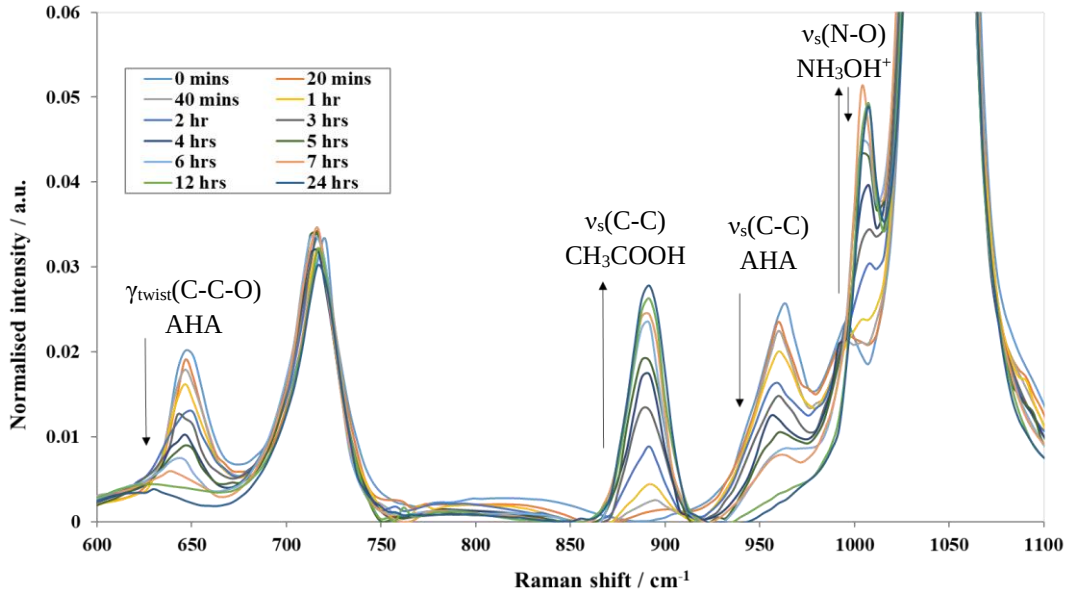

Figure 4.9: Hydrolysis of 0.5 mol dm^{-3} AHA in 3 mol dm^{-3} HNO_3 followed over a 24 hour period. Spectra were taken at 20 minute intervals for the first hour, then automatically every hour thereafter.

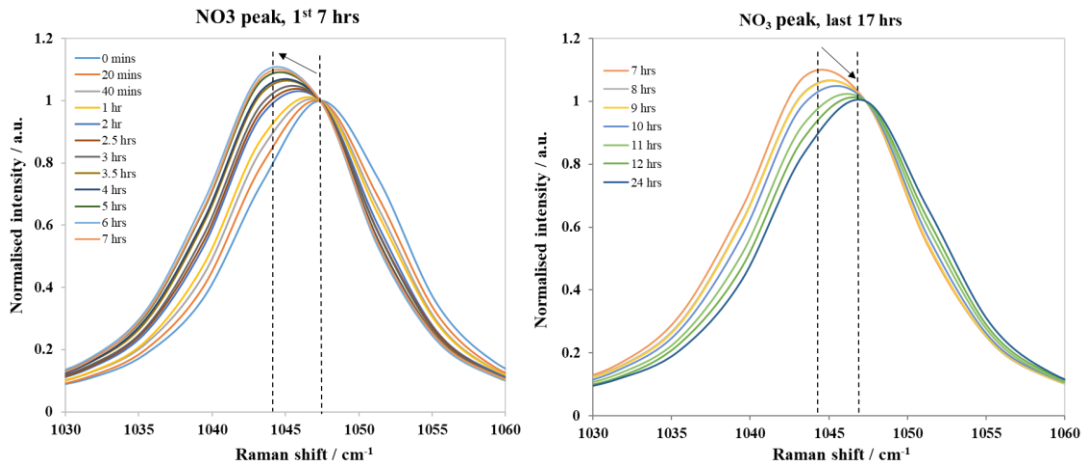

Figure 4.10: Change in peak intensity and shift for the ν_s(N-O) stretching band in HNO_3 observed over the 24 hour period.

Figure 4.10 shows the change in the nitric ν_s(N-O) stretching band throughout the run. It is seen to increase in intensity and shift slightly to lower wavelengths over the first 7 hours, which coincides with an ingrowing ν_s(N-O) stretching band for hydroxylamine. For the remaining 17 hours this peak lowered and shifted back to its' original position, coinciding with a slight decrease in the same stretching band for hydroxylamine over this period. Whilst this could potentially indicate the presence of HNO_2 or changes in HNO_3 concentrations, it appears likely to be an artefact of peaks merging rather than additional species in solution.

4.1.2.2.2 Decomposition at elevated temperature

An equivalent solution of 0.5 mol dm^{-3} AHA in 3 mol dm^{-3} HNO_3 was then allowed to hydrolyse at 333K in the absence and presence of initial Fe(III) in concentrations of 0.25 and 0.5 mol dm^{-3}. Due to the absence of a heating stage on the instrument, the reactions were not followed at high temperature. The final spectra taken after complete hydrolysis are shown in Figure 4.11. For easy visualisation of observed peaks, separate

spectra are shown for the lower and higher wavenumber ranges of 300-1300 cm^{-1} and 1300-3300cm^{-1} respectively. All spectra are normalised to the to the primary ν_s(N-O) stretching band for HNO_3.

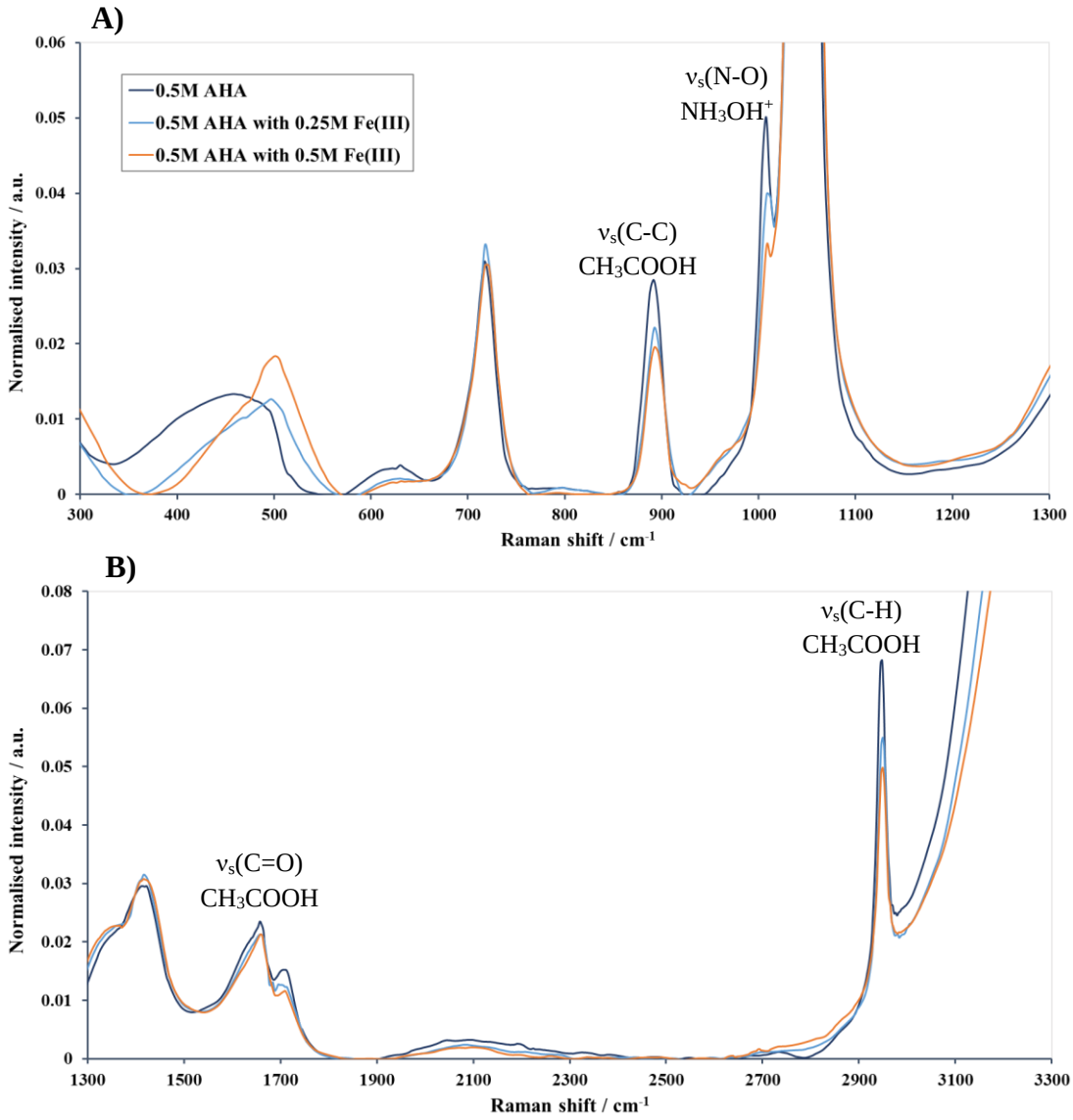

Figure 4.11: Raman spectra taken after hydrolysis of 0.5 mol dm^{-3} AHA in 3 mol dm^{-3} HNO_3 at 333K in the absence and presence of, 0.25 mol dm^{-3} and 0.5 mol dm^{-3} Fe(III) initially present. Spectra show A) lower wavenumbers of 300 – 1300 cm^{-1}, and B) higher wavenumbers of 1300 – 3300cm^{-1}. Intensity is normalised to the primary ν_s(N-O) peak.

Observation of Figure 4.11 shows the peaks for the expected hydrolysis products hydroxylamine and acetic acid. All product peaks are of a lower intensity with

increasing Fe(III), however the ν_s(N-O) assigned to NH_3OH^+ appears significantly reduced in the presence of Fe(III) compared to those for acetic acid. With the absence of additional peaks from the hydrolysis of Fe(III)-complexed AHA, it appears complex hydrolysis produces analogous products to that of free AHA hydrolysis, This suggests that this apparent decrease in hydroxylamine is likely due to its' inherent instability, as it is known to decompose readily by heat and metal ion contamination, and iron can lower the self-accelerating decomposition temperature (SADT) of a hydroxylamine solution even if present in very low concentrations [130]. For example, Iwata and Koseki [142] found the SADT for 50 wt.% solution of hydroxylamine in water to decrease considerably from 353K with 0.1-1.0 ppm Fe^{3+} to 328K with 5.2 ppm Fe^{3+} present. For 85 wt.% solutions of hydroxylamine in water, the required concentration of Fe^{3+} for onset of autocatalytic decomposition has been found to be even lower [143]. Again, this point shall be returned below.

Overall, the Raman studies described suggest the products of AHA hydrolysis do not change when the AHA is complexed to a metal ion, but the resultant yields of the products do. The following sections 4.2 - 4.6 will describe the results of the various methods used for the quantification of the important species including acetic acid, nitrous acid, hydroxylamine and finally Fe(II), both during and after completion of AHA hydrolysis.

4.2 Real-time Quantification of Acetate by Ion Chromatography

The kinetics of the acid catalysed hydrolysis of AHA has been studied previously by several authors, predominantly by a colorimetric method whereby excess Fe(III) is added to the AHA solution to form the mono-complex and its concentration is determined by subsequent spectrophotometric measurement of the maximum absorbance of the complex at 510 nm. This method however introduces uncertainty in the measurements for two reasons. Firstly, it assumes all AHA is complexed as the mono-complex, whereas a small amount of the bis-complex will also be contributing, and this complex absorbs disproportionally more strongly than the mono-complex, illustrated by the respective values of the extinction coefficients for the bis- and mono-complex of $\varepsilon_2 = 165 \pm 14$ m^2 mol^{-1} and $\varepsilon_1 = 101 \pm 1$ m^2 mol^{-1}, measured at 470 nm and 510 nm respectively [57]. This is illustrated in Figure 4.12 from a study utilising this technique to investigate the speciation of acetohydroxamatoion(III) complexes by Andrieux *et al.* [57]. Secondly, Bengtsson *et al.* [99] found that Fe(III) is reduced by NH_2OH under certain conditions, but to what extent this might occur in these systems is currently unclear. If it were to occur, it would have the effect of reducing the concentration of Fe(III) in the system and thus increasing the rate of decrease in the UV-vis absorption associated with the Fe-AHA complex(es) over and above that rate associated with the hydrolysis reaction alone. These two effects therefore needed to be deconvoluted.

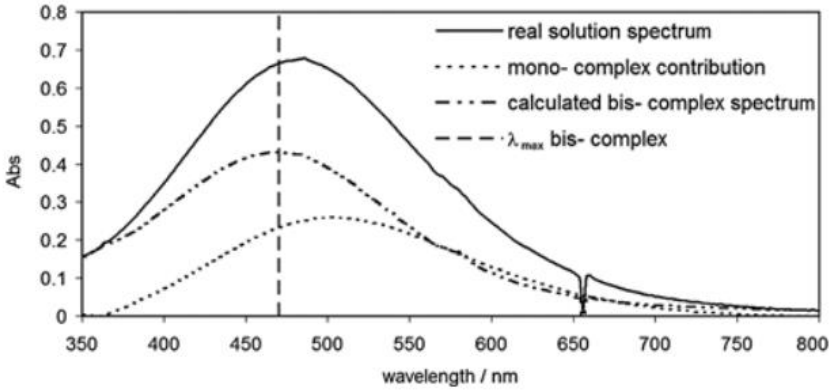

Figure 4.12: Typical deconvolution of a spectrum containing FeL^{2+} and FeL_2^{+} species [57] (reproduced with permission from reference [57], copyright 2008 Springer Nature).

To this end, an alternative analysis method for obtaining kinetic data on the acid-catalysed hydrolysis of AHA was developed; as described in Chapter 3, section 3.4, an ion chromatography system was used to measure the acetate ion (CH_3COO^-) produced from the hydrolysis of AHA for the first time. The acetic acid product of the hydrolysis of AHA is considered redox silent once generated, and its quantification thus provides a direct measurement for the total AHA lost in the system, requiring no assumptions or manipulations of the data.

4.2.1 Free AHA hydrolysis

The ingrowth of the acetate ion from the hydrolysis of 10 mmol·dm^{-3} AHA in 0.1 mol dm^{-3} HNO_3 was followed at different temperatures. The acetate data can be easily converted to the loss of AHA by taking the initial concentration of AHA and subtracting the measured acetate concentration at each time. The resultant AHA loss plots for its' hydrolysis at 313 – 333K are shown in Figure 4.13. In these plots, AHA is expressed as HL and measured concentrations in mmol dm^{-3} have been converted to

units of mol dm^{-3}. Vertical error bars included are the RSD value of the respective calibration functions, but these are minor, ranging between 0.29% and 0.66%.

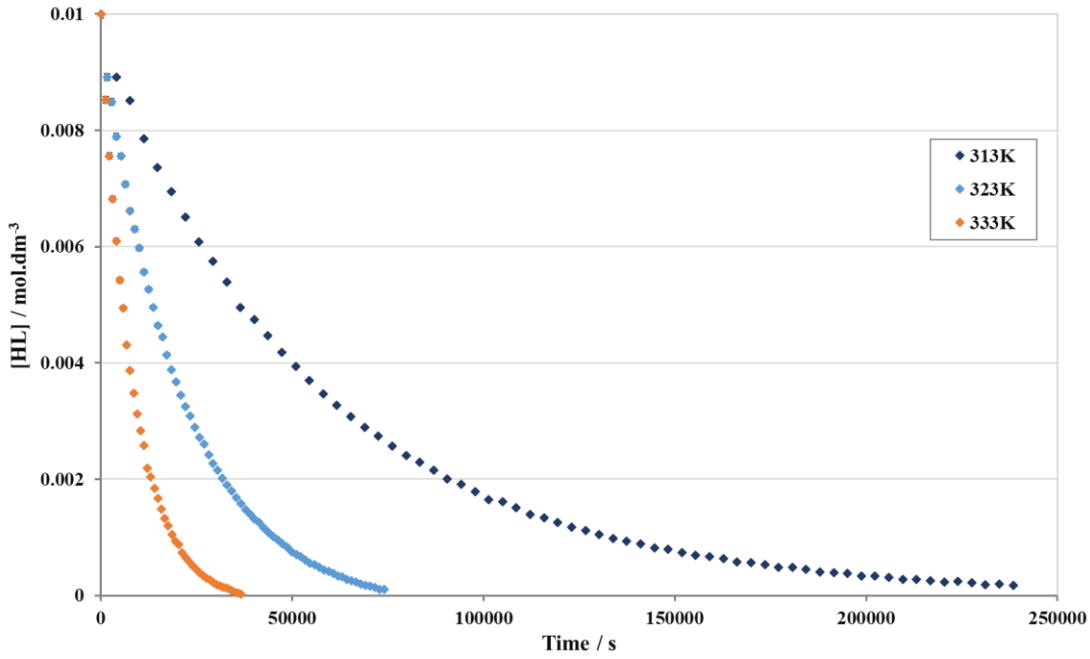

Figure 4.13: Plot of loss of HL over time for the hydrolysis of free AHA in 0.1 mol dm^{-3} HNO_3 at 313, 323 and 333K, calculated as the initial HL concentration of 10 mmol dm^{-3} minus the acetate measurement. Vertical error bars are shown as the %RSD values for the respective calibration curves as written in Table 3.2 in Section 3.4.3, but are minor (between 0.29 and 0.66%) and thus too small to be visible on the plots.

The plots show the expected exponential decay reported in the literature from a rate equation that is pseudo-first order with respect to HL (Eq. 4.6). A linear plot of the natural log of [HL] (ln[HL]) against time (Eq. 4.7) was created from each data set. These plots, shown in Figure 4.14, each have a slope equal to k_0' (= $k_0[H^+]$). The gradients and regression coefficients, and the values of k_0 obtained for each of these plots are summarized in Table 4.2

$$-\frac{d[HL]}{dt} = k_0[H^+][HL]_t = k_0'[HL]_t \quad (4.6)$$

$$\ln[HL]_t = k_0'[HL]_t + \ln[HL]_{t=0} \quad (4.7)$$

$$\ln(k_0) = \ln(A) - \frac{E_a}{RT} \quad (4.8)$$

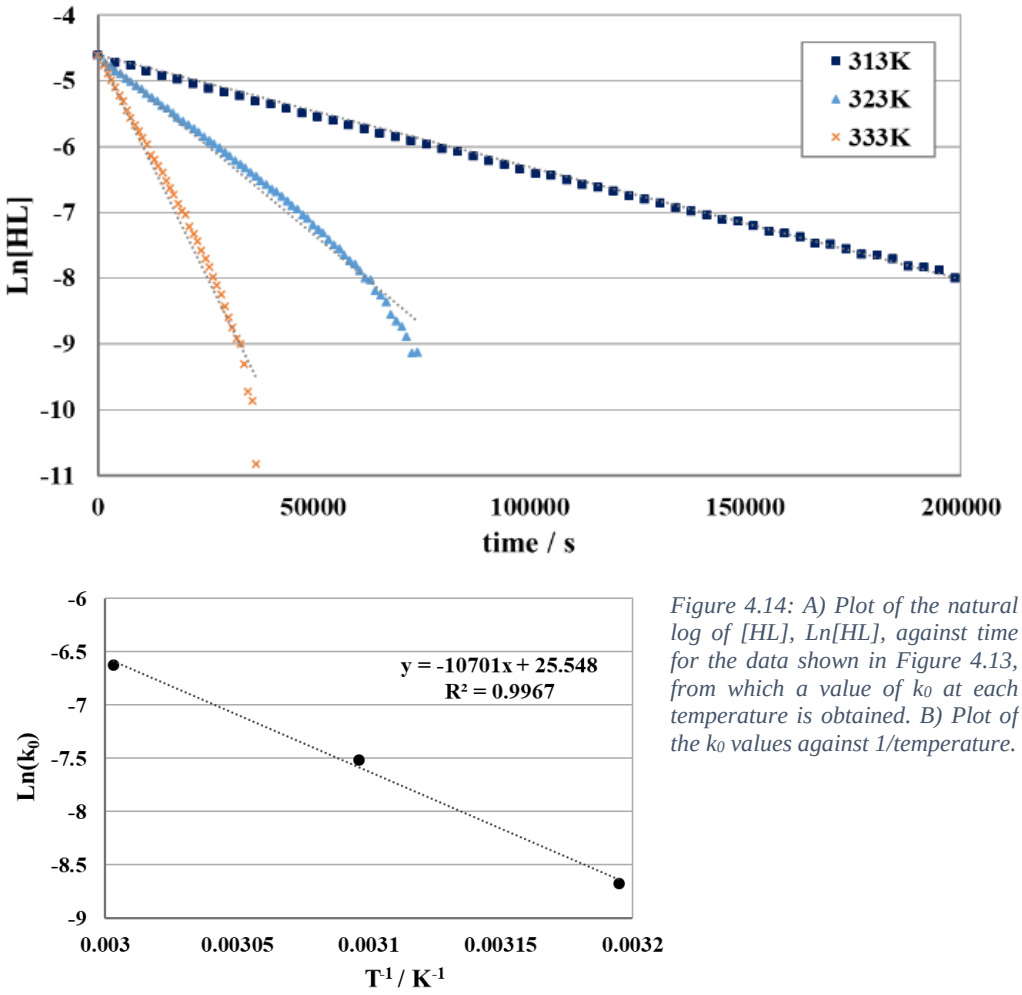

Figure 4.14: A) Plot of the natural log of [HL], Ln[HL], against time for the data shown in Figure 4.13, from which a value of k_0 at each temperature is obtained. B) Plot of the k_0 values against 1/temperature.

Table 4.2: Slope, regression coefficient and k_0 as a function of T obtained from the data.

T / K	Slope	R^2	k_0 / $dm^3.mol^{-1}.s^{-1}$
333	1.33×10^{-4}	0.9678	1.33×10^{-3}
323	5.45×10^{-5}	0.9838	5.45×10^{-4}
313	1.71×10^{-5}	0.9982	1.71×10^{-4}

Using the logarithmic form of the Arrhenius equation (Eq. 4.8), the k_0 values obtained were used to calculate Arrhenius parameters of $A = 1.25 \times 10^{11}$ $dm^3.mol^{-1}.s^{-1}$ and E_a =

89.0 kJ.mol^{-1} for the hydrolysis of free AHA. These values are higher than those obtained by previous authors Andrieux *et al* [83] (A = 4.24 × 10^{9} dm^{3} mol^{-1} s^{-1} and E_a = 80.1 kJ mol^{-1}), Taylor and May [144] (A = 3.46 × 10^{9} dm^{3} mol^{-1} s^{-1} and E_a = 79.9 kJ mol^{-1}), Chung and Lee [69] (A = 4.64 × 10^{9} dm^{3} mol^{-1} s^{-1} and E_a = 81.4 kJ mol^{-1}) and Mane and Jagdale [75] (E_a = 82.4 kJ mol^{-1}). These authors however all used the spectroscopic measurement of the Fe(III)-AHA mono-complex which requires knowledge of speciation, and assumes that i) the absorbance contribution from the bis-complex is minimal, and ii) Fe(III) only complexes with the ligand and does not react with NH_2OH and/or AHA.

A value of k_0 = 3.16 x 10^{-5} dm^{3} mol^{-1} s^{-1} at 298K can be calculated from the Arrhenius parameters determined in this work.

Table 4.3 compares this value to those reported by previous authors for the hydrolysis of free AHA, under a range of conditions and utilizing different analytical techniques. Overall, the value obtained here falls fairly central within the range reported in the literature. Whilst this value of k_0 = 3.16 x 10^{-5} dm^{3} mol^{-1} s^{-1} is lower than those reported by Carrott *et al* [74] and Andrieux *et al* [83] who utilized the colorimetric method, it is higher than those reported Chung and Lee [69] and Sampeth *et al* [145] utilising the same method, and a recent study by Sánchez-García *et al* [79] who utilised Quantitative Raman Spectroscopy (QRS). It also supports the use of an average of these values of k_0 = 3.0 x 10^{-5} dm^{3} mol^{-1} s^{-1} used by Edwards *et al* [14], who used the GPROMS (General PROcess Modelling Software) to produce a full kinetic model of the Np(IV)-AHA system.

*Table 4.3: Summary of rate constants obtained by different authors for the hydrolysis of free AHA under varying conditions, and their analytical methods. *Calculated from Arrhenius parameter obtained in this work.*

Ref.	Conditions	pH range	T / K	k_0 / dm^3 mol^{-1} s^{-1}	Method
[74]	$[HNO_3]$ > [AHA]	-0.48 ≤ pH ≤ 0.30	298	3.42×10^{-5}	Colorimetric λ_{max} = 499 nm
[69]	$[HNO_3]$ > [AHA]	-0.48 ≤ pH ≤ 0	298	2.5×10^{-5}	Colorimetric λ_{max} = 499 nm
[83]	$[HNO_3]$ > [AHA]	pH=1	298 323	3.75×10^{-5} 7.47×10^{-4}	Colorimetric λ_{max} = 498 nm
[145]	$[HNO_3]$ > & < [AHA]	-0.6 ≤ pH ≤ 0.3	298	2.33×10^{-5}	Colorimetric λ_{max} = 500 nm
[79]	$[HNO_3]$ > & < [AHA]	-0.6 ≤ pH ≤ 0.3	298	2.53×10^{-5}	QRS
This thesis	$[HNO_3]$ > [AHA]	pH=1	298* 323	3.16×10^{-5} 5.45×10^{-4}	IC

The value of k_0 = 5.45 x 10^{-4} dm^3 mol^{-1} s^{-1} measured experimentally in this study at 323K is 27% lower than that determined by Andriuex *et al*. [83], who used the colorimetric method to obtain a value of $k_0 = 7.47\times10^{-4}$ under the same pH conditions. A possible explanation for this could be the occurrence of the reduction of Fe(III) by HAN as suggested previously, which is reported to be promoted at high temperatures, but inhibited by high $[H^+]$ concentration [99]. This however has not previously been seen in these systems. Based on work by Barney [95], it has also been assumed by Andrieux *et al*. to be kinetically unlikely [77, 83], and thus requires further analysis.

4.2.2 Complexed AHA hydrolysis

A kinetic model describing the hydrolysis of AHA in the presence of non-oxidizing ions such as Fe(III) and Np(IV) was first developed by Andrieux *et al* [77], who studied the system at 293K under conditions where the mono-complex dominates. The

same authors later used this model to analyse similar systems at elevated temperatures and describe the temperature dependence of free and mono-complexed AHA. Under the conditions of their study and as described above, the model assumes no reduction of Fe(III), either complexed or uncomplexed, by the hydrolytically generated HAN. The model also assumes no formation of Fe(III)-nitrate complexes or hydrolysis of free Fe(III), and assumes that the monoacetohydroxamatoiron(III) complex follows a first-order hydrolysis analogous to that of free AHA, with a reaction and rate equation described by Eqs. 4.9 and 4.10.

$$FeL^{2+} + H^{+} \overset{k_1}{\rightarrow} Fe^{3+} + Ac + NH_3OH^{+} \tag{4.9}$$

$$-\frac{d[FeL^{2+}]}{dt} = k_1[H^{+}][FeL^{2+}]_t = k_1'[FeL^{2+}]_t \tag{4.10}$$

The ingrowth of the acetate ion was therefore followed for the systems described in the preceding section 4.2.1 in the presence of Fe(III). Initial conditions for the Fe-complexed AHA hydrolysis experiments were chosen to be comparable to these authors in terms of the dominant species, with initial Fe(III) added in concentrations of 2.5 and 10 mmol dm^{-3}. Under these conditions, the dominant species are the mono complex and free ferric ions. The acetate measurements obtained for the free and Fe(III)-complexed AHA hydrolysis are shown in Figure 4.15. Error bars are shown (small and thus not visible in most plots), with the error taken as the percentage relative standard deviation (%RSD) obtained from the respective calibration function for each data set.

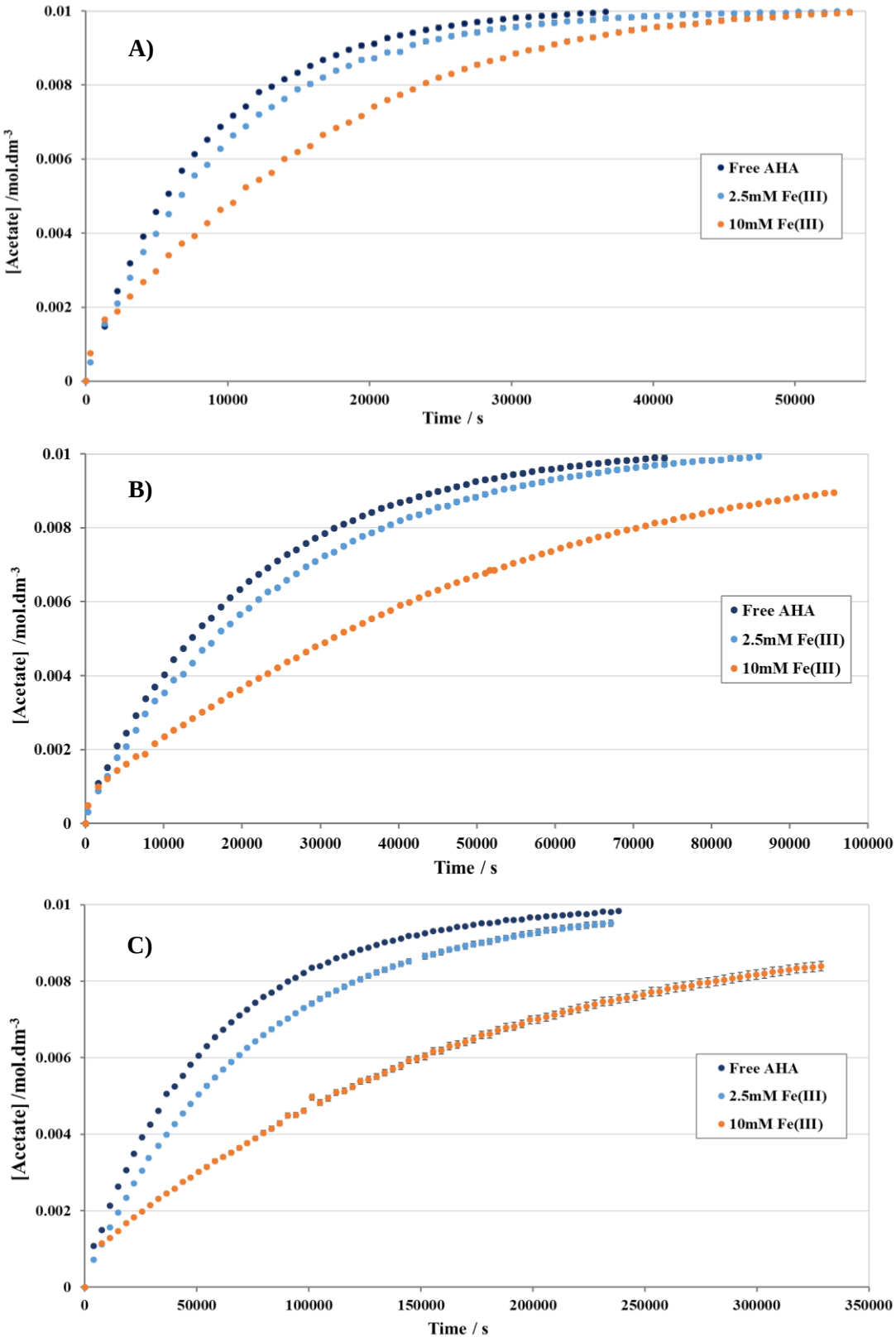

Figure 4.15: CH_3COO^- ingrowth measured from the hydrolysis of 10 mmol dm^{-3} AHA with initial [Fe(III)] of 0 mmol dm^{-3} (dark blue), 2.5 mmol dm^{-3} (light blue), and 10 mmol dm^{-3} (orange) at temperatures of A) 333K, B) 323K and C) 313K. Errors bars are shown as the RSD value from the respective calibration.

First inspection of this data shows a clear trend; for each temperature considered, there is an inhibition in the rate of ingrowth of the acetate as the initial Fe(III) concentration increases. Based on the kinetic model proposed by Andriuex *et al* [83], where Fe(III) is a complexing but non-oxidising metal ion, this would suggest that the hydrolysis of free AHA proceeds at a quicker rate than that of the complexed AHA, i.e. the rate parameter $k_0 > k_1$. As noted above, this conclusion from the data of Figure 4.15 is in direct contrast to that reported by those authors. To investigate this further, the kinetic model proposed by those authors was tested on the obtained data.

4.2.2.1 Simple kinetic analysis

By adapting the previously published kinetic model for the Fe(III)-AHA system derived by Andrieux *et al* [77], a similar model was derived for the ingrowth of acetate from both the free and complexed AHA. The equilibrium for the formation of the mono-complex is described by Eq. 4.11. A mass balance (Eq. 4.12) can be set up, relating the concentration of acetate at time t ($[Ac]_t$) to the initial concentration of HL ($[HL]_{T,0}$), and that present as free HL or the mono-complex at time t ($[HL]_t$).

$$K_1' = \frac{[FeL^{2+}]_t}{[Fe^{3+}]_t[HL]_t} \quad \text{where } K_1' = \frac{K_1}{[H^+]} \tag{4.11}$$

$$[HL]_{T,0} - [Ac]_t = [FeL^{2+}]_t + [HL]_t \tag{4.12}$$

Substitution of Eq. 4.11 into Eq. 4.12 and solving for $[Ac]_t$ yields Eq. 4.13, and rearrangement of Eq. 4.11 to solve for $[Fe^{3+}]_t$ gives Eq. 4.14. Substitution of Eq. 4.14 into Eq. 4.13 then gives a final equation of $[Ac]_t$ in terms of $[HL]_t$ and known parameters and starting concentrations of HL and Fe(III) (Eq. 4.15).

$$[Ac]_t = [HL]_{T,0} - (K_1'[Fe^{3+}]_t + 1)[HL]_t \tag{4.13}$$

$$[Fe^{3+}]_t = \frac{Fe_T}{1 + K_1'[HL]_t} \tag{4.14}$$

$$[Ac]_t = [HL]_{T,0} - [HL]_t - \frac{K'Fe_T[HL]_t}{1 + K'[HL]_t}[Fe_T] \tag{4.15}$$

$[HL]_t$ can be described using Eq. 4.16 derived by Andrieux *et al.* [77]. Using incremental ratios of $HL_t/HL_{T,0}$, theoretical plots of t against [HL]t can be produced for our systems. These values of $[HL]_t$ can then be used in Eq. 4.16 to produce theoretical plots of t against $[Ac]_t$ which can be directly compared to the experimental data.

$$t = \frac{1}{k_1'}\ln\left(\frac{\frac{K_1'[HL]_t}{[H^+]} + 1}{\frac{K_1'[HL]_{T,0}}{[H^+]} + 1}\right) - \left(\frac{\frac{K_1'Fe_T}{[H^+]} + 1}{\frac{k_1'K_1'[HL]_{T,0}}{[H^+]} + k_0'}\right)\ln\left(\frac{[HL]_t}{[HL]_{T,0}}\right) - \left(\frac{\frac{k_1'^2K_1'Fe_T}{[H^+]} + k_0'^2}{\frac{k_0'k_1'^2K_1'Fe_T}{[H^+]} + k_0'^2k_1'}\right)\ln\left(\frac{\frac{K_1'[HL]_t}{[H^+]} + 1 + \frac{k_1'K_1'Fe_T}{k_0'[H^+]}}{\frac{K_1'[HL]_{T,0}}{[H^+]} + 1 + \frac{k_1'K_1'Fe_T}{k_0'k_1'}}\right) \tag{4.16}$$

The final fits to the data are shown in Figure 4.16. However, there were two key observations made when attempting to model the acetate data using this approach. Firstly, the rate parameter k_0 was the dominant factor in controlling the shape and closeness of the fit to the data. Secondly, the order of magnitude of k_1 was significantly more important than the exact value in terms of producing a visible difference of the closeness of fit to the experimental data. The values of k_0 and k_1 used in the final fits of Figure 4.16 are summarized in Table 4.4, the final estimates of k_1 obtained from this analysis being an order of magnitude less than those reported by Andriuex *et al* [83] at the same respective temperatures.

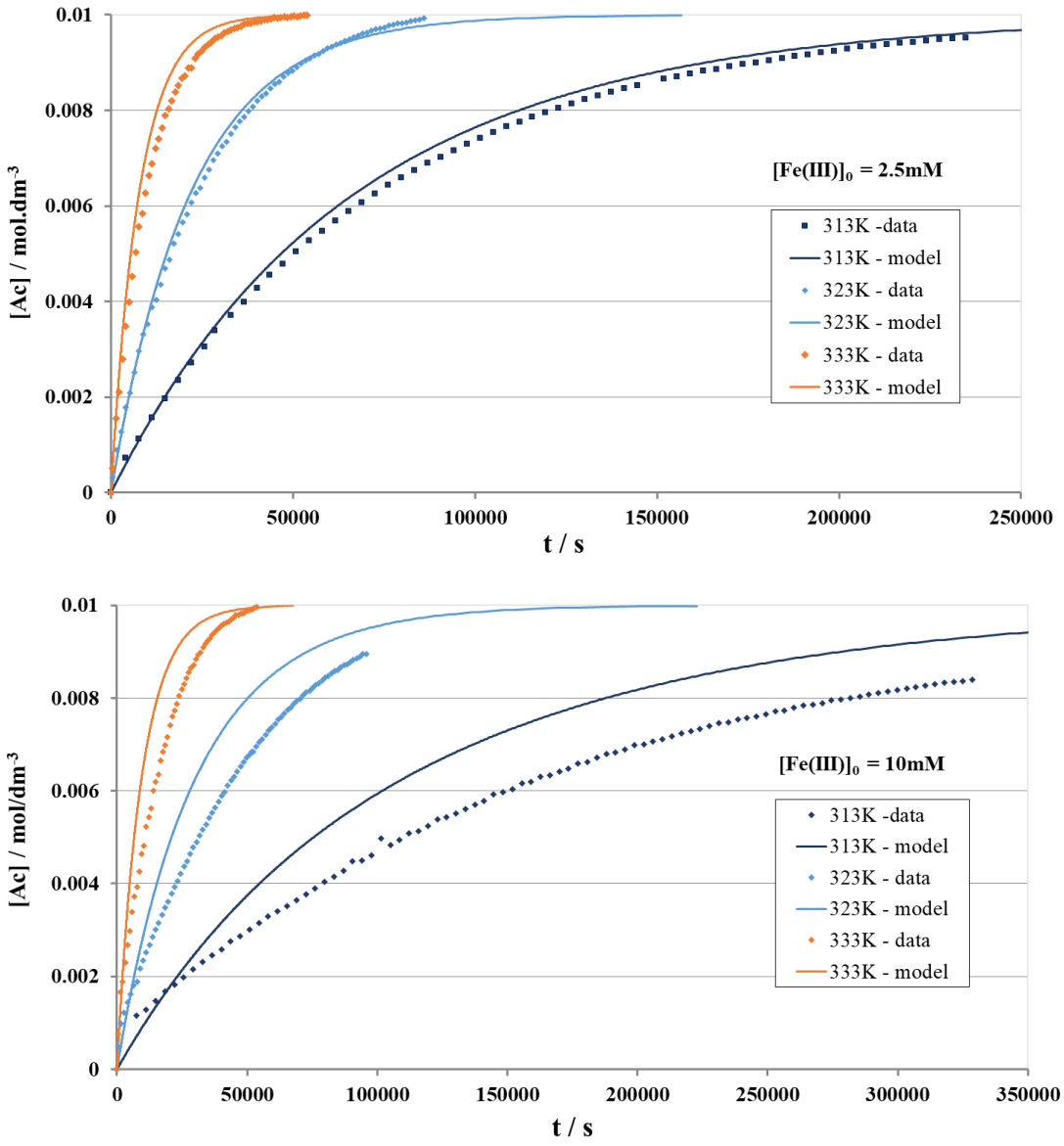

Figure 4.16: Plots of acetate concentration against time (t) measured by experiment and modelled using Eqs. 4.5 & 4.6, for total iron concentrations (Fe_T) of 2.5 and 10 mmol dm^{-3}, for [AHA] = 10 mmol dm^{-3}, [HNO_3] = 0.1 mol dm^{-3} and T = 313K, 323K and 333K.

Inspection of the fits of Figure 4.16 shows this model to be reasonable for the data with initial [Fe(III)] = 2.5 mmol dm^{-3}. Close fits can be obtained at 313K and 323K to the experimental data, and whilst the model fits begin to diverge from the data for the same [Fe(III)] at the elevated temperature of 333K, the fit is still reasonable. It was

found however that this fitting method was unable to provide a close match to the data at any temperature for experiments with the higher initial [Fe(III)] of 10 mmol dm^{-3}.

Table 4.4: Summary of experimentally obtained k_0 values and final fitted k_1 values.

Temperature / K	**313**	**323**	**333**
Experimental k_0 / $dm^3.mol^{-1}.s^{-1}$	1.71 x 10^{-4}	5.45 x 10^{-4}	1.33 x 10^{-3}
Fitted k_1 / $dm^3.mol^{-1}.s^{-1}$	1.75 x 10^{-6}	7.47 x 10^{-6}	4.98 x 10^{-5}

From inspection of Table 4.4 it can be seen that the fitted $k_1 < k_0$ at all temperatures. This indicates that complexation protects the ligand from hydrolysis; again, this is opposite to the trend observed by Andrieux *et al* [83] in their spectrophotometrically-based analysis of the same system under similar conditions. Using these fitted values, a plot of $\ln(k_1)$ against 1/T shown in Figure 4.17, gives Arrhenius parameters of A = 3.71 x 10^{18} $dm^3.mol^{-1}.s^{-1}$ and E_a = 137.4 $kJ.mol^{-1}$ for the hydrolysis of complexed AHA. These values are significantly greater than the analogous values of A = 2.44 x 10^{11} $dm^3.mol^{-1}.s^{-1}$ and E_a = 89.6 $kJ.mol^{-1}$ obtained by Andrieux *et al* [83].

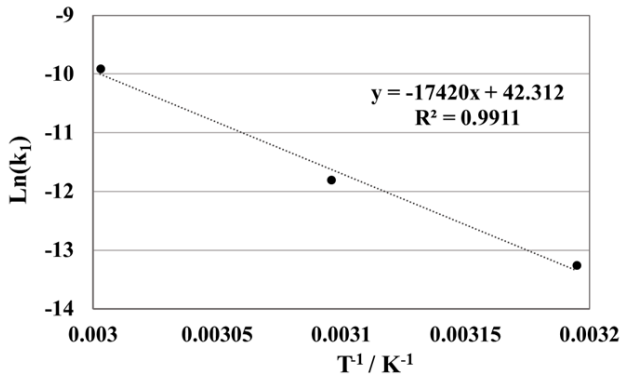

Figure 4.17: Plot of the k_1 values against 1/temperature

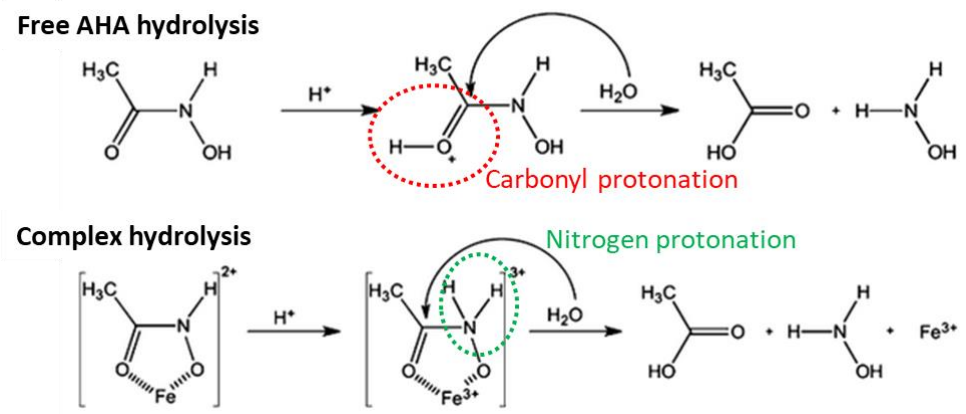

Figure 4.18: Proposed mechanism for the acid catalysed hydrolysis of free and Fe-complexed AHA [83] (reproduced with permission from reference [83], copyright 2014 Springer Nature).

The steps involved in the mechanism for the acid-catalysed hydrolysis of free AHA include; (i) a rapid protonation of the hydroxamic acid on the energetically favoured carbonyl group, (ii) the attack of water on the carbonyl group resulting in a neutral tetrahedral intermediate, and (iii) the recreation of the carbonyl group and the loss of the leaving group NH_2OH [67]. Quantum mechanical calculations carried out by Andrieux *et al* [83] showed that the initial protonation step in the mono-hydroxamate complex must occur at the energetically less favourable nitrogen site to result in cleavage of the C-N bond and produce the same hydrolysis products as for the free AHA hydrolysis. This is illustrated in Figure 4.18. However, in their experiments at elevated temperatures, these authors also observed a significant departure of their experimentally measured rate parameter k_1, from that calculated via Eq. 4.16 using the absorbance of the solution as a proxy for the concentration of the mono-complex, which they suggested could be indicative of other processes taking place alongside the hydrolysis reaction. Whilst a subtle change in hydrolysis mechanism could provide an explanation for the data for low initial Fe(III), the occurrence of additional processes

appears evident from the inability of this model to fit the data with initial [Fe(III)] = 10 mmol dm^{-3}.

Table 4.5: Speciation for 10 mmol dm^{-3} initial AHA and 0.1 mol dm^{-3} HNO_3, for varying Fe_T (where T = total Fe concentration) and temperatures. All concentrations (shown in []) are in mmol dm^{-3}

Temperature / K	[Fe_T]	[free HL]	1:1 complex		2:1 complex		free Fe(III)		Free HL:Fe(III)
			[]	% of all complexes	[]	% of all complexes	[]	% of Fe_T	
313	2.5	8.37	1.26	87.27	0.184	12.27	1.05	42.0	7.97:1
323	2.5	8.83	0.937	88.80	0.118	11.20	1.44	57.6	6.13:1
333	2.5	9.21	0.645	90.15	0.0704	9.85	1.78	71.2	5.17:1
313	10	5.23	4.06	91.87	0.359	8.13	5.59	55.9	0.94:1
323	10	6.39	3.06	91.80	0.273	8.20	6.67	66.7	0.96:1
333	10	7.43	2.19	92.02	0.189	7.98	7.62	76.2	0.93:1

The initial speciation calculated for each of the datasets is in shown in Table 4.5, from which is can be seen that higher concentrations of initial Fe(III) and elevated temperatures each increase the percentage of complexed AHA present as the mono-complex, thus decreasing that of the bis-complex, but also increase the amount of free Fe(III) in solution. The concentration of the bis-complex would be expected to decline rapidly in the initial stages of AHA hydrolysis as the ligand concentration is reduced, likely by decomplexation, as illustrated by equilibrium constants of K_1 = 62.46 and K_2 = 2.81 at 293K for the mono- and bis-complexes respectively [77]. The hydrolysis or decomplexation of the bis-complex is thus assumed to be unimportant and so not addressed in this simple model. Indeed, the best fits using the model described were obtained for the two datasets with the highest proportions of 2:1 complex and thus lowest percentage of Fe_T available as free Fe(III). For an initial Fe(III) concentration of 2.5 mmol dm^{-3} it can be seen that increasing the temperature lowers the ratio of free

ligand to Fe(III) i.e. there is more uncomplexed Fe(III). Observation of the acetate profiles in Figure 4.16 shows this resulted in a departure of this simple analytical model from the experimental data. For the experiments with an initial [Fe(III)] of 10 mmol dm^{-3}, where the free HL:Fe(III) ratio decreases to less than 1, the first order reactions for the free and mono-complexed AHA hydrolysis failed to adequately describe the data. According to Bengtsson *et al.* [7], the reduction of Fe(III) by NH_2OH requires high Fe(III):NH_2OH ratios and/or elevated temperatures. The data obtained here, and the discussion immediately above, suggests that at elevated temperatures and higher Fe_T (total iron concentration), the reduction of Fe(III) by NH_2OH leads to a departure from the initial Fe(III) concentration (i.e Fe_T) on which the derivation of the model of Eqs 4.9 – 4.15 is based. This hypothesis is explored in more detail in sections 4.5 and 4.6 by quantification of both the hydrolysis product NH_2OH and Fe(II) produced by its action on Fe(III).

Understanding the behaviour of hydroxylamine, including both its generation by AHA hydrolysis and loss is therefore as important as understanding the behaviour of acetic acid in this system. However, HAN may be lost not only by a putative reaction with Fe(III); it is also, known under certain reaction conditions, to also react with HNO_3 to produce nitrous acid, and to react with nitrous acid itself. Thus, understanding the behaviour of nitrous acid is also important.

Consequently, experiments were conducted to study the time evolution of both [HAN] and [HNO_2] in the Fe(III)/AHA system. However, before discussing these in detail, it is useful to summarise the literature pertaining to the HAN/nitrous/nitric system and this is the subject of the next section.

4.3 Summary of Relevant Hydroxylamine and Nitrous Acid Chemistry

As discussed in Chapter 2 in section 2.5.1, Eqs. 4.17 – 4.20 describe the series of reactions that result in a nitrous-catalysed overall reaction of HAN with nitric acid (Eq. 4.21) that results in the net generation of still more HNO_2. Eq. 4.17 is a rapid pre-equilibrium, Eqs. 4.19 and 4.20 are also rapid, and Eq. 4.18 is the rate-determining step (see section 2.5.1 for detail).

$$H^+ + HNO_2 + NO_3^- \overset{fast}{\rightleftharpoons} N_2O_4 + H_2O \tag{4.17}$$

$$N_2O_4 + NH_2OH \overset{slow}{\longrightarrow} HNO + N_2O_3 + H_2O \tag{4.18}$$

$$N_2O_4 + HNO \overset{fast}{\longrightarrow} HNO_2 + N_2O_3 \tag{4.19}$$

$$N_2O_3 + H_2O \overset{fast}{\rightleftharpoons} 2HNO_2 \tag{4.20}$$

$$Overall: \quad 2HNO_3 + NH_3OH^+ \overset{HNO_2}{\longrightarrow} 3HNO_2 + H_3O^+ \tag{4.21}$$

The reaction described by Eq. 4.21 has an activation energy E_a of 105 kJ/mol [146] and is dominant at low $[NH_3OH^+]$ and is favoured by an increase in $[HNO_3]$ and temperature. Especially, it has been found to occur under conditions of high $[HNO_3]$ > 2 mol dm^{-3}, and is autocatalytic in HNO_2 that may then result in the acceleration with reaction time of the net production of nitrous acid. However, this autocatalytic acceleration can be inhibited by a competing scavenging reaction of HNO_2 with NH_3OH^+, described by Eq. 4.22.

$$HNO_2 + NH_3OH^+ \rightarrow N_2O + H_3O^+ + H_2O \tag{4.22}$$

$$-\frac{\partial HNO_2}{\partial t} = k[H^+][HNO_2][NH_3OH^+] \quad (4.23)$$

Eq. 4.22 has an E_a of 65 kJ/mol [146] and is observed only at low [HNO_3] and dominates at high [NH_3OH^+]. Hughes and Stedman [89] initially studied the kinetics and mechanism of this scavenging reaction under conditions of excess hydroxylamine and < 0.1 mol dm^{-3} $HClO_4$, providing a rate law described by Eq. 4.23. This rate law was later confirmed by Bourke and Stedman [147] to apply up to acidities of around pH 1-2 in $HClO_4$ and H_2SO_4, with the rate constant increasing steeply as the acidity rises and reaching a sharp maximum close to [acid] = 2 mol dm^{-3}. At higher acidities however, this same rate constant, which in fact consists of a collection of rate constants pertaining to the elementary reactions that describe the mechanism and includes a $[H^+]^2$ term in the denominator [91], decreases slowly with decreasing pH. This is in detail discussed in Chapter 2 section 2.5.1.

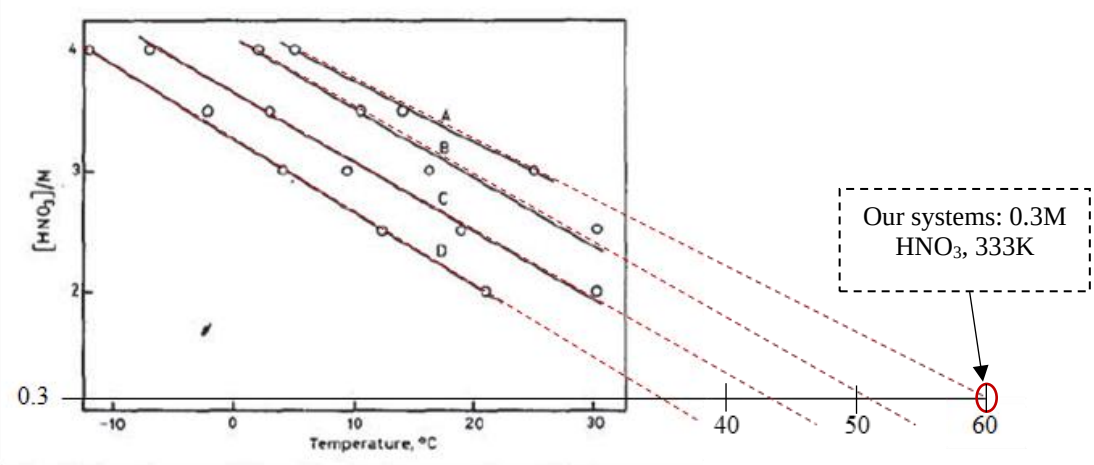

Figure 4.19: Boundary conditions determined by Gowland and Stedman for the decomposition of hydroxylamine in HNO_3 for NH_3OH^+ concentrations of A) 0.05, B) 0.02, C) 0.01, and D) 0.005 mol dm^{-3} [93]. The conditions of 0.3 mol dm^{-3} HNO_3 and 333K used in the experiments here are marked (reproduced with permission from source [93], copyright 1981 Elsevier).

The boundary conditions for which the oxidation of hydroxylamine by HNO_3 (Eq. 4.21) dominates over the scavenging reaction of hydroxylamine with HNO_2 (Eq. 4.22) were studied by Gowland and Stedman [93], and are shown in Figure 4.19 for varying concentrations of hydroxylamine between 5 and 50 mmol dm^{-3}. In the region below the line at any given hydroxylamine concentration, the nitrous acid scavenging reaction of Eq. 4.22 dominates, and NH_2OH is stable in HNO_3, whilst it becomes unstable in the regions above the line where the oxidation of NH_2OH by HNO_3 dominates. The lines have been extrapolated to higher temperatures by assuming the same linear relationship continues beyond the range discussed by the authors. From this is can be seen that there is a possibility that the solutions described previously in 0.3 mol·dm^{-3} HNO_3 at 333K (circle on Figure 4.19) could cross the boundary line associated with a solution concentration of hydroxylamine of 0.05 mol dm^{-3}, so entering a region where the autocatalytic oxidation of hydroxylamine by nitric acid in accordance with Eq. 4.21 dominates.

Another consideration is that any reaction that can increase the nitrous acid concentration can lower the decomposition temperature of the NH_2OH solutions. If Fe(III) is reduced to Fe(II) by HAN via Eq. 4.24a or 4.24b [99], Fe(II) can react with HNO_3 to produce nitrous acid and thus act to promote the autocatalytic reaction of Eq. 4.21 [117]. Several other reactions of Fe(III) and Fe(II) with nitrogen dioxide (NO_2), HNO_2 and NO can also occur [94] described by Eqs. 4.25 – 4.28. In this way Fe(II), generated by the action of HAN on Fe(III), can acts to further catalyse HAN decomposition.

$$Fe^{3+} + NH_3OH^+ \rightarrow Fe^{2+} + 1/2N_2 + 2H^+ + H_2O \quad (4.24a)$$

$$2Fe^{3+} + NH_3OH^+ \rightarrow 2Fe^{2+} + 1/2N_2O + 3H^+ + 1/2H_2O \quad (4.24b)$$

$$3Fe^{2+} + 4H^+ + NO_3^- \rightleftharpoons 3Fe^{3+} + 2H_2O + NO \quad (4.25)$$

$$Fe^{2+} + NO_2 + H^+ \rightarrow Fe^{3+} + HNO_2 \quad (4.26)$$

$$Fe^{2+} + HNO_2 + H^+ \rightleftharpoons Fe^{3+} + NO + H_2O \quad (4.27)$$

$$Fe^{3+} + NO + H_2O \rightarrow Fe^{2+} + HNO_2 + H^+ \quad (4.28)$$

In summary, the reactions of primary importance to the generation and loss of nitrous acid and the loss of hydroxylamine in the presence of Fe(III) in a HAN/nitrous/nitric system are as follows:

Nitrous generated by $2HNO_3 + NH_3OH^+ \xrightarrow{HNO_2} 3HNO_2 + H_2O^+$	Autocatalytic	(Eq. 4.21)
Nitrous lost by $HNO_2 + NH_3OH^+ \rightarrow N_2O + H_2O + H_2O^+$	Bennett *et al.* [91]	(Eq. 4.22)
HAN lost by $Fe^{3+} + NH_3OH^+ \rightarrow Fe^{2+} +$ $N_2O \text{ or } N_2 \text{ depending on } Fe^{3+}/HAN \text{ ratio}.$	Kinetically slow according to Barney *et al.* [95]	(Eq. 4.24a or 4.24b)

Having discussed chemistry relevant to the HAN/nitrous/nitric system, the next section will discuss experiments conducted to study the time evolution of [HNO_2] in the Fe(III)/AHA system.

4.4 Nitrous Acid Analysis

As discussed at the end of section 4.2, an important species in these systems is nitrous acid, the role of which during the hydrolysis of complexed AHA has been discussed by several authors. As mentioned previously, HNO_2 is responsible for the autocatalytic decomposition of HAN in HNO_3 solutions via Eq. 4.21 [93], which has been attributed to a number of industrial accidents [148]. Another area in which it plays a role is in the context of the development of the Advanced PUREX process – specifically, it features in studies of the complexation of AHA with Pu(IV) [74]. In these studies, an ingrowth of Pu(III) is seen during the associated AHA complex hydrolysis, followed by an observed re-oxidation of Pu(III) to Pu(IV) under certain conditions. This re-oxidation is suggested to be catalysed by HNO_2, which accumulates in HNO_3 solutions once hydroxylamine and, potentially, AHA are no longer available in solution to act as a scavenger for HNO_2 [74, 149, 150]. By an analogous reaction, HNO_2 can also oxidise the ferrous ion (Fe^{2+}) in HNO_3 media (see Eq. 4.27), autocatalyzed by oxy-nitrogen species, namely NO and NO_2 [151].

Thus, in order to understand the role that nitrous acid may play in any revision to the Andrieux model of the AHA hydrolysis, a campaign was initiated to quantify its presence in the systems under study here.

4.4.1 Real-time Quantification by Ion Chromatography

Via the same analysis as the acetate ion, the concentration of the nitrite ion (NO_2^-), which would be present in solution from the dissociation of any HNO_2, was determined

during the hydrolysis of free and complexed AHA. It was expected that this species would accumulate and play a more significant role at elevated temperatures [89], and in solutions with higher Fe(III) [117] as a result of Eq. 4.24a and 4.24b interrupting the nitrous scavenging reaction of Eq. 4.22. If present, concentrations were expected to be low, therefore an estimate of the limit of detection (LOD) and limit of quantification (LOQ) was attempted.

4.4.1.1 Limit of Detection

In ion chromatography, the LOD is defined as the minimum concentration of a species that gives a signal of 3 times the baseline noise [152]. It varies for different ions depending on a number of factors, including the molar ionic conductivity (λ_0) of a particular ion, and in what form it exists in solution. In the case of anion analysis, the acetate and nitrite ions are converted to acetic and nitrous acid respectively when they come into contact with the suppressor, and then partially dissociate based on their respective pKa values of 4.74 and 3.14 [113]. Since the uncharged acid does not contribute to the ionic conductivity, there will be a comparatively greater proportion of ions present in nitrous acid than in acetic acid of the same molarity. The values of λ^0, (measured in aqueous solution, 298K) for nitrite and acetate are reported at 71.8 S cm^2 mol^{-1} and 40.9 S cm^2 mol^{-1} respectively [153]. One mole of nitrite ions will therefore produce a greater conductivity measurement than the same amount of acetate ions.

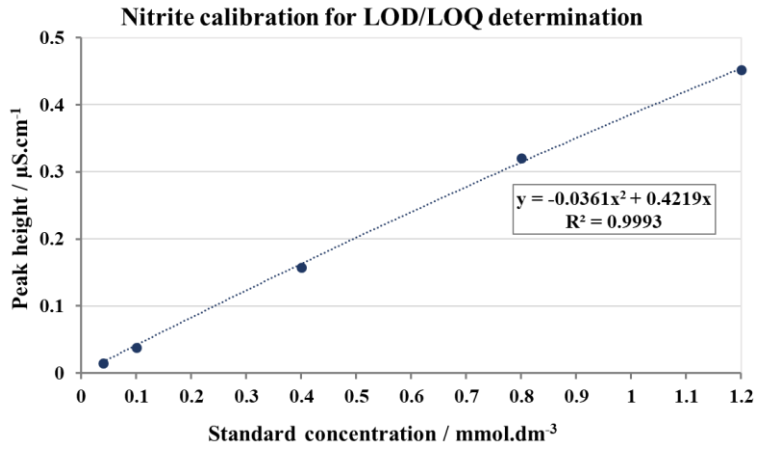

Concentration / mmol dm^{-3}	Peak height / µS.cm^{-1}
0.04	0.015
0.1	0.038
0.4	0.158
0.8	0.321
1.2	0.452

Figure 4.20: Calibration for NO_2^- standards in the range of 0.04 - 1.2 mmol dm^{-3} for determination of LOD and LOQ.

A calibration for nitrite in concentrations < 1 mmol dm^{-3} is shown in Figure 4.20, which was used to determine an approximate value for the LOD and LOQ. The LOQ is defined as the minimum concentration that can be accurately quantified that gives a signal of 10 times the baseline noise [152]. From these standards of the NO_2^- ion in 0.1 mol dm^{-3} HNO_3, the average noise was approximately 0.002 µS cm^{-1}, the LOD and LOQ were calculated as 0.014 mmol dm^{-3} and 0.048 mmol dm^{-3} respectively. From previous calibrations with standards in excess of 1 mmol dm^{-3}, the signal from the acetate ion was approximately 4 times lower than that of nitrite at the same concentration, giving an approximate LOD and LOQ of 0.056 mmol dm^{-3} and 0.19 mmol dm^{-3} respectively for acetate. From these calibrations, it was concluded that determinations of comparatively low concentrations of nitrite would therefore be possible with this method, and measurements were obtained for each of the initial conditions investigated in section 4.2.2 previously.

4.4.1.2 Measurements

In contrast to that expected, the nitrite ion was only detected in any quantity in those experiments performed at the lowest temperature of 313K. These measurements obtained during the hydrolysis of 10 mmol dm^{-3} AHA in 0.1 mol dm^{-3} HNO_3, in the absence and presence of 2.5 and 10 mmol dm^{-3} Fe(III), are shown in Figure 4.21.

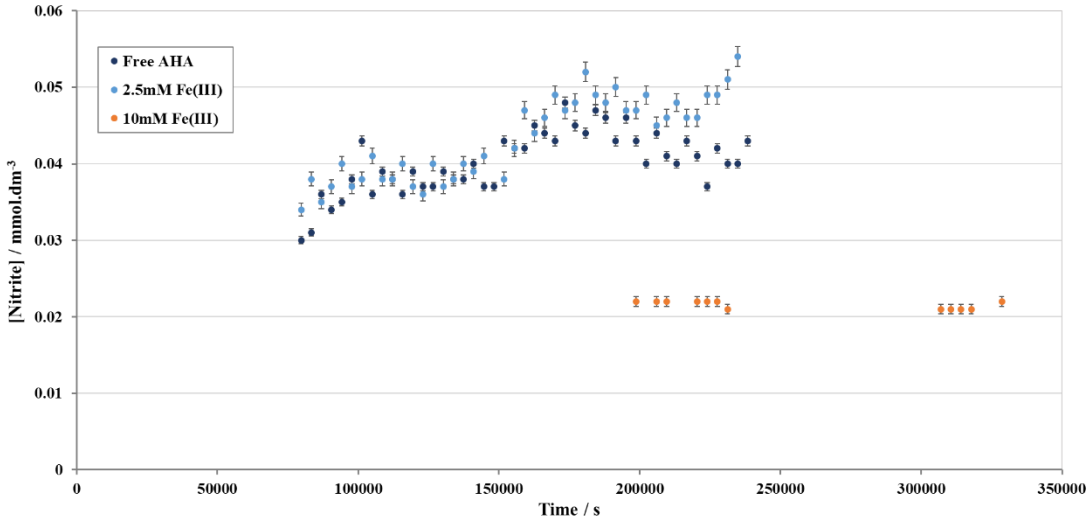

Figure 4.21: NO_2^- ingrowth measured from the hydrolysis of 10 mmol dm^{-3} AHA in 0.1 mol dm^{-3} HNO_3 at 313K with initial [Fe(III)] = 0 mmol dm^{-3} (dark blue), 2.5 mmol dm^{-3} (light blue), and 10 mmol dm^{-3} (orange). Errors bars are shown as the RSD value from the respective calibration.

The first observation is that all the obtained measurements are very small, on the order of 10 µmol dm^{-3}. The maximum nitrite concentration seen is 0.05 mmol dm^{-3}, observed during AHA hydrolysis in the presence of 2.5 mmol dm^{-3} Fe(III). In the presence of 10 mmol dm^{-3} Fe(III), only a few measurements of the NO_2^- ion were obtained of approximately 0.023 mmol dm^{-3}. With the majority of the nitrite measurements however being so very small and falling between the LOD and LOQ, the accuracy of these measurements should be treated with caution.

The shape of profiles for the [NO_2^-] vs t datasets obtained during the hydrolysis of AHA in the absence and presence of 2.5 mmol dm^{-3} Fe(III) however, are intriguing. From Figure 4.21, it can be seen that both are similar; the nitrite concentrations show a general increase over time, with two small peaks in the [NO_2^-] vs. t profile at ~10,000 and 18,000 seconds, both followed by small troughs. These concentrations match initially and only diverge slightly after the second peak, after which they appear to fall at marginally different rates and rise again. It could be suggested the pattern is due to reaction of both the nitric and nitrous acid with NH_2OH under the conditions of Figure 4.21 via equations 4.21 and 4.22, the latter of which might not be observed in those data sets at elevated temperature and high initial [Fe(III)] if the Fe(III) was, via Eq. 4.24a or 4.24b, acting to decrease the concentration of NH_2OH by oxidising it, so interrupting the reaction of Eq. 4.22.

As discussed previously in section 4.3, Gowland and Stedman [93] investigated the borderline conditions for the change in functionality of hydroxylamine as a nitrous acid scavenger in accordance with Eq. 4.22 to a generator in the nitrous-catalysed reaction between hydroxylamine and nitric acid via Eq. 4.21. These authors noted some unusual kinetic phenomena in the borderline region, observing the nitrous acid concentration to decrease in the initial stages of the reaction, pass through a minimum and autocatalytically increase to a concentration greater than the initial value. Bennett *et al*. [91] found the induction period for the onset of the oxidation of hydroxylamine by HNO_3 to increase at high hydroxylamine concentrations, as shown in Figure 4.22. This may be due to the higher concentrations of hydroxylamine consuming nitrous upon its formation from the nitrous-catalysed hydroxylamine/nitric acid reaction – so

inhibiting the capacity of nitrous acid to catalyse the reaction that generates it. Eventually, however, the hydroxylamine concentration may fall below a critical value where the rate of its (HNO_2-catalysed) reaction with HNO_3 and thus generation of HNO_2 outstrips its rate of reaction with HNO_2 – so leading to an acceleration in the rate of nitrous acid generation overall.

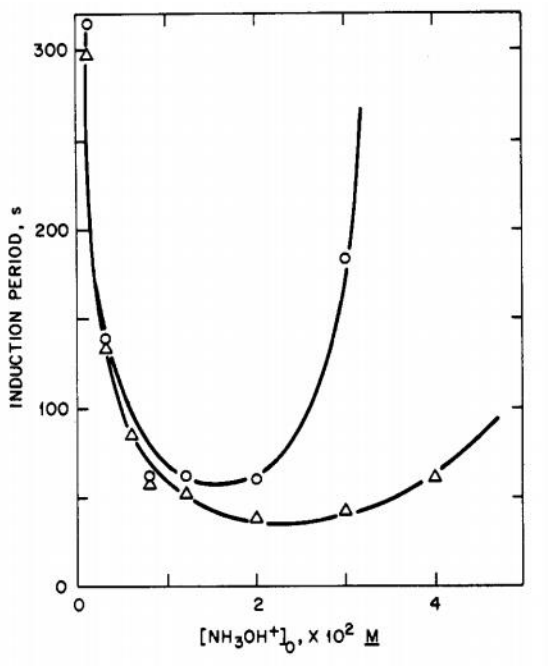

Figure 4.22: Plot of the induction period in seconds (s) for the onset of autocatalytic HNO_2 production from the oxidation of hydroxylamine by HNO_3 vs. the initial hydroxylamine concentration [NH_3OH^+], with an initial HNO_2 concentration of < 10^{-4} mol dm^{-3} (298K): circles, 3 mol dm^{-3} HNO_3; triangles, 4 mol dm^{-3} HNO_3 [91] (reproduced with permission from reference [91], copyright 1982 American Chemical Society).

As mentioned at the start of this section, HNO_2 was only observed in solutions of AHA/Fe(III) hydrolysing at 313K. No nitrous was observed in solutions hydrolysing at higher temperatures. The slower ingrowth of NH_3OH^+ from AHA hydrolysis at 313K compared to the higher temperature could lead to relatively lower HAN concentrations in these solutions, that are high enough to drive the nitrous generating HAN/HNO_3 reaction of Eq. 4.21 but are not high enough to drive the nitrous

consuming HAN/HNO_2 reaction of Eq. 4.22, thus resulting in the appearance of measurable nitrite concentrations.

A study on the thermal decomposition of hydroxylamine nitrate in 1988 by Oxley and Brower [154] also showed the addition of a small amount of the acetate ion to suppress HAN decomposition by several hours. They attributed this to the reduction in the acidity of the solution (i.e., [H+]) due to the formation of acetic acid, and thus reduction in the concentration of HNO_3 available to react with HAN. XHAs are structurally related to carboxylic acids, but with a much weaker dissociation [51] (pKa = 4.74 for acetic acid and 9.2 for AHA). Higher temperatures increase the rate of AHA hydrolysis, producing greater concentrations of acetate over short timescales, which would thus help to retard HAN decomposition. This could therefore also be a contributing factor and help explain why, as stated at the start of this section, the nitrite ion is seen only to accumulate at the lowest temperature studied here, i.e. 313K.

Whilst the results of the IC analysis proved interesting, they required further analysis. To determine the extent of the apparent accumulation of HNO_2 observed here more accurately, a more sensitive method for measurement of the intrinsic HNO_2 in HNO_3 was needed. UV/Vis spectroscopy was therefore utilised as an analytical technique to determine small concentrations of HNO_2/NO_2^- with greater accuracy. Specifically, the so-called Shinn method [120] was utilised, which itself is a modification of the original Griess method for nitrites [155], the implementation and chemistry of which is described in Chapter 3 section 3.5.2.2. Results of this analysis follow.

4.4.2 Quantification by the Shinn Method

4.4.2.1 Measurements

The intrinsic HNO_2 concentration was measured in solutions of 0.1 mol·dm^{-3} HNO_3 over a temperature range of 303 – 333K in the absence of Fe(III). Spectra obtained are shown in Figure 4.23, and compared to the smallest HNO_2 standard of 5 µmol dm^{-3}. The maximum absorbance at 543 nm and calculated [HNO_2] are shown in Table 4.6.

Table 4.6: Measurements of the maximum absorbance at 543nm and the concentration of intrinsic HNO_2 in 0.1 mol dm^{-3} HNO_3 calculated from the calibration function.

Temperature / K	Absorbance at 543 nm	[HNO_2] / µmol dm^{-3}	% [HNO_3]
303	0.094	0.87	8.1×10^{-4}
313	0.093	0.85	7.9×10^{-4}
323	0.091	0.82	7.4×10^{-4}
333	0.091	0.82	7.4×10^{-4}

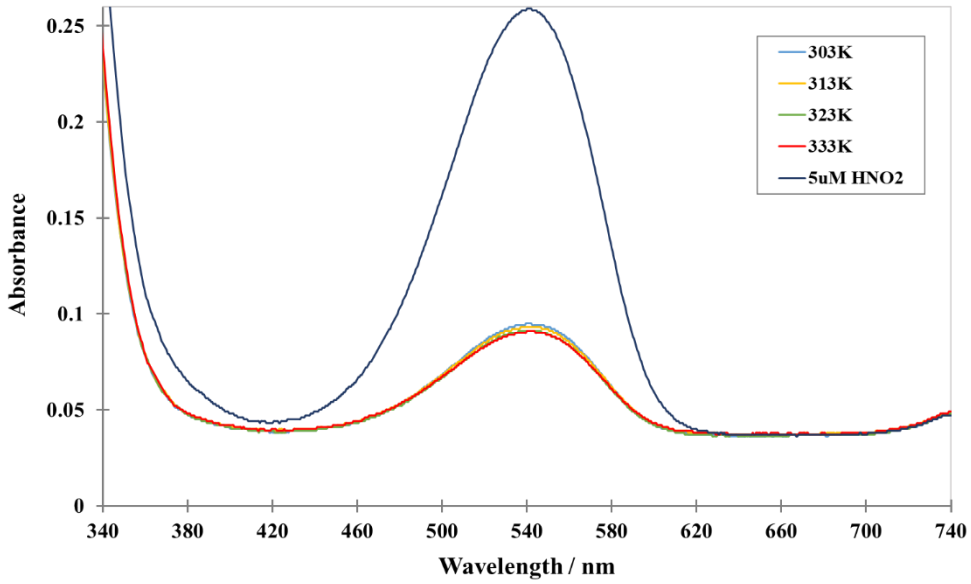

Figure 4.23: Spectra obtained from measurement of intrinsic HNO_2 in a solution of 0.1 mol dm^{-3} HNO_3, equilibrated at 303, 313, 323 and 333K. A spectrum of the smallest 5µmol dm^{-3} HNO_2 standard is shown for reference.

The intrinsic HNO_2 concentration was found to be very small, with an average measurement of 8.4×10^{-7} mol dm^{-3} in 0.1 mol dm^{-3} HNO_3, which was not significantly affected by temperature. The observed non-dependence of the $[HNO_2]$ on temperature is in agreement with a study by Ziouane and Leturcq [156]. Using a colorimetric method also derived from the Griess method [157], these authors demonstrated a linear decrease in nitrous acid concentrations with increasing nitric acid concentration in the range $[HNO_3]$ = 1.5 – 8 mol dm^{-3}, that was unaffected by temperature in the range 323−368K. Their results are shown in Figure 4.24, and from the linear function described we can obtain an estimate of the equilibrium concentrations of HNO_2 of 5.97×10^{-5} mol dm^{-3} in the 0.1 mol dm^{-3} HNO_3 solutions used in the acquisition of the data presented in Figure 4.23 and Table 4.6 above. The measured equilibrium concentrations of HNO_2 in Table 4.6 are 2 orders of magnitude less than this estimate; however, this may be due to Ziouane and Leturcq reporting that the empirically derived linear relationship of Figure 4.24 is only valid in the range 1.5 mol dm^{-3} ≤ $[HNO_3]$ ≤ 8 mol dm^{-3}, and it therefore may not hold for dilute solutions of HNO_3 < 1.5 mol dm^{-3}.

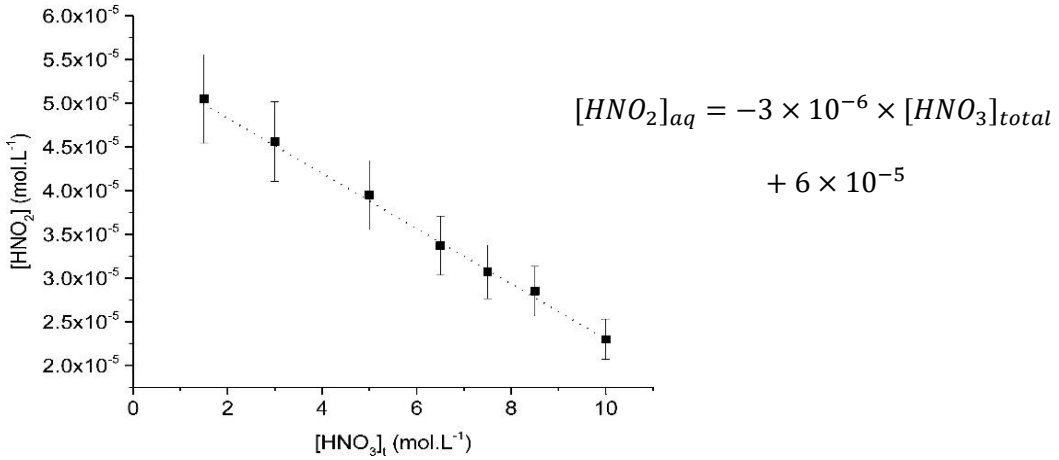

Figure 4.24: Modelled equilibrium concentration of HNO_2 as a function of $[HNO_3]$. Source: [Ziouane et al., 2018]

In the context of the HNO_3/HAN system, the formation of nitrous acid is reported by Gowland and Stedman [93] to be favoured by a decrease in $[NH_3OH^+]$, and an increase in temperature, and once formed, nitrous acid effectively catalyses its own production via Eq. 4.21 [158]. With the accumulation of nitrite seen only at the lowest temperature of 313K in the IC experiments described at the start of section 4.4.1.2, it is reasonable to hypothesize that any significant quantity produced at the higher temperatures might, as well as undergoing reaction with the larger amounts of HAN generated by AHA hydrolysis at higher temperature, also be undergoing a rapid thermal decomposition. The decomposition of 100 µmol dm^{-3} HNO_2 was therefore followed using the Shinn method at the higher temperatures of 323K and 333K. Figure 4.25 shows a plot of $[HNO_2]$ against time obtained for decomposition over a 5 hour period.

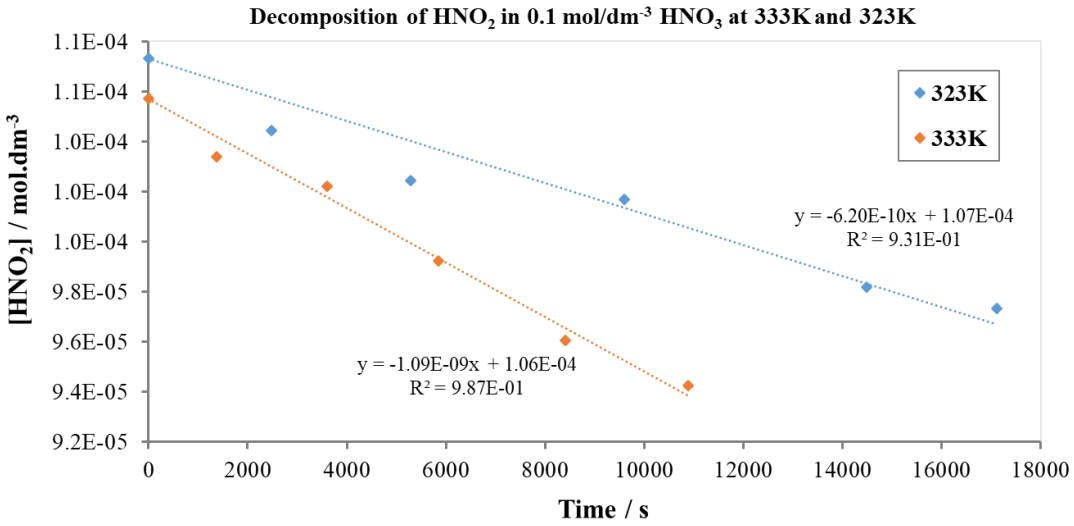

Figure 4.25: Plot of $[HNO_2]$ against time for a solution of 100 µmol dm^{-3} $NaNO_2$ in 0.1 mol dm^{-3} HNO_3, decomposed at 323K and 333K, with $[HNO_2]$ in units of mol dm^{-3}.

Inspection of Figure 4.25 shows that the solutions of 100 µmol dm^{-3} $NaNO_2$ in 0.1 mol dm^{-3} HNO_3 decomposed very slowly, taking approximately 3 and 5 hours to decrease by only 10 µmol dm^{-3} at 333K and 323K respectively. Several different mechanisms

have been suggested for the decomposition of HNO_2 in aqueous solution [159], including; i) by the simultaneous hydration of N_2O_4 and evolution of NO, species that exist in equilibrium with HNO_2, ii) desorptive stripping of nitrous acid molecules from liquid to gas, and iii) decomposition of HNO_2 into NO and NO_2 in the vicinity of the liquid surface. First elucidated by Abel and Schmidt in 1928 [160], the commonly accepted elementary mechanism for the decomposition of HNO_2 can be described by Eqs. 4.29 - 4.32, giving an overall reaction described by Eq. 4.33. Rayson *et al* [161] establish a large activation energy of 107 kJ mol^{-1} for Eq. 4.33, the majority of which, on the basis of quantum chemistry calculations, results from the endothermic nature of the initial equilibrium Eq. 4.29.

$$2HNO_2 \rightleftharpoons N_2O_3 + H_2O \tag{4.29}$$

$$N_2O_3 \rightleftharpoons NO + NO_2 \tag{4.30}$$

$$2NO_2 \rightleftharpoons N_2O_4 \tag{4.31}$$

$$N_2O_4 + H_2O \rightarrow HNO_2 + NO_3^- + H^+ \tag{4.32}$$

$$3HNO_2 \rightarrow 2NO + NO_3^- + H^+ + H_2O \tag{4.33}$$

Irrespective of which mechanisms obtain or dominate in the systems studied in Figure 4.25, the IC results presented previously in section 4.4.1 and Figure 4.21 suggest that net formation of HNO_2 is more likely at lower temperatures in the hydrolysing AHA systems under study here. Once formed from the reaction between nitric acid and hydrolytically generated hydroxylamine, the thermal decomposition of the so-formed HNO_2 is likely to be insignificant, and losses would be by reaction with other species in solution such as hydroxylamine itself or Fe(II).

Thus, quantification of hydroxylamine and Fe(II) rather than nitrous may be of greater use in following the hydrolysis of Fe(III)-AHA systems. Quantification of both species is discussed in the following sections 4.5 and 4.6.

4.5 Techniques for Analysis of Hydroxylamine

Andrieux *et al* [83] have previously used quantum mechanical modelling to suggest a mechanism for the hydrolysis of the monoacetohydroxamatoiron(III) complex that would produce analogous hydrolysis products to free AHA. However these authors did not measure the products of this reaction in their study; rather, they focussed on the loss of the absorbance associated with the monoacetohydroxamatoiron(III) complex. Thus, following on from our analysis of the acetic acid product described in section 4.2, we also sought to quantify the second hydrolysis product, hydroxylamine. This was performed via two analytical techniques. Section 4.5.1 discusses the analysis of NH_2OH in solutions after complete hydrolysis by a redox titration with potassium bromate, and section 4.5.2 will discuss the results of real-time quantification of NH_3OH^+ throughout hydrolysis by ion chromatography. The aims of these studies included; i) to determine whether the product yield during the rapid hydrolysis of AHA changes due to complexation, and ii) determine whether or not the thermodynamically possible, but assigned by Barney *et al*. [95] (see section 2.5.2) as kinetically slow redox reaction between NH_2OH and ferric ions, also occurs during the hydrolysis of the associated complex.

4.5.1 Quantification by Redox Titration

4.5.1.1 Preliminary hydrolysis studies

Preliminary hydrolysis studies were performed on solutions of 4 mmol·dm^{-3} AHA hydrolysed in 0.3 mol dm^{-3} HNO_3 at 333K, in the absence and presence of 2.5 mmol·dm^{-3} Fe(III). This AHA:Fe ratio of 1.6:1 is analogous to that used by Andrieux *et al* [77] and ensures the mono-complex dominates (see speciation diagrams in Chapter 3, section 3.2), whilst the elevated temperature allowed for a rapid hydrolysis reaction after which measurements of NH_2OH were made via a redox titration with potassium bromate. The titration method is described in detail in Chapter 3, section 3.6.1. From the predicted mechanism for the hydrolysis of the monoacetohydroxamatoiron(III) complex, the expectation was for stoichiometric amounts of NH_2OH produced from both free and complexed AHA. The average measurements obtained from three titres of each solution are shown in Table 4.7.

Table 4.7: Preliminary NH_2OH measurements from the hydrolysis of 4 mmol dm^{-3} AHA in 0.3 mol dm^{-3} HNO_3 at 333K, in the absence and presence of 2.5 mmol dm^{-3} Fe(III). Concentrations are given in units of mmol dm^{-3} and measurements are averages of 3 titres. Fe(III) was added as its nitrate salt.

Initial [Fe(III)]	Average [NH_2OH]	Range of measurements	% of maximum
-	1.4	1.2 – 1.8	35
2.5	1.2	0.9 – 1.4	30

Inspection of Table 4.7 shows a significant deviation of the concentration of NH_2OH from that expected based on a stoichiometric hydrolysis of the AHA, measuring only 30-35% of the theoretical maximum both in the absence and presence of Fe(III). Whilst the average NH_2OH concentration measurement appeared slightly less in the presence

of Fe(III), the fact that it is significantly lower than that expected in both solutions suggested the possible occurrence of the autocatalytic reaction of HAN with HNO_3 that results in its decomposition, the mechanism of which was explained by Pembridge and Stedman [92] and discussed in detail in section 4.3. For completeness, it is worth reminding the reader that, according to Barney [95], the exact products of the Fe(III)/HAN reaction depend on the [Fe(III)]:[HAN] ratio. If [Fe(III)] > [HAN] then the reaction proceeds in a 2:1 stoichiometry via Eq. 4.24b, whereas when [Fe(III)] < [HAN] the reaction proceeds in a 1:1 stoichiometry via Eq. 4.24a.

$$Fe^{3+} + NH_3OH^+ \rightarrow Fe^{2+} + 1/2N_2 + 2H^+ + H_2O \quad (4.24a)$$

$$2Fe^{3+} + NH_3OH^+ \rightarrow 2Fe^{2+} + 1/2N_2O + 3H^+ + 1/2H_2O \quad (4.24b)$$

With this in mind, the same titrations were performed using $Fe_2(SO_4)_3$ in H_2SO_4, and $Fe(ClO_4)_3$ in $HClO_4$, to remove all nitrate from the system. It was hoped that this would allow a comparison of the products of the free and Fe(III)-complexed AHA hydrolysis without any other interference. In addition, the concentration of the $Na_2S_2O_4$ titrant was reduced to 0.5 mol dm^{-3} with the aim to minimise errors in measurements (again, see section 3.6.1 for details of the titration method). The results of this analysis for hydrolysis performed at 333K are shown in Figure 4.26, along with those previously obtained in HNO_3. Analogous hydrolysis experiments were also performed at room temperature and pressure (r.t.p) in HNO_3, $HClO_4$ and H_2SO_4, the results of which are shown in Figure 4.27. Error bars show the range of measurements for the same solution over three consecutive titrations.

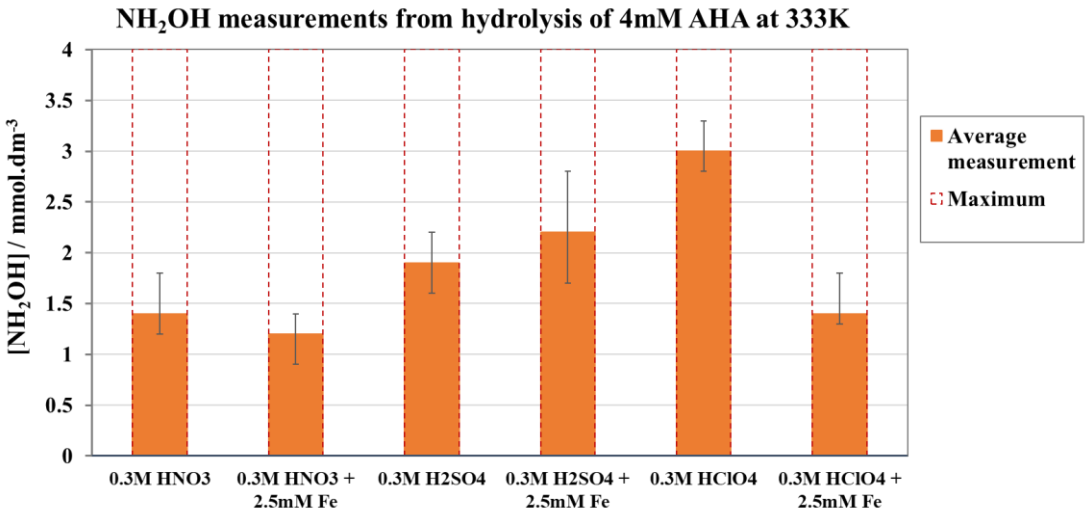

Figure 4.26: Measurements of NH_2OH after hydrolysis of 4 mmol dm^{-3} AHA at 333K in 0.3 mol dm^{-3} HNO_3, H_2SO_4 and $HClO_4$, in the absence and presence of 2.5 mmol dm^{-3} Fe(III). In each case the Fe(III) was added as the corresponding salt.

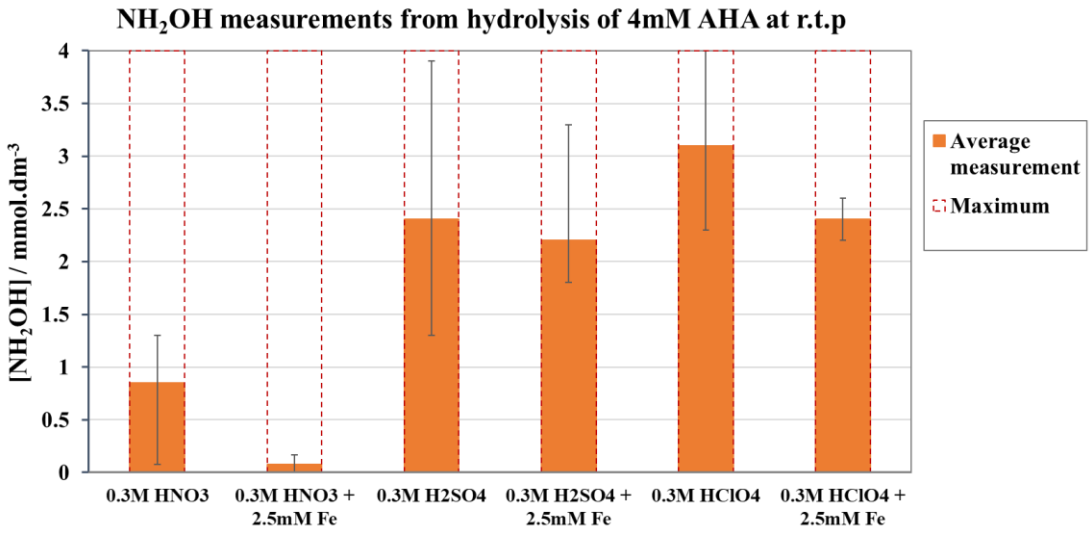

Figure 4.27: Measurements of NH_2OH after hydrolysis of 4 mmol dm^{-3} AHA at r.t.p in 0.3 mol dm^{-3} HNO_3, H_2SO_4 and $HClO_4$, in the absence and presence of 2.5 mmol dm^{-3} Fe(III). In each case the Fe(III) was added as the corresponding salt.

Inspection of Figure 4.26 and Figure 4.27 reveals that, in nearly all cases, the average measurement of NH_2OH in solutions post-hydrolysis was lower in the presence of Fe(III) than in its absence, with the only exception being for the case of hydrolysis in H_2SO_4 at elevated temperature. Dilution of the titrant showed no improvement in the

errors, and the measurements in H_2SO_4 showed the greatest variation over consecutive titrations, and thus proved the most unreliable. Measurements of NH_2OH after hydrolysis in HNO_3 were consistently lower than in any other acid, and surprisingly, those measurements after hydrolysis at r.t.p were lower than at 333K. These solutions however were left to hydrolyse for two weeks to ensure complete hydrolysis, thus the NH_2OH concentration could be continuing to deplete after the hydrolysis was complete, via the reactions with HNO_3 and HNO_2 in accordance with Eqs. 4.21 and 4.22 respectively. This analysis is supported by the previous IC analysis for nitrite (see section 4.4.1) which suggested that nitrous acid accumulated in those systems at lower temperatures. Whilst all the measurements still show significant errors, the observation that the average NH_2OH concentration appeared lower in the presence of Fe(III) in both HNO_3 and $HClO_4$, suggested that reactions of NH_2OH with HNO_3/HNO_2 were only part of the reason for HAN decomposition in acidic media. This observation could be an indication of: (i) a different mechanism for complexed AHA hydrolysis, or (ii) the thermodynamically allowed but kinetically slow (as suggested by Barney [95]) redox reaction of NH_2OH with Fe(III).

4.5.1.2 Revised studies

In an effort to reduce the errors in measurements associated with the titrimetric method used in generating the data of Figures 4.26 and 4.27 immediately above, the original method as described by Burger *et al.* was sourced [162]. Review of this revealed that these authors had used the titrimetric method to measure samples of 3-12 mg hydroxylamine hydrochloride, equivalent to 9–30 mmol dm^{-3}. With these

concentrations being far greater than those expected in the hydrolyzing AHA solutions measured thus far, a series of calibration studies on the bromate titration were performed, this time using hydroxylamine rather than AHA so as to avoid any complications associated with the hydrolytic generation of the former from the latter. To allow for meaningful insight into the errors associated with, and thus the utility of, the bromate titration in measuring the NH_2OH concentrations expected in the AHA solutions under study here, these calibration studies were conducted at two NH_2OH concentrations as follows: (i) at 4 mmol dm^{-3}, the concentration expected in the fully hydrolysed AHA system under study; and (ii) 20 mmol dm^{-3}, a concentration at the mid-point of the concentration range used by Burger *et al* [162] in the initial development of the method. Figure 4.28 shows measurements of these 4 and 20 mmol dm^{-3} NH_2OH standards in aqueous and acidic solution, the latter of which had significantly smaller errors of < 1% in water and < 3% in acidic media.

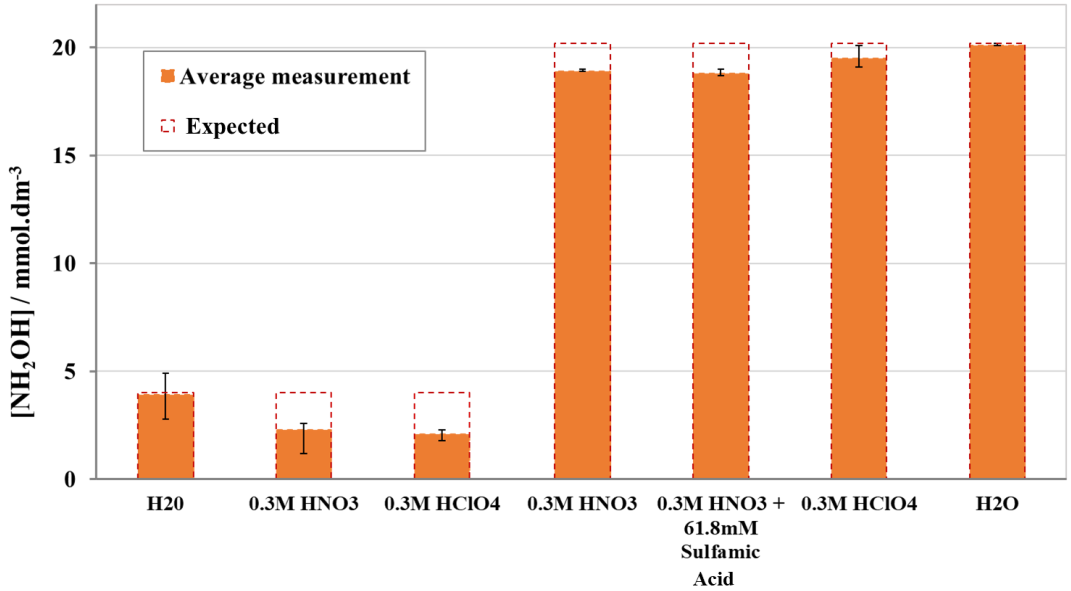

Figure 4.28: Measurements of standard solutions of NH_2OH in the range of 4 and 20 mmol dm^{-3} in aqueous and 0.3 mol dm^{-3} perchloric or nitric acid media. A standard of 20 mmol dm^{-3} NH_2OH in 0.3 mol dm^{-3} HNO_3 with the addition of sulfamic acid was also tested for any possible interference.

It has been reported that a solution of 50% hydroxylamine in water will decompose even if stored at 10°C for a few months, and decompose much more energetically than freshly prepared solution [130]. The measurements of NH_2OH standards in water shown in Figure 4.28 confirmed the stability 50% hydroxylamine stock solution used for standard preparation and the validity of the method, and the small errors on measurements of the 20 mmol dm^{-3} standards in all media confirmed their reliability. Particularly, the NH_2OH standard in $HClO_4$ gave a measured NH_2OH concentration within error of that expected, whilst an apparent loss of ~1 mmol dm^{-3} was seen in HNO_3. This latter observation was also true for a NH_2OH standard in HNO_3 with the addition of sulfamic acid which acts as a nitrous acid scavenger, which occurs by the reaction described in Eq. 4.34. This standard is also shown in Figure 4.28 above.

$$HNO_2 + H_3NSO_3 \rightarrow H_2SO_4 + N_2 + H_2O \quad (4.34)$$

Given the successful validation of the bromate titration method at the higher NH_2OH concentrations used in Figure 4.28, a solution of 20 mmol dm^{-3} AHA was hydrolysed at r.t.p in 0.3 mol dm^{-3} HNO_3 and $HClO_4$, with Fe(III) added in the same ratio as for the previous experiments.

For comparison, a control solution of 20 mmol dm^{-3} AHA was additionally hydrolysed in 0.3 mol dm^{-3} H_2SO_4 in the fridge. As illustrated in Figure 4.29, the final measurement of even this control solution still showed a small decrease with respect to the expected 20 mmol dm^{-3} NH_2OH, of approximately 1 mmol dm^{-3}. With regards to the titrimetric analysis method itself, studies on the closed reaction system of sodium bromate and hydroxylamine sulphate by Adamčíková *et al* [163] showed the reaction

dynamics to be complex, and dependent on both the initial concentrations of hydroxylamine and BrO_3^- and the initial H^+ concentration. Idris *et al* [164] also noted a decrease in the rate of reaction between NH_3OH^+ and BrO_3^- with added SO_4^{2-} and NO_3^- ions. As discussed above, the experimental method of Burger *et al* [162] was developed specifically for the measurement of 3-12mg $NH_2OH.HCl$ in HCl acidic media. Therefore the apparent loss of hydroxylamine in the control experiment, and in the acidic standards measured previously in the calibration study of Figure 4.28, is likely a result of impacts of the composition of the acidic media – both acidity and counter ion used – on the experimental method itself.

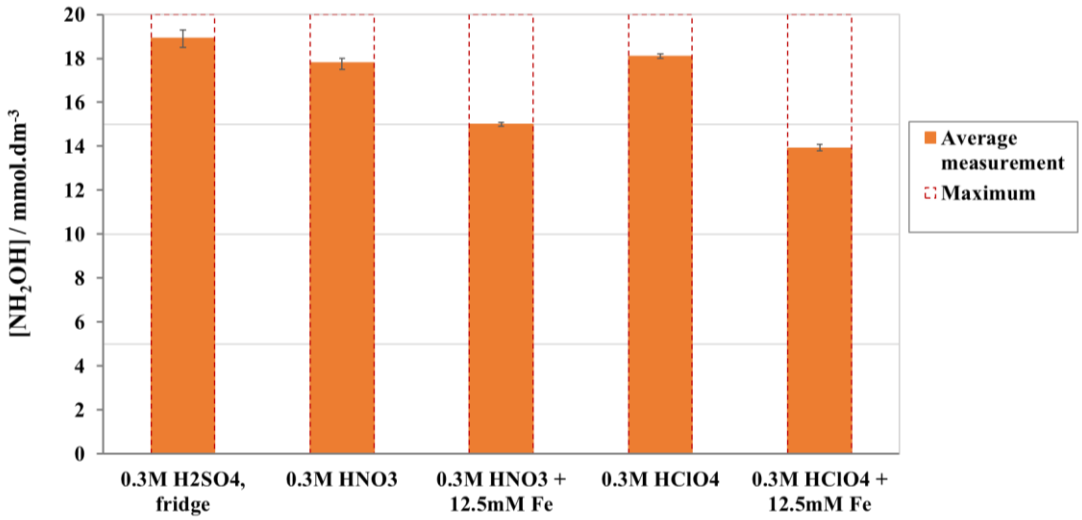

Figure 4.29: Measurements of NH_2OH after hydrolysis of 20 mmol dm^{-3} AHA at r.t.p. in 0.3 mol dm^{-3} perchloric and nitric acid, in the absence and presence of 12.5 mmol dm^{-3} Fe(III). In each case the Fe(III) was added as the corresponding salt.

Figure 4.29 also shows that the resultant NH_2OH measurements for the AHA solutions hydrolysed in 0.3 mol dm^{-3} HNO_3 and $HClO_4$ in the absence of Fe(III) were equal within errors, and only slightly less that the control solution. This similarity in HNO_3 and $HClO_4$ is expected based on a study of the hydrolysis of benzohydroxamic acid

(BHA) by Naumov *et al* [165] who concluded it was a first-order reaction and observed no difference in the effect of HNO_3 and $HClO_4$. Looking next at the solutions of AHA hydrolysed in the presence of 12.5 mmol dm^{-3} initial Fe(III) in HNO_3 and $HClO_4$, it can be seen that the measured NH_2OH concentration is reduced by a similar quantity in comparison to that measured in AHA solutions hydrolysed the absence of Fe(III) in the respective acidic media. This observation would again suggest either (i) a different mechanism for complexed AHA hydrolysis, or (ii) the thermodynamically allowed but kinetically slow (as suggested by Barney [95]) redox reaction of NH_2OH with Fe(III).

Following these studies of NH_2OH solutions at r.t.p, NH_2OH was quantified in solutions after the hydrolysis of 20 mmol dm^{-3} AHA in the same concentration of HNO_3, but in the absence and presence of excess Fe(III) (25 mmol dm^{-3}) and elevated temperature of 333K for comparison. To determine the extent of the instability of NH_2OH in HNO_3, sulfamic acid (H_3NSO_3) was initially added to solutions of the same compositions to act as a scavenger for the HNO_2 catalyst.

As mentioned previously and described in equations 4.24-4.28, Fe(III) is known to react with hydroxylamine to produce Fe(II) which may then act as a catalyst for nitrous production from nitric. The so produced nitrous acid may then lower the self-accelerating decomposition temperature of HAN solutions via Eq. 4.21 by promoting the reaction of nitric acid with hydroxylamine [130, 166]. Marchenko *et al* [167] studied the stability of hydroxylamine in solutions of low acidity containing 350 – 920 g L^{-1} U(VI), and found it to be stable for no less than 6 hours at $[HNO_3] < 1$ mol dm^{-3} at 333K. In the presence of fission and corrosion products however, primarily Fe(III) ions, the stability decreased appreciably, with Fe(III) concentrations of ~50 mg L^{-1} (0.9

mmol dm^{-3}) making hydroxylamine unstable in 0.5 mol dm^{-3} HNO_3 at 333K through production of catalytic HNO_2 in accordance with equations 4.24-4.28. However, inspection of Figure 4.30 shows a clear decrease in the measured NH_2OH concentration in the presence of Fe(III), a decrease that is not significantly attenuated by the addition of sulfamic acid to act as a HNO_2 scavenger. The loss of NH_2OH therefore appears to be as a direct result of the Fe(III), via AHA hydrolysis mechanistic changes, or the reduction of Fe(III) by hydroxylamine.

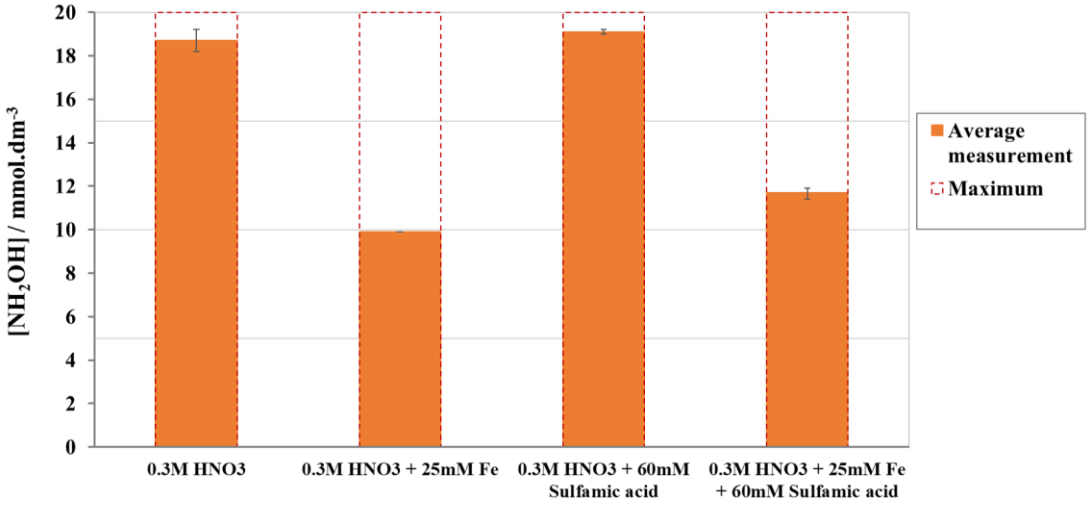

Figure 4.30: Measurements of NH_2OH after hydrolysis of 20 mmol dm^{-3} AHA at 333K in HNO_3 of concentration 0.3 mol dm^{-3}, in the absence and presence of 25 mmol dm^{-3} Fe(III), and the same experiments with an additional 60 mmol dm^{-3} sulfamic acid..

If the loss of NH_2OH was due to its supposedly kinetically slow reduction of Fe^{3+}, this would produce Fe^{2+}, and a re-oxidation of $Fe^{2+}$to Fe^{3+} that can occur in HNO_3 by Eq. 4.25 [117] could result in further loss of hydroxylamine by reaction with the regenerated ferric ions. In an attempt to eliminate the HNO_3-derived complications arising from equations 4.24-4.28, a final set of experiments were conducted in the presence of perchloric, rather than nitric, acid. In these, solutions of 20 mmol dm^{-3}

AHA in 0.3 mol dm^{-3} $HClO_4$ were hydrolysed in the presence of 25 mmol dm^{-3} Fe(III), under an inert atmosphere by purging the solutions with N_2 gas. Two separate solutions were sealed and allowed to hydrolyse at the elevated temperature of 333K, whilst a third was sealed and left for two weeks to hydrolyse at ambient temperature in a glovebox. Results are shown in Figure 4.31.

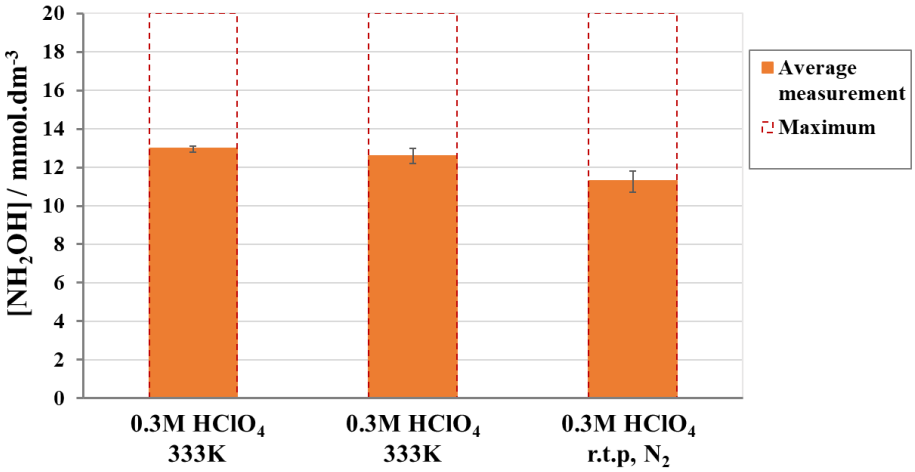

Figure 4.31: Measurements of NH_2OH after hydrolysis of 20 mmol dm^{-3} AHA at 333K and r.t.p. in 0.3 mol dm^{-3} $HClO_4$, in the presence of 25 mmol dm^{-3} Fe(III), under an inert N_2 atmosphere.

Inspection of Figure 4.31 reveals a surprisingly similar reduction in the measured NH_2OH concentration from that theoretically/stoichiometrically possible at both temperatures. Thus, when AHA hydrolysis is performed in the presence of Fe(III) under an inert atmosphere in $HClO_4$, this results in similar levels of loss of NH_2OH as observed in an oxidising atmosphere; the measured NH_2OH concentrations showed further loss of only 1-2 mmol dm^{-3} NH_2OH in comparison to previous measurements from 20 mmol dm^{-3} AHA hydrolysed in $HClO_4$ under an oxidising atmosphere in the presence of the lower concentration of Fe(III) of 12.5 mmol dm^{-3}, see Figure 4.29. This could suggest that, if reduction of Fe(III) by hydrolytically generated HAN is

occurring then, consistent with data from Bengtsson *et al* [99], it is very slow in $HClO_4$ media.

In summary, the titrimetric analyses have shown that a decrease in the stoichiometrically expected concentration of NH_2OH is observed after hydrolysis of Fe(III)-complexed AHA, which could be representative of either i) a different mechanism for Fe(III)-complexed AHA hydrolysis to give differing yields of the same products, or ii) the occurrence of Fe(III) reduction by NH_2OH. Coupled with previous Raman spectroscopy and acetate analysis by IC described in sections 4.1 and 4.2 respectively, the titrimetric results presented suggest the latter. Whilst the likelihood of the ferric/NH_2OH redox reaction was discounted initially on the basis of supposedly slow kinetics, it is clear that, based on the results, this reaction requires further investigation, ideally via a method that allows for continuous monitoring of the reaction throughout the period of AHA hydrolysis. The following section will therefore describe one such method for the real-time quantification of hydroxylamine.

4.5.2 Real-time Quantification by Ion Chromatography

From the previous titrimetric analysis of NH_2OH following the hydrolysis of AHA, it was clear that a method was needed for understanding the ingrowth of NH_2OH throughout the hydrolysis process. With a pKa of 5.96 [130], NH_2OH exists in acidic solution predominantly in its protonated form, NH_3OH^+. Ion chromatography was therefore utilised for quantification of the hydroxylammonium ion (NH_3OH^+) throughout the hydrolysis reaction in real-time. Measurements were taken over the

course of AHA hydrolysis for the free and Fe(III)-complexed systems for which acetate measurements were obtained in a previous analysis, see section 4.2.

4.5.2.1 Limit of detection

The value of λ_0 for the hydroxylammonium ion (at 298K) is reported to be similar to that of the acetate ion, with a value 49.27 ±0.17 S cm^2 mol^{-1} [168], whilst the average noise in the chromatograms was slightly higher than found in anion analysis (see chromatograms of anions and NH_3OH^+, Figures 3.9 and 3.17 respectively in Chapter 3, for illustration), with a value of approximately of 3×10^{-3} µS cm^{-1}. A lower sensitivity of cation analysis compared to anion analysis is however expected due to the absence of chemical suppression, a process which enhances the signal to noise ratio [113]. As was illustrated in Figure 3.18 in section 3.6.2.2 in Chapter 3, the calibration functions varied significantly between calibration runs, so calculation of the LOD/LOQ for NH_3OH^+ was not attempted.

4.5.2.2 Hydrolysis studies

The measurements of NH_3OH^+ obtained for each of the systems studied are shown in Figure 4.32. The errors shown for the measurements were taken as the RSD values of the relevant calibration function, which are in the range of 4.5 – 6.5%, but these could be greater due to the wide variation seen in calibration curves mentioned immediately above.

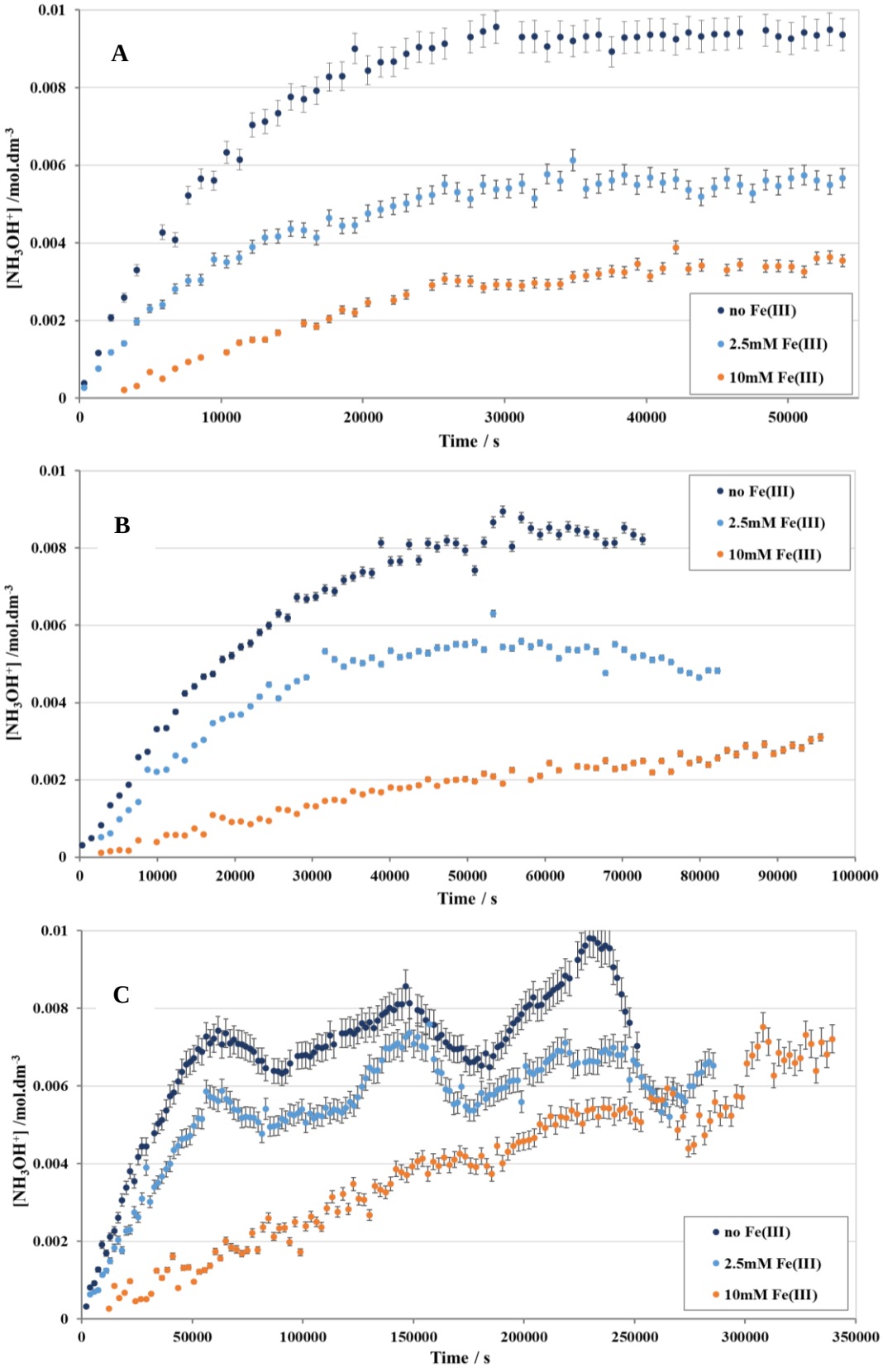

Figure 4.32: NH_3OH^+ ingrowth measured from the hydrolysis of 10 mmol dm^{-3} AHA with initial [Fe(III)] of 0 mmol dm^{-3} (navy blue), 2.5 mmol dm^{-3} (light blue), and 10 mmol dm^{-3} (orange) at temperatures of A) 333K, B) 323K and C) 313K. Errors bars are shown as the RSD value from the respective calibration.

Inspection of the data in Figure 4.32 shows two key patterns. Firstly, a number of the data sets, particularly those at the lowest temperature of 313K, show a loss of NH_3OH^+ that appears to be due to the complex behaviour of HAN in HNO_3 media. Sharp peaks and troughs are seen in two of the [NH_3OH^+] profiles at 313K, which coincide with the small troughs and peaks seen in the nitrite measurements for the same systems described previously in section 4.4.1.2. This observation suggests the occurrence of the rapid, autocatalytic decomposition of HAN in HNO_3. While this process is most evident in the free AHA system at 313K, the increasing initial Fe(III) concentrations appears to inhibit this process at this temperature.

Despite the sharp losses at certain times in the dataset obtained for free AHA hydrolysis in the absence of iron at 313K, the NH_3OH^+ concentration is still seen to grow to close 100% of the theoretical maximum within errors. This illustrates the very complex chemistry that exists in the $NH_2OH/HNO_2/HNO_3$ system. Ashcraft *et al*. [169] computed rate coefficients at 298K for a total of 90 reactions important in the autocatalytic oxidation of hydroxylamine in aqueous nitric acid, including some reactions such as Eqs. 4.35 and 4.36 that would increase the NH_2OH concentration.

$$HNO + HN_2O \rightleftharpoons NH_2OH + NO \qquad \mathrm{k} = 8.4 \times 10^5 \mathrm{mol}\, dm^{-3}\, s^{-1} \qquad (4.35)$$

$$HN_2O + HN_2O \rightleftharpoons NH_2OH + HNO \qquad \mathrm{k} = 7.8 \times 10^{-3} \mathrm{mol}\, dm^{-3}\, s^{-1} \qquad (4.36)$$

The autocatalytic behaviour appears to be absent in the systems shown here at the higher temperatures of 323K and 333K. This is in agreement with the absence of nitrite measurements at the same temperatures as described previously in reference to Figure 4.21 in section 4.4.1. Whilst some decomposition is seen at 323K, the NH_3OH^+

concentration follows a bell-shaped curve, reaching a peak at around 9 mmol dm^{-3} before gradually falling, and no such decomposition is seen at 333K. This is likely a result of a combination of a vast number of reactions that can occur between NH_2OH/NH_3OH^+ and various NO_x species in HNO_3, or from the direct volatilisation of HAN, rather than its autocatalytic reaction with HNO_3.

In summary, the hydroxylamine and nitrous acid data presented in this thesis in the absence of Fe(III) is consistent with the following explanation. Whilst $HAN/HNO_3/HNO_2$ chemistry is complex and there are many elementary reactions known to occur in these systems, the hydroxylamine profiles obtained during the hydrolysis of free AHA in the range 313-333K, as presented in Figure 4.32 A-C and collated in Figure 4.33 below, are expected to be determined largely by three overall reactions. The temperatures at which each reaction is likely to play a major role in the form of the $[NH_3OH^+]$ vs. time (t) plots in Figure 4.33 are shown next to each corresponding equation below.

$AHA \rightarrow NH_3OH^+ + CH_3COOH$	333K, 323K, 313K	(4.37)
$2HNO_3 + NH_3OH^+ \xrightarrow{HNO_2} 3HNO_2 + H_2O^+$	323K, 313K	(4.21)
$HNO_2 + NH_3OH^+ \rightarrow N_2O + H_2O + H_2O^+$	313K	(4.22)

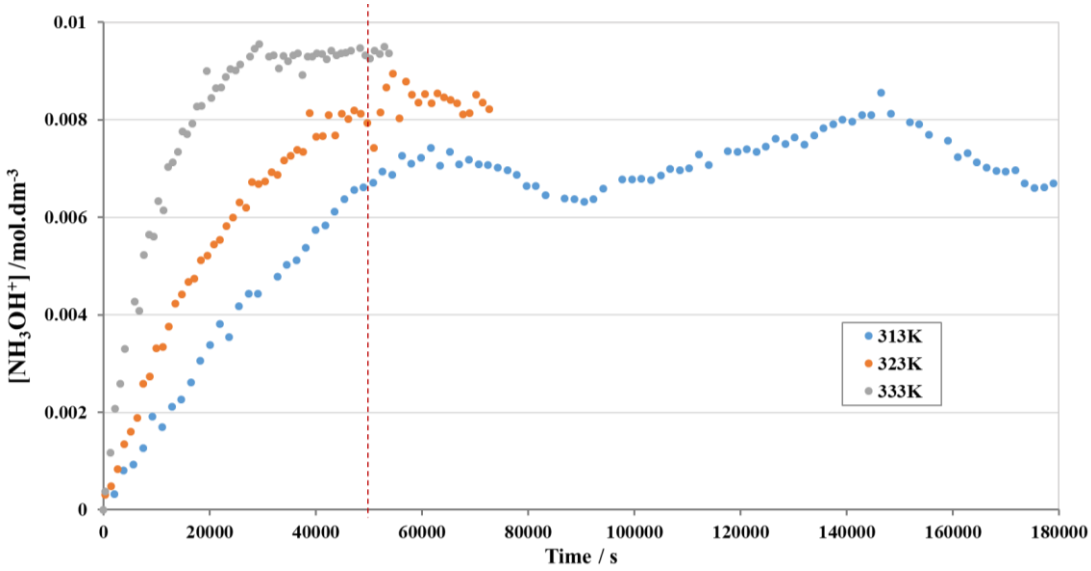

Figure 4.33: NH_3OH^+ ingrowth measured from the hydrolysis of 10 mmol dm^{-3} AHA at 313K (navy blue), 323K (light blue), and 333K (orange).

At all temperatures under study here, the initial ingrowth of hydroxylamine is determined by the rate of the hydrolysis of AHA (Eq. 4.37), which increases with increasing temperature. The oxidation of hydroxylamine by HNO_3, autocatalytic in HNO_2, does occur at high temperature but requires low $[NH_3OH^+]$. The competing scavenging reaction of hydroxylamine with HNO_2 requires and occurs at high $[NH_3OH^+]$. With these points in mind, the forms of the three $[NH_3OH^+]$ vs. time (t) plots in Figure 4.33 can be understood as follows. Taking a point on all the profiles at ~50,000s, the rapid ingrowth of hydroxylamine from AHA hydrolysis at 333K, results in very little visible effect of the reactions of Eqs. 4.21 or 4.22 on the final NH_2OH concentration. Whilst a small amount of hydroxylamine reacts with HNO_3 to produce HNO_2, the scavenging reaction of Eq. 4.22 dominates, inhibiting the possible autocatalysis and enabling the system to stay in the region above the line representing the boundary conditions shown previously in Figure 4.19 (section 4.3), where hydroxylamine is stable in HNO_3. Looking next at the profile at 323K on Figure 4.33,

hydroxylamine is produced from AHA hydrolysis at a slightly lower rate compared to that observed at 333K, but [NH_3OH^+] is still high enough to allow the scavenging reaction of Eq. 4.22 to dominate initially. After a point however, the [NH_3OH^+] starts to decline as the lower hydroxylamine concentrations compared to those observed at 333K start to facilitate and allow the reaction given by Eq. 4.21 to occur. At the lowest temperature of 313K, the much slower ingrowth of hydroxylamine from AHA hydrolysis means that whilst [NH_3OH^+] may still drive the scavenging reaction of Eq. 4.22, that reaction is not happening fast enough to suppress the reaction with HNO_3 (Eq. 4.21), so allowing a net autocatalytic loss of [NH_3OH^+] and visible increase in [HNO_2] by reaction 4.21.

Returning back to the graphs in Figure 4.32, a second observation is that the ingrowth of NH_3OH^+ is seen to be suppressed in the presence of increasing initial Fe(III) at all temperatures studied here. Data at the elevated temperatures of 333K and 323K show similar profiles, with the NH_3OH^+ concentration reaching approximately 60% of the theoretical maximum from AHA hydrolysis in the presence of 2.5 mmol dm^{-3} initial Fe(III), and ~40% with 10 mmol dm^{-3} initial Fe(III), within errors. In these datasets, the chemistry leading to the obtained HAN profiles appears therefore to be influenced to a greater extent by initial [Fe(III)] than temperature. This could be indicative of the reduction of Fe(III) by HAN which, along with the mechanistically analogous reduction of Pu(IV), is known to occur by a variable stoichiometry dependant on the initial ratio of the reactants [99].

While a reduction of Pu(IV) ions has been observed during the associated hydrolysis of the AHA complex [74, 82, 149], a similar reduction of ferric ions during Fe(III)-

AHA complex hydrolysis has not previously been seen. There are currently two candidates for the reducing agent in the Pu(IV)-AHA systems: AHA or its hydrolysis product NH_2OH. The current debate on this matter is based on: i) the observation that Pu(IV) may be reduced by NH_2OH whilst the analogous process for Fe(III) is strongly inhibited at high hydrogen ion concentrations such as those employed here [99], and ii) the suggestion that AHA itself may reduce Pu(IV) ions during complex hydrolysis [82]. Examination of the redox couple ladder shown previously in Figure 2.15 in Chapter 2, suggests that thermodynamically, AHA is only capable of reducing free Pu(IV) or $Pu(NO_3)^{3+}$ to Pu(III) and not AHA complexed Pu(IV) or free Fe(III) ions. In contrast, NH_2OH could reduce free Pu(IV), $Pu(NO_3)^{3+}$, AHA complexed Pu(IV), and free Fe(III) ions [81]. Hydroxylamine is well known as a good reductant for Pu(IV), particularly at low acidities [95, 170, 171]. Thus, whilst kinetically slow due to the above mentioned inhibition at high hydrogen ion concentrations, the possible influence of the analogous reduction of Fe(III) by hydroxylamine on the net rate of hydrolysis of AHA in the presence of Fe(III) was therefore further investigated by quantification of the Fe(II) product.

4.6 Techniques for Analysis of Fe(II)

From the experimental work presented in this thesis thus far, the oxidation of hydroxylamine by Fe(III) was hypothesized as a likely explanation for the inhibited ingrowth of NH_3OH^+ compared to acetate in these systems containing Fe(III). To this end, Fe(II) was quantified both after and during Fe(III)-complexed AHA hydrolysis,

via a spectroscopic and chromatographic method described in sections 4.6.1and 4.6.2 respectively.

4.6.1 Quantification by UV/Vis Spectroscopy

Spectrophotometry offers multiple advantages over other analytical methods for the quantitative determination of iron, including sensitivity, fidelity, rapidness, simplicity and low cost [172]. Some common spectroscopic methods employ 1,10-phenanthroline (phen) [124], 2,2'-bipyridine (byp) [173], and thiocyanate [174], and more recently, *o*-hydroxyhydroquinonephthalein (QP) [175]. In the analyses presented here, the method employing 1,10-phenanthroline was used as described in Chapter 3 section 3.7.1 in this Thesis, involving conversion of the absorbance measured at 511nm to a concentration of Fe(II) using the calibration curve of Figure 3.20. Some advantages of this method include; i) the colour intensity and stability of the orange-red complex with no fading observed for as long as six months [176], ii) the almost complete freedom of the method from interference by most of the common ions, iii) a high working sensitivity, and iv) colour formation in acid solution, eliminating difficulties caused by precipitation of metal hydroxides and hydrated oxides in alkaline solution

4.6.1.1 Measurements

This method was used to quantify Fe(II) after hydrolysis of 20 mmol dm^{-3} AHA for 24 hours at 333K in 0.3 mol dm^{-3} HNO_3 and $HClO_4$, in the presence of 12.5 and 25 mmol dm^{-3} Fe(III). The solution of excess Fe(III) in $HClO_4$ was also hydrolysed in an

inert N_2 atmosphere for comparison. An early study by Fortune and Mellon [177] examined the interferences from a large number of cations and anions on this method. The authors found no interference from acetate and concluded that the nitrite ion did not interfere when the pH of the solution was kept above 2.5. At lower pH values, they noted a brown colouration from the formation of nitrous acid. For the perchlorate ion, these authors noted an interference in the Fe(II) measurement of 1.2% up to a maximum concentration of 100 ppm (1 mmol dm^{-3}). For analysis of the hydrolysed AHA solutions described above, a significant dilution of the samples was required prior to analysis, to the extent that $HClO_4$ was present in a concentration of 1.2 mmol dm^{-3}. The concentration of perchlorate ion present in the samples in $HClO_4$ media were therefore only slightly above the maximum concentration suggested by Fortune and Mellon, and the error in these measurements was thus estimated at 1.2%. For those solutions in HNO_3, errors in measurements were unknown but have been estimated at 2.9% based on the measurement taken for [Fe(II)] from an initial solution of 12.5 mmol dm^{-3} Fe(III) and 20 mmol dm^{-3} AHA in 0.3 mol dm^{-3} HNO_3 calculated as an equivalent conversion of Fe(III) of 103% (see Table 4.8).

The final spectra obtained for all samples and the calculated Fe(II) concentrations in the original solutions, computed using the measured absorbance value at 511nm, are shown in Figure 4.34 and Table 4.8 respectively. All concentrations were determined in ppm and converted to units of mmol dm^{-3}.

Table 4.8: Initial hydrolysis conditions and final Fe(II) concentrations calculated from the spectra in Figure 4.34, including the percentage conversion of Fe(III) to Fe(II). Concentrations are given in mmol dm^{-3}.

Hydrolysis conditions			Measurements after hydrolysis	
Aqueous media	**[AHA]**	**[Fe(III)]**	**[Fe(II)]**	**% Fe(III) converted**
HNO_3	20	12.5	12.9	103 ± 3.0
HNO_3	20	25	24.0	96 ± 2.8
$HClO_4$	20	12.5	9.2	73 ± 0.87
$HClO_4$	20	25	17.6	70 ± 0.84
$HClO_4$ (under N_2)	20	25	17.8	71 ± 0.85

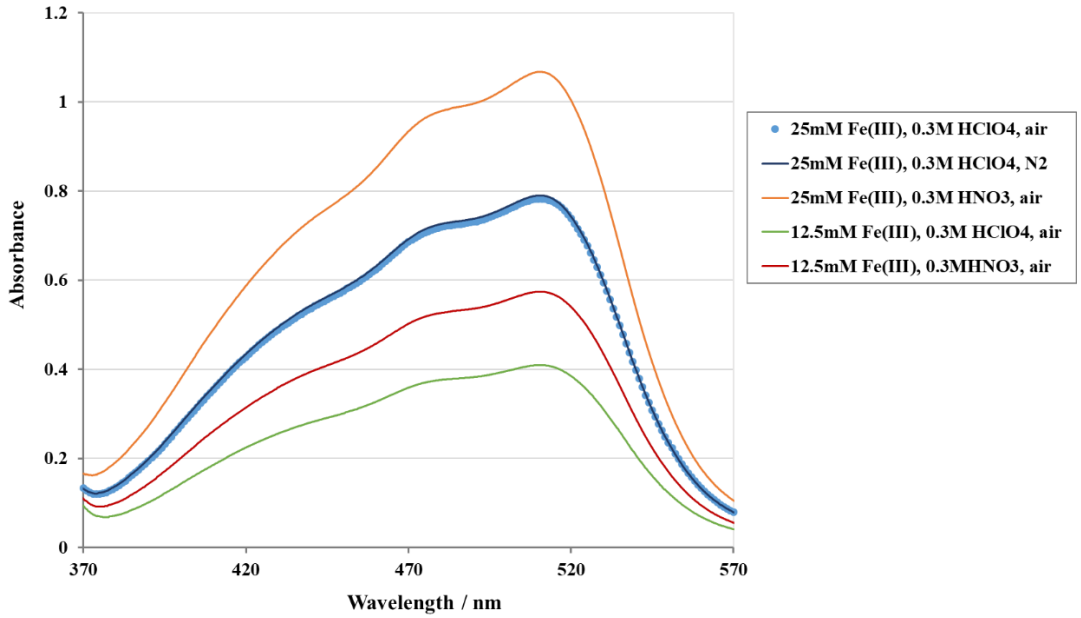

Figure 4.34: Spectra taken for diluted samples of solutions of 20 mmol dm^{-3} AHA post- hydrolysis in the presence of 25 mmol dm^{-3} or 12.5 mmol dm^{-3} initial Fe(III) in 0.3 mol dm^{-3} HNO_3 or $HClO_4$ media at 333K under oxidising (air) and reducing (N_2) atmospheres.

Inspection of Table 4.8 indicates that 100% of the initial Fe(III) had been reduced to Fe(II) by the end of the hydrolysis in HNO_3 media, regardless of the initial [Fe(III)], whereas an approximate conversion of 70% was seen for those solutions hydrolysed in $HClO_4$. For those experiments performed in $HClO_4$ with an initial [Fe(III)] of 25 mmol dm^{-3}, the spectra of the resulting solution after hydrolysis in both oxidising and

inert atmospheres were found to be near identical, and have therefore been plotted on Figure 4.34 as singular points and a smooth line respectively, for ease of visualisation. The similarity in the measurements suggests that re-oxidation of the Fe(II) back to Fe(III) is not occurring in $HClO_4$ media, and the process of Fe(III) reduction in these solutions is not affected by the atmospheric conditions.

For initial solutions of 20 mmol dm^{-3} AHA and 25 mmol dm^{-3} total Fe(III) in HNO_3 and $HClO_4$, previous titrimetric analyses (see section 4.5.1) had given post-hydrolysis measurements for NH_2OH of approximately 10 and 13 mmol dm^{-3} respectively. Pairing this previous analysis with the results presented here gives apparent losses of NH_2OH and Fe(III) of approximately 50% and 100% respectively in HNO_3, which suggests the likelihood of the reduction of Fe(III) by NH_2OH via a 2:1 stoichiometry as shown previously in Eq. 4.24b in section 4.5.1.1. In contrast, measurements in $HClO_4$ show a loss of NH_2OH and corresponding reduction of Fe(III) of approximately 65% and 70% respectively in $HClO_4$, which is suggestive of the reduction of Fe(III) by NH_2OH via a 1:1 stoichiometry as shown in Eq. 4.24a in section 4.3.

Xu *et al* [178] noted the dominant role of the reaction media on the oxidation of hydroxylamine by Ce(IV) in determining the reaction kinetics, mechanism and product(s). In comparison to previous studies conducted by these authors in HNO_3 and H_2SO_4 media, they concluded that the exact mechanism was dependent on the reaction media and that a different rate law operated in $HClO_4$ media than did in HNO_3 or H_2SO_4. This could explain why a smaller conversion of the initial Fe(III) to Fe(II) of approximately 70% is seen in the solution in $HClO_4$ media compared the 100% conversion observed in analogous solutions in HNO_3 media.

Whilst this spectroscopic analysis confirms the occurrence of Fe(III) reduction in the AHA systems here, further analysis is required to understand the mechanism by which this proceeds. The next section therefore describes the results of studies of Fe(III)-complexed AHA systems whereby Fe(II) was quantified in real-time by ion chromatography, with the aim to provide data that can aid in understanding Pu(III) ingrowth seen during Pu(IV)-complexed AHA hydrolysis.

4.6.2 Real-time Quantification by Ion Chromatography

Using the same initial conditions as studied in previous analyses of acetate nitrite and protonated hydroxylamine by IC, the ingrowth of Fe(II) was quantified throughout the Fe(III)-complexed AHA hydrolysis reaction. This would complete a library of data on the ingrowth of the key species in the Fe(III)-complexed AHA systems, and aid in understanding the major chemistry occurring in this system as a non-active analogue to the Pu(IV)-AHA system.

4.6.2.1 Limit of detection

The value of λ^0 for Fe^{2+} is reported as 108.0 S cm^2 mol^{-1} [153], approximately double that of the NH_3OH^+ ion. An equivalent concentration of Fe(II) would thus produce a proportionally greater peak in the chromatogram. However, from inspection of the standard chromatograms used in the creation of the calibration curve in Figure 4.35, (see Figure 3.23 in Chapter 3 for an example chromatogram), the average value for the baseline noise was estimated as 8×10^{-3} µS cm^{-1}, nearly 3 times greater than an average value of 3×10^{-3} µS cm^{-1} estimated for the analysis of NH_3OH^+. The dominant factor

in the comparatively greater noise is likely the flowrate of the eluent, which also heightens the likelihood of bubble formation, and is approximately double that required in the analysis of NH_3OH^+. From the calibration function shown in Figure 4.35, estimates of 0.31 and 1.0 mmol dm^{-3} can be calculated for the LOD and LOQ respectively (see section 4.4.1.1 for definitions of LOD/LOQ).

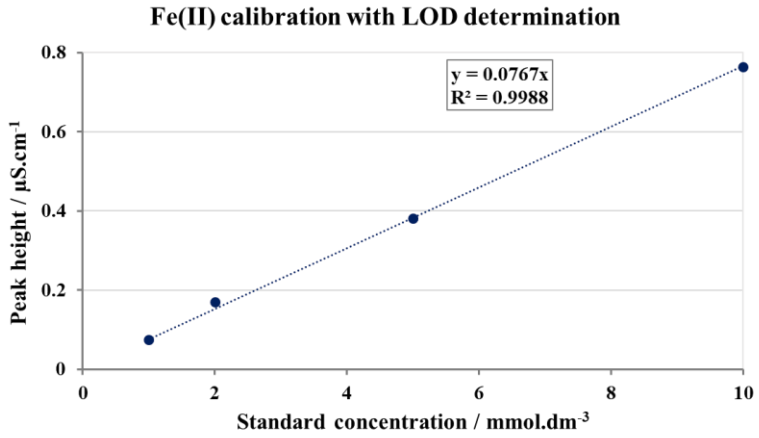

Concentration / mmol dm^{-3}	Peak height / µS.cm^{-1}
1	0.075
2	0.171
5	0.382
10	0.764

Figure 4.35: Calibration of peak height in µS.cm^{-1} against the concentration of a Fe(II) standard in mmol dm^{-3}.

4.6.2.2 Hydrolysis studies

Measurements of Fe(II) concentrations vs. t are shown in Figure 4.36 for the hydrolysis of 10 mmol dm^{-3} AHA hydrolysis in the presence of 2.5 and 10 mmol dm^{-3} Fe(III) at 313, 323 and 333K. Errors taken as the RSD value from the respective calibration. The ingrowth of Fe(II) throughout the course of complexed AHA hydrolysis was observed to occur under all experimental conditions studied here, and the shape of the resulting profile was found to be consistent throughout the range of experiments conducted.

Inspection of Figure 4.36 shows a rapid ingrowth during the initial stages of the hydrolysis reaction, after which the rate of Fe(II) production then gradually slows with

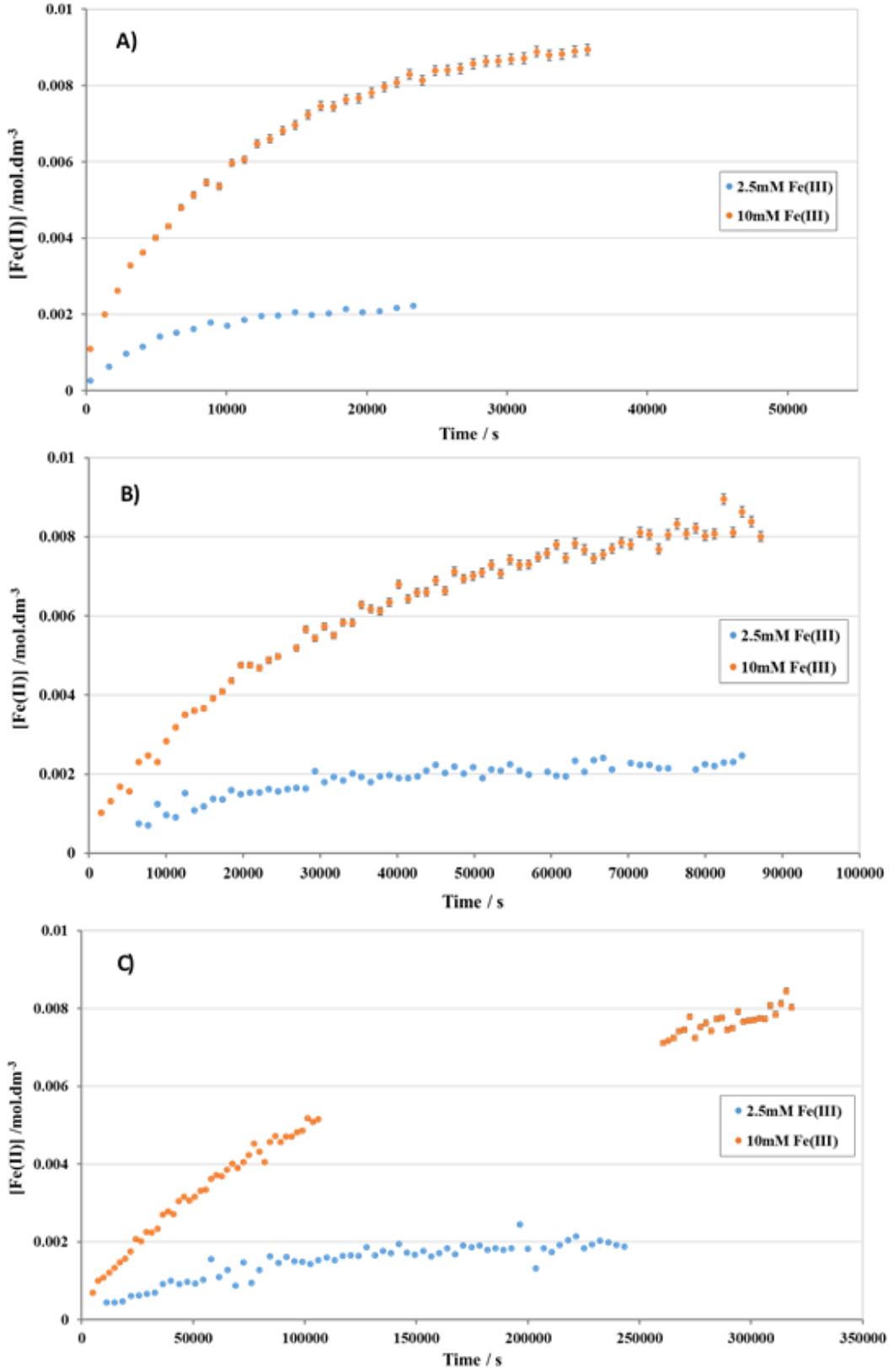

Figure 4.36: Fe^{2+} ingrowth measured from the hydrolysis of 10 mmol dm^{-3} AHA with initial [Fe(III)] = 2.5 mmol dm^{-3} (light blue), and 10 mmol dm^{-3} (orange) at temperatures of A) 333K, B) 323K and C) 313K. For the data obtained at 3131K with 10 mmol dm^{-3} initial Fe(III), a system fault overnight caused a large stoppage period in data acquisition in which the IC system had to be cleaned, re-equilibrated and put back into operation. Errors bars are shown as the RSD value from the respective calibration.

increasing reaction time. This is analogous to the observed profile for the ingrowth of Pu(III) during the hydrolysis of the associated AHA complex as reported by several authors [74, 82, 149].

The rapid rate at which the Fe(II) was seen to grow in meant that the majority of the obtained measurements were above the LOQ, despite this value being higher than estimated in previous anion and cation analyses. The required higher eluent usage resulted in comparatively shorter analytical runs and thus fewer measurements were collected for each system, but despite this, the conversion of Fe(III) to Fe(II) is seen to reach 80-100% in all cases. The experiments with lower initial Fe(III)/AHA ratios of 0.25 reached 100% conversion, whereas those with higher a Fe(III)/AHA ratio of 1 reached between 80-90%. This observation is in agreement with studies by other authors following the ingrowth of Pu(III) in 1 mol dm^{-3} HNO_3 in the presence of AHA [74, 149] whereby lower conversion of Pu(IV) to Pu(III) was observed at higher initial Pu(IV)/AHA ratios.

During the hydrolysis of FHA and AHA in up to 2 mol dm^{-3} HNO_3, Carrott *et al.* [74] noted a variable induction period for the ingrowth of Pu(III) at 278 – 303K, which disappeared at 323K, and initially suggested that the reductant for Pu(IV) was likely HAN, with reduction starting only once HAN reaches a significant concentration. The slower hydrolysis rates of FHA compared to AHA observed by these authors, i.e. they report rate constants for the hydrolysis of FHA and AHA under conditions of 1 mol dm^{-3} H^+ of 2.5 x 10^{-4} min^{-1} and 2.1 x 10^{-3} min^{-1} respectively at 298K, were thought to result in the observation of longer induction periods for experiments involving the former hydroxamic acid. To test their hypothesis, the authors did not however attempt

to quantify HAN during the hydrolysis, and instead noted that the addition of up to 1 mol dm^{-3} HAN to the initial reaction mixture had little discernible effect on the induction period; in agreement with a similar observation made by Karraker [179]. Combining their kinetic data with electrochemical data led them to conclude that, although thermodynamically capable, HAN is likely not the reductant in Pu(IV)-XHA systems due to steric effects that kinetically hinder the reduction with HAN.

By combination of the data presented here with that of the previous IC analyses for acetate and hydroxylamine, it seems apparent however that the reductant for Fe(III) in these Fe(III)-AHA systems is indeed hydroxylamine. Figure 4.37 shows the data obtained for the ingrowth of NH_3OH^+ and Fe(II) in the Fe(III)-containing systems at 323K. The NH_3OH^+ measurements obtained in the absence of initial Fe(III) are also shown in each plot as a reference. Inspection of Figure 4.37 shows a point close to approximately 40,000 seconds where the concentration of Fe(II) and the difference between the measured concentration of NH_3OH^+ obtained in the absence of Fe(III) compared to its presence, fit well for the 1:1 stoichiometry Fe(III):HAN reactions for the lower and higher initial [Fe(III)] of 2.5 and 10 mmol dm^{-3}. This is marked by the red dotted line. This, and the shape of the Fe(II) profiles more generally match well with what is expected if HAN were the reductant.

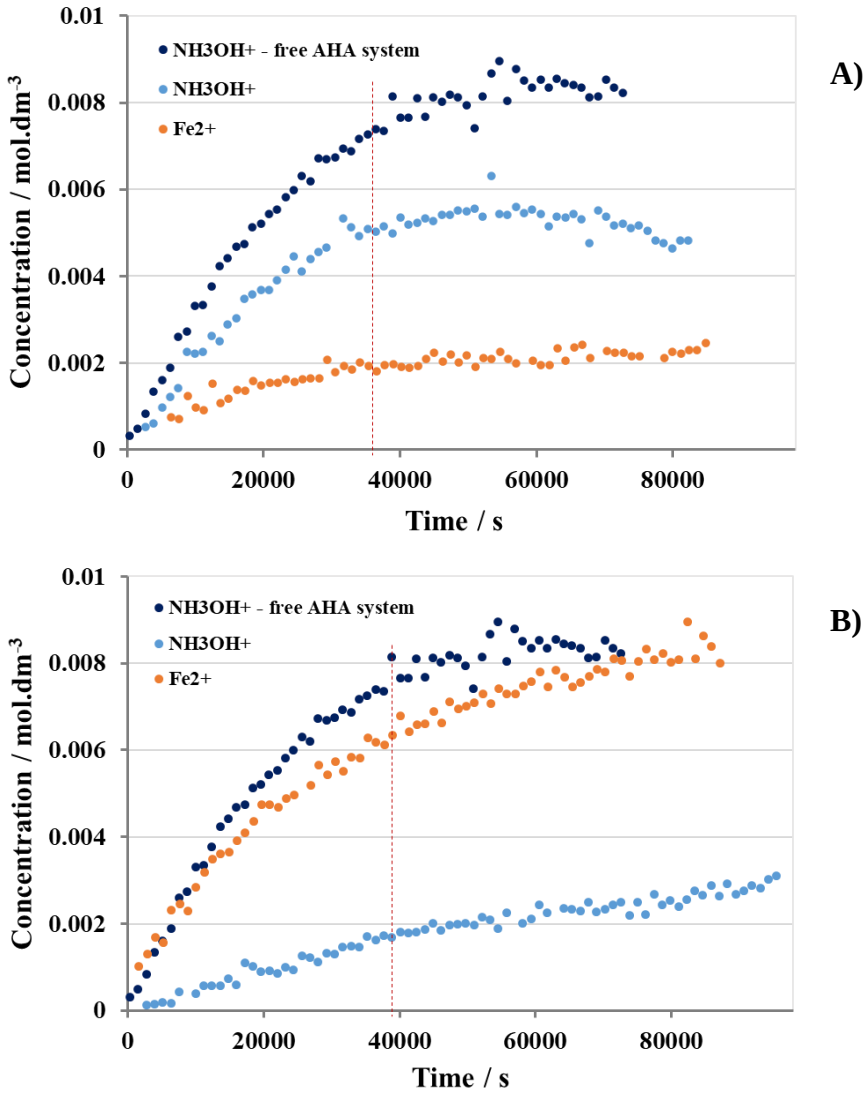

Figure 4.37: Plots of NH_3OH^+ (light blue) and Fe^{2+} (orange) ingrowth measured by IC during the hydrolysis of 10 mmol dm^{-3} AHA in 0.1 mol dm^{-3} HNO_3 at 323K for an initial concentration of Fe^{3+} of A) 2.5 mmol dm^{-3} and B) 10 mmol dm^{-3}. The measurements of NH_3OH^+ for the same system in the absence of initial Fe^{3+} is plotted as a reference (dark blue).

Thus, as a final set of experiments to determine the likelihood of HAN being the reductant in the systems under study here, the ingrowth of Fe(II) was followed from the reduction of Fe(III) by hydroxylamine in the absence of AHA hydrolysis, but under the same conditions of the IC experiments shown in Figure 4.37, i.e. at 323K in 0.1 mol dm^{-3} HNO_3. Before reporting on these final experiments however, it is useful to summarise the literature pertaining to the reduction of Fe(III) by hydroxylamine.

An early study on the reduction of Fe(III) by HAN in 0.1 mol dm^{-3} $HClO_4$ was performed by Bengtsson [180], in which the author observed an inhibiting effect of Fe(II). Barney [95] later performed the first study of the reduction of Pu(IV) by hydroxylamine, defining a rate expression in 1.5 – 2.5 mol dm^{-3} HNO_3, by varying the acid concentration and HAN/Pu ratio, and keeping the total ionic strength (*I*) constant at 2.5 by the addition of $NaClO_4^-$. The rate law is shown in Eq. 4.38 below. They noted a large dependence of the [Pu(IV)]/[Pu(III)] ratio on the rate due to a rate-suppressing effect of the reduced Pu(III), which he attributed to a back reaction of Pu(III) with a key intermediate in the HAN driven Pu(IV) reduction process, NH_2O (see section 4.6.3 below), and suggested an analogous mechanism would explain the inhibiting effect of Fe(II) on the reduction of Fe(III) [180].

$$-\frac{d[Pu^{4+}]}{dt} = k' \frac{[Pu^{4+}]^2[NH_3OH^+]^2}{[Pu^{3+}]^2[H^+]^4(K_d + [NO_3^-])^2} \tag{4.38}$$

Whilst Carrot *et al.* [74] found they were unable to fit Barney's kinetics [95] to their data, the HAN/Pu(IV) ratios likely present after the induction period would be much higher than those studied by Barney, whose rate expression was sufficient to describe the initial rate of reaction for high [HAN]/[Pu(IV)] ratios in the range of 4-16. A re-examination of Barney's work was then later performed by Koltunov and Zhuravleva [170], with HAN in large excess. The authors derived a similar rate equation with the exception of any nitrate dependence, since this was not varied in their study. Fewer kinetic studies have been performed at low [HAN]/[Pu(IV)] or [HAN]/[Fe(III)] ratios due to difficulties in rate measurement. One study by Yarbro *et al.* [98] investigated the effects of $[H^+]$, $[NO_3^-]$, [Pu(IV)]/[Pu(III)] and [HAN] on the reaction rate,

performing a few experiments at [HAN]/[Pu(IV)] ratios as low as 0.09. These authors fit their data with an expression in terms fractional conversion of Pu(IV) to Pu(III) rather than actual concentrations. The conditions studied by all these authors are summarised in Table 4.9.

Table 4.9: Comparison of conditions studied by several authors for the reduction of Pu(IV) or Fe(III) by HAN and assumed metal:HAN stoichiometric reaction under study..

Reference	**R = [HAN]/[Metal]**	**Media**	***Ionic strength (I) / mol dm^{-3}***	***Assumed Metal:HAN stoichiometry***
[95]	$4 \leq R \leq 16$ Metal = Pu^{4+}	$1.5 \leq [HNO_3] \leq 2.5$	2.5	1:1
[170]	R = 40 Metal = Pu^{4+}	$0.985 \leq [H^+] \leq 2.8$	3	1:1
[98]	$0.09 \leq R \leq 3.58$ (Most at $R \leq 1.7$) Metal = Pu^{4+}	$0.7 \leq [HNO_3] \leq 2.4$	2.5	n/a
[180]	$2.25 \leq R \leq 17.5$ Metal = Fe^{3+}	0.100M $HClO_4$	1.0 – 1.3	2:1
[99]	$0.1 \leq R \leq 5$ Metal = Fe^{3+}	0.100M $HClO_4$	1	1:1

The most recent work by Bengtsson *et al.* [99] on the kinetics of the reduction of Fe(III) by HAN confirmed an analogous mechanism and rate expression to that derived by Barney [95] for the Pu system for the high [HAN]/[Fe(III)] ratios where the 1:1 stoichiometry reaction dominates. Using a steady state approximation these authors also derived a separate kinetic expression for the 2:1 stoichiometry pathway but could not verify it with experimental data. Whilst mechanistically analogous to Pu(IV) reduction, they concluded that kinetic hinderances resulted in requirement of very high temperatures and/or high [Fe(III)]/[HAN] ratios of at least 5-10 fold for Fe(III) reduction to proceed purely via a 2:1 stoichiometry, and we shall return to this point

below. The derived rate laws for the 1:1 and 2:1 stoichiometry reactions are shown in Eqs. 4.39 and 4.40 respectively, where *B, B'* and *C* are combinations of various elementary rate constants, stability and equilibrium constants.

$$-\frac{d[Fe^{3+}]}{dt} = B\frac{[Fe^{3+}]^2[NH_3OH^+]^2}{[Fe^{2+}]^2[H^+]^4} \tag{4.39}$$

$$-\frac{d[Fe^{3+}]}{dt} = B'\frac{[Fe^{3+}]^2[NH_3OH^+]}{[Fe^{2+}][H^+]^2 + C[Fe^{3+}][H^+]} \tag{4.40}$$

Having discussed the available literature relevant to the reduction of Fe(III) by hydroxylamine, the next section will discuss final IC experiments conducted to study the time evolution of [Fe(II)] from solutions of varying [Fe(III)]/[NH_2OH] ratios, including higher ratios where it is suggested that the 2:1 reaction may operate.

4.6.2.3 Studies on the Reduction of Fe(III) by HAN.

As final IC experiments, aiming to aid our understanding of the ingrowth of Fe(II) seen during the hydrolysis of Fe(III)-complexed AHA, Fe(II) ingrowth was followed whilst heating solutions of Fe(III) and hydroxylamine in 0.1 mol dm^{-3} HNO_3 at 323K, with [Fe(III)]/[NH_2OH] ratios in the range of 1 – 10. The aim of following these solutions at high temperatures and the high [Fe(III)]/[NH_2OH] ratios of 5 and 10 suggested by Bengtsson *et al.* [99], was to determine whether or not the occurrence of the 2:1 stoichiometry pathway in this system was viable.

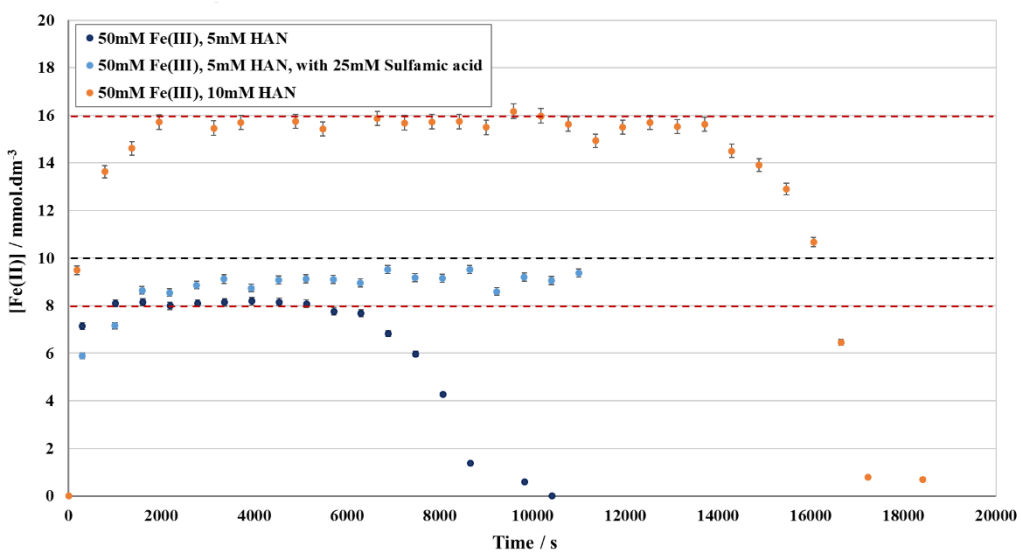

Figure 4.38: Ingrowth of Fe(II) from solutions of Fe(III):HAN in initial ratios of i) 50:5 mM (10:1), ii) 50:5 mM (10:1) in the presence of additional sulfamic acid, and iii) 50:10 mM (5:1). Dotted lines show the maximum concentration reached, with black and red representing 100% and 80% respectively of the theoretical maximum based on a purely 2:1 stoichiometry reaction. Errors bars are shown as the RSD value from the respective calibration.

The results are shown in Figure 4.38, observation of which shows that the initial rate of reaction was very rapid, with the concentration of Fe(II) increasing at a rate far above what can be measured by this technique. In the solutions with 5 and 10-fold excess Fe(III) in the absence of sulfamic acid, the Fe(II) concentration soon levelled off to reach a maximum of 80% of that expected for a complete reaction consistent with a 2:1 stoichiometry. Once this level was reached, the Fe(II) concentration remained steady for some time before falling sharply to zero, presumably as a result of re-oxidation of Fe(II) by HNO_2 [117], the latter species generated by Eq. 4.26 and 4.28. The same reason was suggested by Carrott *et al* [74] for the observation of a reduction of Pu(IV) to Pu(III) followed by a rapid re-oxidation at long timescales in the Pu/AHA system, shown in Figure 4.39.

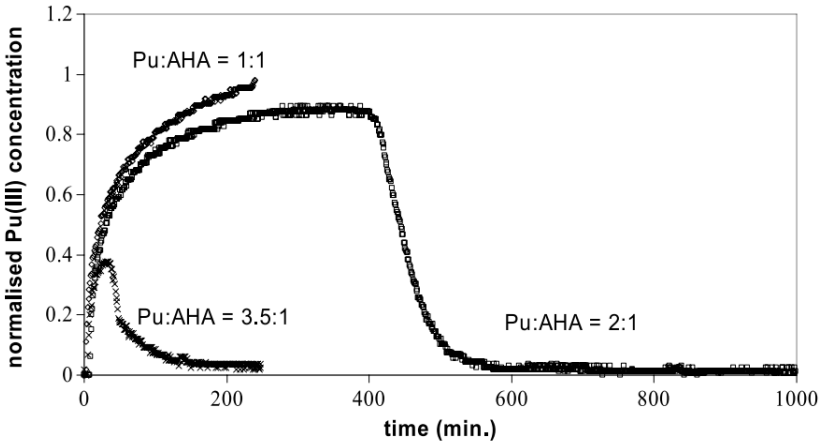

Figure 4.39: Plot of the Pu(III) concentration (measured by UV-Vis electronic absorption spectroscopy and normalised to initial P(IV)) vs time during Pu(IV)-AHA hydrolysis, showing the reduction of Pu(IV) at low molar AHA: Pu ratios ([Pu] = 1 g L^{-1}; [HNO_3] = 1 mol dm^{-3}; [AHA] = 0.0042–0.001 mol dm^{-3}; T = 298K) [74] (reproduced under Creative Commons License through Lancaster University).

This explanation for the behaviour at long time in the Fe/AHA system was confirmed by a repeat experiment with the addition of sulfamic acid as a HNO_2 scavenger to the solution with 5-fold excess Fe(III), which removed the rapid re-oxidation of Fe(II) by HNO_2. As an additional observation for this particular experiment, the concentration of Fe(II) climbed towards twice that of the initial NH_2OH, or 100% of that expected, for a complete reaction via the 2:1 stochiometric pathway.

Lower ratios of [Fe(III)]/[NH_2OH] of 2:1 and 1:1 were also measured under the same temperature and [HNO_3] conditions, with the expectation that the dominant pathway under these conditions would be the 1:1 stoichiometry. The Fe(II) profiles obtained under these conditions are shown in Figure 4.41.

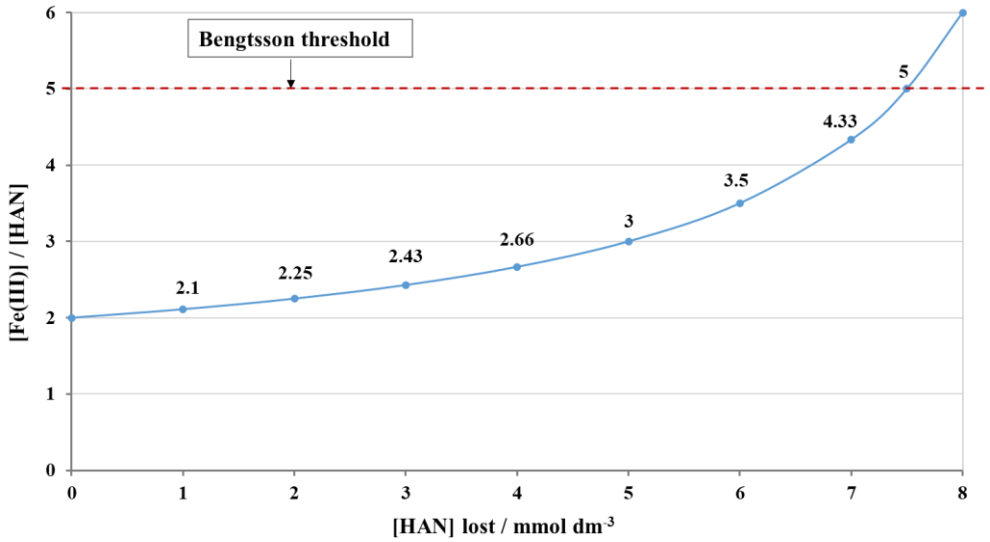

Figure 4.40: Plot showing the [Fe(III)]/[HAN] ratio as a function of loss of HAN concentration for a system with initial composition of 20 mmol dm^{-3} Fe(III) and 10 mmol dm^{-3} HAN, reacting with a 1:1 stoichiometry.

However, the experiment with an initial [Fe(III)]/[NH_2OH] ratio of 2 climbed to approximately 80% of the theoretical maximum based on a 2:1 stoichiometry. This is most likely due to the reaction starting off and proceeding in accordance with a 1:1 stoichiometry but then transitioning to a 2:1 stoichiometry as the [Fe(III)]/[NH_2OH] ratio increases as the reaction proceeds. This is illustrated in Figure 4.40 which shows the Fe(III)/NH_2OH ratio as a function of loss of NH_2OH concentration for a system with an initial composition of 20 mmol dm^{-3} Fe(III) and 10 mmol dm^{-3} HAN, reaction with a 1:1 stoichiometry. For the initial [Fe(III)]/[NH_2OH] ratio of 1, the Fe(II) concentration was seen to reach 100% of that expected for complete reaction via a 1:1 stoichiometry.

As can be seen in Figure 4.40, the Bengtsson threshold for a [Fe(III)]/[HAN] ratio of 5, above which a 2:1 stoichiometry will dominate, is achieved after 7.5 mmol dm^{-3} of Fe(III) and HAN have reacted away in accordance with a 1:1 stoichiometry. This point is obtained at <1000s in Figure 4.41, implying that the majority of the data obtained at

an initial solution composition of 20 mmol dm^{-3} Fe(III) and 10 mmol dm^{-3} HAN in Figure 4.41 has been generated in accordance with 2:1 Fe(III):HAN stoichiometry, with the ratio then being determined by Eq. 4.41.

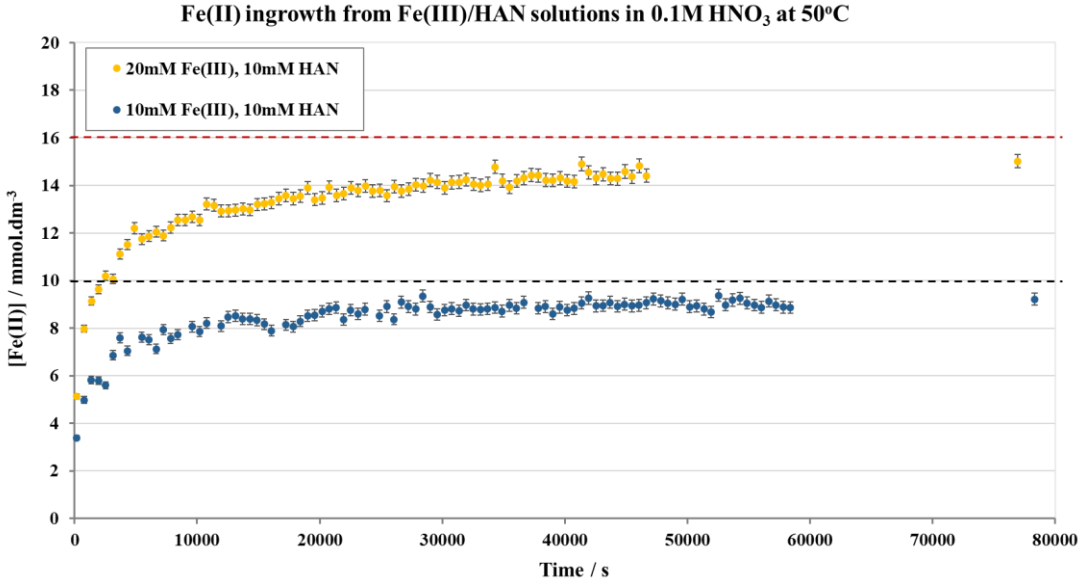

Figure 4.41: Ingrowth of Fe(II) from solutions of Fe(III):NH_2OH in initial ratios of i) 20:10 mM (2:1), and ii) 10:10 mM (1:1). Dotted lines show the maximum concentration reached, with black and red representing 100% and 80% respectively of the theoretical maximum based on purely 1:1 and 2:1 stoichiometry reactions. Errors bars are shown as the RSD value from the respective calibration. A final point in each dataset was taken some time after completion of the main experimental run to check the trajectory of the Fe(II) ingrowth profile.

Consistent with the form of Eq. 4.39, for the initial [Fe(III)]/[NH_2OH] ratio of 2:1 investigated, the observed initially rapid reduction and gradual decrease in rate as the reaction proceeds is consistent with the observation that Fe(II) inhibits the reduction by NH_2OH as it is produced [180], analogous to the inhibition of the Pu(IV) reduction by Pu(III) [95]. The shape of these profiles for Fe(II) ingrowth is also consistent with that obtained during the hydrolysis of Fe(III)-complexed AHA. Before concluding however that hydroxylamine was the reductant for Fe(III) in these systems, a final validity check was conducted by investigation of the underlying mechanism and thermodynamics.

4.6.3 Examining the mechanism of iron(III) reduction by HAN

The 1:1 mechanism for Pu(IV) reduction by HAN was first suggested by Barney [95] to be a two-step process whereby i) the reduction of the $PuOH^{3+}$ cation by NH_2OH to form Pu^{3+} and the aminoxyl radical species H_2NO^* rapidly approaches an equilibrium condition, and ii) the so-formed unstable radical H_2NO^*also undergoes a dimerization which becomes the final rate-controlling step to yield water and N_2 as the exclusive nitrogen-containing species as end-products. An analogous mechanism for the reduction of Fe(III) by HAN was suggested by Bengtsson and co-workers [99] and is outlined in Eqs. 4.41 – 4.44. For the 2:1 reduction of Fe(III) by HAN, reaction of the H_2NO^* aminoxyl radical instead with Fe(III) is suggested to produce HNO via Eq. 4.45, which can itself dimerize to produce N_2O as a product. These dimerization reactions for H_2NO^* and HNO, described by Eqs. 4.44 and 4.46, are the rate-determining steps in the reduction of Fe(III) by HAN in a 1:1 and 2:1 stoichiometry respectively.

$$NH_3OH^+ \overset{K_a}{\rightleftharpoons} NH_2OH + H^+ \tag{4.41}$$

$$Fe^{3+} + NH_2OH \overset{\beta_1'}{\rightleftharpoons} Fe(NH_2OH)^{3+} \tag{4.42}$$

$$Fe(NH_2OH)^{3+} \rightleftharpoons Fe^{2+} + H_2NO^* + H^+ \tag{4.43}$$

$$2H_2NO^* \rightarrow N_2 + 2H_2O \tag{4.44}$$

$$Fe^{3+} + H_2NO^* \rightleftharpoons Fe^{2+} + HNO + H^+ \tag{4.45}$$

$$2HNO \rightarrow N_2O + H_2O \tag{4.46}$$

The thermodynamic properties of the aminoxyl radical, the one-electron oxidation product of hydroxylamine, were studied by Lind and Merenyi [181], who calculated a standard potential of $E^0(H_2NO^*, H^+ / H_2NOH) = 0.90V$ using the experimental data for Pu(IV) [95] and Fe(III) [99] reduction by HAN.

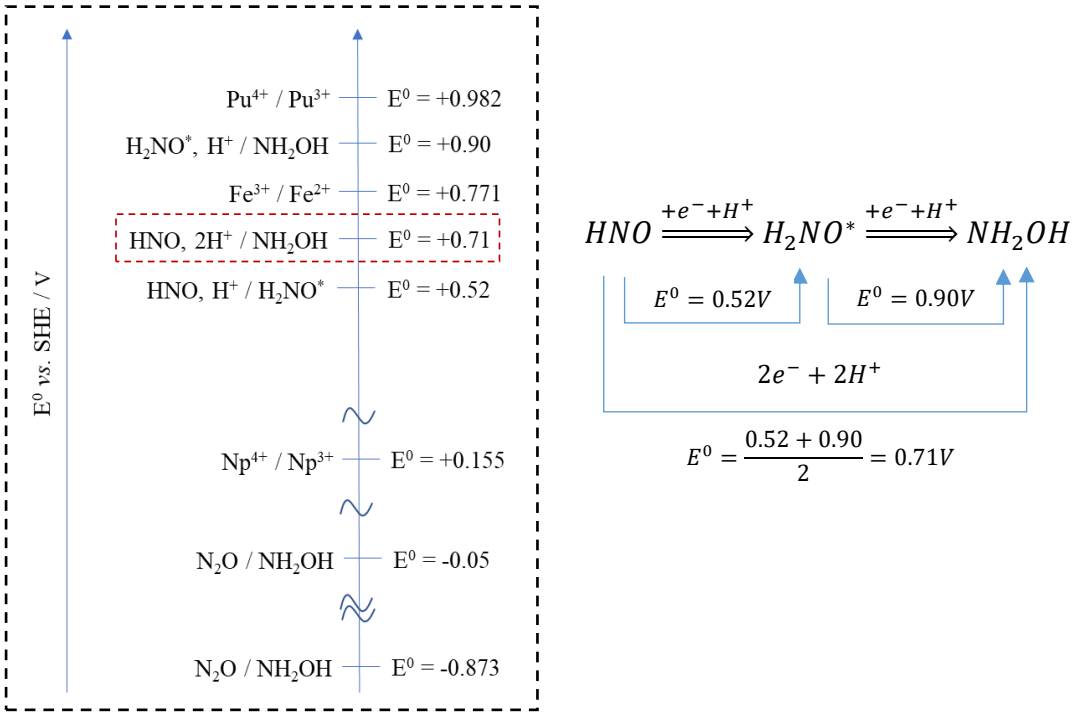

Figure 4.42: Redox ladder showing standard Pu(IV)/Pu(III), Fe(III)/Fe(II) and Np(IV)/Np(III) couples and those relating to NH_2OH, including an illustration of the calculating of the redox potential for the 2-electron oxidation of HNO to NH_2OH..

Figure 4.42 shows a redox ladder incorporating, inter alia, the standard redox potentials for the Pu(IV)/Pu(III), Fe(III)/Fe(II) and H_2NO^*/H_2NOH couples. Inspection of this ladder indicates that Pu(IV) is thermodynamically capable of oxidising NH_2OH to H_2NO^* but Fe(III) is not i.e. hydroxylamine may appear to be incapable of reducing Fe(III). The implication of this observation is that hydroxylamine will be capable of reducing Pu(IV) to Pu(III) in accordance with the 1:1 mechanism described by Pu redox equations analogous to those given in Eqs 4.41-

4.44 – but may be incapable of reducing Fe(III) in an analogous manner. In light of this, it is informative to broaden this discussion in three ways:

i) To include the thermodynamics of the 1 electron oxidation of the unstable radical that plays a key role in the 2:1 mechanism i.e. Eq 4.45,

ii) To move away from the standard redox potentials to the actual redox potentials that will obtain as a function of the concentration of key solution species, and

iii) To include Np(IV) which has long been considered a non-oxidising cation in terms of its interaction with AHA i.e. it is reduced by neither AHA or its hydrolysis product hydroxylamine, even though the standard redox potential for the Np(IV)/Np(III) couple is +0.155 V and the redox potential for the N_2O/NH_2OH and N_2/NH_2OH couples are -0.05 and -0.873 V respectively [182].

Addressing point (i) first, in the context of the hydroxylamine oxidation process described by Eqs. 4.41-4.44, H_2NO^* is unstable and may deprotonate to yield HNO^{-*}. This is a radical species that has been shown to be oxidisable, e.g. by O_2, to form the more stable nitroxyl species (HNO), even at high acidities down to and below pH 0 [181]. If the oxidant under consideration here (Pu(IV), Fe(III) or Np(IV)) is in large excess, it can also react with H_2NO^* to produce HNO, the dimerization of which produces N_2O as the end-product via the 2:1 mechanism. From the same study, Lind and Merényi [181] calculated a value of $E^0(HNO, H^+ / H_2NO^*) = 0.52V$. Using this value in combination with $E^0(H_2NO^*, H^+ / H_2NOH) = 0.90V$, a value of $E^0(HNO, 2H^+ / H_2NOH) = 0.71V$ can be calculated for the 2-electron oxidation of NH_2OH to HNO

(see Figure 4.42) i.e. the overall hydroxylamine oxidation reaction that dominates in the 2:1 mechanism. Placing this on a redox ladder as illustrated in Figure 4.42 indicates that both Fe(III) and Pu(IV) are capable of oxidising H_2NO^* to HNO, so providing a thermodynamic explanation of the observed reduction by the 2:1 mechanism of both Fe(III) and Pu(IV) by NH_2OH. Similarly, and addressing point (iii), this also explains why Np(IV) is non-reducible by the 2:1 mechanism as it can be seen from Figure 4.42 that Np(IV) is incapable of oxidising H_2NO^* to HNO or NH_2OH to H_2NO^* in the first place for that matter, although we shall address this point in more detail below.. However, this does not explain the apparent thermodynamic incapability of hydroxylamine to reduce Fe(III) in accordance with the 1:1 mechanism i.e solely by Eqs. 4.41-4.44.

Using the standard E^0 values and Eqs. 4.47 and 4.48, where based upon the overall stoichiometries of Eqs. 4.41-4.43 we assume that at short reaction times $[Fe^{2+}] \approx [H_2NO^*]$, values of the redox potentials E may be calculated for both the Fe^{3+}/Fe^{2+} and H_2NO^*/ NH_2OH couples as a function of $[H_2NO^*]$, for the specific pHs, temperatures, Fe(III) and NH_2OH concentrations employed in this study. The redox potentials for each couple may then be compared with each other at any one $[H_2NO^*]$ value to determine the range of $[H_2NO^*]$ values over which hydroxylamine is thermodynamically capable of reducing Fe^{3+} to Fe^{2+}. An analogous process can be followed for the 1 electron reduction of Np(IV) using Eq. 4.49 – so again addressing point (iii) above. The resultant E values for all three systems, plotted as a function of $[H_2NO^*]$ for a system of 0.1 mol dm^{-3} H^+ at 313K, 323K and 333K are shown in Figure 4.43.

$$E(NH_2O^*/NH_2OH) = E^0 + \frac{RT}{F}\ln\frac{[H_2NO^*][H^+]}{[NH_2OH]} \quad (4.47)$$

$$E(Fe^{3+}/Fe^{2+}) = E^0 + \frac{RT}{F}\ln\frac{[Fe^{3+}]}{[Fe^{2+}]} \approx E^0 + \frac{RT}{F}\ln\frac{[Fe^{3+}]}{[H_2NO^*]} \quad (4.48)$$

$$E(Np^{4+}/Np^{3+}) = E^0 + \frac{RT}{F}\ln\frac{[Np^{4+}]}{[Np^{3+}]} \approx E^0 + \frac{RT}{F}\ln\frac{[Np^{4+}]}{[H_2NO^*]} \quad (4.49)$$

The data of Figure 4.43 is instructive. According to these calculations, as long as H_2NO^* has a concentration of less than ~1 mmol dm^{-3}, it is thermodynamically possible for NH_2OH to reduce Fe(III) via a 1 electron transfer to form H_2NO^* and Fe(II) respectively i.e. via the 1:1 mechanism; however, a concentration of H_2NO^* of less than ~0.1 µmol dm^{-3} would be required before it would be thermodynamically possible for NH_2OH to reduce Np(IV). The concentration of a radical species is expected to be low, however it is not unreasonable to assume that a concentration of H_2NO^* greater than 0.1 µmol dm^{-3} is plausible. These calculations therefore suggest that a mechanism involving a radical species, analogous to that suggested for the reduction of Pu(IV), could explain the occurrence of the reduction of Fe(III) by hydroxylamine observed here during Fe(III)-complexed AHA hydrolysis i.e. the reduction of Fe(III) by hydroxylamine is possible by both the 2:1 and 1:1 mechanisms described by Barney. The same calculations indicate that Np(IV) may not be reduced by hydroxylamine by either mechanism. Thus, whilst this analysis confirms that the current definition of Np(IV) as a complexing but non-oxidising metal ion with regards to AHA may still hold (as evidenced by the work of Edwards *et al*. [58]), the same definition of Fe(III) requires revision based on the results presented in this thesis.

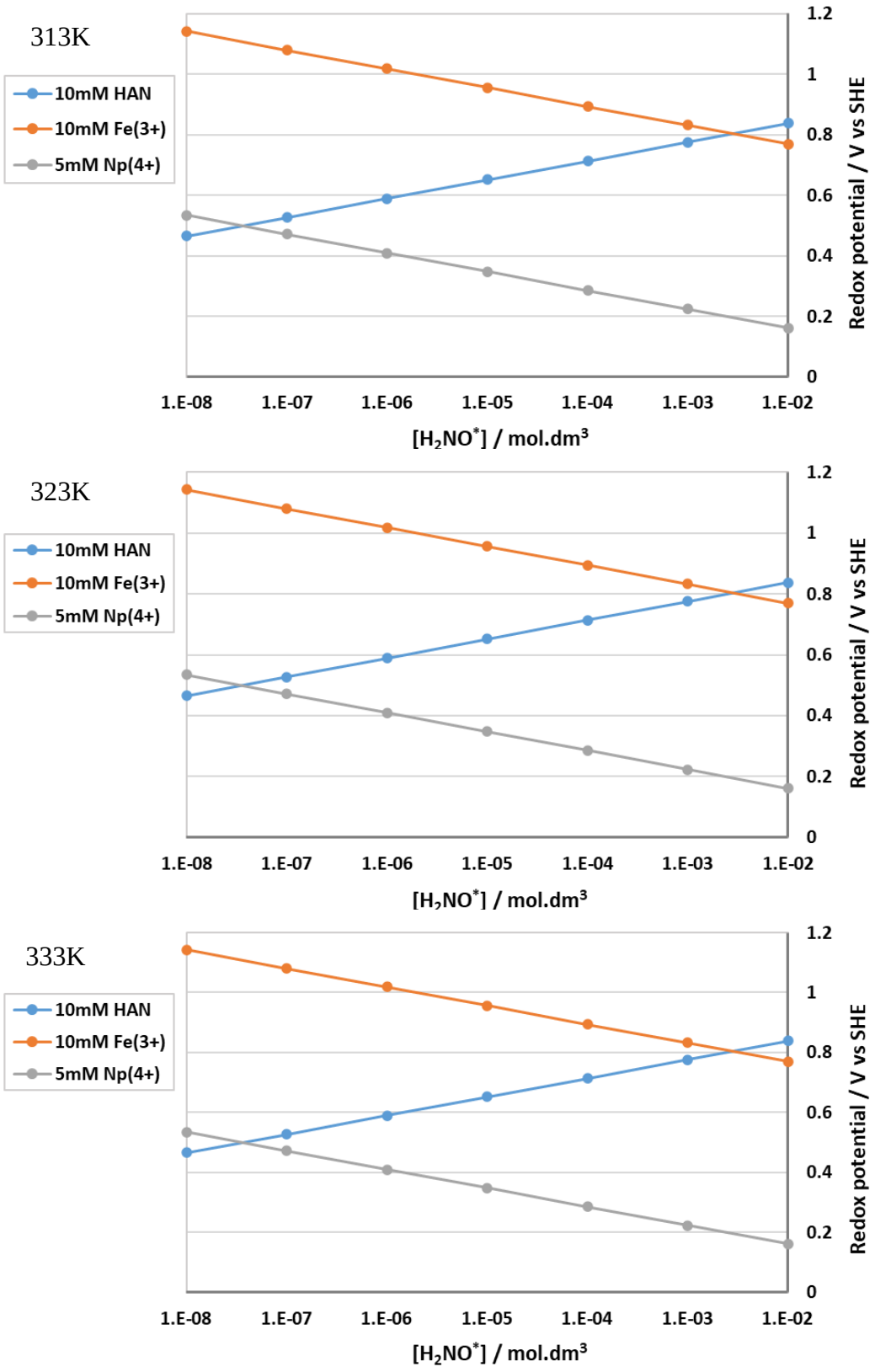

Figure 4.43: Redox potentials as a function of [H_2NO^*] for the (H_2NO^*/NH_2OH), (Fe^{3+}/Fe^{2+}) and (Np^{4+}/Np^{3+}) couples for a 0.1 mol dm^{-3} H^+ system at 313K, 323K and 333K. Calculated for concentrations of NH_2OH and Fe^{3+} = 10 mmol dm^{-3} and Np^{4+} = 5 mmol dm^{-3}

4.7 Summary

To summarise the discussions of primary important in this Chapter, initial Raman spectroscopy studies showed that the products of AHA hydrolysis appear to be unchanged when the hydroxamic acid is complexed to a metal ion, although the resultant yields, particularly of the hydroxylamine product, do differ.

The most significant experimental results presented in this thesis, are those provided by the use of ion chromatography to quantify key species throughout the course of free and complexed AHA hydrolysis, including the acetate ion, NH_3OH^+ and Fe(II). The acetic acid product of the hydrolysis of AHA is considered silent once generated, and its' quantification thus provided a direct measurement for the total AHA lost in the system, requiring no assumptions or manipulations of the data. The analyses of the acetate ion presented in this Chapter showed that, in contrast to that reported in the literature, AHA hydrolysis to form acetate is inhibited in the presence of Fe(III). A simple analytical model applied to this data suggested that the inhibition was likely due to the initially discounted reduction of Fe(III) by the AHA hydrolysis product, hydroxylamine.

Subsequent IC measurements of NH_3OH^+ and Fe(II) obtained for the same systems supported this hypothesis, and a review into the mechanism of the reduction of Fe(III) by hydroxylamine showed that, thermodynamically, this reaction was possible via both the 1:1 and 2:1 mechanism under the conditions of these particular IC studies.

Overall, the experimental work presented in this Chapter shows that the current definition of Fe(III) as a complexing but non-oxidising metal ion with regards to AHA

thus requires revision. To this end, Chapter 5 of this thesis will discuss the creation of a revised kinetic model of the Fe(III)-AHA system using this IC data.

CHAPTER 5

Whole System Kinetic Modelling

5 Whole System Kinetic Modelling

Using the library of temperature dependent data gathered from the ion chromatography (IC) experiments at the three different sets of initial conditions described in Chapter 3, section 3.4.4, a kinetic model of the system was developed in order to provide insight into the key reactions operating in this chemical system, their associated kinetics, and ultimately inform future modelling of the Pu(IV)-AHA system. This Chapter describes several different iterations of the kinetic model, and how each model iteration informs the development of the next, ultimately in order to reach a final model that most closely describes the generated experimental data.

It is important to clarify that, in all iterations of the model described in this Chapter, parameter estimations of kinetic rate constants and equilibrium constants were performed using only the data obtained for the evolution of the acetate and Fe^{2+} ions as a function of time. Whilst NH_3OH^+ was incorporated into the model equations and concentration profiles for this species were produced as a model output, the NH_3OH^+ data obtained by the ion chromatography experiments was not itself used in the estimations of kinetic parameters. This approach was taken due to the fact that its' degradation is complicated by multiple pathways including; i) its' oxidation by Fe(III), and ii) the non-trivial nature of the chemistry of this species in nitric acid media, including the possible autocatalytic reaction of HAN with HNO_3/HNO_2, the latter of which is not under study here.

PhD student Alexander Jackson performed the computational parameter estimation work described in the following sections, using the gPROMS (General PROcess Modelling Software) software.

5.1 Initial Parameter Estimations in gPROMS

The parameter estimation process involves the simultaneous estimation of the values of key unknown rate parameters within the chosen kinetic model by best-fitting of computationally generated theoretical concentration *vs.* time plots to real experimental data. Thus, as a starting point for parameter estimations, an initial basic kinetic model was developed in the gPROMS software package, outputting concentration profiles for the ingrowth of acetate (Ac) and Fe^{2+} for comparison to experimental data.

These initial models were based on a modified version of the kinetic model for the hydrolysis of AHA in the presence of Fe(III) published by Andrieux and co-workers [77]. Note, the model described here differs from these authors in the definition of Fe(III) as a redox active ion, i.e. in contrast to the original Andrieux model, it is assumed here that the reduction of free Fe(III) by NH_3OH^+ occurs, evidence of which was presented in the experimental results in Chapter 4 sections 4.5 and 4.6 of this thesis.

5.1.1 Fe(III) Reduction by HAN via a Single Stoichiometric Pathway

5.1.1.1 Model description

In the systems studied in this thesis by ion chromatography, Fe(III) complexes with AHA to form predominantly the mono-hydroxamate complex along with a small proportion of the bis-hydroxamate complex. The tris-complex concentration is shown to be negligible (by speciation diagrams shown in section 3.2) and thus its hydrolysis and products of that hydrolysis are not considered further. The set of reactions input into the model are shown by R1-R6 in Table 5.1 below. These included; i) the formation of the mono- and bis-hydroxamate complexes, FeL^{2+} and FeL_2^{+} with equilibrium constants K_1 and K_2 respectively, ii) the acid-catalysed hydrolysis of free AHA, defined as 'HL' in Table 5.1, and the mono-complex as described by Andrieux *et al* [77], the associated second order rate parameter for each reaction being k_0 and k_1 respectively, and iii) the reduction of free Fe(III) by NH_3OH^{+}, produced from the hydrolysis of free and complexed AHA. Analogous to the reduction of Pu(IV) by NH_3OH^{+}, the same reduction of Fe(III) occurs by a variable stoichiometry that depends on the initial [Fe(III)]/[NH_3OH^{+}] ratio [99]. The effective rate parameter for the metal ion reduction reaction occurring with a 1:1 Fe(III):NH_3OH^{+} stoichiometry, R5, is given by $k_{red,1,HAN}$ – which itself is a lumped parameter comprised of the equilibrium constants and rate parameters associated with the elementary mechanistic steps of this process. The reduction reaction that occurs with a 2:1 stoichiometry, R6, has a more complicated rate law that requires use of two such lumped rate parameters, $k_{red,2,HAN}$

and $k'_{red,2,HAN}$. We shall return to the exact form of this rate law below. Standard Arrhenius temperature dependence was assumed for all reaction rate constants.

Table 5.1: Chemical reactions included in the initial model to describe the Fe(III)/AHA system.

$HL + Fe^{3+} \overset{K_1}{\rightleftharpoons} FeL^{2+} + H^+$		(R1)
$HL + FeL^{2+} \overset{K_2}{\rightleftharpoons} FeL_2^+ + H^+$		(R2)
$HL + H_3O^+ \overset{k_0}{\rightarrow} Ac + NH_3OH^+$		(R3)
$FeL^{2+} + H_3O^+ \overset{k_1}{\rightarrow} Ac + NH_3OH^+ + Fe^{3+}$		(R4)
$Fe^{3+} + NH_3OH^+ \xrightarrow{k_{red,1,HAN}} Fe^{2+} + 0.5N_2 + 2H^+ + H_2O$	$Pathway\ 1$	(R5)
$2Fe^{3+} + NH_3OH^+ \xrightarrow{k_{red,2,\mathrm{HAN}},\ k'_{red,2,HAN}} 2Fe^{2+} + 0.5N_2O + 3H^+$	$Pathway\ 2$	(R6)

Using the Van't Hoff equation (Eq. 5.1), the temperature dependence of the equilibrium constants K_1 and K_2 as described by Andrieux *et al* [57] are given in Eqs. 5.2 and 5.3 respectively, where T is temperature, R is the universal gas constants and ΔH^0 and ΔS^0 are the enthalpies and entropies of formation for the mono- and bis-complexes. The temperature dependence of the equilibrium constants was written into the model code by Eqs. 5.2 and 5.3, and values for the constants were initially set to those published by the same authors, i.e. $\eta_{c,1}$ = 6783.7, $\alpha_{c,1}$ = -19.0, $\eta_{c,2}$ = 2055.6 and $\alpha_{c,2}$ = -6.0 [57].

$$\ln(K_1) = -\frac{\Delta H^0}{RT} + \frac{\Delta S^0}{R} \qquad Van't\ Hoff\ equation \tag{5.1}$$

$$K_1 = e^{\frac{\eta_{c,1}}{T} + \alpha_{c,1}} \qquad where\ \eta_{c,1} = -\frac{\Delta H_1^0}{R}\ and\ \alpha_{c,1} = \frac{\Delta S_1^0}{R} \tag{5.2}$$

$$K_2 = e^{\frac{\eta_{c,2}}{T}+\alpha_{c,2}} \qquad where\ \eta_{c,2} = -\frac{\Delta H_2^0}{R}\ and\ \alpha_{c,2} = \frac{\Delta S_2^0}{R} \tag{5.3}$$

To model the kinetics of the complex formation, equilibrium constants were written into the model code as a ratio of rate constants equivalent to the forward complexation reactions, $k_{1,f}$ and $k_{2,f}$, over the backward decomplexation reactions, $k_{1,b}$ and $k_{2,b}$, where the subscripts 1 and 2 correspond to K_1 and K_2 respectively. These are shown in Eqs. 5.4 and 5.5. Calculating values of K_1 and K_2 by Eqs. 5.2 and 5.3 and setting the respective forward reaction rate constants in Eqs. 5.4 and 5.5, $k_{1,f}$ and $k_{2,f}$, to very large values (1 x 10^5 $M^{-1}.s^{-1}$), gPROMS then estimates values of $k_{1,b}$ and $k_{2,b}$ to allow the equilibria to proceed on a much faster timescale than that of the various hydrolysis and reduction reactions, to the point that it is essentially instantaneous.

$$K_1 = \frac{k_{1,f}}{k_{1,b}} \tag{5.4}$$

$$K_2 = \frac{k_{2,f}}{k_{2,b}} \tag{5.5}$$

Eqs. 5.6-5.12 in Table 5.2 describe the differential equations written into the model code to create the time profiles of the various species involved, including the appropriate rate laws for HL hydrolysis [77] and Fe(III) reduction via pathways 1 and 2, R5 and R6 in Table 5.1 respectively [99]. The forward and backward kinetic rate constants in Eqs. 5.4 and 5.5 are used in the relevant Eqs. in Table 5.2 to model the kinetics of the complex equilibria for the species affected by this process, which includes HL, FeL^{2+}, FeL_2^{+} and Fe^{3+}.

Table 5.2: Rate equations used in the model. for calculation of HL, Ac, NH_3OH^+, FeL^{2+}, Fe^{2+} and Fe^{3+} concentrations. Rate equations used to describe the Fe(III) reduction by NH_3OH^+ are as published by Bengtsson et al. [99] and those describing the hydrolysis of HL and FeL^{2+} are as published by Andrieux et al. [83].

$$\frac{d[Ac]}{dt} = k_0[HL][H^+] + k_1[FeL^{2+}][H^+] \tag{5.6}$$

$$\frac{d[Fe^{2+}]}{dt} = k_{red,1,\mathrm{HAN}}\frac{[Fe^{3+}]^2[NH_3OH^+]^2}{[Fe^{2+}]^2[H^+]^4} + 2k_{red,2,HAN}\frac{[Fe^{3+}]^2[NH_3OH^+]}{[Fe^{2+}][H^+]^2 + k'_{red,2,\mathrm{HAN}}[Fe^{3+}][H^+]} \tag{5.7}$$

$$\frac{d[NH_3OH^+]}{dt} = k_0[HL][H^+] + k_1[FeL^{2+}][H^+] - k_{red,1,HAN}\frac{[Fe^{3+}]^2[NH_3OH^+]^2}{[Fe^{2+}]^2[H^+]^4} - 2k_{red,2,HAN}\frac{[Fe^{3+}]^2[NH_3OH^+]}{[Fe^{2+}][H^+]^2 + k'_{red,2,HAN}[Fe^{3+}][H^+]} \tag{5.8}$$

$$\frac{d[HL]}{dt} = -k_0[HL][H^+] - k_{1,f}[HL][Fe^{3+}] - k_{2,f}[HL][FeL^{2+}] + k_{1,b}[FeL^{2+}][H^+] + k_{2,b}[FeL_2^+][H^+] \tag{5.9}$$

$$\frac{d[FeL^{2+}]}{dt} = -k_1[FeL^{2+}][H^+] + k_{1,f}[HL][Fe^{3+}] - k_{2,f}[HL][FeL^{2+}] - k_{1,b}[FeL^{2+}][H^+] + k_{2,b}[FeL_2^+][H^+] \tag{5.10}$$

$$\frac{d[FeL_2^+]}{dt} = k_{2,f}[HL][FeL^{2+}] - k_{2,b}[FeL_2^+][H^+] \tag{5.11}$$

$$\frac{d[Fe^{3+}]}{dt} = k_1[FeL^{2+}][H^+] - k_{red,1,HAN}\frac{[Fe^{3+}]^2[NH_3OH^+]^2}{[Fe^{2+}]^2[H^+]^4} - 2k_{red,2,HAN}\frac{[Fe^{3+}]^2[NH_3OH^+]}{[Fe^{2+}][H^+]^2 + k'_{red,2,HAN}[Fe^{3+}][H^+]} - k_{1,f}[HL][Fe^{3+}] + k_{1,b}[FeL^{2+}][H^+] \tag{5.12}$$

In addition to the approach to the temperature dependence (Eqs. 5.2 and 5.3) and the kinetics of the complex equilibria (Eqs. 5.4 and 5.5), the concentrations of individual Fe(III)-containing species were also related to the equilibrium constants via the incorporation of Eqs. 5.13-5.16, where Fe_T and L_T are the total concentrations of ferric ions (initially added as $Fe(NO_3)_3$) and AHA added respectively. This was a method previously adopted by Andrieux *et al* to define the initial conditions for a kinetic model of the Fe(III)-AHA system [77]. An analogous approach was also used by the same

authors for the modelling of Np(IV)-AHA data [58]. By determining the speciation at each time step during a model simulation using Eqs. 5.13-5.16, in conjunction with gPROMS generated values of [HL] at each time step, concentration profiles of Fe^{3+}, FeL^{2+} and FeL_2^{+} as a function of time can be produced and compared with those output directly by gPROMS. This comparison thus provides a way to validate the kinetic approach to modelling equilibria described by Eqs. 5.4 and 5.5 and confirm that complex formation in the model is rapid to the point it is essentially instantaneous.

$$[Fe^{3+}] = \frac{Fe_T}{1 + K_1\gamma + K_2K_1\gamma^2 + K_3K_2K_1\gamma^3} \tag{5.13}$$

$$[FeL^{2+}] = \frac{K_1\gamma Fe_T}{1 + K_1\gamma + K_2K_1\gamma^2 + K_3K_2K_1\gamma^3} \tag{5.14}$$

$$[FeL_2^{+}] = \frac{K_2K_1\gamma^2 Fe_T}{1 + K_1\gamma + K_2K_1\gamma^2 + K_3K_2K_1\gamma^3} \tag{5.15}$$

$$where \quad \gamma = \frac{[HL]}{[H^+]} = \frac{[NO_3^-]}{[H^+]} + \frac{L_T}{[H^+]} - 1 \tag{5.16}$$

The initial model as written into the gPROMS code can thus be described by Eqs. 5.2 – 5.16. In this initial model it was hypothesized that a single pathway would be dominant in the reduction of Fe(III) by NH_3OH^+ in any one experimental dataset, and as such, it could be assumed that only a single pathway existed i.e. either R5 or R6 would be operating in any one data treatment – not both. For these initial gPROMS model tests two different groups of experimental datasets were defined and it was assumed that these datasets follow one of either of the two different pathways shown in Table 5.1; a pure 1:1 stoichiometry (R5) when the initial concentration of Fe(III), $[Fe(III)]_0$, was 2.5 mmol dm^{-3} and the ratio $[Fe(III)]/[NH_3OH^+]$ is assumed to remain

≤1 throughout the experimental run, and a pure 2:1 stoichiometry (R6) when $[Fe(III)]_0$ was equal to 10 mmol dm^{-3} and the ratio $[Fe(III)]/[NH_3OH^+]$ is assumed to remain >1 throughout the experimental run.

Table 5.3: Concentrations of freely available HL and Fe(III) for the defined datasets: 10 mmol dm^{-3} initial AHA in 0.1 mol dm^{-3} HNO_3 for varying Fe_T (total iron concentration) and temperatures, including calculated ratios of fee Fe(III):HL. All concentrations (shown in []) are in mmol dm^{-3}

Temperature / K	**[Fe_T]**	**[free HL]**	**free Fe(III)**		**Free Fe(III):HL**
			[]	% of Fe_T	
313	2.5	8.37	1.05	42.0	0.13:1
323	2.5	8.83	1.44	57.6	0.16:1
333	2.5	9.21	1.78	71.2	0.19:1
313	10	5.23	5.59	55.9	1.07:1
323	10	6.39	6.67	66.7	1.04:1
333	10	7.43	7.62	76.2	1.03:1

Table 5.3 shows the speciation data relating to the initial concentrations of freely available AHA and Fe(III) in each experimental dataset, presented previously in Table 4.5 in section 4.2.2 of Chapter 4. It has been previously suggested by Bengtsson and co-workers [99] that the 2:1 stoichiometry only occurs when $[Fe(III)]_0$ is at least 5-10 times that of NH_3OH^+. The initial ratios of free [Fe(III)]/[HL] were less than 5 for all datasets considered, with a maximum of 1.07:1 for the dataset with $[Fe(III)]_0$ = 10 mmol dm^{-3} at 313K. However, uncomplexed HL hydrolysis would be expected to rapidly convert the hydroxamate to NH_3OH^+, and the high temperatures and reasonably low acidity studied here would also be expected to promote the Fe(III) reduction reaction – the latter as a result of the form of the rate laws for R5 and R6 given respectively by the second and third terms in the right-hand side of equation 5.12. Thus, particularly in the early stages of the hydrolysis reaction for those datasets with $[Fe(III)]_0$ = 10 mmol dm^{-3}, the concentration of freely available Fe(III) in solution

is expected to be significantly greater than hydrolytically generated NH_3OH^+, and the conditions may reasonably be expected to promote the reduction by reaction R6 throughout the length of AHA hydrolysis.

Two separate gPROMS runs were performed initially in which the equilibrium constants were set in accordance with equations 5.2 and 5.3 to values of Andrieux *et al* [57]. Although robust literature values are available for the rate constant for free AHA hydrolysis, k_0, [69, 77-79, 83], Arrhenius parameters of $A = 1.25 \times 10^{11}$ M^{-1} s^{-1} and $E_a = 89$ kJ mol^{-1} were used for determination of values of k_0 at each temperature; these Arrhenius parameters have been calculated in Chapter 4 section 4.2.1 of this thesis from simple kinetic analysis of the acetate data. This approach was adopted because, unlike the commonly used spectroscopic method for determination of k_0 involving measurement of the maximum absorbance of the FeL^{2+} complex, quantification of the acetic acid product of hydrolysis by IC provides a direct measurement for the total AHA lost in the system, requiring no assumptions or manipulations of the data; the values of A and E_a derived from the IC method are thus expected to be more accurate. Arrhenius temperature dependence was assumed to hold for all kinetic rate constants and the parameters A and E_a are estimated (i.e left to float) by the parameter estimation function of gPROMS for all other kinetic rate parameters, including the complexed AHA hydrolysis rate parameter k_1, and the appropriate active Fe(III) reduction rate parameters. These Fe(III) reduction rate parameters are, of course, $k_{red,1,HAN}$ for the datasets that are assumed to follow pathway 1 (where $[Fe(III)]_0 = 2.5$ mmol dm^{-3}), and $k_{red,2,HAN}$ and $k'_{red,2,HAN}$ for the datasets that are assumed to follow pathway 2 (where $[Fe(III)]_0 = 10$ mmol dm^{-3}). Separation of

pathways 1 and 2 in the fitting process was achieved by setting the appropriate rate parameter(s) $k_{red,1,HAN}$, or $k_{red,2,HAN}$ and $k'_{red,2,HAN}$ equal to 0 in the data fitting runs in which they were not required.

5.1.1.2 Model output and discussion

The output of this modelling approach is shown in Figure 5.1, with concentrations shown in units of mol m^{-3} as used in the simulation. These are equivalent to units of mmol dm^{-3}.

Figure 5.1 reveals that the fits calculated by gPROMS are generally poor for those experimental runs conducted in the presence of Fe(III), and are particularly poor at the high total Fe(III) concentration employed of 10 mmol dm^{-3}. Specifically, whilst the model is able to provide a profile for acetate ingrowth that closely follows the experimental data at all temperatures when no iron is present, fits to the data start to deviate when $[Fe(III)]_0$ = 2.5 mmol dm^{-3}, Figure 5.1 graphs A-C, and this deviation from the data increases with temperature. For the data in these same plots obtained at the higher Fe(III) concentration of 10 mmol dm^{-3} , the model shows a large deviation from the data at all temperatures. Looking next at the Fe^{2+} data when $[Fe(III)]_0$ = 2.5 mmol dm^{-3}, Figure 5.1 graphs D-F, there is good agreement between both the modelled and experimental data fits across the explored temperature range. However, at the higher $[Fe(III)]_0$ of 10 mmol dm^{-3} in these same plots, the model $[Fe^{2+}]$ *vs*. t output starts to deviate significantly from the measured experimental data with increase in temperature.

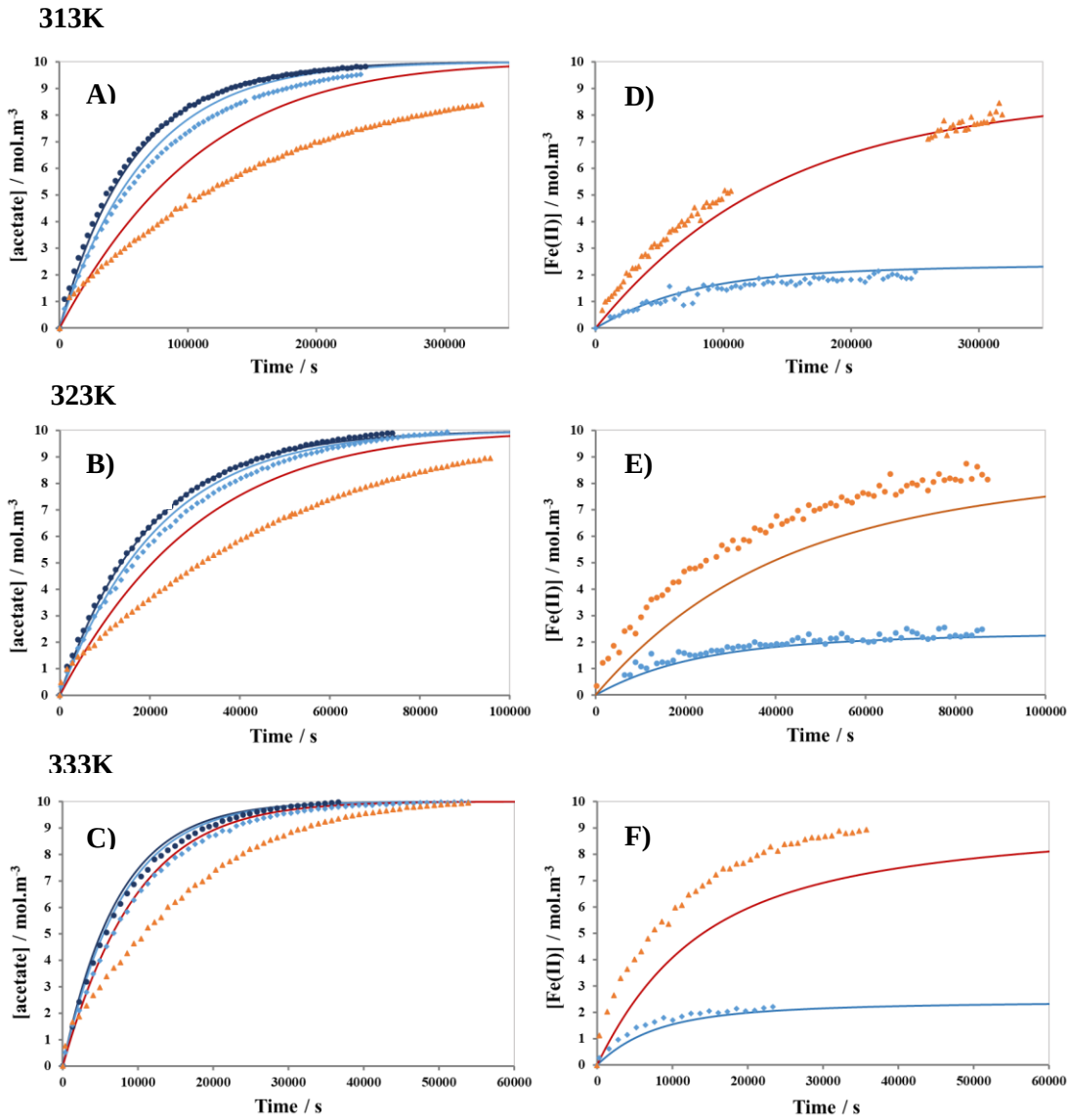

Figure 5.1: Plots of experimental data and model output at 313K (A &D), 323K (B &E) and 333K (C & F) from which parameter estimations were obtained. Plots A-C: Experimental data (points) and model output (lines) for Ac, when $[Fe(III)]_0$ = 0 (dark blue), 2.5 (light blue) and 10 mmol dm^{-3} (orange). Plots D-F: Experimental data (points) and model output (lines) for Fe^{2+}, when $[Fe(III)]_0$ = 2.5 (light blue) and 10 mmol dm^{-3} (orange). For the data obtained at 3131K with 10 mmol dm^{-3} initial Fe(III), a system fault overnight caused a large stoppage period in data acquisition in which the IC system had to be cleaned, re-equilibrated and put back into operation.

Figure 5.2 shows plots of the concentration profiles of the FeL^{2+} (A-C) and FeL_2^{+} complexes (D-F) calculated using Eqs. 5.13-5.16 and values of L_T, Fe_T and HL generated as outputs from the gPROMS model. These plots are identified on Figure 5.2 as polynomial plots. They are shown along with plots of the same complex concentration profiles obtained as direct outputs by the gPROMS model itself using

the set of differential equations in Table 5.2 that incorporate the kinetic treatment of the complexation constants described by Eqs. 5.4 and 5.5. It can be seen that both the derived polynomial plots and the directly generated gPROMS model plots are identical for all simulations with $[Fe(III)]_0$ = 2.5 or 10 mmol dm^{-3}, thus validating the kinetic approach to speciation used in the model.

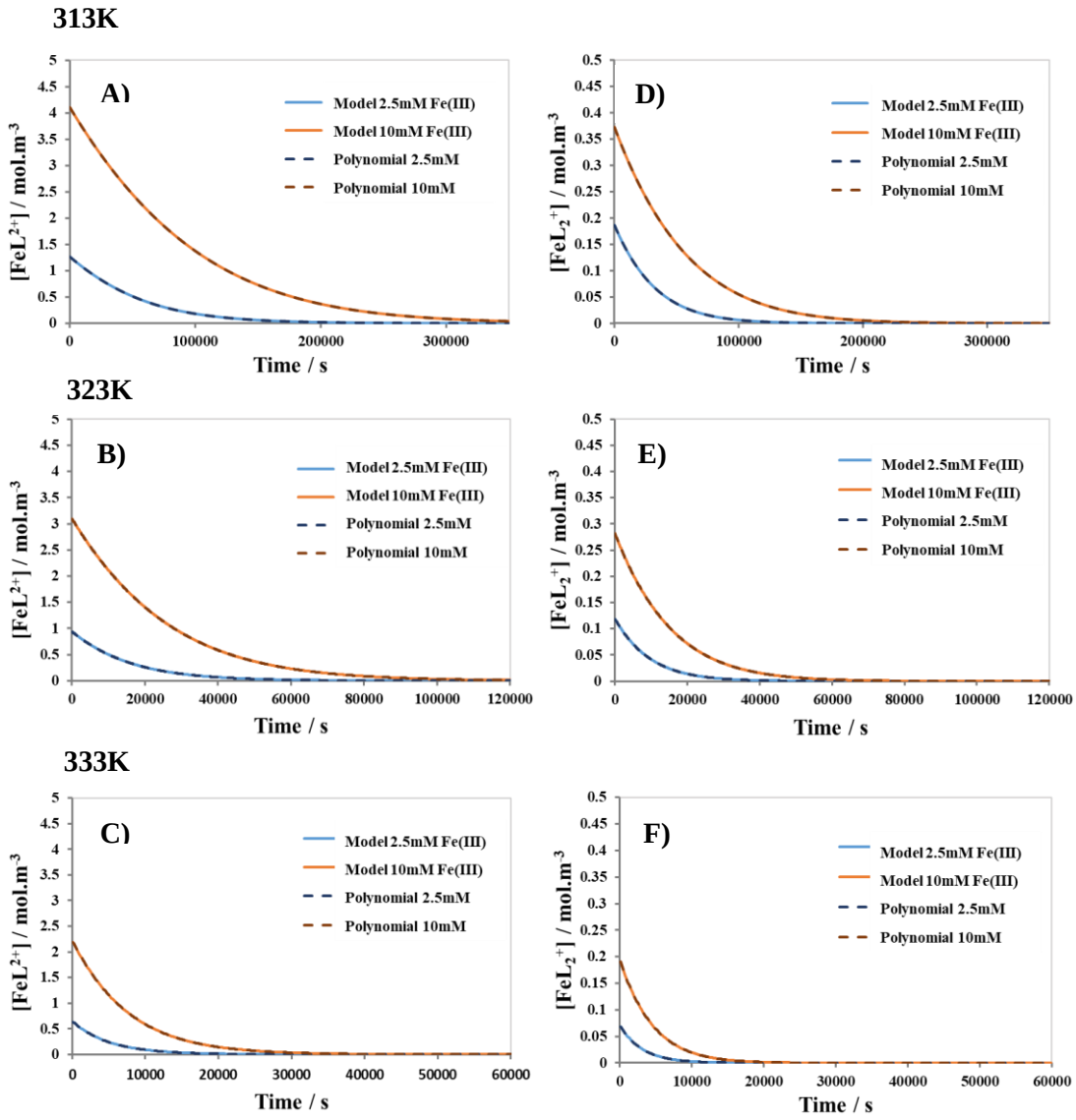

Figure 5.2: Polynomial plots of the concentrations of the FeL^{2+} complex (A-C) and the FeL_2^{+} complex (D-F) as calculated from Eqs. 5.13-5.16, and those output from the model, for the fits shown in Figure 5.1.

The parameter estimations obtained for the kinetic rate constants using the experimental datasets when $[Fe(III)]_0$ is equal to 2.5 mmol dm^{-3} and the 1:1 pathway is assumed to operate, and 10 mmol dm^{-3} where the 2:1 pathway is assumed to operate, are shown in Table 5.4 and Table 5.5 respectively. Note, units for concentration and related parameters have been converted to mol dm^{-3} (*M*).

Table 5.4: Initial parameter estimations for the datasets with $[Fe(III)]_0$ = 2.5 mmol dm^{-3}, assuming only pathway 1 operates. Rate constants are given in units of mol dm^{-3} (M). Shaded values are set parameters.

Plots	T / K	K_1	K_2	k_0 / $M^{-1}.s^{-1}$	k_1 / $M^{-1}.s^{-1}$	$k_{red,1,HAN}$ / $M^3.s^{-1}$
A & D	313	14.5	1.77	1.75×10^{-4}	2.05×10^{-21}	1.47×10^{-7}
B & E	323	7.41	1.44	5.05×10^{-4}	1.75×10^{-20}	3.33×10^{-7}
C & F	333	3.94	1.19	1.37×10^{-3}	1.31×10^{-19}	7.20×10^{-7}

Table 5.5: Initial parameter estimations for the datasets with $[Fe(III)]_0$ = 10 mmol dm^{-3}, assuming only pathway 2 operates. Rate constants are given in units of mol dm^{-3} (M). Shaded values are set parameters.

Plots	T / K	K_1	K_2	k_0 / $M^{-1}.s^{-1}$	k_1 / $M^{-1}.s^{-1}$	$k_{red,2,HAN}$ / $M.s^{-1}$	$k'_{red,2,HAN}$ / M
A & D	313	14.5	1.77	1.75×10^{-4}	2.05×10^{-21}	9.43×10^{-6}	9.79×10^{-18}
B & E	323	7.41	1.44	5.05×10^{-4}	1.75×10^{-20}	2.04×10^{-5}	4.06×10^{-17}
C & F	333	3.94	1.19	1.37×10^{-3}	1.31×10^{-19}	4.23×10^{-5}	1.55×10^{-16}

Considering first the data shown in Table 5.4 for the lower initial Fe(III) concentration, $[Fe(III)]_0$ = 2.5 mmol dm^{-3}, values of the pre-exponential factor, $A = 4.80\times10^4$ $M^3.s^{-1}$ and the activation energy, E_A = 69 kJ mol^{-1} are obtained for the kinetic rate constant $k_{red,1,HAN}$ for Fe(III) reduction by pathway 1. The statistical data output by the gPROMS software, including the 95% confidence interval, standard deviation and t-values for these Arrhenius parameters are given in Table 7.1 of Appendix B section 7.2.4.4, and illustrate the importance of $k_{red,1,HAN}$ to the obtained model fits. Specifically, the t-value test is a statistical test which poses as its null hypothesis that an estimated parameter

is equal to zero. Only if the t-value calculated for that parameter is greater than the reference t-value, the latter calculated to have a value of 1.649 in this model iteration based on the confidence interval and number of degrees of freedom, can the null hypothesis be rejected and the parameter considered different from zero and therefore important in the model fit. The t-value test is described in a little more detail in Appendix B section 7.2.4.3. The calculated t-values for these Arrhenius parameters *Ea* and *A* for $k_{red,1,HAN}$, as stated in Appendix B section 7.2.4.3, are 15.108 and 0.579 respectively. From these parameters, a value for $k_{red,1,HAN}$, at 298K of 3.86×10^{-8} $M^3.s^{-1}$ is obtained. This is approximately an order of magnitude larger than the mean value for the observed rate constant for the analogous process (Fe(III) reduction by NH_3OH^+ with a 1:1 stoichiometry) of 1.85×10^{-9} (± 0.07) $M^3.s^{-1}$ published by Bengtsson *et al.* from their studies at this temperature in solutions of 0.1M $HClO_4$, μ = 1.0M [99]. It is however important to note that differences in the acidic media employed, in this case HNO_3 rather than $HClO_4$, may have some effect on the value of the rate constant. For example, Xu *et al.* [178] noted the dominant role of the reaction media on the oxidation of hydroxylamine by Ce(IV) in determining the reaction kinetics, mechanism and product(s). Specifically, these authors found the oxidation of hydroxylamine by Ce(IV) to be much faster in perchloric media than that reported in sulfuric acid [183, 184], producing different reaction products due to a complex formation of Ce(IV) with sulfate that results in the redox potential of the Ce(IV)/Ce(III) couple being driven to more negative values [185]. Totally different rate laws were obtained and therefore different reaction mechanisms proposed by Xu *et al.* [178]. Additionally, as described in Chapter 4 section 4.6.1 of this thesis, UV/Vis spectroscopy measurements of Fe(III)-containing AHA solutions following hydrolysis showed a decrease in the percentage

conversion of Fe(III) to Fe(II) in $HClO_4$ media compared to HNO_3, suggesting a slower reduction of Fe(III) by hydroxylamine in $HClO_4$ – an observation consistent with the values of the rate constant for the reduction of Fe(III) by HAN via a 1:1 stoichiometry, $k_{red,1,HAN}$, in HNO_3 and $HClO_4$ discussed above.

Focussing next on the hydrolysis of Fe(III)-complexed AHA when $[Fe(III)]_0$ = 2.5 mmol dm^{-3}, the parameter estimations for k_1 shown in Table 5.4 do not compare favourably with those determined by Andrieux *et al.* [83] at the equivalent temperatures. The values of k_1 presented in Table 5.4 are smaller than those calculated by Andrieux *et al.* by 10^{15} - 10^{16} orders of magnitude at each temperature studied, suggesting that, in our study at least, the hydrolysis of FeL^{2+} is minimal. Using the estimated values of k_1 reported in Table 5.4, values of the Arrhenius parameters of A = 2.25 x 10^9 M^{-1} s^{-1} and E_a = 180 kJ mol^{-1} may be calculated. The statistical data for these values is given in Table 7.1 of Appendix B section 7.2.4.4, from which it can be seen that the t-values for these Arrhenius parameters are on the order of 10^{-17} and 10^{-18}. Based on the criteria outlined in Appendix B section 7.2.4.3, these are significantly smaller than the reference t-value of 1.649, indicating that k_1 is insignificant in the model fits.

Finally, we turn to the parameter estimations obtained for an initial Fe(III) concentration of 10 mmol dm^{-3}, Table 5.5, inspection of which shows that the estimations k_1 are completely unchanged from those obtained when $[Fe(III)]_0$ = 2.5 mmol dm^{-3} at the respective temperatures. However, care shall be taken in the interpretation of the identical values for k_1 reported here. In its parameter estimation process, gPROMS requires the input of seed values. In selecting seed values for k_1, we

have taken account of the observation in Chapter 4 that acetate ingrowth is always slower in the presence of Fe(III) than in its absence, giving a strong qualitative indication that the hydrolysis of the complexed ligand as described by k_1 is substantially slower than the hydrolysis of the free ligand as described by k_0. Consequently, in providing a seed value for k_1, we have assumed a worst case scenario in the context of values that gPROMS can compute i.e. values on the order of 10^{-20}. The similarity of k_1 values between Table 5.4 and Table 5.5 is then due to gPROMS not adjusting the value of k_1 away from the seed values during the fit – again implying that k_1 is insignificant in the fitting process. This implication is further supported by the t-values associated with the A and E_a values for k_1 reported in Table 7.1 and Table 7.2. These are on the order of 10^{-18} and 10^{-16} respectively and, as discussed above, being less than the reference t-value of 1.649, confirms the insignificance of k_1 estimations to the model fits. We shall return to the appropriateness of the seed values of k_1 and associated implicit assumption of its insignificance below.

Turning our attention now to the values of the rate parameter $k_{red,2,HAN}$ in the numerator of the term for the reduction of Fe(III) by pathway 2 in the rate equation of Table 5.5, these are estimated to be approximately 1-2 orders of magnitude larger than the values of the rate parameter $k_{red,1,HAN}$, estimated for the reduction of Fe(III) via pathway 1 for the datasets where $[Fe(III)]_0 = 2.5$ mmol dm^{-3} at the respective temperatures, although caution should be exercised in the direct comparison of $k_{red,1,HAN}$ and $k_{red,2,HAN}$ given the different unitary systems. As can be seen from Table 7.2 in Appendix B section 7.2.4.4, $k_{red,2,HAN}$ is the most important parameter to these model fits, with t-values of 30.115 and 1.204 for the Arrhenius parameters E_a and A respectively, approximately

twice that of the equivalent values of these parameters relating to $k_{red,1,HAN}$ in the previous model fits. On the other hand, the denominator in the kinetic rate expression for pathway 2, $k'_{red,2,HAN}$, is estimated to be very small, on the order of 10^{-18} – 10^{-16}, and thus insignificant. Too, as can be seen from Table 7.2, the t-values for the Arrhenius parameters associated with $k'_{red,2,HAN}$, A and E_a, are on the order of 10^{-14} and 10^{-12} respectively – again suggesting that $k'_{red,2,HAN}$ is insignificant in the estimation of the model fits.

In summary, this initial modelling approach has provided values for the reduction of free Fe(III) by HAN for the 1:1 pathway generally in line with previous literature, and generally good fits to the Fe^{2+} data when $[Fe(III)]_0$ = 2.5 mmol dm^{-3}. The model is however unable to provide good fits to the Fe^{2+} data when $[Fe(III)]_0$ = 10 mmol dm^{-3} or to the acetate data except in the absence of initial Fe(III). In all cases, the rate of free hydrolysis of AHA, k_0, has the greatest influence on all these model fits, whilst estimations of the rate parameter for the complex hydrolysis, k_1, are predicted to be many orders of magnitude smaller than the literature values reported by Andrieux *et al*. [83] to the point they are insignificant. Indeed, the statistical values presented in Table 7.1 and Table 7.2 for the Arrhenius parameters that give the values of k_1 presented in Table 5.4 and Table 5.5 respectively, illustrate the insignificance of k_1 to the model fits. The kinetic constants for the reduction of Fe(III) by HAN, $k_{red,1,HAN}$ and $k_{red,2,HAN,}$ are estimated to be many orders of magnitude greater than k_1 and $k'_{red,2,HAN}$, suggesting a significantly greater influence of the two former parameters on the overall model fit. This is confirmed by inspection of t-values for the Arrhenius parameters for $k_{red,1,HAN}$ and $k_{red,2,HAN}$, Table 7.1and Table 7.2 respectively in Appendix B section

7.2.4.4, which are found to be greater than the reference t-value in the case of activation energy, and within one order of magnitude smaller than the reference t-value in the case of the pre-exponential factor.

It is suspected that the lack of agreement between the modelled values of k_1 reported here and the values reported previously by Andrieux *et al*. [83] are due to over simplifications in the assumed reaction mechanism employed here, in the original treatment by Andrieux *et al*. or, most likely, in both. While reaction pathway 1 or 2 (Table 5.1, R5 and R6) may dominate the datasets obtained at low (2.5 mmol dm^{-3}) and high (10 mmol dm^{-3}) initial Fe(III) concentrations respectively, in reality there may also be a minor contribution from the other pathway within each dataset. Incorporation of the different contributions of the two pathways was thus included in the next gPROMS model iteration via a switching mechanism, which is the subject of the following section.

5.1.2 Switching Between Stoichiometric Pathways for Fe(III) Reduction by HAN Using the "IF-statement" Inequality

5.1.2.1 Model description

From the initial parameter estimations, it was determined that the ingrowth of Fe(II) in all the experimental datasets was likely the result of a mixture of pathways 1 and 2 in each dataset, but with a single pathway still dominating at any one time. In the 10 mmol dm^{-3} $[Fe(III)]_0$ experimental dataset in particular, the high ratios of $[Fe(III)]/[NH_3OH^+]$ leads us to assume that pathway 2 will certainly dominate in the

initial stages of reduction when NH_3OH^+ is first being produced from AHA hydrolysis before switching to a situation where pathway 1 is dominant during the course of the rest of the hydrolysis reaction as Fe(III) is depleted. However, and to a smaller extent, the same is likely to be true for those datasets with $[Fe(III)]_0$ = 2.5 mmol dm^{-3}. Thus, in order to determine a ratio where the reaction stoichiometry might switch, an inequality was incorporated into the gPROMs model with the following conditions;

$$IF\ n\left(\frac{[Fe(III)]}{[NH_3OH^+]}\right) < 1 \qquad Pathway\ 1\ is\ active \tag{5.17}$$

$$IF\ n\left(\frac{[Fe(III)]}{[NH_3OH^+]}\right) > 1 \qquad Pathway\ 2\ is\ active \tag{5.18}$$

where *n* is a constant which is optimised to create the best fit for the data, and [Fe(III)] is equal to either the total iron concentration, Fe_T ($= [Fe^{3+}] + [FeL^{2+}] + [FeL_2^+]$), or the free iron concentration, $\left[Fe_{(aq)}^{3+}\right]$. Both definitions of [Fe(III)] in the inequality were tested. At the beginning of the reaction when no NH_3OH^+ is present and $[Fe(III)]_0$ is equal to 2.5 mmol dm^{-3} or 10 mmol dm^{-3}, pathway 2 is assumed active. After a period of time, the value of the inequality falls below 1 and pathway 1 becomes active.

As in the previous model iteration, the Arrhenius parameters for the kinetic rate constant for the free AHA hydrolysis, $k_{0,}$ were set to those obtained previously in this thesis (Chapter 4 section 4.2.1), and the constants relating to the temperature dependence of the equilibrium constants K_1 and K_2 set to literature values as described in Eqs. 5.2 and 5.3. As well as the value of the pathway switching parameter n. the Arrhenius parameters for all other rate parameters including $k_{1,}$ $k_{red,1,HAN}$, $k_{red,2,HAN}$ and $k'_{red,2,HAN}$, were estimated by gPROMS.

5.1.2.2 Model output and discussion

The closest fits of the data, determined by a chi-squared test performed by gPROMS during each simulation, were obtained for a value of n = 0.25 in the inequality, i.e. there is a switch from pathway 2 to pathway 1 when the [Fe(III)]/[NH_3OH^+] ratio falls below 4. This is slightly lower than the ratio of 5-10 that has previously been suggested by Bengtsson *et al*. as being the value above which the 2:1 stoichiometry reduction of Fe(III) by NH_3OH^+ dominates [99]. Nevertheless, the overall lowest error fits, obtained for the experimental [acetate] *vs.* time (t) and [Fe(II)] *vs*. time (t) data when [Fe(III)] in equation 5.17 and 5.18 is equal to $\left[Fe_{(aq)}^{3+}\right]$ and n = 0.25 in the inequality, are shown in Figure 5.3.

Considering first only the acetate concentration data of Figure 5.3 (A-C), it can be seen that the fits are not substantially different from those obtained from the previous model in section 5.1.1.

However, consideration of the Fe(II) concentration data of Figure 5.3 (D-F), it can be seen that this new IF-statement method graphically provides very different fits to the 10 mmol dm^{-3} $[Fe(III)]_0$ datasets than those obtained from the previous model in section 5.1.1, with each of the fits displaying a large and obvious kink, presumably at the point upon switching from pathway 2 to pathway 1. For these datasets at the higher temperatures of 323 and 333K, this new model provides improved fits to the data in the very early stages of Fe(II) ingrowth, whilst the remainder of the fit after the kink follows a similar trajectory to the previous model fits in section 5.1.1. The fits to the

Fe(II) data from the datasets with 2.5 mmol dm^{-3} $[Fe(III)]_0$ are however visually unchanged.

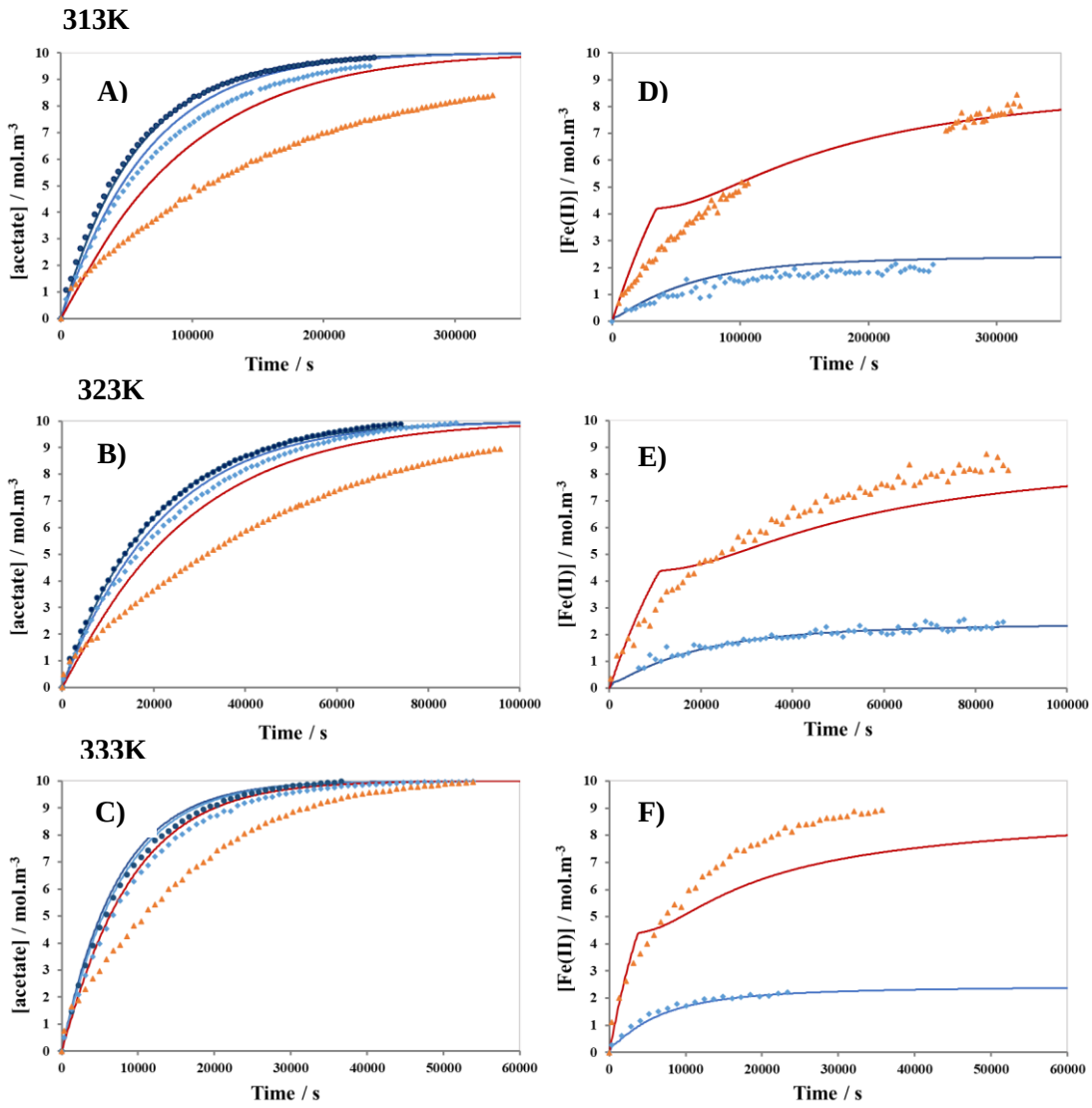

Figure 5.3: Plots of experimental data and model output at 313K (A &D), 323K (B &E) and 333K (C & F) from which parameter estimations were obtained using the IF-statement model with [Fe(III)] = $[Fe^{3+}_{(aq)}]$ and n=0.25 in the inequality. Plots A-C: Experimental data (points) and model output (lines) for Ac, when $[Fe(III)]_0$ = 0 (dark blue), 2.5 (light blue) and 10 mmol dm^{-3} (orange). Plots D-F: Experimental data (points) and model output (lines) for Fe^{2+}, when $[Fe(III)]_0$ = 2.5 (light blue) and 10 mmol dm^{-3} (orange). For the data obtained at 3131K with 10 mmol dm^{-3} initial Fe(III), a system fault overnight caused a large stoppage period in data acquisition in which the IC system had to be cleaned, re-equilibrated and put back into operation

The parameter estimations obtained for the kinetic rate constants using experimental datasets where $[Fe(III)]_0$ is equal to 2.5 mmol dm^{-3} and 10 mmol dm^{-3}, where [Fe(III)]

is equal to $\left[Fe^{3+}_{(aq)}\right]$ or Fe_T and n = 0.25 in the inequality are shown in Table 5.7 (see page 283).

Before discussing this table in detail though, it is instructive to briefly examine what the fits of Figure 5.3 and the data of Table 5.7 tell us about the point at which the Fe(III) reduction path switches from a 2:1 to a 1:1 stoichiometry in each run. This was easily visualised by using the outputs from the gPROMS to plot separately and as a function of time, the value of the entire rate equations for pathway 1 and 2, as given by Eqs. 5.19 and 5.20 respectively.

$$\left(\frac{d[Fe^{2+}]}{dt}\right)_{pathway\ 1} = k_{red,1,HAN}\frac{[Fe^{3+}]^2[NH_3OH^+]^2}{[Fe^{2+}]^2[H^+]^4} \tag{5.19}$$

$$\left(\frac{d[Fe^{2+}]}{dt}\right)_{pathway\ 2} = 2k_{red,2,HAN}\frac{[Fe^{3+}]^2[NH_3OH^+]}{[Fe^{2+}][H^+]^2 + k'_{red,2,HAN}[Fe^{3+}][H^+]} \tag{5.20}$$

The plots of these are shown in Figure 5.4 and Figure 5.5 for the runs where $[Fe(III)]_0$ is equal to 2.5 mmol dm^{-3} and 10 mmol dm^{-3} respectively. The point at which the switch from pathway 2 to pathway 1 occurs is circled in red in each plot.

As was expected using this modelling approach, datasets where Fe_T was equal to 2.5 mmol dm^{-3} showed pathway 2 to be active for only a very short proportion of time (< 1% of the total experiment length), whereas when Fe_T was equal to 10 mmol dm^{-3}, pathway 2 is active longer, in the range of 5-10% of the total experimental length.

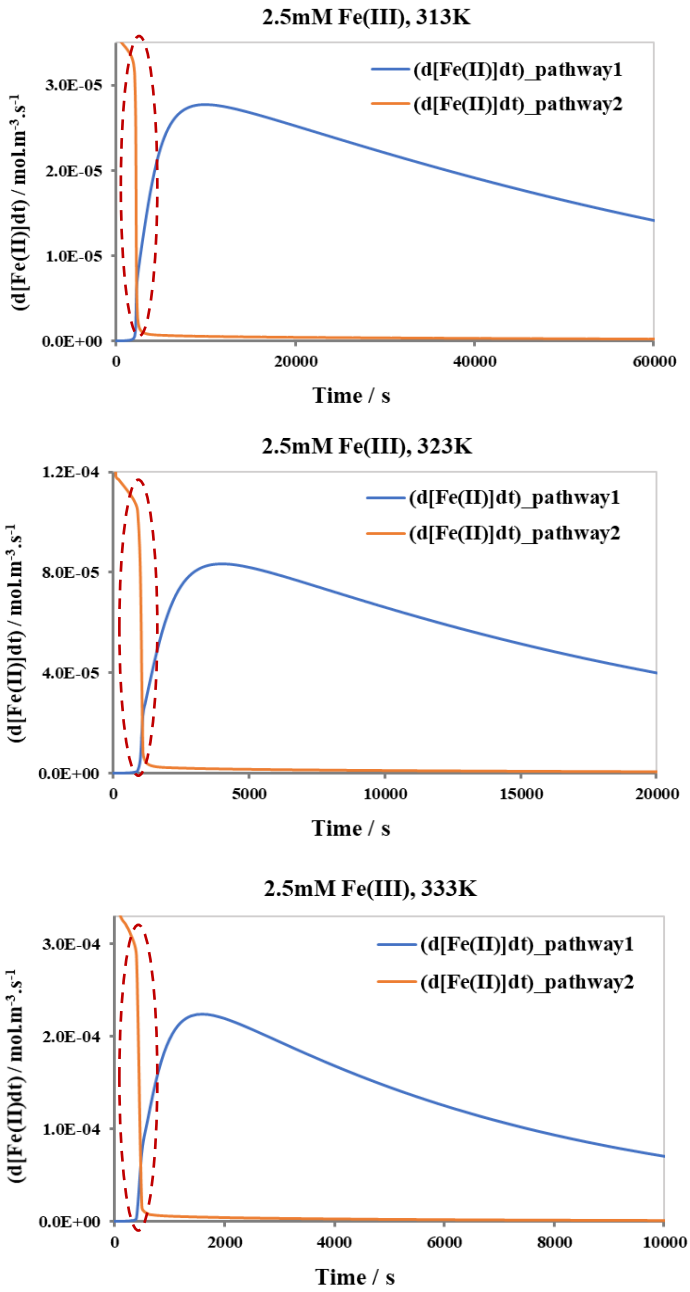

Figure 5.4: Plots of the rate equations (5.19 and 5.20) for the reduction of Fe(III) by NH_3OH^+ via pathway 1 and 2, denoted as (d[Fe(II)]dt)_pathway1 and (d[Fe(II)]dt)_pathway2 respectively, in the datasets where $[Fe(III)]_0$ = 2.5 mmol dm^{-3}, showing where the stoichiometric pathway switches during each run in Figure 5.3 from 2 to 1 as a result of the inequality in this model.

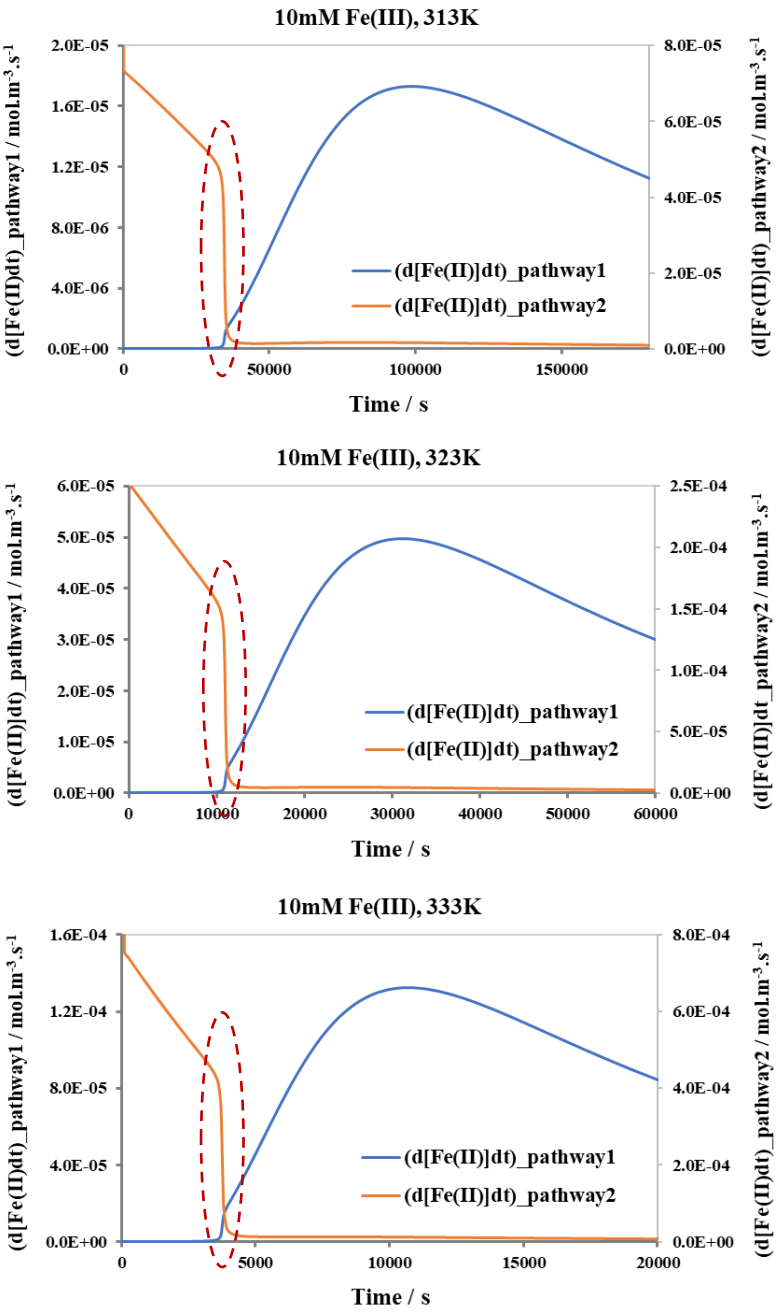

Figure 5.5: Plots of the rate equations (5.19 and 5.20) for the reduction of Fe(III) by NH_3OH^+ via pathway 1 and 2, denoted as (d[Fe(II)]dt)_pathway1 and (d[Fe(II)]dt)_pathway2 respectively, in the datasets where $[Fe(III)]_0$ = 10 mmol dm^{-3}, showing where the stoichiometric pathway switches during each run in Figure 5.3 from 2 to 1 as a result of the inequality in this model

Table 5.6: Concentrations of $Fe^{3+}_{(aq)}$ and NH_3OH^+ calculated at the point of the inequality switch for each dataset in Figure 5.3.

Initial conditions		Calculated values at the point of inequality switch			
[Fe(III)] / mM	Temperature / K	Time / s	$[Fe^{3+}_{(aq)}]$ / mM	$[NH_3OH^+]$ / mM	$\left(\frac{[Fe(III)]}{[NH_3OH^+]}\right)$
2.5	313	2300	1.00	0.26	3.89
2.5	323	1100	1.33	0.37	3.65
2.5	333	500	1.61	0.47	3.42
10	313	34600	3.43	0.86	3.99
10	323	11000	4.02	1.01	3.97
10	333	3800	4.56	1.17	3.90

Table 5.6 shows the concentration of Fe(III) and HAN calculated at each crossover point for the 6 runs in Figure 5.4 and Figure 5.5, as well as the calculated value of Fe(III)/HAN that may be consequently obtained. In each instance, concentrations of Fe(III) and NH_3OH^+ calculated at the crossover point correspond to a calculated value of the ratio of $[Fe^{3+}_{(aq)}]/[NH_3OH^+]$ close to 4, as expected from a value of n=0.25 giving the best fits in Figure 5.3. During a simulation, the model calculates the concentrations of each species at a set time step, in this case 100 seconds. For the 6 experimental datasets modelled, some of the calculated ratios of $[Fe^{3+}_{(aq)}]/[NH_3OH^+]$ at which the switch from pathway 2 to pathway 1 occurs are therefore further from the expected value of 4 than others, dependant on the length of the experimental run and how quickly the species concentrations change over time. For example, as shown in Table 5.6, the crossover point in the simulations at 333K occurs at a calculated $[Fe^{3+}_{(aq)}]/[NH_3OH^+]$ ratio of 3.42 and 3.90 for an initial Fe(III) concentration of 2.5 and 10 mmol dm^{-3} respectively, the latter ratio being closer to the expected value of 4 because the 100 second timestep is relatively less on the timescale of the complete simulation.

Table 5.7: Parameter estimations using the IF-statement model on Ac and Fe(II) datasets at each temperature, where n=0.25 and [Fe(III)] = $Fe^{3+}_{(aq)}$ or Fe_T (total iron concentration) in the inequality. Rate constants are given in units of mol dm^{-3} (M). Shaded values are set parameters.

[Fe(III)]	T / K	K_1	K_2	k_0 / $M^{-1}.s^{-1}$	k_1 / $M^{-1}.s^{-1}$	$k_{red,1,HAN}$ / $M^3.s^{-1}$	$k_{red,2,HAN}$ / $M.s^{-1}$	$k'_{red,2,HAN}$ / M
$Fe^{3+}_{(aq)}$	313	14.5	1.77	1.75×10^{-4}	2.05×10^{-21}	2.70×10^{-7}	5.39×10^{-5}	8.46×10^{-18}
$Fe^{3+}_{(aq)}$	323	7.41	1.44	5.05×10^{-4}	1.75×10^{-20}	5.69×10^{-7}	1.13×10^{-4}	3.53×10^{-17}
$Fe^{3+}_{(aq)}$	333	3.94	1.19	1.37×10^{-3}	1.31×10^{-19}	1.15×10^{-6}	2.28×10^{-4}	1.35×10^{-16}
Fe_T	313	14.5	1.77	1.75×10^{-4}	2.05×10^{-21}	2.84×10^{-7}	1.16×10^{-4}	8.43×10^{-18}
Fe_T	323	7.41	1.44	5.05×10^{-4}	1.75×10^{-20}	5.99×10^{-7}	2.35×10^{-4}	3.51×10^{-17}
Fe_T	333	3.94	1.19	1.37×10^{-3}	1.31×10^{-19}	1.21×10^{-6}	4.59×10^{-4}	1.33×10^{-16}

Let us now consider the data of Table 5.7 in more detail. In the first instance, we will focus on the estimations for the kinetic parameter $k_{red,1,HAN}$ in first three rows which relate to the lowest error fits shown in Figure 5.3, where [Fe(III)] is equal to $\left[Fe^{3+}_{(aq)}\right]$ in the inequality of Eqs. 5.17 and 5.18. Statistical errors are shown in Table 7.3 in Appendix B, section 7.2.4.4, inspection of which shows that incorporation of both pathway 1 and pathway 2 for the reduction of Fe(III) by HAN results in the E_a associated with $k_{red,1,HAN}$ and $k_{red,2,HAN}$ being the most important parameters to the model fits, followed by the values of A associated with the same kinetic rate constants. The E_a parameter associated with $k_{red,1,HAN}$ has slightly more influence than that associated with $k_{red,2,HAN}$, as illustrated by a t-value of 9.504 and 5.662 respectively, but both are greater than the reference t-value of 1.648 and thus statistically important. In this model iteration, the Arrhenius relationship obtained for $k_{red,1,HAN}$ gives an estimated value of 8.04×10^{-8} $M^3.s^{-1}$ at 298K in 0.1M HNO_3, slightly larger than the estimate obtained using the model in section 5.1.1, and approaching two orders of magnitude greater than that of 1.85×10^{-9} (± 0.07) $M^3.s^{-1}$ published by Bengtsson *et al.*

from their studies at this temperature in solutions of 0.1M $HClO_4$, μ = 1.0M [99]. This value is however still thought to be feasible based on the same reasons as stated previously in section 5.1.1.2; i) differences in the acidic media employed may affect the value of the rate constant as noted for the oxidation of hydroxylamine by Ce(IV) [178], and ii) described in Chapter 4 section 4.6.1 of this thesis, semi-quantitative UV/Vis spectroscopy measurements of Fe(III)-containing AHA solutions following hydrolysis suggesting a slower reduction of Fe(III) by hydroxylamine in $HClO_4$.

As explained previously in Chapter 4 (section 4.6.3), the reactions for the reduction of freely available Fe(III) and Pu(IV) by hydroxylamine are thought to follow analogous mechanisms. An average rate constant of 2.9 x 10^{-2} M^5 in HNO_3 at 303K was obtained by Barney [95] for the reduction of Pu(IV) by hydroxylamine under conditions of 1.5 – 2.5M HNO_3, i.e. higher $[H^+]$ than studied here, higher acidities being expected to inhibit the reaction as per equations 5.19 and 5.20. It has been suggested by Barney that this reduction of Pu(IV) is ultimately driven by the strength of Pu(IV) as an oxidising agent and this author predicted that the Pu(IV) reaction should be thermodynamically favoured and expected to be proceed at a rate of approximately 10^6 times greater than the Fe(III) reaction, based on a difference in redox potentials of approximately 0.18V [95]. For the set of runs shown in Figure 5.3, a calculated value of $k_{red,1,HAN}$ = 1.22 ×10^{-7} M^3 s^{-1} at 303K in 0.1M HNO_3 is obtained from the Arrhenius relationship, approximately 10^5 times less than the value of 2.9 x 10^{-2} M^5 quoted by Barney for the same reduction of Pu(IV), and thus in relatively close agreement with this prediction.

Turning our attention to the estimations of $k_{red,2,HAN}$ in the first three rows of Table 5.7, these are now seen to be approximately 1 order of magnitude greater at each temperature studied than the values obtained at the same temperatures in the previous modelling approach in which only a single pathway was assumed to occur in any one dataset, see Table 5.5. For these fits, $k_{red,2,HAN}$ is also 2-3 orders of magnitude greater than the estimations of $k_{red,1,HAN}$ at each temperature studied, the latter not being significantly changed from those obtained using the methodology of section 5.1.1, see Table 5.4. Once again, $k'_{red,2,HAN}$ is estimated to be very small using this approach, on the order of 10^{-18} – 10^{-16} as in Table 5.5. As can be seen from Table 7.3 in Appendix B section 7.2.4.4, the t-values for the Arrhenius parameters associated with $k'_{red,2,HAN}$, A and E_a, are on the order of 10^{-12} and 10^{-10} respectively – 2 orders of magnitude greater than those obtained for the previous model in section 5.1.1 where it was assumed that only the 2:1 stoichiometric pathway for the reduction of Fe(III) by HAN was active for the datasets with $[Fe(III)]_0$ = 10 mmol dm^{-3}, but once again very small, suggesting that $k'_{red,2,HAN}$ is insignificant in the estimation of the model fits

Looking next at the remaining parameter estimations for $k_{red,1,HAN}$ and $k_{red,2,HAN}$ in Table 5.7, it can be seen that, particularly in the case of $k_{red,1,HAN,}$ surprisingly little difference is observed in the kinetic parameter estimations between simulation outputs when [Fe(III)] is defined as $\left[Fe^{3+}_{(aq)}\right]$ or Fe_T in the inequality conditions given by Eqs. 5.17 and 5.18. Indeed, the plots obtained for the later definition of $[Fe(III)] = Fe_T$, shown in Figure 7.1 in Appendix B section 7.2.3, are visually identical to those presented in Figure 5.3 for the former definition of $[Fe(III)] = \left[Fe^{3+}_{(aq)}\right]$. This would suggest that either; i) the "active" species being reduced by hydroxylamine is both free and

complexed Fe(III), a theory that been previously suggested for the Pu(IV)/FHA/HNO_3 system [186], or ii) Fe(III) is not remaining bound in the complex. The former theory will be explored further in section 5.2.

Turning our attention now back to the fits for the acetate data also shown in Figure 5.3 (A-C), it can be seen that the fits to the acetate data are generally poor and very similar visually to those of the previous model iteration described in section 5.1.1. As before, the model is only able to provide a profile for acetate ingrowth that closely follows the experimental data at all temperatures when no iron is present. Fits to the data start to deviate when $[Fe(III)]_0$ = 2.5 mmol dm^{-3}, Figure 5.3 graphs A-C, and this deviation of fit from the data increases with temperature, whereas the fits to the data in these same plots obtained at the higher Fe(III) concentration of 10 mmol dm^{-3} show a large deviation from the data at all temperatures.

Looking at the parameter estimations in Table 5.7, this model once again predicts the values of k_1 on the order of 10^{-21}-10^{-19},as before, completely unchanged from either of the models in section 5.1.1 as a result of the model not adjusting the value of k_1 away from the seed values during the fit (as previously discussed in detail in section 5.1.1.2). This implies that k_1 is insignificant in the fitting process and leads to the assumption that FeL^{2+} hydrolyses at such a slow rate as to be non-existent, a conclusion in contrast to that published previously by Andrieux *et al.* [77, 83]. The insignificance of this parameter to the model fit is once again evidenced by t-values in Table 7.3 in Appendix B section 7.2.4.4, being of the order of 10^{-17} and 10^{-18}.

Overall, the kinetic modelling described thus far in both this section and in section 5.1.1, with the values of the complex equilibrium constants K_1 and K_2 set to those published in the literature, illustrates an inability of all of these models to both fit the experimentally measured [Ac] *vs*. t and [Fe(II)] *vs*. t data , and/or provide estimates of the complex hydrolysis rate constant in line with previously published values. This observation suggests omissions in the sequence of fundamental reactions considered in the mechanism that has been used in model development thus far, specifically those relating to acetate formation. Especially, additional reactions might be needed to prevent the model from over-estimating the rate of acetate production as it currently does, most noticeably for experiments conducted at higher $[Fe(III)]_0$.

5.2 Incorporating the Reduction of Complexed Fe(III) by HAN

One reaction that has already been identified as being omitted is the possible reduction of Fe(III) in complexed form. A reduction of the higher Fe(III)-AHA complexes by $NH_2OH.HCl$ has been reported previously by Hassan *et al* [187], and it has been suggested that the reduction of Fe(III) in hydroxamate-siderophore complexes may be crucial in Fe(III) transport in biological systems [188]. The reduction of AHA-complexed Fe(III) by a reductant such as the NH_2OH generated by the hydrolysis of AHA was not been explicitly included in the mechanism/sequence of reactions presented in Table 5.1 and that has underpinned the modelling presented thus far. Thus, in the next model iteration we incorporate a reduction of complexed Fe(III) by

hydroxylamine produced by the hydrolysis of AHA. The potential involvement of this reaction is indicated by:

(i) the similarity in all parameter estimations (particularly for the kinetic rate constant $k_{red,1,HAN}$) from the IF-statement model when [Fe(III)] is defined as $\left[Fe_{(aq)}^{3+}\right]$ or Fe_T in the inequality conditions of Eqs. 5.17 and 5.18; and

(ii) the thermodynamics, E_0 values presented in Figure 2.15 in Chapter 2 for the analogous Pu(IV)-AHA complexes. Specifically, Carrott *et al*. [74] obtained electrochemical measurements from which they calculated formal potentials (vs. SHE) of E^0 = +0.743V and E^0 = +0.695V for the reduction of the $Pu(AHA)^{3+}$ and $Pu(AHA)_2^{2+}$ complexes respectively. Compared with the redox potentials of E^0 = -0.05V for the N_2O/NH_2OH couple and E^0 = -0.873V for the N_2/NH_2OH [182], it can be seen that hydroxylamine should be thermodynamically capable of reducing the Pu(IV)-AHA complexes, and by analogy, might be expected to also be thermodynamically capable of reducing Fe(III)-AHA complexes.

Redox potentials of Pu(IV/III) complexes are usually higher than the analogous Fe(III/II) complexes for the same ligand. Boukhalfa and co-workers [189] investigated the redox properties of Pu(IV) complexes with natural siderophores via cyclic voltammetry, observing that the difference in redox potentials measurements between Pu(IV) complexes and the Fe(III) analogues was approximately equal to the difference between the redox potentials of their fully hydrated ions, where E^0_{aq} = +0.77 V for $Fe(III)(H_2O)_6^{3+}$ is about 0.18 V lower than E^0_{aq}= +0.95 V for $Pu(IV)(H_2O)_9^{4+}$. If we assume the same trend for the AHA-complexed ions, then E^0 for Fe(III)(AHA) would

be approximately +0.63 V in 0.1M HNO_3, based on the measured value of +0.81 V for the reduction of Pu(IV)(AHA) in 0.1M HNO_3 [74]. Compared with the redox potentials of E^0 = -0.05V for the N_2O/NH_2OH couple and E^0 = -0.873V for the N_2/NH_2OH couple shown in Figure 4.42, this would suggest that hydroxylamine is thermodynamically capable of reducing the Fe(III)(AHA) complex.

However, as discussed in section 4.6.3, the mechanism for the 1-electron reduction of free Fe^{3+} cations by NH_2OH is a 2-step process whereby; i) Fe^{3+} is reduced by NH_2OH to form Fe^{2+} and the aminoxyl radical species H_2NO^* in a series of rapid equilibrium processes, and ii) the so-formed unstable radical H_2NO^*, as well as participating in the reverse of the aforementioned equilibrium processes, may also undergo a dimerization which serves as a final, rate-controlling step in the generation of the products water and N_2. This is shown in Eqs 4.41-4.44 in Chapter 4, reproduced here for the convenience of the reader as Eqs. 5.21–5.24.

$$NH_3OH^+ \overset{K_a}{\rightleftharpoons} NH_2OH + H^+ \tag{5.21}$$

$$Fe^{3+} + NH_2OH \overset{\beta_1'}{\rightleftharpoons} Fe(NH_2OH)^{3+} \tag{5.22}$$

$$Fe(NH_2OH)^{3+} \rightleftharpoons Fe^{2+} + H_2NO^* + H^+ \tag{5.23}$$

$$2H_2NO^* \rightarrow N_2 + 2H_2O \tag{5.24}$$

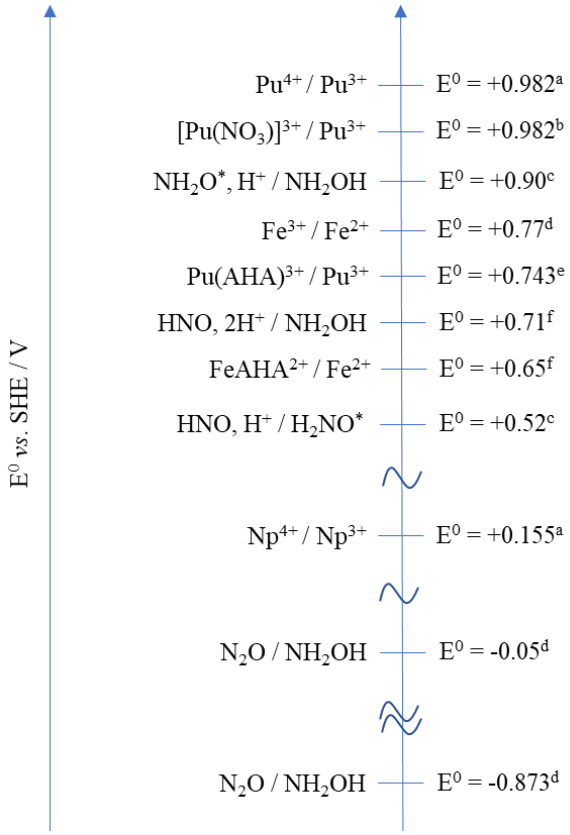

Figure 5.6: Schematic diagram showing formal redox potentials E^0 in volts (V) vs. standard hydrogen electrode (SHE). [a][Lemire, 2001], [b][Carrot et al., 2008], [c][Lind and Merenyi], [d][Bard et al., 1985], [e][Andrieux et al., unpublished], [f]calculated in this thesis.

It is not unreasonable to assume that an analogous mechanism operates in the putative reduction of the monoacetohydroxamatoiron(III) complex i.e. this proceeds by a 1-electron reduction of the 1:1 Fe(III)(AHA) complex by NH_2OH which therefore involves the oxidation of NH_2OH to the aminoxyl radical. In this context, it is informative to consider the relative positions of the redox potentials for the Fe(III)-AHA complex and the hydroxylamine/aminoxyl radical couple within a modified version of the redox ladder of Figure 4.42. This is shown in Figure 5.6. From this, it can be seen that the above estimated value of E^0 = +0.63V for the reduction of the Fe(III)-AHA complex would fall below the standard redox potential for the 1-electron

oxidation of hydroxylamine, $E^0(H_2NO^*, H^+ / H_2NOH)$ = 0.90V [181], suggesting that hydroxylamine is thermodynamically incapable of reducing the 1:1 Fe(III)(AHA) complex via a 1-electron reduction analogous to Eqs 5.22 and 5.23 under the conditions of our datasets, i.e 0.1M HNO_3.

However, the value of +0.63 V for the reduction of the Fe(III)-AHA complex is an estimate based on the value of the reduction potential for the Pu(IV)-AHA complex, see above. A more robust value for the reduction potential for the Fe(III)-AHA complex can be obtained from Eq. 5.25, which describes how the standard redox potential for the mono-complex/Fe^{2+} couple, $E^0_{FeL^{2+}/Fe^{2+}}$ can be determined from the standard redox potential of the Fe^{3+}/Fe^{2+} couple, $E^0_{Fe^{3+}/Fe^{2+}}$, and the equilibrium constant for the formation of the mono-complex, K_1. The derivation of Eq. 5.25, in which complexed AHA is defined as L, is shown in the Appendix B section 7.2.1.

$$E^0_{FeL^{2+}/Fe^{2+}} = E^0_{Fe^{3+}/Fe^{2+}} - \frac{RT}{F}\ln K_1 \qquad (5.25)$$

In deriving Eq.5.25, it is assumed that the reduction of AHA-complexed Fe(III) would produce a less stable Fe(II)-AHA complex which is likely to immediately dissociate (the K value for the formation of the monoacetohydroxamatoiron(II) complex, Fe(II)-AHA, is small at 1.95×10^{-5} [188]); thus complexation of Fe(II) with AHA to form Fe(II)-AHA does not need to be considered in the derivation of Eq. 5.25.

Incorporating into Eq, 5.25 the value of the mono-complex equilibrium constant at a temperature (T) of 298K, K_1=109 [190] (the value that will be used in our final model iteration described in section 5.3), and the values for Faraday's constant, F=96,485 C

mol^{-1}, and the universal gas constant, R=8.314 J K^{-1} mol^{-1}, we can obtain a value of +0.65V for the standard redox potential of the FeL^{2+}/Fe^{2+} couple. This value is in close agreement with the value of E^0 = +0.63V for this same redox couple obtained from the estimate described above. As per that estimate, it once again suggests that a 1-electron reduction of the 1:1 Fe(III):AHA complex by NH_2OH is thermodynamically unlikely.

However, we can now use the calculated value of $E^0_{FeL^{2+}/Fe^{2+}}$=0.65V to perform an analogous investigation as we did previously in Chapter 4 section 4.6.3 whereby we examined the mechanism of the reduction of free Fe^{3+} by NH_2OH and the thermodynamic feasibility of that reaction under the specific pHs, temperatures, Fe^{3+} and NH_2OH concentrations employed in that study.

That approach resulted in the generation of plots showing the dependence of the redox potentials (as opposed to the standard redox potentials) for the Fe^{3+}/Fe^{2+} and hydroxylamine/aminoxyl radical couple as a function of the concentration of the generated aminoxyl radical. From this, a radical concentration range over which Fe(III) may be reduced by NH_2OH to form the radical could be identified. Here, we adopt an analogous approach for the reduction of the Fe(III)AHA complex by NH_2OH.

Using standard E^0 values and Eqs. 5.26 and 5.27, where based upon the overall stoichiometries of Eqs. 5.21-5.24 we assume that at short reaction times $[Fe^{2+}] \approx [H_2NO^*]$, values of the redox potentials E may be calculated for both the FeL^{3+}/Fe^{2+} and H_2NO^*/NH_2OH couples as a function of $[H_2NO^*]$.

$$E(NH_2O^*/NH_2OH) = E^0 + \frac{RT}{F}\ln\frac{[NH_2O^*][H^+]}{[NH_2OH]} \quad (5.26)$$

$$E(FeL^{3+}/Fe^{2+}) = E^0 + \frac{RT}{F}\ln\frac{[FeL^{3+}]}{[Fe^{2+}]} \approx E^0 + \frac{RT}{F}\ln\frac{[FeL^{3+}]}{[NH_2O^*]} \quad (5.27)$$

The resulting plots of this analysis, shown in Figure 5.7 for a concentration of FeL^{2+} = 5 mmol dm^{-3} at 313, 323 and 333K, are compared to those previously calculated for concentrations of Fe^{3+} = 10 mmol dm^{-3} and Np^{4+} = 5 mmol dm^{-3} in Chapter 4 section 4.6.3. According to these previous calculations, a concentration of H_2NO^* of less than ~0.1 µmol dm^{-3} would be required before it would be thermodynamically possible for NH_2OH to reduce Np(IV), and whilst the concentration of a radical species is expected to be low, it is not unreasonable to assume that a concentration of H_2NO^* greater than 0.1 µmol dm^{-3} is plausible – i.e. the reduction of Np(IV) by NH_2OH to form Np(III) and H_2NO^* is unlikely to occur, as is observed experimentally. To allow for NH_2OH to reduce Fe^{3+}, the required concentration of this same radical species was calculated to be less than approximately 1 mmol dm^{-3}. Given the reactivity of radical species, it is not unreasonable to assume that the concentration of the H_2NO^* does not exceed this threshold and that the reduction of Fe(III) by NH_2OH can be deemed to be thermodynamically possible by this analysis – in contrast to the same reduction of Np(IV) as discussed above.

Using the calculated standard redox potential of E^0=0.65V for the FeL^{2+}/Fe^{2+} couple, analogous plots to those obtained for the Fe^{3+}/Fe^{2+} and Np^{4+}/Np^{3+} couples in Figure 5.7 can now be generated for the FeL^{2+}/Fe^{2+} couple, see Figure 5.7 also. From this, it can be seen that a NH_2O^* concentration of less than ~0.1 mmol dm^{-3} is required for it to be thermodynamically possible for NH_2OH to reduce FeL^{2+} via a 1 electron transfer to form H_2NO^* and Fe(II) respectively. Following the approach adopted above, given

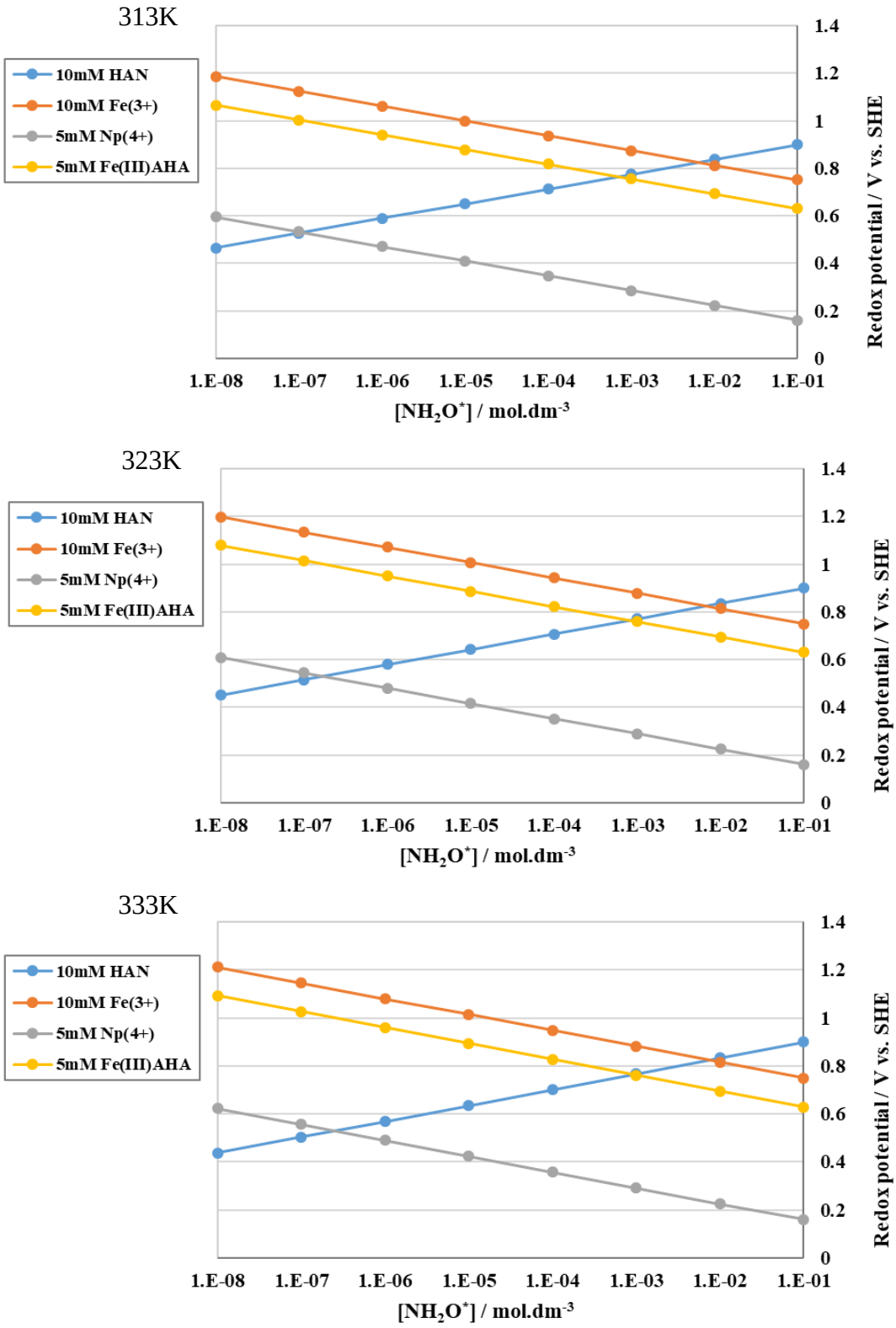

Figure 5.7: Redox potentials as a function of [NH_2O] for the (NH_2O^*/NH_2OH), (Fe^{3+}/Fe^{2+}), (Np^{4+}/Np^{3+}) and ($FeAHA^{2+}/Fe^{2+}$) couples for a 0.1 mol dm^{-3} H^+ system at 313K, 323K and 333K. Calculated for concentrations of NH_2OH and Fe^{3+} = 10 mmol dm^{-3}, and for Np^{4+} and $FeAHA^{2+}$ = 5 mmol dm^{-3}.*

the reactivity of radical species, it is again not unreasonable to assume that the concentration of the H_2NO^* radical does not exceed this threshold and that the 1 electron reduction of FeL^{2+} by NH_2OH with a 1:1 stoichiometry to form Fe^{2+} and H_2NO^* may be thermodynamically possible.

It might therefore be acceptable to predict the occurrence of the reduction of mono-complexed Fe(III) by NH_3OH^+ in the systems under study here in accordance with the reaction given below in Eq. 5.28. As discussed above, the reduction of the AHA-complexed Fe(III) (complexed AHA defined as L in Eq. 5.28) would produce a less stable Fe(II)-AHA complex which is likely to dissociate, in turn producing free AHA (defined as HL in Eq. 5.28) which could re-complex free Fe(III) or hydrolyse.

$$NH_3OH^+ + Fe(III)L^{2+} \rightarrow Fe(II)L^+ \rightarrow Fe^{2+} + HL \qquad (5.28)$$

The direct 1 electron reduction of the complex, and the resultant decrease in total Fe(III) concentration, may ultimately supress the concentration of the Fe(III)-AHA mono-complex and thus opportunity for its hydrolysis. This would be in keeping with the findings of the previous model iterations described in section 5.1, which have shown the hydrolysis of the mono-complex to be insignificant i.e. the hydrolysis of the mono-complex may be rendered insignificant by the dominance of the complex reduction reaction. We shall explore this idea in more detail in the next section.

5.2.1.1 Model description

As mentioned at the start of section 5.1.2.2, the reduction of the higher Fe(III)-AHA complexes by $NH_2OH.HCl$ has been reported previously by Hassan *et al* [187]. These

authors utilised UV/Vis spectroscopy and stopped flow techniques to investigate this reduction reaction at pH 4.5 – 5.5 with relevance to biological systems where the more stable bis- and tris-complexes dominate. They report a biphasic reaction; a slow phase which they attributed to the dissociation of $Fe(AHA)_3$ to produce $Fe(AHA)_2^+$, followed by a fast phase attributed to the reduction of $Fe(AHA)_2^+$ to $Fe(AHA)^{2+}$. A simple rate equation, first order with respect to $Fe(AHA)_2^+$ and NH_3OH^+, was suggested for the latter process. In relation to the general trend in complex stability, the susceptibility of the complexes to reduction is expected to be $Fe(AHA)^{2+} > Fe(AHA)_2^+ > Fe(AHA)_3$ i.e. the mono-complex is reduced faster than the bis-complex which, in turn, is reduced faster than the tris-complex.

For our system at pH 1 where the mono-complex dominates, the reduction of FeL^{2+} was thus modelled as a single reaction (R7) below, using an equivalent rate equation to that suggested by Hassan *et al* [187] for the reduction of $Fe(AHA)_2^+$ (Eq. 5.29), with a rate constant $k_{red,1,FeL}$.

$$NH_3OH^+ + FeL^{2+} \xrightarrow{k_{red,1,FeL}} Fe^{2+} + HL + products \quad \text{(R7)}$$

$$\frac{d\left[Fe^{2+}\right]}{dt} = k_{red,1,FeL}\left[FeL^{2+}\right]\left[NH_3OH^+\right] \quad (5.29)$$

The earlier iterations of the model described in section 5.1 showed the rate constant k_1 for the hydrolysis of the ligand in the FeL^{2+} complex to be insignificant and thus the loss of the ligand to be dominated by the hydrolysis of the free AHA with rate constant k_0. This, and the fact that the experimentally observed ingrowth of acetic acid is always slower that that calculated during the modelling of Figure 5.3, together suggest that more of the ligand may exist in the complex than allowed by the equilibrium constants

currently used in the modelling. In addition, this would therefore also mean that more of the total Fe(III) will be in complexed form than expected based on published literature and thus complex reduction must be considered, particularly considering the similarity in all parameter estimations (especially those for the kinetic rate constant $k_{red,1,HAN}$) from the IF-statement model when [Fe(III)] is defined as $\left[Fe^{3+}_{(aq)}\right]$ or Fe_T in the inequality conditions of Eqs. 5.17 and 5.18.

In addition to the incorporation of the reduction of the FeL^{2+} complex in this model iteration, values of the complex equilibrium constants, K_1 and K_2, were therefore also estimated rather than set to values derived from the literature as described in section 5.1. By allowing the values of K_1 and K_2 to float, the gPROMS software can obtain statistical data for these parameters, particularly t-values, which allows us to see how important they are to the fits in relation to other parameters.

5.2.1.2 Model output and discussion

Thus the data was modelled using the approach of section 5.1.2.2 (i.e. implementing the IF statement) modified (i) to include the reduction of the mono-complex and (ii) to let K_1 and K_2 float during the parameter estimation process. The closest fits obtained using this new model are shown in Figure 5.8.

Considering first the acetate data of Figure 5.8 A-C, it can be seen that the fits obtained using this model are much closer to the experimental data compared to those fits obtained from previous model iterations described in section 5.1. This suggests that along with the estimation of the equilibrium constants K_1 and K_2, the incorporation of

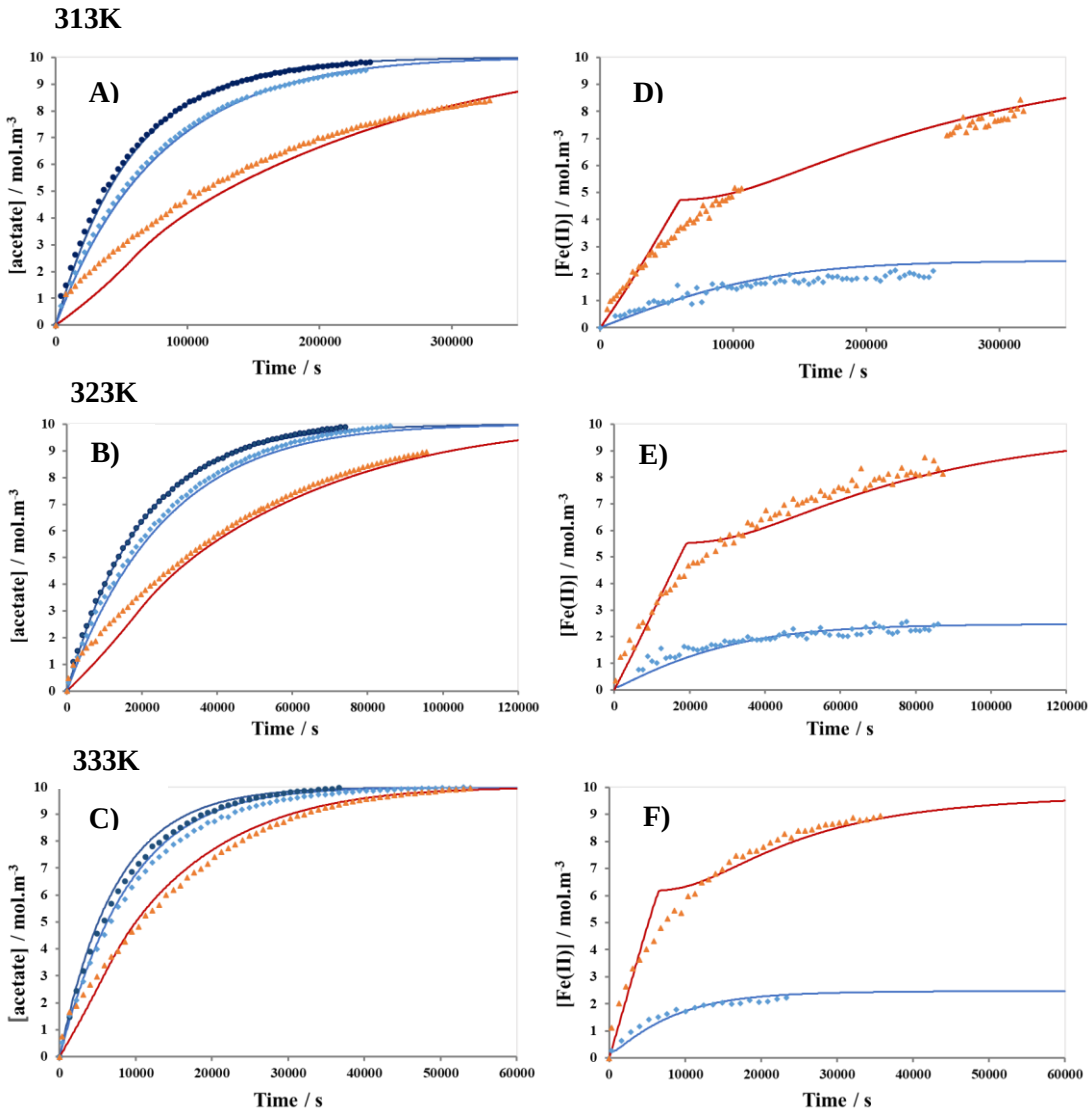

Figure 5.8: Plots of experimental data and model output at 313K (A &D), 323K (B &E) and 333K (C & F) from which parameter estimations were obtained using the IF-statement model with [Fe(III)] = [$Fe^{3+}_{(aq)}$] and n=0.25 in the inequality, with the addition of FeL^{2+} reduction by NH_3OH^+. Plots A-C: Experimental data (points) and model output (lines) for Ac, when [Fe(III)]$_0$ = 0 (dark blue), 2.5 (light blue) and 10 mmol dm^{-3} (orange). Plots D-F: Experimental data (points) and model output (lines) for Fe^{2+}, when [Fe(III)]$_0$ = 2.5 (light blue) and 10 mmol dm^{-3} (orange). For the data obtained at 3131K with 10 mmol dm^{-3} initial Fe(III), a system fault overnight caused a large stoppage period in data acquisition in which the IC system had to be cleaned, re-equilibrated and put back into operation

the reduction of FeL^{2+} by NH_3OH^+ as an additional reaction here, might be engendering in some way the more gradual ingrowth of acetate that is seen experimentally in these chemical systems, but which has not been as successfully simulated in any of our previous gPROMS model iterations. The argument for

including the reduction of Fe(III) in the FeL^{2+} complex by NH_3OH^+ is further strengthened by considering previous gPROMS simulations presented in section 5.1.2.2 – specifically the simulation in which an inequality was incorporated that allowed for switching between a 2:1 and 1:1 stoichiometry for the reduction of Fe(III) by NH_3OH^+ in any one modelled experimental run. The results of this previous simulation suggested the "active" Fe species in the inequality could potentially be either $Fe^{3+}_{(aq)}$ or complexed Fe(III).

Inspection next of the Fe(III) data of Figure 5.8 D-F shows significantly improved fits to all the datasets obtained at $[Fe(III)]_0$ = 10 mmol dm^{-3} than have been obtained in previous model iterations in section 5.1, particularly to those datasets at the elevated temperatures of 323K and 333K, although an obvious "kink" is still observed in the model fit upon switching from pathway 2 to pathway 1. Incorporation of the reduction of Fe(III) in the FeL^{2+} complex by NH_3OH^+ into the model and allowing equilibrium constants K_1 and K_2 to be estimated thus appears to have now allowed gPROMS to successfully reproduce the high Fe(II) concentrations seen at longer timescales in our experimental data at the higher temperatures.

Parameter estimations obtained by this approach, i.e. incorporating reaction R7 and fitting for values of K_1 and K_2, are shown in Table 5.8.

Table 5.8: Parameter estimations using the IF-statement model on Ac and Fe(II) datasets at each temperature, where n=0.25 and [Fe(III)] = $Fe^{3+}_{(aq)}$ or Fe_T in the inequality, and the inclusion of FeL^{2+} reduction by NH_3OH^+. Rate constants are given in units of mol dm^{-3} (M). Shaded values are set parameters.

T / K	K_1	K_2	k_0 / $M^{-1}.s^{-1}$	k_1 / $M^{-1}.s^{-1}$	$k_{red,1,HAN}$ / $M^3.s^{-1}$	$k_{red,2,HAN}$ / $M.s^{-1}$	$k'_{red,2,HAN}$ / M	$k_{red,1,FeL}$ / $M^{-1}.s^{-1}$
313	203	0.26	1.75×10^{-4}	2.05×10^{-21}	1.95×10^{-6}	1.66×10^{-2}	8.45×10^{-18}	1.32×10^{-7}
323	101	0.21	5.05×10^{-4}	1.75×10^{-20}	3.93×10^{-6}	3.03×10^{-2}	3.52×10^{-17}	3.97×10^{-7}
333	52.9	0.18	1.37×10^{-3}	1.31×10^{-19}	7.61×10^{-6}	5.33×10^{-2}	1.35×10^{-16}	1.12×10^{-6}

Focussing our attention first on the estimates for $k_{red,1,HAN}$ and $k_{red,2,HAN}$ relating to pathway 1 and 2 respectively for the free Fe(III) reduction by hydroxylamine in Table 5.8, the estimates of $k_{red,1,HAN}$ are now of the order of 10^{-6} M^3 s^{-1}, approximately an order of magnitude greater than those obtained in either of the previous gPROMS iterations described in sections 5.1.1 and 5.1.2. The estimations for $k_{red,2,HAN}$ are now of the order of 10^{-2} M s^{-1}, approximately 2-3 orders of magnitude greater than estimations obtained in any of the previous model iterations. Inspection of the statistical parameter values in Table 7.4 Appendix B section 7.2.4.4 reveals that, whilst very similar, the t-values for each of the Arrhenius parameters for $k_{red,2,HAN}$ are now slightly larger than those t-values for the corresponding Arrhenius parameters for $k_{red,1,HAN}$ – indicating that $k_{red,2,HAN}$ is slightly more important than $k_{red,1,HAN}$ in the model fit. This is in contrast to the previous model iteration in section 5.1.2 (which did not incorporate the reduction of the FeL^{2+} complex by hydroxylamine) wherein $k_{red,1,HAN}$ was found to be more important than $k_{red,2,HAN}$ in the model fit.

Focussing next on the parameter estimations of k_1, these are once again on the order of 10^{-21}-10^{-19} and completely unchanged from any of the model iterations described in section 5.1 as a result of the model not adjusting the value of k_1 away from the seed values during the fit (as previously discussed in detail in section 5.1.1.2). The t-values in Table 7.4 are also unchanged, on the order of 10^{-17} and 10^{-18} and thus evidence the insignificance of this parameter to the model fit.

Next we turn our attention to the estimations for the kinetic rate constant $k_{red,1,FeL}$ for the reduction of the FeL^{2+} complex. Parameter estimations for this rate constant are found to be on the order of 10^{-7} – 10^{-6} M^{-1} s^{-1}. With regards to its significance to the

model fit, t-values for the Arrhenius parameters A and E_a are on the order of 10^{-6} and 10^{-4} respectively, which places the significance of the parameter estimations for $k_{red,1,FeL}$ beneath those for $k_{red,1,HAN}$ and $k_{red,2,HAN}$, in determining the quality of the model fits – but markedly greater than those for $k'_{red,2,HAN}$ and k_1 in the order of importance to the model fit. This observation thus suggests that consideration of the reduction of Fe(III) in the FeL^{2+} complex by NH_3OH^+ is of marginal necessity at best.

Inspection of Table 5.8 reveals in this model iteration, parameter estimations of K_1 and K_2, obtained at the temperatures of the experimental data modelled are, respectively, approximately one order of magnitude greater than and less than those reported in the literature [83]. Inspection of the t-values, Table 7.4 Appendix B section 7.2.4.4, reveals that the $\alpha_{c,1}$ parameter relating to K_1 is the most important to the model fit, followed by the activation energies relating to the kinetic rate constants for the reduction of free Fe(III) by hydroxylamine by pathway 1 and 2, $k_{red,1,HAN}$ and $k_{red,2,HAN}$, - the latter two parameters having had the highest t-values in all previous model iterations.

In the parameter estimation process, bounds must be set within which the value of the estimated parameter is allowed to vary before converging on a final value. When modelling a complicated chemical system that includes a large number of parameter estimations, this involves performing several gPROMS simulations whereby bounds are initially set very wide to obtain a rough value for any one parameter, and slowly and systematically lowering the range of the bounds in subsequent simulations to allow gPROMS to converge on the optimal value for that parameter. The value of $\eta_{c,1}$relating to K_1 hit the upper bound and therefore values of statistical parameters were not able to be computed.

The t-value associated with the $\alpha_{c,1}$ value for K_2 is much less than that for K_1 (0.055 compared to 69.04) and is probably a reflection of the small size of K_2 in an absolute sense and thus an associated low concentration of the 2:1 complex in the solutions under study here.

In this iteration of the model, the van't Hoff relationships estimated for the temperature dependence of the equilibrium constants gives values at 298K of 624 and 0.353 for K_1 and K_2 respectively. The estimation of the former parameter is significantly higher than other values reported in the literature, with Monzyk *et al*. [190] suggesting K_1 = 109 and Andrieux *et al.* [57] reporting a value of K_1 = 40.65 at 298K. In contrast, the estimation for K_2 obtained at 298K is approximately an order of magnitude lower than the equivalent value of K_2 = 2.56 reported by Andrieux *et al.* [57]. Thus, along with the observation that the value $\eta_{c,1}$relating to K_1 hit the upper bound in this simulation, these results suggest that the approach to estimation of the equilibrium constants K_1 and K_2 requires further modification.

Whilst there are several determinations of the equilibrium constants of formation for Fe(III)-AHA complexes at 298K described in the scientific literature base [57, 190, 191], it is worthwhile pointing out that data pertaining to the same values at elevated temperatures is limited to a single study by Andrieux *et al.* [57], and it is therefore possible that the temperature dependence of the equilibrium constants for the formation of the complexes, particularly the mono-complex, may differ to that previously published i.e. the elevated temperature data of Andrieux *et al.* [57]. should be used with caution. We shall return to this point below.

Overall, this model iteration shows great promise providing, in particular, significantly improved fits to the acetate data which shows a more gradual ingrowth of acetate with increasing $[Fe(III)]_0$, and reproduction of the high Fe(II) concentration seen at longer timescales in the experimental datasets with $[Fe(III)]_0$ = 10 mmol dm^{-3}. These fits are achieved in this model iteration in two ways, namely; i) by allowing the equilibrium constants to float, and ii) by incorporation of the reduction of the FeL^{2+} complex by hydroxylamine into the mechanism/sequence of reactions presented in Table 5.1 that underpins the modelling; in comparison, in the previous model iterations described in section 5.1, the acetate production was controlled solely by the hydrolysis of the free and complexed AHA.

There are however two primary issues still with this model iteration that need to be rectified, namely; i) in fitting the Fe(II) data, use of the inequality to switch from pathway 2 to pathway 1 for the reduction of free Fe(III) by hydroxylamine results in a large kink in the model fit that does not match the smooth ingrowth of Fe(II) observed experimentally, and ii) allowing the equilibrium constants to float produces estimates of these values, particularly K_1, that are significantly different to those previously published at the elevated temperatures considered here [57]. Thus, two final model iterations were performed to address both these issues and ultimately produce the final best fits to the experimental datasets, discussion of which is the subject of the next section.

5.3 Final Modelling

To address the issues outlined above, two final model iterations were performed with the following changes:

iv) A single rate equation, which will be referred to in the remainder of this thesis as a modified Bengtsson equation, was derived to describe the reduction of free Fe(III) by hydroxylamine and incorporated into the model. This is used in place of the rate expressions derived by Bengtsson [99] used thus far in our kinetic models described in sections 5.1 and 5.2, which are for two limiting cases of the reduction of Fe(III) by HAN by either a 1:1 or 2:1 stoichiometric pathway to produce either N_2 or N_2O as a product.

v) The values of K_1 and K_2 were set to published literature values at 298K only but are estimated at all other temperatures used in this study. Whilst there are several determinations of the equilibrium constants of formation for Fe(III)-AHA complexes at 298K described in the scientific literature base [57, 190, 191], data pertaining to the same values at elevated temperatures is limited to a single study by Andrieux *et al.* [57], and it is therefore possible that the temperature dependence of the equilibrium constants for the formation of the complexes, particularly the mono-complex, may differ to that reported in Andrieux's singleton paper.

Both of these model iterations will be discussed in turn the following sections 5.3.1 and 5.3.2.

5.3.1 Incorporation of a Single Modified Bengtsson Equation

The original rate expression published for the reduction of Pu(IV) by HAN was obtained primarily under conditions of high initial HAN/Pu(IV) ratios, between approximately 4-16, and was found to fit reasonably well to experimental data by Koltunov and Zhuravleva [171] when HAN was in vast excess. However Yarbro [98] later showed the fit using this expression is poor when low HAN/Pu ratios are used, said ratios typical of those found in reprocessing plants. Instead, they derived a single rate expression for all HAN/Pu ratios in terms of a fractional conversion rather than concentrations, overall obtaining improved fits to the data in this way.

The rate expressions used thus far in our kinetic models, as derived by Bengtsson [99], are for two limiting cases of the mechanistically analogous reduction of Fe(III) by HAN to produce either N_2 or N_2O as a product. In reality an intermediate region will likely exist between these two limiting cases whereby a mixture of N_2 and N_2O will be obtained, and consequently, a single rate expression is likely to produce better fit results as found in the case of Pu(IV) systems with low HAN/Pu ratios modelled by Yarbro and described above [98]. Thus, the following sections describe the derivation and incorporation of a single expression for the reduction of Fe(III) by hydroxylamine to replace the inequality switch in our kinetic model described in the previous section 5.2, with an aim to remove the kink and provide smoother and improved model fits to the Fe(II) data.

In order to produce a single kinetic rate equation for the reduction of Fe(III) by HAN, an examination of the mechanism for the two stoichiometric pathways as suggested by

Bengtsson [99] was required. This is shown in Eqs 4.41 - 4.46 in Chapter 4, reproduced here for the convenience of the reader as reactions R8 – R11 (shown previously at the start of section 5.2 as Eq. 5.21 – 5.24) and R12 – R13. Rate constants for reactions R9 – R13 have been assigned as k_{9-13}, the number corresponding to the relevant reaction number. These are ultimately used in the derivation of the modified Bengtsson equation.

$$NH_3OH^+ \overset{K_a}{\rightleftharpoons} NH_2OH + H^+ \quad \text{(R8)}$$

$$Fe^{3+} + NH_2OH \overset{\beta_1'}{\rightleftharpoons} Fe(NH_2OH)^{3+} \quad where\ \beta_1' = k_9, k_{-9} \quad \text{(R9)}$$

$$Fe(NH_2OH)^{3+} \overset{k_{10},\ k_{-10}}{\rightleftharpoons} Fe^{2+} + H_2NO^* + H^+ \quad \text{(R10)}$$

$$2H_2NO^* \overset{k_{11}}{\longrightarrow} N_2 + 2H_2O \quad \text{(R11)}$$

$$Fe^{3+} + H_2NO^* \overset{k_{12},\ k_{-12}}{\rightleftharpoons} Fe^{2+} + HNO + H^+ \quad \text{(R12)}$$

$$2HNO \overset{k_{13}}{\longrightarrow} N_2O + H_2O \quad \text{(R13)}$$

The suggested first step is the deprotonation of NH_3OH^+ to produce NH_2OH as the reactive species, followed by a rapid formation of a precursor complex $Fe(NH_2OH)^{3+}$ formed with Fe^{3+} or $Fe(OH)^{2+}$. The decomposition of the complex produces the H_2NO^* radical which dimerizes to form N_2 as a product. However, when Fe(III) is in excess, it can participate in a second step in the mechanism for the oxidation of hydroxylamine, reacting with the H_2NO^* radical species to form the HNO radical by R12, the latter of which radical species can dimerize and produce N_2O as the end product, R13. and ultimately competing with the dimerization of H_2NO^* (R11).

In deriving a single rate equation however, we consider the dimerization of the H_2NO^* radical to be unlikely due to the low availability of the radical species in solution.

Whilst the simple aminoxyl radical has no steric encumberment near the radical centre and is thus highly reactive [192], the low concentrations of the H_2NO^* radical that will be present are expected to make a dimerization reaction unlikely, whereas the reaction of this radical with the significantly more abundant $Fe^{3+}_{(aq)}$ ion is therefore suggested to be a more likely pathway.

Based on the above mechanism (R8 – R13) proposed by Bengtsson a steady-state analysis was performed based on no dimerization of H_2NO^*, and by analogy HNO, with the aim to derive a single equation for the reduction of Fe(III) by hydroxylamine and thus a smoother fit. The final rate expression obtained, described in the remainder of this thesis as the modified Bengtsson equation, is given by Eq. 5.30 below, the derivation of which is shown in Appendix B section 7.2.2.

$$\frac{d[Fe^{2+}]}{dt} = B\frac{[Fe^{3+}]^2[NH_3OH^+]^2}{[Fe^{2+}]^2[H^+]^4}\left(1 + C\frac{[Fe^{3+}]^2}{[Fe^{2+}]^2[H^+]^2}\right) \qquad (5.30)$$

$$where \quad B = \frac{2k_{11}{k_{10}}^2{\beta_1'}^2{K_a}^2}{{k_{-10}}^2} \quad and \quad C = \frac{4k_{13}{k_{12}}^2{k_{10}}^2{\beta_1'}^2{K_a}^2}{{k_{-12}}^2{k_{-10}}^2}$$

In order to guide the parameter estimations using the above single modified Bengtsson equation of Eq. 5.30, an attempt was made to obtain an initial approximation for the parameters *B* and *C* by looking at available literature on the elementary reactions of which they are composed. This is the subject of section 5.3.1.1 below.

5.3.1.1 Estimation of B and C from the literature

First we consider the combination of elementary rate constants that make up the parameter *B*. The dimerization of the aminoxyl radical, H_2NO^*, was investigated

recently by Lind and Merenyi [181] via pulse radiolysis. With relevance to the thermochemistry of the H_2NO^* radical, these authors also studied the thermodynamics of the 1:1 stoichiometry reaction of Fe^{3+} and NH_3OH^+ to obtain only N_2 as the product. They describe a simplified mechanism shown by Eq. 5.31, the overall reaction of R8 – R10 with $K_{eq} = \frac{K_a \beta_1 k_{10}}{k_{-10}}$, and R11, to give the overall reaction R5.

$$Fe^{3+} + NH_3OH^+ \overset{K_{eq}}{\rightleftharpoons} Fe^{2+} + H_2NO^* + 2H^+ \quad (5.31)$$

$$2H_2NO^* \xrightarrow{k_{11}} N_2 + 2H_2O \quad (R11)$$

$$Fe^{3+} + NH_3OH^+ \xrightarrow{k_5} Fe^{2+} + 0.5N_2 + 2H^+ + H_2O \quad R5$$

By performing stopped flow experiments at an ionic strength of ca. 1 M, with the ionic medium composed mainly of $HClO_4$ and $NaClO_4$, Lind and Merenyi [181] report an observed rate constant $k_{11} = 1.4 \times 10^8$ M^{-1} s^{-1}. Utilising their simplified mechanism for which they suggest $k_5 = (K_{eq}^2) \times (2k_{11})$, the authors own experimental value for the dimerization of the aminoxyl radical of $2k_{11} = 2.8 \times 10^8$ M^{-1} s^{-1}, and the observed value of k_5 reported by Bengtsson [99] of 1.85×10^{-9} M^3 s^{-1} in 0.1M $HClO_4$, these authors also obtain a value of $K_{eq} = 2.6 \times 10^{-9}$ M^2 for Fe^{3+}/Fe^{2+} [181].

The values published by Lind and Merenyi [181] have also recently been used in simulations at environmental pH's by Li *et al* [193] to calculate individual values of β_1' for the complexation reaction of Fe^{3+} and NH_2OH, and the forward and backward rate constants, k_{10} and k_{-10}, for the production of the dissociation of the $Fe(NH_2OH)^{3+}$ intermediate to produce H_2NO^*. These, amongst values available in the literature for other elementary reactions involved in the parameters *B* and *C* which are discussed below, are summarized in Table 5.9.

Whilst literature relating to any of the elementary rate constants under acidic conditions is sparse, there has been one such study on the complexation between Fe^{3+} and NH_3OH^+ (R9) at 25ºC, and under acidic conditions of pH 1 and a constant ionic strength 0.1 mol dm^{-3}, in which an observed rate constant of 8.1 M^{-1} s^{-1} is calculated [194]. No detail is given for the backward reaction rate, k_{-9} but the complex is suggested to be stable under these conditions and it is assumed to be small.

Table 5.9: Rate constants for elementary reactions used in estimation of B and C. Values are given at 298K. [a]Independent of pH, [b]Calculated from observed rate constant of Bengtsson, k_{TOT} =1.85 × 10^{-9} M^3 s^{-1} (= (K_{eq}^2) × $2k_{11}$) and the authors own experimentally derived value for k_{11}. [b]calculated using values of k_{TOT} from Bengtsson and K_{eq} from Lind and Merenyi.

Reference	Parameter(s)	Value	pH
Robinson & Bower [195]	K_a	1.1×10^{-6}	[a]
Lind & Merenyi [181]	K_{eq}	2.6×10^{-9} M^2	[b]
Li *et al* [193]	K_ak_9 / k_{-9} ($=K_a\beta_1$)	6.88×10^{7} M^{-1} s^{-1}/ 9.42×10^{10} M^{-1} s^{-1} ($=7.3\times10^{-4}$)	3
	k_{10} / k_{-10}	5.97×10^{5} M^{-1} s^{-1}/ 1.67×10^{11} M^{-1} s^{-1} ($=3.57\times10^{-6}$)	3
Billeter *et al* [194]	k_9	8.1 M^{-1} s^{-1}	1
Lind & Merenyi [181]	k_{11}	1.40×10^{8} M^{-1} s^{-1}	0
Bazylinski & Hollocher [196]	k_{13}	$1.8 - 7.2\times10^{9}$ M^{-1} s^{-1}	7
Shafirovich & Lymar [197]	k_{13}	8×10^{6} M^{-1} s^{-1}	7

Looking next at the rate constants involved solely in the make up of the parameter *C*, literature values relating to the rate constants for the HNO dimerization reaction involved in the 2:1 stoichiometry reaction of Fe^{3+} and NH_3OH^+ is sparse, and what little information is available is only recorded under conditions of higher pH relevant to biological systems [196, 197]. Rate coefficients are generally high for radical recombination reactions, often on the order of 10^9 and 10^{10} dm^3 mol^{-1} s^{-1} [169], as was suggested for HNO dimerization in an early study by Bazylinski & Hollocher [196]. Shafirovich & Lymar [197] have more recently suggested that HNO has a much lower

acidity than previously thought and dimerization occurs more slowly with a k_{13} value of the order of 10^6 M^{-1} s^{-1}, as shown in Table 5.9. For the other elementary reaction relating to *C*, the reaction between Fe(III) and H_2NO^* with rate parameter k_{12}, no previous literature was found.

Finally, with relevance to both *B* and *C*, a value of $K_a = 1.1\times10^{-6}$ is given for the acid dissociation constant of NH_3OH^+ by Robinson & Bower [195]. This value results in an initial estimate for *B* of 1.9 x 10^{-9} M^3 s^{-1} at the pH at which k_{11} was recorded, pH 0 (all other parameters can be considered equilibrium constants or components of equilibrium constants and thus invariant with pH).

In summary, there is lack of available literature on the elementary reactions that make up *B* and *C* that ultimately means that obtaining accurate estimations of the parameters prior to any simulation is near impossible, particularly considering the non-availability of data pertaining to k_{12}, one of the constituent rate constants of the lumped parameter *C*. It was therefore left to see what gPROMS estimated for these values, and how they compared to the very sparse literature available.

5.3.1.2 Model output and discussion

The closest fits obtained from gPROMs using this new model are shown in Figure 5.9.

Considering first the acetate data of Figure 5.9 A-C, it can be seen that the fits to the datasets obtained at the higher initial Fe(III) concentrations of 10 mmol dm^{-3} are visually much worse than the same fits for the previous model iteration described in

section 5.2 and which implemented the IF-statement for the reduction of free Fe(III) by NH_2OH.

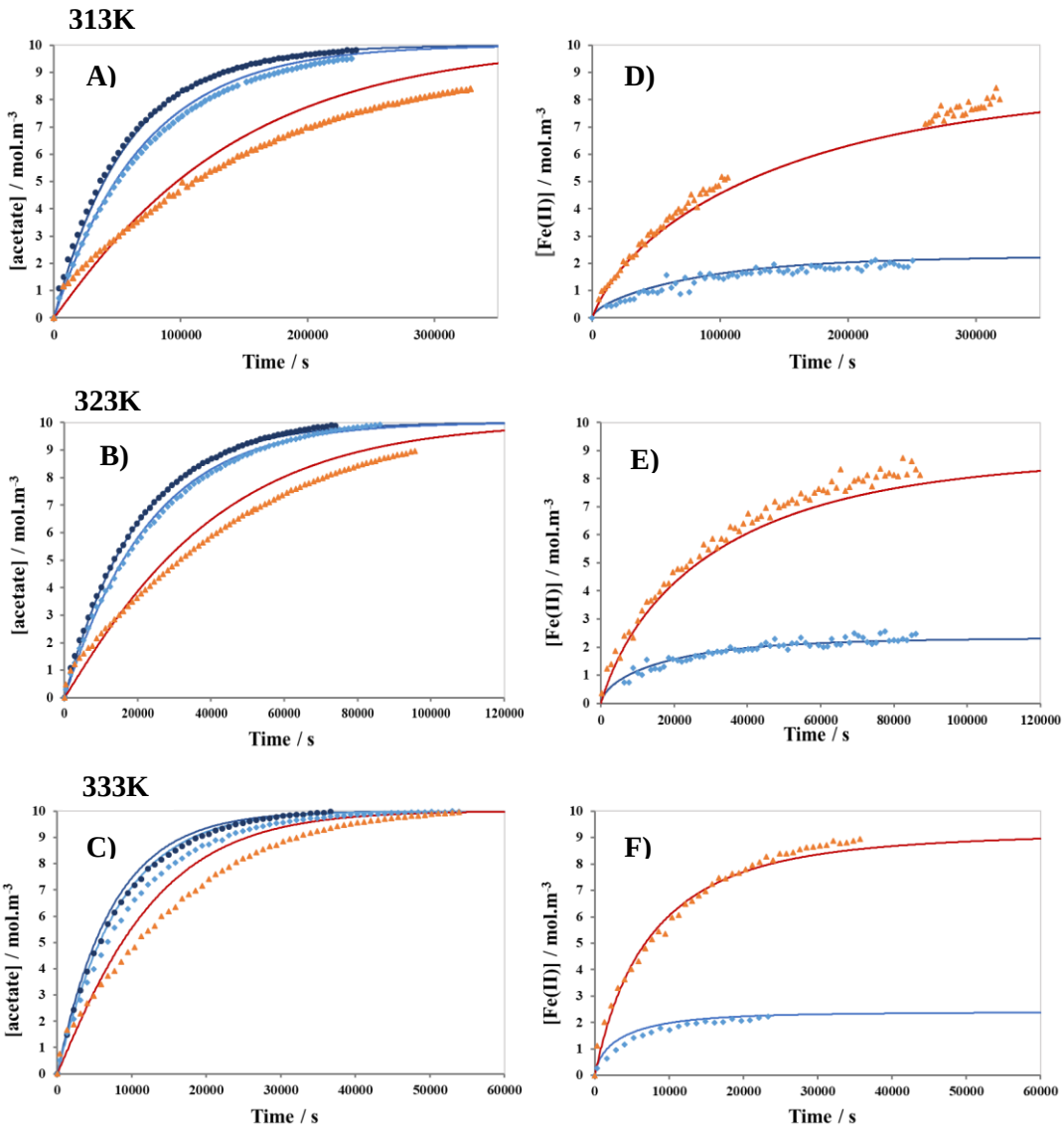

Figure 5.9: Plots of experimental Ac (A-C) and Fe(II) (D-F) data (points) and model output (lines) for the model with the inclusion of the reduction of FeL^{2+} by NH_3OH^+, FeL^{2+} hydrolysis, $Fe^{3+}_{(aq)}$ reduction by NH_3OH^+ modelled with the modified Bengtsson equation, and equilibrium constants K_1 and K_2 estimated. Experimental data (points) and model output (lines) for Ac, when $[Fe(III)]_0$ = 0 (dark blue), 2.5 (light blue) and 10 mmol dm^{-3} (orange). Plots D-F: Experimental data (points) and model output (lines) for Fe^{2+}, when $[Fe(III)]_0$ = 2.5 (light blue) and 10 mmol dm^{-3} (orange). For the data obtained at 3131K with 10 mmol dm^{-3} initial Fe(III), a system fault overnight caused a large stoppage period in data acquisition in which the IC system had to be cleaned, re-equilibrated and put back into operation.

However, focussing next on the Fe(II) data of Figure 5.9 D-F indicates that implementation of the modified Bengtsson equation in place of the IF-statement has

been successful in producing smoother and visually improved fits to all the experimental Fe(II) datasets than seen previously. Especially it has been successful in removing the kink in the fits to the Fe(II) datasets that was previously associated with the switching from pathway 2 to pathway 1 for the reduction of Fe(III) by NH_2OH via a 2:1 and 1:1 stoichiometry respectively in the modelling of section 5.2.

The parameter estimations for the fits of Figure 5.9 are shown in Table 5.10.

*Table 5.10: Parameter estimations performed in gPROMS, with the reduction of FeL^{2+} by NH_3OH^+, FeL^{2+} hydrolysis, and $Fe^{3+}_{(aq)}$ reduction by NH_3OH^+ modelled with the modified Bengtsson equation and equilibrium constants K_1 and K_2 estimated. Rate constants are given in units of mol dm^{-3} (M). Shaded values are set parameters. *all values stated at 298K are calculated from estimations of Arrhenius relationships. Shaded values are set.*

T / K	K_1	K_2	k_0 / $M^{-1}.s^{-1}$	k_1 / $M^{-1}.s^{-1}$	B / $M^3.s^{-1}$	C / $M^5.s^{-1}$	$k_{red,1,FeL}$ / $M^{-1}.s^{-1}$
298*	101.63	0.14	3.13×10^{-5}	6.31×10^{-23}	4.95×10^{-22}	8.49×10^{-10}	4.89×10^{-17}
313	49.95	0.10	1.75×10^{-4}	2.05×10^{-21}	4.55×10^{-20}	$2.64. \times 10^{-8}$	1.08×10^{-15}
323	32.27	0.08	5.05×10^{-4}	1.75×10^{-20}	7.33×10^{-19}	2.19×10^{-7}	7.24×10^{-15}
333	21.40	0.07	1.37×10^{-3}	1.31×10^{-19}	1.00×10^{-17}	1.59×10^{-6}	4.33×10^{-14}

Looking first at the parameter estimations for the lumped pseudo-rate parameters *B* and *C* in the modified Bengtsson equation for the reduction of free Fe(III) by hydroxylamine, estimations for the parameter *C* indicate that it has a value on the order of 10^{-10}–10^{-6} at the relevant temperatures. Inspection of the statistical information in Table 7.5 in Appendix B section 7.2.4.4 reveals that the lumped Arrhenius parameters *A* and E_a that relate to *C,* are the most important to the model fit, particularly *A* which has a t-value of 4.85×10^{11}, 10 orders of magnitude greater than the t-value of 44.45 for the next most important parameter, E_a. In comparison, parameters estimations in Table 5.10 for the parameter *B* are on the order of 10^{-22}–10^{-17} at the respective temperatures, suggesting that this lumped pseudo-rate constant is insignificant to the

model fits. This is confirmed by inspection of the t-values in Table 7.5 in Appendix B section 7.2.4.4, which shows that the Arrhenius parameters A and E_a relating to B are on the order of 10^{-10} and 10^{-11} respectively. Whilst these values are less than the reference t-value of 1.648 and thus statistically insignificant, they are however greater than those t-values relating to the Arrhenius parameters for the kinetic rate constants k_1 and $k_{red,1,FeL}$ by several orders of magnitude and therefore comparatively, the parameter B is more important to the model fit than those kinetic rate constants for the hydrolysis or reduction of the complex. We will return to this point later.

In this model, we have assumed a simple lumped Arrhenius relationship for B and C. As can be seen from Eqs. 5.32 and 5.33, the Arrhenius parameters using this assumption are unreasonably large, particularly those for the pre-exponential factors, with values on the order of 10^{19} and 10^{22} for B and C respectively.

$$\mathrm{B} = 4.60 \times 10^{19} e^{\frac{-233717}{RT}} \tag{5.32}$$

$$\mathrm{C} = 1.20 \times 10^{22} e^{\frac{-177708}{RT}} \tag{5.33}$$

The parameters B and C do not however relate to elementary reactions and are instead complex rate parameters consisting of multiple reaction rate and equilibrium constants. Caution should thus be exercised in the interpretation of the estimated values for these parameters as the simple Arrhenius relationships given in Eq. 5.32 and 5.33 are just convenient summary relationships derived from the combination of several analogous relationships associated with the constituent elementary steps of B and C.

Turning our attention next to the parameter estimations for the kinetic rate constant for the hydrolysis of the FeL^{2+} complex k_1, these are once again completely unchanged from any of the model iterations described thus far in sections 5.1 or 5.2 as a result of the model not adjusting the value of k_1 away from the seed values during the fit (as previously discussed in detail in section 5.1.1.2). Also unchanged from any previous model iterations are the t-values relating to A and E_a in Table 7.5, which are on the order of 10^{-18} and 10^{-17} respectively.

Focussing now on the estimations for the kinetic rate constant $k_{red,1,FeL}$ for the reduction of the FeL^{2+} complex, inspection of Table 5.10 reveals that incorporating the modified Bengtsson equation into the model to replace the previous approach to modelling the reduction of free Fe(III) described in section 5.2 (using the IF-statement to switch between pathway 2 and pathway 1) has had a profound impact on these parameter estimations. In this model iteration, values output by gPROMS for the kinetic rate constant $k_{red,1,FeL}$ are now on the order of 10^{-15}-10^{-14} M^{-1} s^{-1} at the respective temperatures of 313-333K, in comparison to values on the order of 10^{-7} – 10^{-6} M^{-1} s^{-1} output previously using the IF-statement model. With regards to the significance of this parameter to the model fit, the statistical t-values for the Arrhenius parameters A and E_a are on the order of 10^{-19} and 10^{-18} respectively (in comparison to 10^{-6} and 10^{-4} using the IF-statement model), which places the parameter estimations for $k_{red,1,FeL}$ below those of all other parameters in its importance, including those for k_1.

Finally, we turn our attention to the parameter estimations for the equilibrium constants. Using the estimated values of $\eta_{c,1}$ and $\alpha_{c,1}$, and $\eta_{c,2}$ and $\alpha_{c,2}$ used in the temperature dependence relationships described by Eqs. 5.2 and 5.3 for K_1 and K_2

respectively (shown again below for the convenience of the reader), we can obtain values at 298K of 101.63 and 0.14 respectively.

$$K_1 = e^{\frac{\eta_{c,1}}{T}+\alpha_{c,1}} \qquad where\ \eta_{c,1} = -\frac{\Delta H_1^0}{R}\ and\ \alpha_{c,1} = \frac{\Delta S_1^0}{R} \tag{5.2}$$

$$K_2 = e^{\frac{\eta_{c,2}}{T}+\alpha_{c,2}} \qquad where\ \eta_{c,2} = -\frac{\Delta H_2^0}{R}\ and\ \alpha_{c,2} = \frac{\Delta S_2^0}{R} \tag{5.3}$$

The former is significantly greater than the value of K_1 = 40.65 reported by Andrieux *et al.* [57] but in very close agreement with a value of K_1 = 109 suggested by Monzyk *et al.* [190]. The latter is however still an order of magnitude smaller than the equivalent value of K_2 = 2.56 reported by Andrieux *et al.* [57] using a spectral deconvolution method. However, these authors note the comparatively large standard deviation values of up to 78% that they observe in respect to their determinations of K_2 using this method. In comparison, they report standard deviations up to a maximum of 40% and 29% for determinations of K_1 and K_3 respectively, thus the accuracy of their value for K_2 in particular, may be in question.

As described previously in section 5.1.1.1, the temperature dependence relationships of Eqs. 5.2 and 5.3 used in all model iterations are derived using the Van't Hoff equation (Eq. 5.1), from which we can obtain values for the enthalpy (ΔH^0) and entropy (ΔS^0) of formation for the mono- and bis-complexes. These values for the work presented here are shown below in Table 5.11 and compared to the same values calculated by Andrieux *et al.* [57] using their spectroscopic method.

Table 5.11: Thermodynamic data relating to the formation of the mono- and bis-complexes obtained from the parameter estimation in Table 5.10, in comparison to that obtained by Andrieux et al. [3] using an experimental spectroscopic approach with spectral deconvolution.

Andrieux *et al.* [57]			This work		
Temperature dependence	ΔH^0 / kJ.mol^{-1}	ΔS^0 / J.mol^{-1}.K^{-1}	Temperature dependence	ΔH^0 / kJ.mol^{-1}	ΔS^0 / J.mol^{-1}.K^{-1}
$K_1 = e^{\frac{6783.7}{T} - 19.0}$	-56.4	-158.2	$K_1 = e^{\frac{4416.62}{T} - 10.20}$	-36.72	-84.80
$K_2 = e^{\frac{2055.6}{T} - 6.0}$	-17.09	-49.7	$K_2 = e^{\frac{2056.37}{T} - 8.86}$	-17.10	-73.69

In agreement with these authors, negative values are obtained for ΔH^0 and ΔS^0 relating to both K_1 and K_2, indicating that the formation of the complexes are accompanied by a loss of entropy and thus are enthalpically driven. The same trend noted by these authors is also observed; the enthalpy and entropy values both move progressively more positive as the number of ligands bound to the metal ion increases. Focussing first on the temperature dependence relationships for K_1 in Table 5.11, the estimated values of $\eta_{c,1}$ and $\alpha_{c,1}$ give rise to ΔH^0 and ΔS^0 relating to the formation of the mono-complex that are approximately 35% and 45% more positive than the same values reported by Andrieux *et al.* [57] respectively. Looking at the statistical information relating to the parameter estimation in Table 7.5 in Appendix B section 7.2.4.4, we can see that the t-values for $\eta_{c,1}$ and $\alpha_{c,1}$ are 1.296 and 0.962 respectively. Whilst these are less than the reference t-value of 1.648 and thus classed as statistically insignificant according to the t-test, these t-values are several orders of magnitude greater than those relating to any other estimated parameters except for the Arrhenius parameters relating to the kinetic rate constant C. Thus, in comparison to other estimated parameters, K_1 is found to be very important to the model fit.

Looking next at the temperature dependence relationships for K_2 in Table 5.11, the estimation of $\eta_{c,2}$ is nearly identical to that reported by Andrieux *et al.* [57] and gives rise to the same value of ΔH^0 = -17.10 kJ mol^{-1}. The parameter estimation of $\alpha_{c,2}$ gives rise to a value of ΔS^0 = -73.69 J mol^{-1} K^{-1}, approximately 48% more negative than the equivalent value of ΔS^0 = -49.7 J mol^{-1} K^{-1} determined by Andrieux *et al.* [57], . From inspection of the t-values relating to the estimations of $\eta_{c,2}$ and $\alpha_{c,2}$ in Table 7.5 Appendix B section 7.2.4.4, we can see that both of these are on the order of 10^{-3}, thus statistically unimportant to the model fit, but comparatively more important than the parameters B, k_1 or $k_{red,1,FeL}$.

In summary, implementation of the modified Bengtsson equation for modelling the reduction of free Fe(III) by hydroxylamine via a single kinetic rate equation has provided significantly smoother and improved fits to the Fe(II) datasets in comparison to those obtained in the previous model iteration in section 5.2 in which the IF-statement was used to switch between two different stochiometric pathways. The lumped rate parameter C, which consists of kinetic rate constants for the elementary reactions involved in the 2:1 Fe(III):hydroxylamine stoichiometric pathway, is seen to be the most important to the model fit by inspection of the t-values.

Next in the order of importance to the model fit is the equilibrium constant relating the formation of the Fe(III)-AHA mono-complex, K_1, followed by that relating to the bis-complex, K_2. In comparison to the temperature dependent equilibrium constants of formation for the mono- and bis-acetohydroxamatoiron(III) complexes previously reported by Andrieux *et al.* [57], this model estimates values of K_1 to be larger than those reported by these authors, and values of K_2 to be smaller by up to 2 orders of

magnitude at the highest temperature of 333K. The model is thus trying to fit the slower ingrowth of acetate at higher initial Fe(III) concentrations by assuming that more of the ligand is bound in complexed form, specifically as the mono-complex, than previously published, and thus unable to participate in the hydrolysis of the free ligand to produce acetic acid and hydroxylamine, the primary reaction that determines acetate production in these systems.

Finally, the remaining estimated kinetic parameters decrease in order of importance to the model fit from B > k_1 > $k_{red,1,FeL}$, although they are all found to be statistically unimportant with t-values on the order of 10^{-10} or less. In terms of the least important parameter according to this model iteration, $k_{red,1,FeL}$, this in contrast to the previous model iteration incorporating the IF-statement (as described in section 5.2) in which, whilst still statistically unimportant to the model fit according to t-values, $k_{red,1,FeL}$ was found to markedly more important than k_1 by several orders of magnitude.

Whilst we obtain good fits to the experimental Fe(II) data with this model iteration at all $[Fe(III)]_0$ and temperatures modelled, fits to the acetate data still require some improvement, particularly those at the higher $[Fe(III)]_0$ of 10 mmol dm^{-3} and elevated temperature of 333K. In allowing the equilibrium constants of formation of the complexes K_1 and K_2 to float in this model iteration and the previous one in section 5.2, it can be seen that these parameters are statistically important to the model fit, but estimations differ from those reported in the literature by some way, including at 298K where there is an abundance of literature values against which to benchmark our approach. This observation suggests that the approach to estimation of K_1 and K_2 requires further modification. This is the subject of the final section.

5.3.2 Setting K_1 and K_2 at 298K

The determination of temperature dependent equilibrium constants of formation for acetohydroxamatoiron(III) complexes, previously investigated by Andrieux *et al.* [57] via a UV-Vis absorption spectroscopy technique followed by spectral deconvolution, relies on two primary assumptions: i) Fe(III) is a complexing but non-oxidising metal ion with regards to AHA/hydroxylamine, ii) the calculations of K_1, K_2 and K_3 are conducted under conditions where one or more of the acetohydroxamatoirion(III) complexes are present in negligible amounts only. The first assumption has been proved to be incorrect by the experimental results described in section 4.6 of this thesis, with the effects of the identified reduction of Fe(III) by hydroxylamine being more pronounced at higher temperatures. The second assumption requires sufficient prior knowledge of the speciation behaviour.

Spectral deconvolution techniques require knowledge of the shape and bandwidth of spectra relating to the individual species present in a mixture, as band overlap makes the direct observation of the individual component bands near impossible otherwise. The selection of bandwidths can therefore become somewhat arbitrary and user-dependent, raising doubts about the objectivity of any analysis based on deconvolution [198]. Andrieux *et al.* [57] also note the comparatively large standard deviation values, up to a maximum of 78%, that they observe in respect to their determinations of K_2. In comparison, the determinations of K_1 and K_3 are reported to have smaller standard deviation values, up to a maximum of 40% and 29% respectively, an observation which is explained by these authors based on the respective molar absorptivities of the three Fe(III)-AHA complexes. The interferent for the determination of K_2 is the tris-

complex, which is thought to have a molar absorptivity 2.2× and 3.6× that of the bis- and mono-complex respectively. The reliability of their determinations may therefore be in question.

Taking into account the described lack of reliability in the spectral deconvolution techniques employed by Andrieux *et al* [57] and thus the assumptions used in the previously published determination of the complex equilibrium constants, the values at higher temperatures in particular could potentially be subject to significant errors.

With this in mind, K_1 and K_2 were set instead to those determined at 298K only, a temperature at which the afore-mentioned interfering reduction of Fe(III) by hydroxylamine would be minor, and the previously reported equilibrium constants would be expected to be reliable. Estimations of K_2 provided by either of the model iterations thus far in which equilibrium constants have been allowed to float have been much smaller than those reported in the literature by Andrieux *et al* [57], whereas the opposite is true for estimations of K_1. In relation to the latter, the model iteration incorporating the modified Bengtsson equation described previously in section 5.3.1 provided an estimated value of K_1 = 101 at 298K, in close agreement with that reported by Monzyk *et al.* [190]. Based on the estimations of K_1 and K_2 obtained in the above mentioned model iteration, it therefore seemed reasonable to set K_1 to 109 [190] and K_2 to 2.04 [199] at 298K, the same values used by Andrieux *et al.* [77] in the development of a kinetic model for the hydrolysis of AHA in the presence of Fe(III).

As in the previous model iterations, the Arrhenius parameters for the kinetic rate constant for the free AHA hydrolysis, $k_{0,}$ were set to those obtained previously in this

thesis (Chapter 4 section 4.2.1). The equilibrium constants were set at 298K as described above, but estimated at all other temperatures. The Arrhenius parameters for all other rate parameters including the kinetic rate constants for the complex hydrolysis and reduction by hydroxylamine, k_1 and $k_{red,1,FeL}$, and the newly derived lumped parameters *B* and *C* in the modified Bengtsson equation, were estimated by gPROMS.

5.3.3 Model output and discussion

Model results are shown in Figure 5.10 and the parameter estimations for the fits of Figure 5.10 are shown in Table 5.12.

Inspection of the plots in Figure 5.10 shows that visually, significantly improved fits to both the acetate (plots A-C) and Fe(II) (plots D-F) experimental datasets are obtained in nearly all cases. Considering first the acetate data of Figure 5.10 A-C, the most deviation between the modelled and experimental lines is seen for the data in the presence of 2.5 mmol dm^{-3} initial Fe(III) at 333K (light blue data on plot C), but this is still fairly minor deviation. Furthermore, the original aim of smoothing the fit in the Fe(II) modelling profiles has also been achieved, with the previously observed 'kink' in the previously modelled traces, Figure 5.3 and Figure 5.8, now replaced with a gradual curve in-line with the recorded experimental datasets.

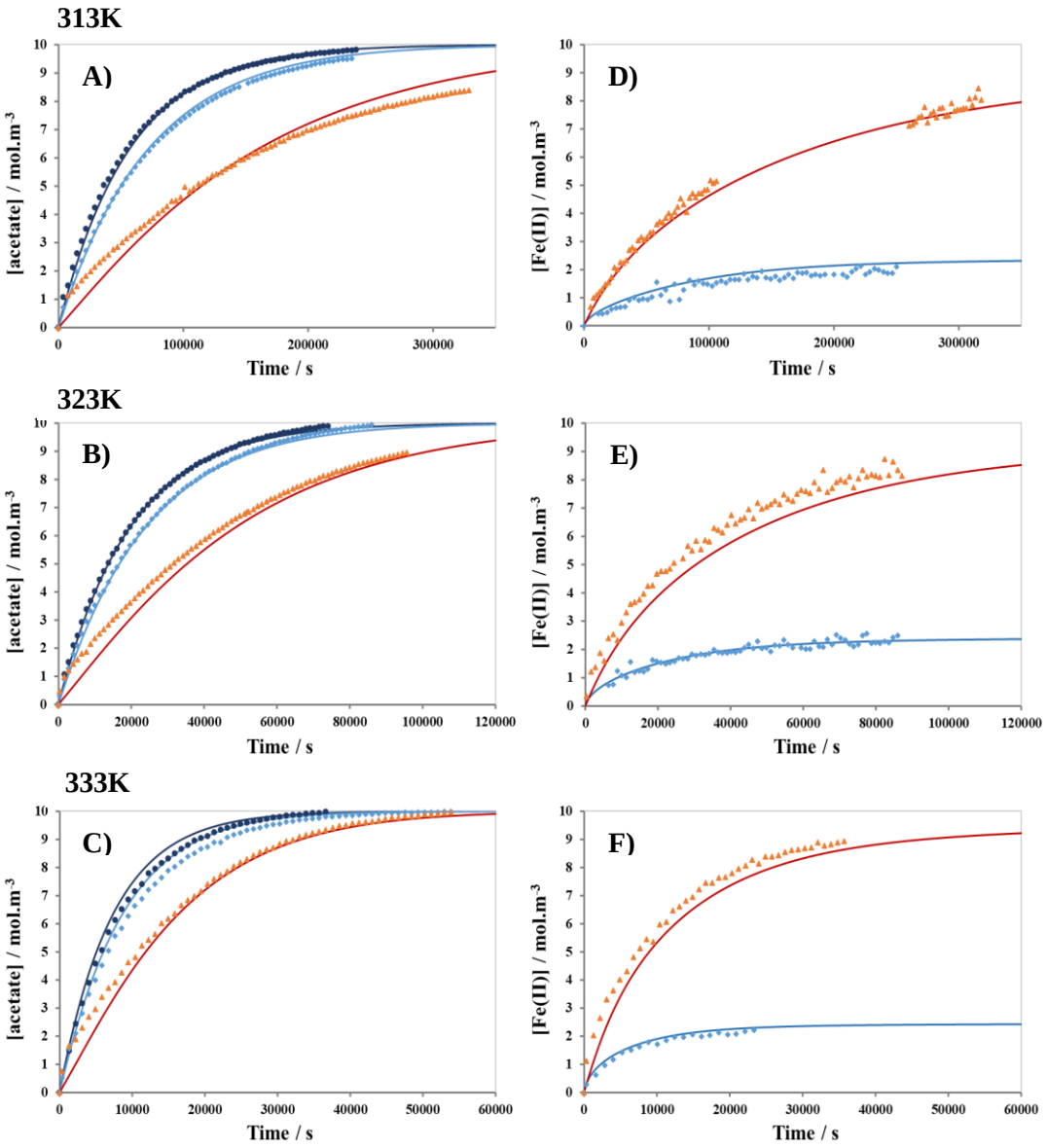

Figure 5.10: Plots of experimental Ac (A-C) and Fe(II) (D-F) data (points) and model output (lines) for the model with the inclusion of the reduction of FeL^{2+} by NH_3OH^+, FeL hydrolysis, and $Fe^{3+}_{(aq)}$ reduction by NH_3OH^+ modelled with the modified Bengtsson equation, and equilibrium constants K_1 and K_2 set at 298K, with $[Fe(III)]_0$ = 0 mmol dm^{-3} (dark blue), 2.5 mmol dm^{-3} (light blue) and 10 mmol dm^{-3} (orange). For the data obtained at 3131K with 10 mmol dm^{-3} initial Fe(III), a system fault overnight caused a large stoppage period in data acquisition in which the IC system had to be cleaned, re-equilibrated and put back into operation

*Table 5.12: Parameter estimations performed in gPROMS, with the reduction of FeL^{2+} by NH_3OH^+, FeL^{2+} hydrolysis, and $Fe^{3+}_{(aq)}$ reduction by NH_3OH^+ modelled with the modified Bengtsson equation. Rate constants are given in units of mol dm^{-3} (M). Shaded values are set parameters. *all values stated at 298K are calculated from estimations of Arrhenius relationships. Shaded values are set*

T / K	K_1	K_2	k_0 / $M^{-1}.s^{-1}$	k_1 / $M^{-1}.s^{-1}$	B / $M^3.s^{-1}$	C / $M^5.s^{-1}$	$k_{red,1,FeL}$ / $M^{-1}.s^{-1}$
298*	109	2.04	3.13×10^{-5}	6.31×10^{-23}	8.80×10^{-15}	5.98×10^{-9}	4.89×10^{-17}
313	84.3	0.61	1.75×10^{-4}	2.05×10^{-21}	3.63×10^{-13}	1.69×10^{-7}	1.08×10^{-15}
323	71.9	0.29	5.05×10^{-4}	1.75×10^{-20}	3.58×10^{-12}	1.33×10^{-6}	7.24×10^{-15}
333	62.0	0.14	1.37×10^{-3}	1.31×10^{-19}	3.08×10^{-11}	9.16×10^{-6}	4.33×10^{-14}

Before discussing Table 5.12 in detail though, Figure 5.11 shows a final validation check on the kinetic approach to speciation used in the model, the same approach that was taken for the initial modelling described in section 5.1.

Identified on Figure 5.11 as polynomial plots, concentration profiles of the FeL^{2+} (A-C) and FeL_2^+ complexes (D-F) calculated via Eqs. 5.13-5.16 in section 5.1 and using values of L_T, Fe_T and HL calculated from the output of this final model are shown. These are compared with plots of the same complex concentration profiles obtained as direct outputs by the model itself using the set of differential equations in Table 5.2 in section 5.1 that incorporate the kinetic treatment of the complexation constants described by Eqs. 5.4 and 5.5. As was the case previously for the initial model iteration described in section 5.1, both the polynomial plots and model plots are identical for all simulations with $[Fe(III)_0]$ = 2.5 or 10 mmol dm^{-3}, thus this once again validates the kinetic approach to speciation used in the model.

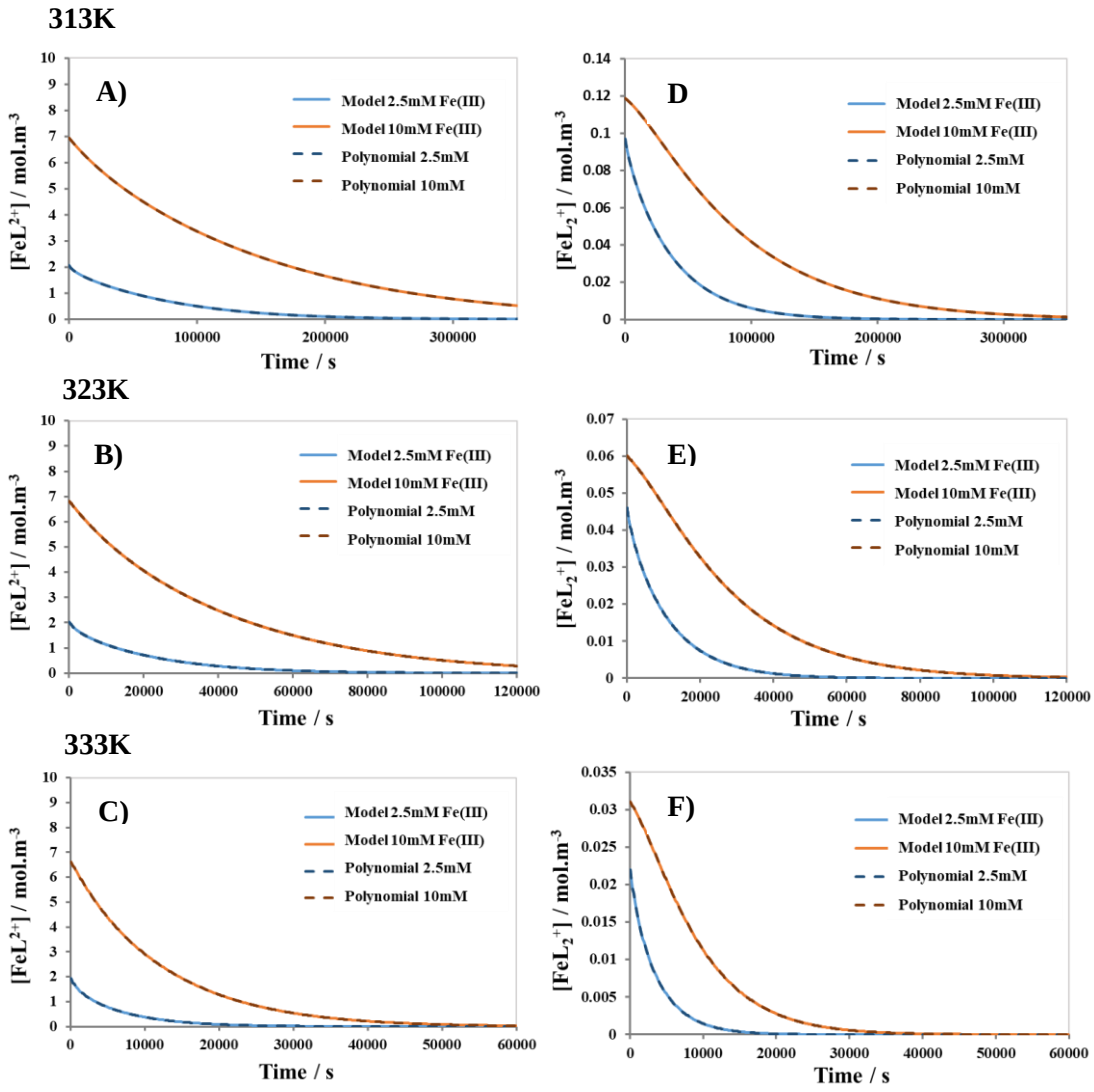

Figure 5.11: Polynomial plots of the concentrations of the FeL^{2+} complex (A-C) and the FeL_2^{+} complex (D-F) as calculated from Eqs. 5.13-5.16, and those output from the model, for the fits shown in Figure 5.10.

Returning to the parameter estimations of Table 5.12 and we consider first the estimations for the lumped pseudo-rate parameters *B* and *C* in the modified Bengtsson equation. Estimations for the parameter *C* are of a similar order of magnitude to those obtained in the previous model iteration in section 5.3.1, with values on the order of 10^{-9}–10^{-6} at the relevant temperatures. Inspection of the statistical information in Table 7.6 in Appendix B section 7.2.4.4 reveals that the lumped Arrhenius parameters *A* and

E_a that relate to C are again the most important to the model fit, particularly A which has a t-value of 1.63 x 10^{12}, 10 orders of magnitude greater than the t-value of 1.10 x 10^2 for the next most important parameter, E_a. Returning back to Table 5.12, the estimations for the parameter B are on the order of 10^{-15} – 10^{-11} at the relevant temperatures using our datasets obtained at pH = 1, an increase of 6-7 orders of magnitude from the previous model iteration in which K_1 and K_2 were fully estimated. This increase in the estimations of B by several orders of magnitude brings them significantly closer to our initial estimate of B = 1.9 x 10^{-9} M^3 s^{-1} at pH = 0 calculated from the sparse literature available for rate parameters pertaining to the elementary reactions that make up this lumped pseudo-rate parameter, thus adding support to the approach taken here to set K_1 and K_2 to literature values at 298K. Inspection of the t-values in Table 7.6 for the Arrhenius parameters A and E_a relating to B reveals that, while still less than the reference t-value of 1.648 and thus statistically insignificant, the t-values for A and E_a and now on the order of 10^{-4}. This is a significant increase in comparison to t-values for A and E_a relating to B of 10^{-10} and 10^{-11} respectively obtained in the previous model iteration in section 5.3.1.

As in the previous model iteration in section 5.3.1, the actual values we obtain for the Arrhenius parameters described above are unreasonably large using the assumption of a simple Arrhenius relationship, Eq. 5.34 and Eq. 5.35 for parameters B and C respectively. In particular, the estimated values for the pre-exponential factors relating to these lumped pseudo-rate parameters are unchanged from the estimations obtained in the previous model iteration in section 5.3.1 and are once again on the order of 10^{19} and 10^{22} for B and C respectively. For the parameter C, Eq. 5.35 shows that the value

of the activation energy obtained in this model iteration, E_a = 173 kJ mol^{-1} (3sf), is not significantly changed from the value of E_a = 178 kJ mol^{-1} (3sf) estimated in the previous model iteration (shown in Eq. 5.33). Looking however at Eq, 5.34, it can be seen that the differences in the parameter estimations of *B* obtained in this model iteration in comparison to the last (see Table 5.12 and Table 5.10), stem from a more significant change in the activation energy, with an estimate of E_a = 192 kJ mol^{-1} (3sf) for this model iteration compared to E_a = 234 kJ mol^{-1} (3sf) in the previous iteration.

$$\mathrm{B} = 4.60 \times 10^{19} e^{\frac{-192358}{RT}} \tag{5.34}$$

$$\mathrm{C} = 1.20 \times 10^{22} e^{\frac{-172869}{RT}} \tag{5.35}$$

However as before, caution should be exercised in the interpretation of the estimated values for these lumped parameters as the simple Arrhenius relationships given in Eq. 5.34 and 5.35 are just convenient summary relationships derived from the combination of several analogous relationships associated with the constituent elementary steps of *B* and *C*.

Turning our attention next to the parameter estimations for the kinetic rate constants relating to the hydrolysis of AHA, we previously obtained Arrhenius parameters of *A* = 1.25 × 10^{11} M^{-1} s^{-1} and E_a = 89 kJ mol^{-1} for k_0 from a simple kinetic analysis of the acetate data in the absence of Fe(III) described in Chapter 4 section 4.2, which have been incorporated into the model via Eq. 5.36. Whilst these Arrhenius parameters differ to those published by Andrieux *et al.* [83] of *A* = 4.24 × 10^{9} M^{-1}.s^{-1} and E_a = 80.1 kJ.mol^{-1}, the authors' analysis based on the spectroscopic method assumes that Fe(III)

only complexes with the ligand and does not react with NH_2OH, an assumption which has been proved incorrect in this thesis.

Turning next to k_1 then, as with all previous model iterations, the equivalent estimated Arrhenius parameters for the hydrolysis of the Fe-AHA mono-complex have not been adjusted by gPROMS from the seed values. The t-values shown in Table 7.6 for E_a and A relating to k_1 are again on the order of 10^{-17} and 10^{-18} respectively, illustrating thus these parameters are statistically unimportant to the model fit. If we therefore assume that our original worse-case scenario assumption in the context of values that gPROMS can compute holds true i.e. values of k_1 at the temperatures considered are on the order of 10^{-20}, and that the Arrhenius relationship for k_1 is as described by Eq. 5.37, then the value of E_a = 180 kJ mol^{-1} calculated for this relationship would indicate a very large barrier to the hydrolysis of complexed AHA.

$$k_0 = 1.25 \times 10^{11} e^{\frac{-89000}{RT}} \tag{5.36}$$

$$k_1 = 2.25 \times 10^{9} e^{\frac{-180000}{RT}} \tag{5.37}$$

$$\ln\left(\frac{k}{T}\right) = -\frac{\Delta H^{\#}}{RT} + \ln\left(\frac{k_B}{h}\right) + \frac{\Delta S^{\#}}{R} \qquad Eyring's\ equation \tag{5.38}$$

Using Eyring's equation (Eq. 5.38) values can be obtained for the enthalpy and entropy of activation related to the acid-catalysed hydrolysis of both free and Fe(III)-complexed AHA, said data shown in Table 5.13. It can be seen in Table 5.13 that the gPROMS model suggests that $\Delta H^{\#}$ and $\Delta S^{\#}$ for the hydrolysis of complexed AHA are significantly different than those published by Andrieux *et al.* [83] for the same reaction, and those used in this model for the hydrolysis of free AHA.

Table 5.13: Thermodynamic data relating to the hydrolysis of free and Fe(III)-complexed AHA obtained from the final model described here, in comparison to that obtained by Andrieux et al. [5] using an experimental spectroscopic approach with spectral deconvolution.

	Free ligand hydrolysis		Complexed ligand hydrolysis	
	$\Delta H^{\#}$ / kJ.mol^{-1}	$\Delta S^{\#}$ / J.mol^{-1}.K^{-1}	$\Delta H^{\#}$ / kJ.mol^{-1}	$\Delta S^{\#}$ / J.mol^{-1}.K^{-1}
Andrieux *et al.* [83]	77.2	-70.3	87.0	-35.7
This work	86.4	-41.2	177.4	-74.6

The enthalpy of bond formation and breaking in the transition state forms a major part of the $\Delta H^{\#}$. Quantum mechanical calculations by Andrieux and co-workers [83] showed that the initial step in the hydrolysis of free AHA was the protonation of the carbonyl oxygen, energetically favoured over protonation of the nitrogen site by nearly 200 kJ mol^{-1}, allowing for cleavage of the C-N bond and the formation of NH_2OH as a leaving group. Similar calculations by these authors for the hydrolysis of bound AHA suggested that protonation of either of the oxygen sites (carbonyl or nitro) is more favourable than the same protonation at the nitrogen site by 64.6 kJ mol^{-1}, however, the initial protonation step must occur at the energetically less favourable nitrogen site to result in cleavage of the C-N bond and produce the same hydrolysis products as for free AHA hydrolysis. Despite this calculated energy difference in the protonation step, Andrieux et al. [83] obtain a value of $\Delta H\#$ for the hydrolysis of the complexed AHA that is only 10 kJ mol^{-1} greater than that for the free AHA hydrolysis. Using our original worse-case scenario assumption for the Arrhenius relationship for k_1, a value of $\Delta H^{\#}$ =177.4 kJ mol^{-1} can be calculated for the complexed AHA hydrolysis from this model, approximately 90 kJ mol^{-1} greater that published previously [83] and that calculated for the free AHA hydrolysis from experimental work in this thesis (as shown in Table 5.13). However as explained previously, k_1 is statistically unimportant

to the model fit to the point that PROMS was unable to converge on true values for the Arrhenius parameters A and E_a, thus the estimations are unlikely to be particularly accurate. It is also important to note that the possible occurrence of hydrolysis of the bis-complex has not been considered in this model, although this is expected to be insignificant and unlikely to be a major influence on the overall ligand hydrolysis process. This is because the concentration of the bis-complex would be expected to decline rapidly in the initial stages of AHA hydrolysis as the ligand concentration is reduced, likely by decomplexation, as illustrated by respective equilibrium constants of K_1 = 62.46 and K_2 = 2.81 at 293K for the mono- and bis-complexes respectively [77].

Consideration next of the parameter estimations for the kinetic rate constant for the AHA-facilitated reduction of FeL^{2+} by NH_3OH^+, $k_{red,1,FeL}$, the values we obtain are similar to those in the previous model iteration, on the order of 10^{-17} – 10^{-14} at the relevant temperatures. With regards to the significance of this parameter to the model fit, it once again is the least important parameter according to gPROMS, with t-values for the Arrhenius parameters A and E_a are on the order of 10^{-19} and 10^{-17} respectively. The actual obtained values $A = 5.44 \times 10^{11}$ M^{-1} s^{-1} and E_a = 160.0 kJ mol^{-1} are shown in the simple Arrhenius relationship described by Eq. 5.39. The value of the latter parameter indicates a very large barrier to the reduction of complexed AHA similar to that for the hydrolysis of complexed AHA,

$$k_{\mathrm{red,1,FeL}} = 5.44 \times 10^{11} e^{\frac{-160000}{RT}} \tag{5.39}$$

Finally, we consider the equilibrium constants K_1 and K_2 for the formation of the mono- and bis-complexes. Inspection of Table 5.12 shows that whilst setting the value of K_1 at 298K to 109 in this model is only a very small increase on the estimation of K_1 = 101 at 298K obtained in the previous model iteration described in section 5.3.1, all other values of K_1 at the respective temperatures have increased significantly. The estimated value of K_1 = 62 at 333K in Table 5.12 is nearly a 3-fold increase over the equivalent estimated value of K_1 = 21 at 333K obtained by gPROMS when the parameters K_1 and K_2 were fully estimated at all temperatures. Unsurprisingly, in setting K_2 to a value of 2.04 at 298K (compared to a previously estimated value of K_2 = 0.14 at 298K), estimations of K_2 have also significantly increased at the respective temperatures.

Described by Eqs. 5.2 and 5.3 respectively, (shown again below for the convenience of the reader) temperature dependence relationships based on the van't Hoff isochore for K_1 and K_2 are shown below.

$$K_1 = e^{\frac{\eta_{c,1}}{T}+\alpha_{c,1}} \qquad where\ \eta_{c,1} = -\frac{\Delta H_1^0}{R}\ and\ \alpha_{c,1} = \frac{\Delta S_1^0}{R} \tag{5.2}$$

$$K_2 = e^{\frac{\eta_{c,2}}{T}+\alpha_{c,2}} \qquad where\ \eta_{c,2} = -\frac{\Delta H_2^0}{R}\ and\ \alpha_{c,2} = \frac{\Delta S_2^0}{R} \tag{5.3}$$

The same relationships including the actual values of $\eta_{c,1}$ and $\alpha_{c,1}$, and $\eta_{c,2}$ and $\alpha_{c,2,}$ are shown in Table 5.14. Also shown in Table 5.14 are calculated values of the enthalpy (ΔH^0) and entropy (ΔS^0) of formation for the mono- and bis-complexes obtained from these relationships, along with the same thermodynamic parameters published by Andrieux and co-workers [57] using their spectral deconvolution method.

Table 5.14: Thermodynamic data relating to the formation of the mono- and bis-complexes obtained from the parameter estimation in Table 5.12, in comparison to that obtained by Andrieux et al. [3] using an experimental spectroscopic approach with spectral deconvolution.

Andrieux *et al.* [57]			This work		
Temperature dependence	ΔH^0 / kJ.mol^{-1}	ΔS^0 / J.mol^{-1}.K^{-1}	Temperature dependence	ΔH^0 / kJ.mol^{-1}	ΔS^0 / J.mol^{-1}.K^{-1}
$K_1 = e^{\frac{6783.7}{T}-19.0}$	-56.4	-158.2	$K_1 = e^{\frac{1600}{T}-0.68}$	-13.30	-5.64
$K_2 = e^{\frac{2055.6}{T}-6.0}$	-17.09	-49.7	$K_2 = e^{\frac{7533.71}{T}-24.57}$	-62.64	-204.26

In agreement with these authors, negative values are obtained for both the enthalpies and entropies of formation for the mono- and bis-complexes, indicating that the formation of the complexes are accompanied by a loss of entropy and are thus enthalpically driven. However, in contrast to the previous model iteration in section 5.3.1, the exact values of ΔH^0 and ΔS^0 calculated from the estimations of the temperature dependent parameters for K_1 and K_2 obtained in this model are themselves significantly different from those calculated using the spectral deconvolution method of Andrieux *et al*. [57].

To explain this, we look at the workings of the model. In the previous model iteration described in section 5.3.1 in which K_1 and K_2 were left to float at all temperatures, gPROMS requires that both the temperature dependent parameters $\eta_{c,1}$ and $\alpha_{c,1}$ relating to K_1, and $\eta_{c,2}$ and $\alpha_{c,2}$ relating to K_2 are either specified or parameter estimated. In setting the value of the equilibrium constants at 298K, gPROMS now requires that only one of the pair of parameters are specified or parameter estimated. For example, one of the variables $\eta_{c,1}$ or $\alpha_{c,1}$ converges during a parameter estimation run, whilst the other can subsequently only be a single value based on the temperature dependence relationship of K_1 at 298K; i.e. $\eta_{c,1}$ and $\alpha_{c,1}$, and by the same argument $\eta_{c,2}$ and $\alpha_{c,2}$, now

become a pair of dependent variables. In this iteration of the model, gPROMS allows $\eta_{c,1}$ and $\eta_{c,2}$ to converge on a value during the parameter estimation run, which in turn then confines the values of $\alpha_{c,1}$ and $\alpha_{c,2}$ to a single value based on the temperature dependence relationship equation at 298K.

Based on the explanation above, inspection of Table 7.6 in Appendix B section 7.2.4.4 thus shows that no statistical information is output by gPROMS for $\alpha_{c,1}$ and $\alpha_{c,2}$ because they are entirely dependent upon $\eta_{c,1}$ and $\eta_{c,2}$. Looking at the estimated value of the parameter $\eta_{c,1}$ = 1.60 x 10^3, a low standard deviation of only 4.67 suggests a good degree of accuracy in this estimation, and a t-value of 163.47 shows that it is the most important parameter to the model fit. In contrast, the t-value for $\eta_{c,2}$ is 0.23, less than the reference t-value of 1.648 and thus statistically insignificant, although this is likely in part due to the smaller concentrations of the FeL_2^+ complex present. Comparatively however, this still places the temperature dependent parameter relating to K_2 significantly above the Arrhenius parameters relating to other kinetic rate constants in terms of its significance to the model fit, in the order K_2 > B >k_1 > $k_{red,1,FeL}$.

In summary, in setting the values of K_1 and K_2 to published literature values at 298K in this final model iteration, the temperature dependence relationships relating to the equilibrium constants of complex formation now involve a pair of dependent variables, the values of which are rooted in widely accepted literature data. Returning to Table 5.12, it is therefore likely that the estimated values for K_1 and K_2 at the relevant elevated temperatures and the thermodynamic data obtained using this approach are more representative of the actual chemistry of the system than those obtained in the previous model described in section 5.3.1, where parameters relating to the equilibrium

constants were allowed to float at all temperatures. In comparison to those reported in the literature from the single study by Andrieux *et al* [57] at the same temperatures, the estimations provided by this final model iteration for K_1 and K_2 show an increase and decrease respectively of approximately an order of magnitude. However, as described previously at the start of section 5.3.2, the lack of reliability in the spectral deconvolution techniques employed by Andrieux *et al* [57] and the assumptions made regarding the absence of Fe(III) reduction and prior speciation knowledge required, the values reported by these authors at higher temperatures in particular could potentially be subject to significant errors.

As a final note on this model, Figure 5.12 compares the calculated NH_3OH^+ profiles to those obtained experimentally.

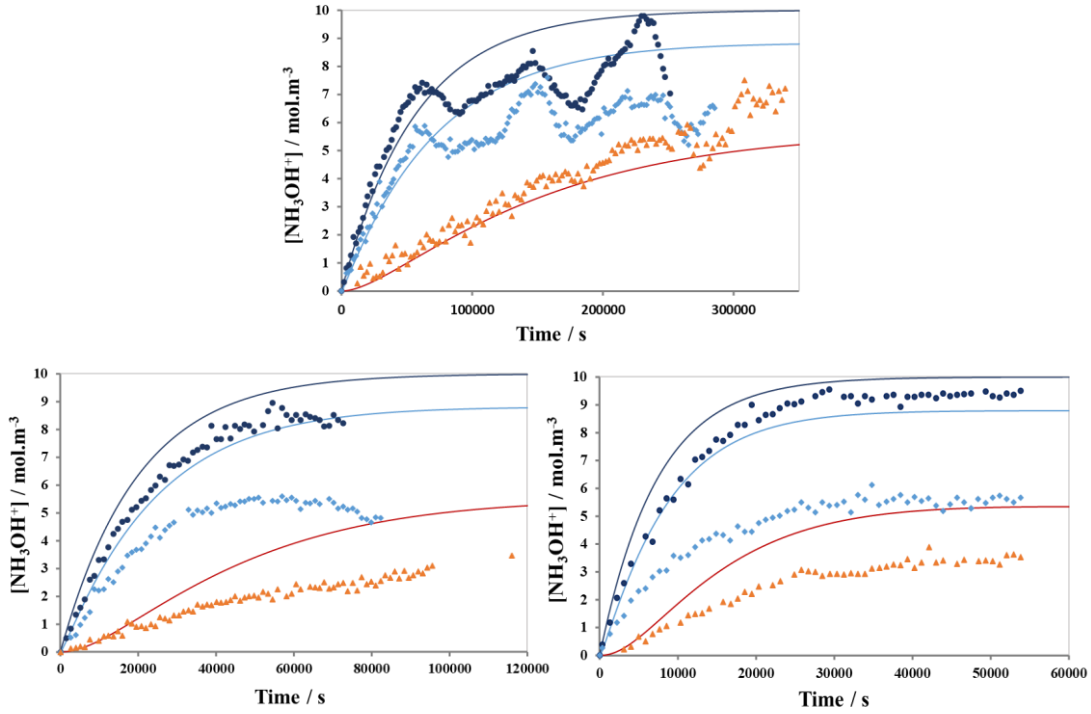

Figure 5.12: Plots of experimental NH_3OH^+ data (points) and model output (lines) for the final model, including the reduction of FeL^{2+} by NH_3OH^+, the hydrolysis of FeL^{2+}, the reduction of $Fe^{3+}_{(aq)}$ by NH_3OH^+ modelled with the modified Bengtsson equation, and K_1 and K_2 set at 298K, with $[Fe(III)]_0$ = 0 mmol dm^{-3} (dark blue), 2.5 mmol dm^{-3} (light blue) and 10 mmol dm^{-3} (orange).

Inspection of these figures shows that, with the exception of the dataset in which $[Fe(III)]_0 = 10$ mmol dm^{-3} at 313K, the model generally predicts greater concentrations of NH_3OH^+ throughout the timescale of the AHA hydrolysis than is seen in the experimental dataset. This is expected due to the fact that the non-trivial nature of the chemistry of this species in nitric acid media, including the possible autocatalytic reaction of HAN with HNO_3/HNO_2 that ultimately leads to its depletion, is not under consideration in this model. This observation thus strengthens the validity of the approach taken in this Chapter to use only the data obtained by ion chromatography experiments for the acetate and Fe^{2+} species, and not that for NH_3OH^+, in the estimations of kinetic parameters.

5.3.4 Summary

This Chapter has described the development of a kinetic model for the Fe(III)/AHA system by fitting of experimental temperature dependent data obtained by ion chromatography for the ingrowth of acetate and Fe(II) during the hydrolysis of free and Fe(III)-complexed AHA. Several different iterations of the kinetic model have been discussed, and how each model iteration informed the development of the next, ultimately in order to reach a final model that most closely describes the generated experimental data.

Overall, the modelling suggests that acetate production during the hydrolysis of Fe(III)-complexed AHA is driven primarily by free AHA hydrolysis, with only a minimal contribution from the hydrolysis of complexed AHA to the point that FeL^{2+} hydrolyses at such a slow rate as to be nearly non-existent. Therefore, in contrast to

that previously reported by Andrieux *et al.* [83], complexation with Fe(III) appears to protect the ligand from hydrolysis, as is true for the complexation of Pu(IV) with AHA [74, 82]. The discrepancy between our findings and the findings of Andrieux *et al.* [83] is due to the fact that these authors used an analysis method based on a spectroscopic technique which assumes that Fe(III) only complexes with the ligand and does not react with NH_2OH, an assumption which has been proved incorrect in this thesis by the observed appearance of Fe(II) during the hydrolysis of Fe(III)-complexed AHA.

Thus, in relation to the above mentioned assumption, the primary difference between our kinetic model of the Fe(III)/AHA system and that previously published by Andrieux *et al.* [77] is the inclusion of the reduction of free Fe(III) by hydroxylamine. The initial approach taken to modelling this reaction was to incorporate rate expressions derived by Bengtsson [99] for the two limiting cases of the reduction of free Fe(III) by HAN by either a 1:1 or 2:1 stoichiometric pathway to produce either N_2 or N_2O respectively as a product. These two stoichiometric pathways were assumed to occur independently in the first model iterations in the following ways; i) in the initial model iterations it was assumed that only the 1:1 pathway was active in the datasets with $[Fe(III)]_0$ = 2.5 mmol dm^{-3} and the 2:1 was active in the datasets with $[Fe(III)]_0$ = 10 mmol dm^{-3}, ii) in the preceding model iteration incorporation of an inequality switch via an IF-statement allowed for the model to move from a 2:1 stoichiometry at the beginning of the run to a 1:1 stoichiometry at a point during the AHA hydrolysis reaction when the $[Fe(III)]/[NH_2OH]$ ratio reached a defined number.

Neither of these approaches however proved entirely successful, with the latter model producing Fe(II) profiles containing an obvious “kink” at the switching point rather

than matching the smooth curvature of the experimental Fe(II) data. In adopting the IF-statement model, two separate simulations were performed in which [Fe(III)] was defined as either free ($Fe^{3+}_{(aq)}$) or total iron (Fe_T) in the inequality. Interestingly, species concentration profiles and parameter estimations output by gPROMS were found to be nearly identical in both cases, suggest that either; i) the "active" species being reduced by hydroxylamine is both free and complexed Fe(III), a theory that been previously suggested for the Pu(IV)/FHA/HNO_3 system [186], or ii) Fe(III) is not remaining bound in the complex. The former assumption was tested by incorporation of an additional reaction of the reduction of complexed Fe(III) in the form of the mono-complex by hydroxylamine. The initial model iteration including this reaction and those proceeding it suggested that whilst it was a reaction potentially worth consideration in these systems, its contribution is minor to an equivalent degree to that of the hydrolysis of complexed AHA.

Following these two approaches to modelling Fe(III) reduction by hydroxylamine, a thorough examination of the mechanism of the reduction of free Fe(III) by hydroxylamine was undertaken, and a steady-state analysis performed with the aim to derive a single kinetic rate expression for this reaction. Whilst the mechanism suggested by Bengtsson [99] involved a radical dimerization as the rate-determining step for each of the two stoichiometric pathways, we considered the dimerization of the H_2NO^* radical for the 1:1 pathway, and by analogy that of the HNO radical for the 2:1 pathway, to be unlikely due to the low concentrations of both the radical species present. Instead, a reaction of the H_2NO^* radical with the significantly more abundant $Fe^{3+}_{(aq)}$ ion, leading ultimately to the reduction of Fe^{3+} by NH_3OH^+ via a 2:1

stoichiometry, was assumed to be more likely. The final derived modified Bengtsson equation involved lumped pseudo-rate parameters *B* and *C*, consisting of elementary reactions relating primarily to the original 1:1 and 2:1 stoichiometric pathway respectively. Parameter estimations for the pseudo kinetic rate constant *C* in the modified Bengtsson equation were found to be much higher than for those for *B*. If we consider this observation in the context of our original assumption in the derivation of the modified Bengtsson equation, that the dimerization reactions of the H_2NO^* and HNO radical species are unlikely, it suggests that the reaction of Fe^{3+} with the radical H_2NO^*, a key additional elementary reaction that is involved only in the description of the lumped pseudo-rate parameter *C*, is rapid.

The other major difference in our kinetic model of the Fe(III)/AHA system to that previously published [77] is in the values of the equilibrium constants, K_1 and K_2, for the formation of the mono- and bis-acetohydroxamatoiron(III) complexes, FeL^{2+} and FeL_2^+. Our initial approach to modelling speciation was to set the values of K_1 and K_2 at the relevant temperatures to those reported by Andrieux *et al.* [57], the single available published study at elevated temperatures, where values of K_1 and K_2 were determined via a spectroscopic method. However, this approach proved unsuccessful in replicating the slower ingrowth of acetate observed experimentally in the presence of increasing initial Fe(III) concentrations. Instead, the equilibrium constants were thus fully estimated by gPROMS in a later model iteration. This allowed the model to produce good fits to the acetate data by assuming a greater amount of the ligand bound in complexed form, specifically as the mono-complex, than previously published, and thus unable to participate in the hydrolysis of the free ligand to produce acetic acid and

hydroxylamine, the primary reaction that determines acetate production in these systems. With the exception of those values calculated at 298K, the estimated temperature dependence relationship for the equilibrium constants provides values for K_1 and K_2 at the relevant elevated temperatures that showed an increase and decrease respectively of approximately an order of magnitude from those of Andrieux *et al* [57].

The spectral deconvolution techniques employed by Andrieux *et al* [57] requires assumptions to be made regarding; i) the absence of Fe(III) reduction, and ii) prior speciation knowledge. With the former assumption proved incorrect, the values reported by these authors at higher temperatures in particular, could therefore potentially be subject to significant errors. Thus, in the final model iteration, the approach taken was to set K_1 and K_2 instead to those determined at 298K only, a temperature at which the interfering reduction of Fe(III) by hydroxylamine would be minor, and the previously reported equilibrium constants would be expected to be reliable. As before, the resulting estimations of K_1 and K_2 using this approach suggested that the values of the equilibrium constants for complex formation at elevated temperatures differs to that published by some way, thus further study in this area is recommended based on the modelling described in this thesis.

Overall, the combined experimental results and modelling work presented in this thesis show that the definition of Pu(IV) as an oxidising metal ion in the presence of AHA must be extended to Fe(III), and thus Fe(III) can be regarded as a significantly better analogue for Pu(IV) in these systems than previously thought. The final model described in this Chapter, particularly with regards to the identity of hydroxylamine as the reducing agent for both free, and to a significantly smaller extent potentially

complexed metal ions, could form a basis for modelling the similar data in relation to Pu(IV)/AHA/HNO_3 systems.

From the modelling presented in this Chapter, two key conclusions can be drawn. It has been shown that there are three principal reactions/processes of importance in the Fe(III)/AHA system, namely; i) the acid-catalysed hydrolysis of free AHA, ii) the complexation between Fe(III) and AHA to produce the 1:1 complex, and iii) the reduction of free Fe(III) by hydroxylamine released as a product of AHA hydrolysis. Complexation of the ligand with Fe(III), and by analogy Pu(IV), thus protects both the complexed ligand from acid-catalysed hydrolysis, and the complexed metal ion from a reduction by the AHA hydrolysis product hydroxylamine. The latter conclusion provides significant promise for the use of AHA as a suitable reagent for the management of Pu(IV) and Np(IV) in an Advanced PUREX.

CHAPTER 6

Conclusions and Further Work

6 Conclusions and Further Work

6.1 Thesis Objectives

The primary objective of this thesis was to study the Fe(III)-AHA system as a non-active analogue to Np(IV) and Pu(IV) systems and, in particular, to address two key scientific and technology gaps that remain around actinide-AHA systems of relevance to the Advanced PUREX recycle process:

iii) Is there any change in the products of AHA hydrolysis when the hydroxamic acid is complexed to a metal ion?

iv) What is the nature of the reducing agent responsible for the observed ingrowth of Pu(III) during the associated Pu(IV)-AHA hydrolysis?

This Chapter will discuss the main conclusions drawn from the experimental work performed in this thesis in relation to these key project aims, in the order in which of the work has been presented.

6.2 Conclusions

6.2.1 Identification of Hydrolysis Products by Raman Spectroscopy

Experiments were performed using Raman spectroscopy as a means to identify the products of AHA hydrolysis in the absence and presence of Fe(III), at both ambient and elevated temperatures. The overall aim of these experiments was to investigate whether the mechanism of AHA hydrolysis and subsequent product distribution changes when AHA is complexed with a metal ion. These studies were performed via two separate methods described below.

SERS studies were initially performed using a Voyage Confocal Microscope (B&WTek, USA) Raman spectrometer equipped with a 785 nm laser, by loading small volume solution samples onto a highly polished gold disk deposited on a quartz crystal. Specifically, spectra were taken of; i) a solution of 0.5 mol dm^{-3} AHA in 5 %wt. HNO_3, and ii) the same solution in the presence of 0.32 mol dm^{-3} $Fe(III)(NO_3)_3$, corresponding to a AHA:Fe ratio of 1.6:1 where the mono-complex dominates, before and after hydrolysis at r.t.p.

The spectra obtained from these SERS studies revealed that there is no difference in the nature of the products of AHA hydrolysis in the absence or presence of initial Fe(III). The intensity of the relevant bands assigned to acetic acid were very similar in all spectra obtained, suggesting similar yields of this hydrolysis product from both free and Fe(III)-complexed AHA. For the hydroxylamine product however, a reduction in the intensity of the primary ν_s(N-O) stretching band was observed in the acquired

spectra of the solutions of AHA in the presence of initial Fe(III), suggesting a lower overall yield of this product from the hydrolysis of complexed AHA compared to free AHA. A reaction of hydroxylamine with HNO_3, which ultimately leads to its loss and is autocatalyzed by HNO_2, is well known [93]. Thus, Raman peaks for HNO_2 were identified from standards with the aim to determine if this reaction was the cause of the apparent lower yield of hydroxylamine. However, no evidence for HNO_2 was seen in the spectra of the hydrolysed AHA solutions that might suggest the hydroxylamine was reacting with the HNO_3 media.

Following on from the SERS studies, experiments were performed using a Horiba XplorRa ONE^{TM} Raman spectrometer fitted with a 532nm wavelength laser and a solution adapter, within which samples are housed in a 3ml cuvette. Solutions of 0.5 mol dm^{-3} AHA in 3 mol dm^{-3} HNO_3 were hydrolysed under conditions of; i) r.t.p, with spectra taken at set time intervals throughout AHA hydrolysis, and ii) at 333K in the absence and presence of initial Fe(III) concentrations of 0.25 and 0.5 mol dm^{-3}, with spectra taken only on completion of hydrolysis.

For AHA hydrolysis performed at r.t.p. in the absence of Fe(III), small wavelength shifts and changes in intensity of the primary ν_s(N-O) stretching band for hydroxylamine were observed throughout the hydrolysis reaction, suggesting a possible decomposition of this species during the hydrolysis reaction via its reaction with HNO_3/HNO_2. However, the absence of any conclusive evidence for HNO_2 suggested these peak variations were likely an artefact of the ν_s(N-O) stretching bands in hydroxylamine and HNO_3 merging instead. For the elevated temperature studies however, final spectra showed the intensity of the ν_s(N-O) assigned to NH_3OH^+ to be

significantly reduced in the presence of Fe(III) compared to those bands for acetic acid, in agreement with the SERS studies.

In summary, some differences in peak intensities in some of the obtained Raman spectra suggested that the yields of the AHA hydrolysis product, hydroxylamine, differs in the presence of Fe(III). No evidence however was seen for any products additional to hydroxylamine and acetic acid using either instrumental setup. These initial studies suggest that the products of AHA hydrolysis do not change when the AHA is complexed to a metal ion, but the resultant yields of those products do.

6.2.2 Real-time Quantification of Acetate by Ion Chromatography

Whilst the kinetics of the acid catalysed hydrolysis of AHA have been examined previously by several authors [69, 77-79, 83], reported studies are done predominantly by a colorimetric method whereby excess Fe(III) is added to form the mono-complex, the concentration of which is then determined by a subsequent spectroscopic measurement of the maximum absorbance of the complex. However, this spectroscopic determination method introduces uncertainty into the measurement for two reasons. Firstly, it assumes all AHA is complexed as the mono-complex, whereas a small amount of the bis-complex will also be contributing, and this complex absorbs disproportionally more strongly than the mono-complex, illustrated by the respective values of the extinction coefficients for the bis- and mono-complex of $\varepsilon_2 = 165 \pm 14$ $m^2\ mol^{-1}$ and $\varepsilon_1 = 101 \pm 1\ m^2\ mol^{-1}$ [57]. Additionally, whilst it is unclear as to what extent it occurs in these systems, the reduction of Fe(III) by NH_2OH has been found to obtain under certain conditions [99]. If it were to occur, it would have the effect of

reducing the concentration of Fe(III) in solution and thus increasing the rate of decrease in the UV-vis absorption associated with the Fe-AHA complex(es) over and above that rate associated with the hydrolysis reaction alone. These two effects therefore needed to be deconvoluted.

To this end, ion chromatography was used as an alternative and novel method for obtaining kinetic data on the hydrolysis of AHA by measuring the ingrowth of the acetate ion in real-time produced from the hydrolysis of free and complexed AHA. The acetic acid product of the hydrolysis of AHA is considered silent once generated, and its quantification thus provides a direct measurement for the total AHA lost in the system, requiring no assumptions or corrections of the data.

Experiments were performed following the hydrolysis of 10 mmol dm^{-3} AHA in 0.1 mol dm^{-3} HNO_3, in the absence and presence of 2.5 and 10 mmol dm^{-3} Fe(III), at elevated temperatures of 313K, 323K and 333K. Results showed that, whilst the final quantity of acetate was equal to the initial AHA as expected by reaction stoichiometry, the observed rate of ingrowth of acetate was inhibited in the presence of Fe(III). This suggested that, in contrast to findings of a previously published kinetic analysis of the complex hydrolysis by Andrieux *et al.* [77, 83] using the spectroscopic method, complexation protects the ligand from hydrolysis.

The data was then further examined by adaptation of the simple kinetic model for the Fe(III)-AHA system derived by Andrieux *et al.* [77], in which the authors assume that no redox chemistry between Fe(III) and hydroxylamine occurs. From this simple kinetic model, in which the authors derive an equation for the concentration of the

ligand in terms of the absorbance of the mono-complex, we derived an equation to describe the ingrowth of acetate from both free and complexed AHA hydrolysis. Testing our equation on the acetate data obtained allowed us to make two key observations, namely; i) fitted values of the hydrolysis reaction rate constant for the hydrolysis of complexed, k_1, was less than that for the hydrolysis of free AHA hydrolysis, k_0, at all temperatures, meaning complexation protects the ligand from hydrolysis, and ii) the simple kinetic model was insufficient to provide accurate fits to the data, particularly for those experiments with high initial Fe(III) concentrations.

With regards to the latter observation, speciation data had shown that, aside from that present in the form of the Fe-AHA mono-complex, the systems with higher initial Fe(III) concentrations also exhibited a greater proportion of the remaining Fe(III) present in the form of free Fe(III) than in the form of the bis-complex. According to Bengtsson *et al.* [99], the reduction of Fe(III) by NH_2OH requires high Fe(III)/NH_2OH ratios and/or elevated temperatures. Overall, the described acetate data analysis suggested that at elevated temperatures and higher total iron, Fe_T, the reduction of Fe(III) by NH_2OH leads to a departure from the initial Fe(III) concentration (i.e Fe_T) on which the derivation of the model was based. This hypothesis was later explored by quantification of both the hydrolysis product NH_2OH and Fe(II) produced by its action on Fe(III).

6.2.3 Nitrous Acid Analysis

The role of HNO_2 during the hydrolysis of complexed AHA has been discussed previously by several authors in studies of the complexation of AHA with Pu(IV),

specifically within the context of the development of an Advanced PUREX process [74]. In these systems, an ingrowth of Pu(III) is seen during the associated AHA complex hydrolysis, followed by an observed re-oxidation of Pu(III) to Pu(IV) under certain conditions. The latter is suggested to be catalysed by HNO_2, which accumulates in HNO_3 solutions once hydroxylamine and, potentially AHA, are no longer available to act as a scavenger for HNO_2 [74, 149, 150].

Alongside that of the acetate ion during the ion chromatography studies of the hydrolysis of free and complexed AHA, the concentration of the NO_2^- ion, a product of the dissociation of HNO_2, was also quantified. Whilst it was expected that both higher initial Fe(III) concentrations, and higher temperatures would be required to promote the accumulation of HNO_2 [93], the obtained data suggested this was not the case. The nitrite ion was in fact only observed in those experiments performed at the lowest temperature of 313K, and although very small, the maximum observed NO_2^- measurement of 0.05 mmol dm^{-3} was obtained during AHA hydrolysis in the presence of 2.5 mmol dm^{-3} initial Fe(III), not 10 mmol dm^{-3} Fe(III).

Whilst the accuracy of the obtained NO_2^- measurements was uncertain, due to the majority of them falling between the LOQ and LOD, the profiles obtained for the two experiments at 313K in the presence of initial Fe(III) were interesting, with each profile showing several peaks and troughs. The induction period for the reaction of NH_2OH and HNO_3 to form HNO_2 as a product, is known to increase at high hydroxylamine concentrations [91]. It is therefore suggested that the peaks and troughs in the data observed in those Fe(III)-containing systems at 313K is due to an interaction of HNO_2 with NH_2OH, which might not be observed in those data sets at elevated

temperature and high initial [Fe(III)] if the Fe(III) was acting to reduce NH_2OH. From these IC studies, it was thus hypothesised that the slower ingrowth of NH_3OH^+ from AHA hydrolysis at 313K compared to the higher temperature of 333K could lead to relatively lower HAN concentrations, shorter induction periods, and thus the appearance of measurable nitrite concentrations.

In addition to the IC studies, a more accurate colorimetric method was used for the quantification of nitrite in solution with the aim to determine the extent of apparent HNO_2 accumulation observed in some experiments. Two experiments were performed including; i) measurement of small concentrations of intrinsic HNO_2/NO_2^- in a solution of 0.1 mol dm^{-3} HNO_3 over the temperature range 303–333K, and ii) determination of the rate of the decomposition of 100 µmol dm^{-3} HNO_2 at the higher temperatures of 323K and 333K. The results of the first analysis showed intrinsic HNO_2 to be minimal and independent of temperature, with all measurements in the range of 0.82–0.87 µmol dm^{-3}. Considering the previous IC analysis of NO_2^-, the second analysis was prompted by a hypothesis that any significant quantity of HNO_2 produced at the higher temperatures might be undergoing a rapid thermal decomposition. However, the colorimetric results showed that, once formed, the thermal decomposition of HNO_2 is insignificant, and losses are instead expected to be by reaction with other species in solution such as hydroxylamine or Fe(II).

6.2.4 Analysis of Hydroxylamine

Andrieux *et al.* [83] have previously studied the kinetics of the hydrolysis of AHA and used quantum mechanical modelling to suggest a mechanism for the hydrolysis of the

monoacetohydroxamatoiron(III) complex that would produce analogous hydrolysis products to free AHA, however these authors did not directly quantify the hydrolysis products in their study. Having studied the production of the acetic acid product previously in section 4.2 of this thesis, the second hydrolysis product, hydroxylamine, was also quantified using two different techniques namely; i) a titrimetric analysis on solutions of free and Fe(III)-complexed AHA post-hydrolysis, and ii) an IC analysis to quantify the concentration of the protonated ion, NH_3OH^+, in real-time during the hydrolysis reaction.

Using a redox titration with potassium bromate as described in Vogel's textbook of Quantitative Chemical Analysis [124], hydroxylamine was initially quantified following hydrolysis of 4 mmol dm^{-3} AHA at the elevated temperature of 333K in the absence and presence of 2.5 mmol dm^{-3} Fe(III). Hydrolysis was performed in differing acidic media, in 0.3 mol dm^{-3} HNO_3, $HClO_4$ and H_2SO_4, and the resulting hydroxylamine quantified. However, preliminary analysis of hydroxylamine from these hydrolysed solutions proved inconclusive due to significant errors in measurements and a missing step in the described analysis method. These issues were resolved in further studies by; i) experimental method modification, and ii) increasing the initial concentration of AHA to minimise the percentage errors in hydroxylamine measurements.

Further analysis was then done on solutions of 20 mmol dm^{-3} AHA hydrolysed in varying acidic media of 0.3 mol dm^{-3} in the absence and presence of excess Fe(III), both at r.t.p. and 333K. To determine the extent of any contribution of the possible reaction of hydroxylamine with HNO_3/HNO_2 on resulting NH_2OH concentrations, in

the case of those hydrolysis studies in HNO_3, some were also performed in the presence of sulfamic acid to act as a HNO_2 scavenger, and thus remove the possibility of reactions of hydroxylamine with HNO_3/HNO_2. In comparison to the equivalent experiments in HNO_3 in the absence of sulfamic acid, no significant differences in the final measured NH_2OH concentrations were seen. Overall, the collection of titrimetric analyses showed a reduction in the expected concentration of NH_2OH after hydrolysis of Fe(III)-complexed AHA compared to that from free AHA regardless of acidic media used, which could be representative of either i) a different mechanism for Fe(III)-complexed AHA hydrolysis to give differing yields of the same products, or ii) the occurrence of Fe(III) reduction by NH_2OH. Coupled with previous Raman spectroscopy and acetate analysis by IC, the titrimetric studies suggested the latter.

Following the titrimetric analyses, IC was utilised to determine the concentration of NH_3OH^+ during the hydrolysis of free and complexed AHA under the same conditions as studied previously for the acetate ion. It is important to note that the measurements of this particular species were the most uncertain of all the species studied by IC, showing the greatest variation in calibration functions. Despite this, several key observations of the data were made.

Firstly, the reaction of HAN in HNO_3/HNO_2 that leads to its decomposition was evident in some of the NH_3OH^+ measurement profiles obtained from IC experiments at 313K, particularly in those obtained for AHA hydrolysis in the absence and presence of 2.5 mmol dm^{-3} initial Fe(III). The experiments showed a pattern of peaks and troughs in the NH_3OH^+ concentration profiles that coincided with those observed in measurements of NO_2^- under the same conditions. The same pattern of peaks and

troughs was not seen in the dataset obtained at 313K with the higher initial Fe(III) concentration of 10 mmol dm^{-3}. This therefore agrees with the lack of measurable nitrite ion concentrations observed in the same experimental run, suggesting that a slower ingrowth of NH_3OH^+ from AHA hydrolysis in the presence of higher initial Fe(III) concentrations at this temperature appears to inhibit the autocatalytic decomposition of NH_3OH^+ by HNO_3/HNO_2.

Secondly, the ingrowth of NH_3OH^+ was seen to be retarded in the presence of increasing initial Fe(III) concentrations at all temperatures studied. When compared to data previously obtained for acetate concentration profiles under the same conditions, that recorded for AHA hydrolysis at 323K and 333K showed NH_3OH^+ to reach only around 60% and 40% of the theoretical maximum in the presence of 2.5 mmol dm^{-3} and 10 mmol dm^{-3} initial Fe(III) respectively. With no evidence of interfering reactions of HAN with HNO_3/HNO_2 at these higher temperatures, it appeared that a reduction of Fe^{3+} by hydroxylamine was the most likely explanation for this loss of NH_3OH^+ at higher temperatures. Whilst the likelihood of the occurrence of the latter reaction had been discounted initially based an expected kinetic hinderance, it therefore required further investigation based on these IC results and the previously described titrimetric analyses.

6.2.5 Analysis of Fe(II)

Based on the findings of previous analyses, particularly those for the hydroxylamine product, the final species worthy of investigation in these systems was Fe(II), a product of the now expected reaction between the AHA hydrolysis product hydroxylamine and

Fe(III). In this thesis Fe(II) was quantified in two ways, namely; i) a spectroscopic method to determine the final concentrations of this species on completion of the AHA hydrolysis, and ii) ion chromatography experiments to quantify the ingrowth of this ion in real-time in the same systems studied previously for acetate, nitrite and NH_3OH^+.

Spectroscopic analysis was performed on solutions of 20 mmol dm^{-3} AHA hydrolysed at 333K in 0.3 mol dm^{-3} HNO_3 and $HClO_4$, in the presence of 12.5 and 25 mmol dm^{-3} Fe(III), equivalent to a AHA:Fe(III) ratio of 1.6:1 where the dominant Fe(III) species are the mono-complex and free Fe(III). For comparison to HNO_3, an equivalent solution of excess Fe(III) to AHA in 0.3 mol dm^{-3} $HClO_4$ was also hydrolysed in an inert N_2 atmosphere, to ensure no possibility of the re-oxidation of Fe(II) back to Fe(III). The results showed that final concentrations of Fe(II) were approximately 100% of the initial Fe(III) for all solutions hydrolysed at this elevated temperature of 333K in HNO_3, whilst approximately 70% of the initial Fe(III) was converted to Fe(II) following hydrolysis in $HClO_4$ in each case. This is likely due to a different mechanism operating for the reduction of NH_2OH by Fe(III) in $HClO_4$ media compared to HNO_3. The use of an inert N_2 atmosphere in a solution hydrolysed in $HClO_4$ had no effect on the Fe(II) measurement (within experimental error).

Following the spectroscopic analyses of Fe(II), IC experiments involving the quantification of Fe(II) concentrations throughout the hydrolysis of complexed AHA were performed. Consistent throughout the temperature range 313 - 333K, the obtained Fe(II) concentration profiles followed a similar shape to that of the AHA hydrolysis products acetate and NH_3OH^+, with the rate of ingrowth being initially more rapid and

gradually decreasing as the hydrolysis reaction proceeded. The shape of the resulting Fe(II) profile was also found to be analogous to that observed for the ingrowth of Pu(III) during the hydrolysis of the associated Pu(IV)-AHA complex in HNO_3. [74, 82, 149]. The reduction of Fe(III) and Pu(IV) by HAN is known to proceed via two separate pathways of variable stoichiometry (2:1 or 1:1 metal ion/HAN) and rate, dependent on which of the reactants is in excess. It was expected that the Fe(II) concentration profiles obtained from this analysis were representative of an initial dominant 2:1 stoichiometry reaction mechanism with a higher rate constant when Fe(III) is in vast excess of NH_3OH^+, followed by the slower reaction mechanism with 1:1 stoichiometry becoming dominant as NH_3OH^+ is produced by the hydrolysis of AHA and Fe(III) is used up. By analogy to the reduction of Pu(IV) by HAN, which is thought to proceed by the same mechanism, the reduced form of the metal ion is also known to have an inhibiting effect on the reaction rate.

In contrast to experiments by Carrott *et al.* [74] in which the authors investigated the ingrowth of Pu(III) during the hydrolysis of the associated Pu(IV)-AHA or Pu(IV)-FHA complex, an induction period for the ingrowth of NH_3OH^+ was not evident in any of the experiments presented in this thesis. However, the authors note that the observed length of this period was variable, totalling only a few minutes in some of their experiments involving AHA. Thus, such an induction period would not have been noticeable with the IC analysis presented here due to the greater LOD and length of time required for each sample measurement in comparison to that for the UV-Vis spectroscopic method used by Carrott *et al.* [74]. The authors attribute this induction period to the hydrolysis of the free hydroxamic acid in the bulk solution, which occurs

at a quicker rate for AHA than for FHA, and when a threshold is passed, de-complexed Pu(IV) becomes available for reduction by HAN or AHA.

Final experiments presented in this thesis quantified the ingrowth of Fe(II) from initial solutions of varying Fe(III)/NH_2OH ratios of 1– 10 in 0.1 M HNO_3 at 323K. These experiments suggested the ratio of Fe(III)/HAN required for a purely 2:1 stoichiometry reaction pathway was higher than that required for the equivalent Pu(IV)/HAN 2:1 stoichiometry reaction. Interestingly, the shorter timescales of these IC experiments compared to those involving AHA hydrolysis, allowed for the observed re-oxidation of Fe(II) when initial Fe(III)/HAN ratios were 5:1 or above. The addition of sulfamic acid to the initial solution as a HNO_2 scavenger inhibited this re-oxidation, providing evidence to suggest that HNO_2 is the species responsible for the re-oxidation of Fe(II), and by analogy, Pu(III).

Finally, by examination of the reaction mechanism proposed by Bengtsson *et al.* [99], a preliminary thermodynamic analysis of redox couples confirmed the possibility of Fe(III) reduction by NH_2OH by both the 1:1 and 2:1 stoichiometry pathways under the specific conditions of all the described IC experiments.

6.2.6 Whole System Kinetic Modelling

Using the library of temperature dependent data gathered from the IC experiments for the ingrowth of the acetate and Fe^{2+} ions during the hydrolysis of free and Fe(III)-complexed AHA, Chapter 5 of this thesis described the development of a revised kinetic model for the Fe(III)/AHA system using the gPROMS software, the overall

aim of which was to provide insights on the key reactions operating within this system and ultimately inform future modelling of the Pu(IV)-AHA system. The data for the AHA hydrolysis product NH_3OH^+ was not used in parameter estimations for the various kinetic rate constants and equilibrium constants because this data was expected to be affected by the non-trivial chemistry of hydroxylamine with HNO_3/HNO_2, which was not a focus here and not included in the model.

The initial gPROMS model was based on the kinetic model for the hydrolysis of AHA in the presence of Fe(III) published by Andrieux *et al* [77], but differed from these authors in the definition of Fe(III) as a redox active ion, i.e. the reduction of free Fe(III) by NH_3OH^+ is assumed to occur, experimental evidence of which was presented in Chapter 4 section 4.5. Reactions included in the model as described by Andrieux *et al.* [77] were as follows; i) the formation of the mono- and bis-hydroxamate complexes, FeL^{2+} and FeL_2^+ with equilibrium constants K_1 and K_2 respectively, and ii) the acid-catalysed hydrolysis of free AHA and the mono-complex as described by the associated second order rate parameter for each reaction being k_0 and k_1 respectively. The bis-complex was assumed to dissociate rapidly in the initial stages of the reaction to the point that its hydrolysis could be ignored. Thus, by the inclusion of the formation of the bis-complex via K_2 it was assumed that this complex affected the mono-complex concentration through its speciation, whereas by the exclusion of its expected insignificant hydrolysis, it was assumed this complex had no affect the loss of the ligand. Additionally, the reduction of free Fe(III) by hydroxylamine in a 1:1 and 2:1 stoichiometry was included with individual rate equations as described by Bengtsson *et al.* [99].

Overall, all model iterations suggested that the production of acetate during the hydrolysis of Fe(III)-complexed AHA was driven primarily by the hydrolysis of free AHA, with only a minor contribution from the hydrolysis of the mono-complex to the point that FeL^{2+} hydrolyses at such a slow rate as to be nearly non-existent. Thus, as is true for the complexation of Pu(IV) with AHA, complexation with the Fe(III) metal ion appears to protect the ligand from hydrolysis, a finding in contrast to that previously reported by Andrieux *et al*. [83]. These authors however utilised a spectroscopic method that assumes Fe(III) is a non-oxidising metal ion with regards to AHA i.e. Fe(III) only complexes with the ligand and does not undergo an interfering redox reaction with the AHA hydrolysis product NH_2OH, an assumption that has been proved incorrect in this thesis.

In the initial models, the two stoichiometric pathways for the reduction of Fe(III) by hydroxylamine were assumed to occur entirely independently in the following ways; i) it was assumed that only the 1:1 pathway was active in the datasets with an initial Fe(III) concentration, $[Fe(III)]_0$, of 2.5 mmol dm^{-3}, and only the 2:1 pathway was active in the datasets with $[Fe(III)]_0$ = 10 mmol dm^{-3}, and ii) an inequality switch via an IF-statement allowed for the model to move from a 2:1 stoichiometry reaction at the beginning of a run to a 1:1 stoichiometry reaction at a point during the AHA hydrolysis when the Fe(III)/NH_2OH concentration ratio reached a defined number. Both these approaches however proved less successful than expected. In respect to the IF-statement model, two simulations were performed in which [Fe(III)] in the inequality was defined as either free ($Fe^{3+}_{(aq)}$) or total iron (Fe_T), and interestingly, the concentration profiles and parameter estimations output by the gPROMS models were

found to be nearly identical in each case. A theory suggested previously for the Pu(IV)/FHA/HNO_3 system [186], this observation suggested that the "active species being reduced by hydroxylamine might be both the free and complexed metal ion. However, testing this assumption by incorporation of the reduction of the FeL^{2+} mono-complex by hydroxylamine into the model showed that whilst it was a reaction that was potentially worth consideration, its contribution in the systems modelled here was minor to a degree equivalent to that of the hydrolysis of the FeL^{2+} complex.

For the determination of a suitable approach to modelling the reduction of free Fe(III) by hydroxylamine, a thorough examination of the mechanism of this reaction as suggested by Bengtsson [99] was then undertaken. Analogous to the same mechanism suggested for the reduction of free Pu(IV) by hydroxylamine, a dimerization reaction of the HNO and H_2NO^* radical species is considered as the rate determining step for the 1:1 and 2:1 stoichiometric pathways respectively. Despite the highly reactive nature of these radical species, we considered the dimerization reactions unlikely due to the very low concentrations of the HNO and H_2NO^* radicals that will be present in solution. Instead, we consider the reaction of the H_2NO^* radical with the significantly more abundant $Fe^{3+}_{(aq)}$ ion, which ultimately leads to the reduction of Fe^{3+} by NH_2OH via a 2:1 stoichiometry, to be more likely, and performed a steady state analysis based on this assumption. From this analysis, a single equation was derived involving lumped pseudo-rate parameters *B* and *C*, consisting of elementary reactions relating primarily to the 1:1 and 2:1 stoichiometric pathways respectively. Described as the modified Bengtsson equation in this thesis, this kinetic rate expression proved highly successful in fitting the Fe(II) data.

Finally, the initial approach taken to modelling complex speciation was to set the values of K_1 and K_2 in our model to those previously published in the single available study of complex speciation at the elevated temperatures of our datasets by Andrieux *et al*. [57]. This approach unfortunately proved unsuccessful in replicating the slower ingrowth of acetate observed experimentally in the presence of increasing initial Fe(III) concentrations. However, the spectral deconvolution techniques employed by Andieux *et al*. [57] require the assumption to be made that no reduction of free Fe(III) by hydroxylamine occurs, as this reaction would have the effect of reducing the concentration of Fe(III) in the system and thus increasing the rate of decrease in the UV-vis absorption associated with the Fe-AHA complex(es) over and above that rate associated with the hydrolysis reaction alone. In this way, the published values of the equilibrium constants at elevated temperatures in particular, could therefore be subject to significant errors. In the final model, K_1 and K_2 were thus set to literature values at 298K only, a temperature at which the interfering reaction of Fe(III) by NH_2OH would be minor. The estimations of K_1 and K_2 were found to differ from those published by some way, in particular, those for K_1 were significantly larger, suggesting a greater stability of the mono-complex at higher temperatures than previously thought.

Overall, two key conclusions were drawn from the modelling presented in this thesis. Firstly, there are three principal reactions/processes of importance in the Fe(III)/AHA system; including i) the acid-catalysed hydrolysis of free AHA, ii) the complexation of Fe(III) and AHA to form the mono-complex, and iii) the reduction of freely available Fe(III) by the hydroxylamine product of AHA hydrolysis. Thus, complexation of the ligand with Fe(III), and by analogy Pu(IV), protects both the

complexed ligand from hydrolysis in acidic media, and the complexed metal ion from reduction by hydroxylamine.

6.3 Further Work

Overall, the experimental and kinetic modelling work presented in this thesis has shown that in the context of AHA in an advanced PUREX process, Fe(III) is a better analogue to Pu(IV) than previously thought. In answer to the initial aims of the project, we have shown that; i) there is no change in the nature of the products of AHA hydrolysis when the hydroxamic acid is complexed to a metal ion, and ii) the reducing agent responsible for the observed ingrowth of Pu(III) during the associated Pu(IV)-AHA complex hydrolysis is the hydrolysis product hydroxylamine. However, there are several key areas of further work still outstanding in order to gain a better understanding of these systems:

i) Further IC experiments on the Fe(III)/AHA system described in this thesis should be performed under a range of different conditions to determine the effect of not only temperature, but also [HNO_3] and Fe:AHA concentration ratios on the AHA hydrolysis reaction and the reduction of the metal ion.

ii) Similar IC experiments should be performed on Pu(IV)/AHA systems under a range of conditions including [HNO_3], temperature and Pu:AHA concentration ratios, to quantify the acetate, NH_3OH^+ and Pu(III) ingrowth, and ultimately, gain further understanding of the of the roles of these key species in a more complex system than studied in this thesis.

iii) The Pu(IV)/AHA/HNO_3 system has an additional complexity compared to the Fe(III)-AHA system in terms of speciation, with the formation of additional Pu(IV)-nitrate complexes. The rate equation for the one-equivalent reduction of Pu(IV) to Pu(III) by HAN has been reported to differ from that of Fe(III) to Fe(II) by an additional (K_d + [NO_3^-]) term due to nitrate complex formation [95]. This could additionally be interrogated in the reduction of Fe(III) by HAN via the use of chloride as a nitrate analogue, as it is well known that ferric chloride complexes form in neutral and acidic solutions [200-203].

iv) Experiments should be performed to measure and further interrogate the role of HNO_2 in these systems in terms of: i) its interaction with the AHA hydrolysis product hydroxylamine, ii) its role in the observed reoxidation of Pu(III) to Pu(IV) in the presence of AHA [74] and iii) its role in the suspected reoxidation of Fe(II) to Fe(III) in the presence of AHA at longer timescales than studied in this thesis.

v) Kinetic modelling of available experimental data pertaining to the Pu(IV)/AHA system should be undertaken using the revised kinetic model of the Fe(III)/AHA system presented here as a basis, but also including the added complexity of Pu(IV)-nitrate complex speciation. Further work on refinement of the model should then be performed, and the addition of the non-trivial chemistry between HAN and HNO_3/HNO_2 into the model should be considered.

7 Appendix

7.1 Appendix A

7.1.1 Calculations for titrations:

1) Calculation of HAN from titre

$$Total\ moles\ KBrO_3 = 0.02L \times 0.02\ mol.L^{-1}$$

$$Moles\ Br_2 = \frac{titre\ vol\ (L)\ \times 0.1 mol.L^{-1}}{2}$$

$$Moles\ excess\ BrO_3^- = \frac{Moles\ Br_2}{3}$$

$$Moles\ NH_2OH = Total\ moles\ KBrO_3 - Moles\ excess\ BrO_3^-$$

2) Sodium thiosulphate standardisation

$$Moles\ BrO_3^- added = 0.02L \times 0.02\ mol.L^{-1}$$

$$[Na_2S_2O_3] = \frac{6\ \times Moles\ BrO_3^-}{titre\ vol\ (L)}$$

7.1.2 Calculation of calibration function in MagicNET

The injected quantity, Q_i, is calculated as a product of the component's concentration, C_i, to the adjusted volume, V'. This corrects the injected volume, V, to that which passes through the column using the dilution coefficient, D. The software calculates a calibration function for each component, $W_i(R)$, using the relative standard deviation (RSD) method, providing value for the RSD and correlation coefficient (R^2) for the function. This function is then used during analysis to calculate absolute concentration of a component in a sample, C_i, as a ratio of the component quantity to the corrected volume of the injected sample [204].

$$Q_i = C_i \times V' \qquad where\ V' = V/D$$

$$W_i(R) = RSD\left(Q_{ij}, R_{ij}\right) \qquad where\ i\ stands\ for\ the\ component\ number$$

$$C_i = W_i(R_i)/V'$$

7.2 Appendix B

7.2.1 Derivation of E^0 for the FeL^{2+}/Fe^{2+} couple

$$FeL^{2+} + e^- + H^+ \rightarrow Fe^{2+} + HL \qquad Reduction\ reaction$$

$$E = E^0_{FeL^{2+}/Fe^{2+}} + \frac{RT}{F}\ln\frac{[FeL^{2+}][H^+]}{[HL][Fe^{2+}]} \qquad Nernst\ equation$$

$$K_1 = \frac{[FeL^{2+}][H^+]}{[Fe^{3+}][HL]} \quad so \quad \frac{[FeL^{2+}][H^+]}{[HL]} = K_1[Fe^{3+}]$$

$$E = E^0_{FeL^{2+}/Fe^{2+}} + \frac{RT}{F}\ln\frac{K_1[Fe^{3+}]}{[Fe^{2+}]}$$

$$E = E^0_{FeL^{2+}/Fe^{2+}} + \frac{RT}{F}\ln K_1 + \frac{RT}{F}\ln\frac{[Fe^{3+}]}{[Fe^{2+}]} \qquad A)$$

$$E^0 = E^0_{Fe^{3+}/Fe^{2+}} + \frac{RT}{F}\ln\frac{[Fe^{3+}]}{[Fe^{2+}]} \qquad B)$$

$$Coupling\ A)\ with\ B)\ gives: \quad E^0_{Fe^{3+}/Fe^{2+}} = E^0_{FeL^{2+}/Fe^{2+}} + \frac{RT}{F}\ln K_1$$

$$So \quad E^0_{FeL^{2+}/Fe^{2+}} = E^0_{Fe^{3+}/Fe^{2+}} - \frac{RT}{F}\ln K_1$$

$$= 0.77 - \frac{8.314 \times 298}{96485.33}\ln(109)$$

$$= 0.77 - 0.12$$

$$= 0.65V$$

7.2.2 Incorporation of a Single Modified Bengtsson Equation

Derivation of the final rate equation (Eq. 5.30)

$$\frac{d[Fe^{2+}]}{dt} = k_{11}(H_2NO^*)^2 + 4k_{13}\frac{{k_{12}}^2(Fe^{3+})^2}{{k_{-12}}^2(Fe^{2+})^2(H^+)^2}(H_2NO^*)^2$$

$$\frac{d[Fe^{2+}]}{dt} = \left[2k_{11} + 4k_{13}\frac{{k_{12}}^2(Fe^{3+})^2}{{k_{-12}}^2(Fe^{2+})^2(H^+)^2}\right](H_2NO^*)^2$$

$$\frac{d[Fe^{2+}]}{dt} = \left[2k_{11} + 4k_{13}\frac{{k_{12}}^2(Fe^{3+})^2}{{k_{-12}}^2(Fe^{2+})^2(H^+)^2}\right]\frac{{k_{10}}^2}{{k_{-10}}^2(Fe^{2+})^2(H^+)^2}$$

$$\times\frac{{\beta_1'}^2(Fe^{3+})^2{K_a}^2(NH_3OH^+)^2}{(H^+)^2}$$

$$\frac{d[Fe^{2+}]}{dt} = \left[2k_{11} + \frac{4k_{13}{k_{12}}^2(Fe^{3+})^2}{{k_{-12}}^2(Fe^{2+})^2(H^+)^2}\right]\frac{{k_{10}}^2{\beta_1'}^2(Fe^{3+})^2{K_a}^2(NH_3OH^+)^2}{{k_{-10}}^2(Fe^{2+})^2(H^+)^4}$$

$$\frac{d[Fe^{2+}]}{dt} = B\frac{[Fe^{3+}]^2[NH_3OH^+]^2}{[Fe^{2+}]^2[H^+]^4}\left(1 + C\frac{[Fe^{3+}]^2}{[Fe^{2+}]^2[H^+]^2}\right) \qquad (Eq.\ 5.30)$$

$$where \quad B = \frac{2k_{11}{k_{10}}^2{\beta_1'}^2{K_a}^2}{{k_{-10}}^2} \quad and \quad C = \frac{4k_{13}{k_{12}}^2{k_{10}}^2{\beta_1'}^2{K_a}^2}{{k_{-12}}^2{k_{-10}}^2}$$

7.2.3 Output from IF-statement model with when [Fe(III)] is defined as Fe_T in the inequality

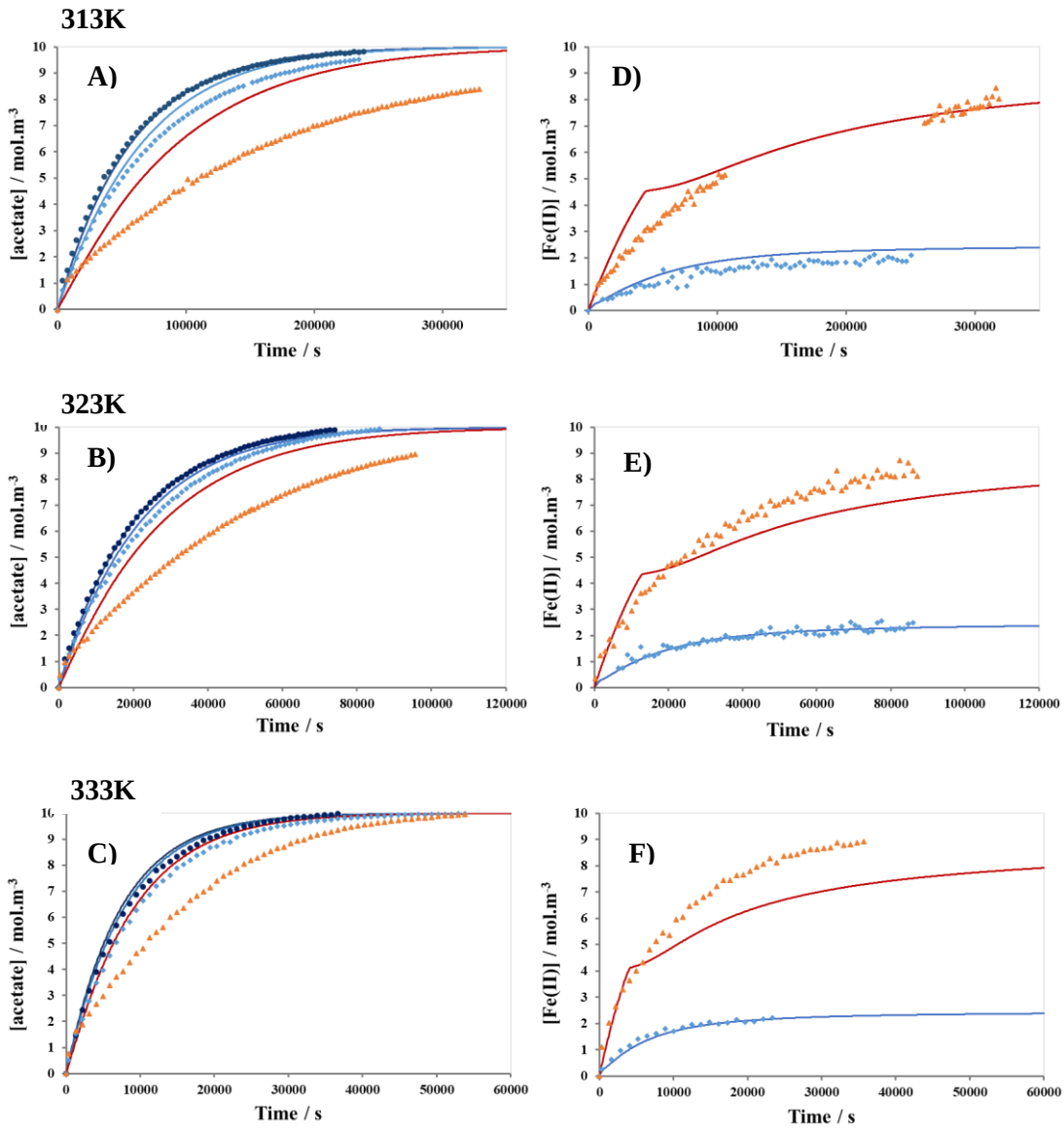

Figure 7.1: Plots of experimental data and model output at 313K (A &D), 323K (B &E) and 333K (C & F) from which parameter estimations were obtained using the IF-statement model with [Fe(III)] = [Fe$_T$] and n=0.25 in the inequality. Plots A-C: Experimental data (points) and model output (lines) for Ac, when [Fe(III)]$_0$ = 0 (dark blue), 2.5 (light blue) and 10 mmol dm^{-3} (orange). Plots D-F: Experimental data (points) and model output (lines) for Fe^{2+}, when [Fe(III)]$_0$ = 2.5 (light blue) and 10 mmol dm^{-3} (orange). For the data obtained at 3131K with 10 mmol dm^{-3} initial Fe(III), a system fault overnight caused a large stoppage period in data acquisition in which the IC system had to be cleaned, re-equilibrated and put back into operation

7.2.4 Errors in gPROMS parameter estimations

Errors in parameters estimated in the gPROMS software included the standard deviation, 95% confidence interval and T-values, each of which are described in the following sections 7.2.4.1 - 7.2.4.3. Section 7.2.4.4 then shows the value of these errors for the relevant model iterations described in this Chapter.

7.2.4.1 Standard Deviation

The standard deviation, σ, is a measure of the amount of variation of a set of values relative to the mean value. Standard deviation is defined mathematically as:

$$\sigma = \sqrt{\frac{\sum_{i=1}^{N}(X_i - \mu_i)^2}{N}}$$

where X_i and μ_i are the model variable final result and the experimental or expected value of this variable respectively, with N being the number of experimental datapoints. σ is in the same units as the parameter.

7.2.4.2 95% Confidence Interval

The amount by which an estimated parameter can either increase or decrease whilst maintaining a 95% probability that it represents the true value, is known as the 95% confidence interval. It is thus given in the same units as the parameter itself. For each independent parameter within a user specified range, the model records all combinations of a parameter for which 95% of the model values are within error of the

experimental data, and the confidence interval is defined as the extent to which the individual parameters vary within these successful combinations. Confidence intervals are given in the same units as the respective parameter.

7.2.4.3 T-value

The t-value test is a statistical test which poses as its null hypothesis that an estimated parameter is equal to zero, i.e. the parameter is unimportant to the model fit. A t-value, X, is calculated for each parameter using the equation below, where $\bar{X} - 0$ is the difference between the mean value of the parameter and zero, and $\delta_{95\%}$ is the 95% confidence interval.

$$X = \frac{\bar{X}-0}{\delta_{95\%}}$$

The calculated values are then compared with a reference t-value, found in a one-tailed or two-tailed statistical t-table that computes a t-value based on the confidence interval and number of degrees of freedom in the system. Only if the t-value for the variable is *greater* than the reference t-value can the null hypothesis be rejected; in which case the parameter *is* different from zero and therefore important in the model fit. In Tables 7.1 – 7.6 in section 7.2.4.4, only those 95% t-values shaded in dark grey are greater than the reference t-value and therefore classed as statistically significant according to the t-test. However, in most model iterations, a large number of parameters are being estimated and most are known to be chemically important, thus a relative inspection of the various t-values shows how important individual parameters are compared to each other. For parameters in Tables 7.1 – 7.6 with 95% t-values shaded in light grey,

these statistical values are within an order of magnitude of the reference t-value and thus comparatively, those parameters are of significance to the model fit.

7.2.4.4 Errors in Estimations

Table 7.1: Errors calculated by gPROMS for estimations of Arrhenius parameters for k_1 and $k_{red,1,HAN}$ in Table 5.4. Values of standard deviations and 95% confidence intervals are in the units of the estimated parameter. t-value is unitless.

Parameter	Units	Estimated value	Standard deviation	95% confidence interval	95% t-value
k_1 , A	$M^{-1}.s^{-1}$	2.25×10^{9}	9.93×10^{26}	1.95×10^{27}	1.15×10^{-18}
k_1 , E_a	kJ. mol^{-1}	180	1.22×10^{18}	2.40×10^{18}	7.50×10^{-17}
$k_{red,1,HAN}$, A	$M^{3}.s^{-1}$	4.80×10^{4}	4.22×10^{4}	8.29×10^{4}	0.579
$k_{red,1,HAN}$, E_a	kJ. mol^{-1}	69	2.322	4.567	15.108
				Reference t-value	1.64893

Table 7.2: Errors calculated by gPROMS for estimations of Arrhenius parameters for k_1, $k_{red,2,HAN}$ and $k'_{red,2,HAN}$ in Table 5.5. Values of standard deviations and 95% confidence intervals are in the units of the estimated parameter. t-value is unitless.

Parameter	Units	Estimated value	Standard deviation	95% confidence interval	95% t-value
k_1 , A	$M^{-1}.s^{-1}$	2.25×10^{9}	1.05×10^{27}	2.06×10^{27}	1.09×10^{-18}
k_1 , E_a	kJ. mol^{-1}	180	1.29×10^{18}	2.54×10^{18}	7.09×10^{-17}
$k_{red,2,HAN}$, A	$M.s^{-1}$	6.90×10^{5}	2.92×10^{5}	5.73×10^{5}	1.204
$k_{red,2,HAN}$, E_a	kJ. mol^{-1}	65.1	1.100	2.162	30.115
$k'_{red,2,HAN}$, A	M	8.99×10^{2}	5.58×10^{15}	1.10×10^{16}	8.20×10^{-14}
$k'_{red,2,HAN}$, E_a	kJ. mol^{-1}	119.6	8.80×10^{13}	1.73×10^{13}	6.91×10^{-12}
				Reference t-value	1.64893

Table 7.3: Errors calculated by gPROMS for estimations of Arrhenius parameters for $k_{red,1,HAN}$, $k_{red,2,HAN}$ $k'_{red,2,HAN}$ in Table 5.6 for when Fe(III) = $[Fe^{3+}_{(aq)}]$ in the inequality and n=0.25. Values of standard deviations and 95% confidence intervals are in the units of the estimated parameter. t-value is unitless.

Parameter	Units	Estimated value	Standard deviation	95% confidence interval	95% t-value
k_1 , A	$M^{-1}.s^{-1}$	2.25×10^{9}	1.01×10^{27}	1.99×10^{27}	1.13×10^{-18}
k_1 , E_a	kJ. mol^{-1}	180	1.24×10^{18}	2.44×10^{18}	7.39×10^{-17}
$k_{red,1,HAN}$, A	$M^3.s^{-1}$	7.57×10^{3}	9.54×10^{3}	1.87×10^{4}	0.404
$k_{red,1,HAN}$, E_a	kJ. mol^{-1}	62.6	3.35	6.59	9.504
$k_{red,2,HAN}$, A	$M.s^{-1}$	1.51×10^{6}	3.03×10^{6}	7.83×10^{6}	0.254
$k_{red,2,HAN}$, E_a	kJ. mol^{-1}	59.1	5.31	13.73	5.662
$k'_{red,2,HAN}$, A	M	9.00×10^{2}	3.15×10^{12}	6.18×10^{12}	1.46×10^{-10}
$k'_{red,2,HAN}$, E_a	kJ. mol^{-1}	120	2.04×10^{13}	4.01×10^{13}	2.99×10^{-12}
				Reference t-value	1.64795

Table 7.4: Errors calculated by gPROMS for estimations of constants in relationship for K_1 and K_2, and of Arrhenius parameters for $k_{red,1,HAN}$, $k_{red,2,HAN}$ and $k'_{red,2,HAN,}$ and $k_{red,1,FeL}$ in Table 5.8. Values of standard deviations and 95% confidence intervals are in the units of the estimated parameter. t-value is unitless. The value of $\eta_{c,1}$ relating to K_1 hit the upper bound and therefore statistical values were not able to be computed,

Parameter	Units	Estimated value	Standard deviation	95% confidence interval	95% t-value
K_1, $\eta_{c,1}$	K	7.00×10^{3}	n/a	n/a	n/a
K_1, $\alpha_{c,1}$	unitless	-17.05	0.126	0.247	69.04
K_2, $\eta_{c,1}$	K	2.00×10^{3}	2.25×10^{4}	4.42×10^{4}	0.045
K_2, $\alpha_{c,1}$	unitless	-7.75	72.02	1.86×10^{2}	0.055
$k_{red,1,HAN}$, A	$M^3.s^{-1}$	1.37×10^{4}	6.13×10^{4}	1.20×10^{5}	0.114
$k_{red,1,HAN}$, E_a	kJ. mol^{-1}	59.00	12.09	31.25	2.485
$k_{red,2,HAN}$, A	$M.s^{-1}$	4.54×10^{6}	1.38×10^{7}	2.71×10^{7}	0.168
$k_{red,2,HAN}$, E_a	kJ. mol^{-1}	50.56	8.40	16.51	3.063
$k'_{red,2,HAN}$, A	M	8.99×10^{2}	2.31×10^{13}	4.53×10^{13}	1.98×10^{-11}
$k'_{red,2,HAN}$, E_a	kJ. mol^{-1}	1.20×10^{2}	3.96×10^{13}	7.78×10^{13}	1.54×10^{-12}
k_1 , A	$M^{-1}.s^{-1}$	2.25×10^{9}	1.01×10^{27}	1.99×10^{27}	1.13×10^{-18}
k_1 , E_a	kJ. mol^{-1}	1.80×10^{2}	1.24×10^{18}	2.44×10^{18}	7.38×10^{-17}
$k_{red,1,FeL}$, A	$M^{-1}.s^{-1}$	3.62×10^{8}	3.93×10^{13}	7.71×10^{13}	4.70×10^{-6}
$k_{red,1,FeL}$, E_a	kJ. mol^{-1}	92.50	2.86×10^{5}	5.62×10^{5}	1.64×10^{-4}
				Reference t-value	1.64795

Table 7.5: Errors calculated by gPROMS for estimations of constants in relationship for K_1 and K_2, and of Arrhenius parameters for B and C, and $k_{red,1,FeL}$ in Table 5.10. Values of standard deviations and 95% confidence intervals are in the units of the estimated parameter. t-value is unitless.

Parameter	Units	Estimated value	Standard deviation	95% confidence interval	95% t-value
K_1, $\eta_{c,1}$	K	4416.62	1734.97	3408.09	1.296
K_1, $\alpha_{c,1}$	unitless	-10.20	0.962	10.60	0.962
K_2, $\eta_{c,1}$	K	2056.37	3.42×10^{5}	6.72×10^{5}	3.06×10^{-3}
K_2, $\alpha_{c,1}$	unitless	-8.86	1.08×10^{3}	2.12×10^{3}	4.18×10^{-3}
B , A	$M^3.s^{-1}$	4.60×10^{19}	7.50×10^{28}	1.47×10^{29}	3.12×10^{-10}
B , E_a	kJ. mol^{-1}	2.34×10^{2}	2.04×10^{12}	4.01×10^{12}	5.82×10^{-11}
C , A	$M^5.s^{-1}$	1.20×10^{22}	1.26×10^{10}	2.47×10^{10}	4.85×10^{11}
C , E_a	kJ. mol^{-1}	1.78×10^{2}	2.035	3.998	44.448
k_1 , A	$M^{-1}.s^{-1}$	2.25×10^{9}	1.01×10^{27}	1.99×10^{27}	1.13×10^{-18}
k_1 , E_a	kJ. mol^{-1}	1.80×10^{2}	1.24×10^{18}	2.44×10^{18}	7.38×10^{-17}
$k_{red,1,FeL}$, A	$M^{-1}.s^{-1}$	5.44×10^{11}	1.83×10^{30}	3.59×10^{30}	1.51×10^{-19}
$k_{red,1,FeL}$, E_a	kJ. mol^{-1}	1.60×10^{2}	8.76×10^{18}	1.72×10^{19}	9.30×10^{-18}
				Reference t-value	1.64795

Table 7.6: Errors calculated by gPROMS for estimations of constants in relationship for K_1 and K_2, and Arrhenius parameters for k_1, B, C and $k_{red,1,FeL}$ in Table 5.11. Values of standard deviations and 95% confidence intervals are in the units of the estimated parameter. t-value is unitless.

Parameter	Units	Estimated value	Standard deviation	95% confidence interval	95% t-value
K_1, $\eta_{c,1}$	K	1.60×10^{3}	4.67	9.17	163.466
K_1, $\alpha_{c,1}$	unitless	-0.68	n/a	n/a	n/a
K_2, $\eta_{c,1}$	K	7.53×10^{3}	1.66×10^{4}	3.25×10^{4}	0.232
K_2, $\alpha_{c,1}$	unitless	-24.57	n/a	n/a	n/a
B , A	$M^3.s^{-1}$	4.60×10^{19}	4.45×10^{22}	8.73×10^{22}	5.27×10^{-4}
B , E_a	kJ. mol^{-1}	1.92×10^{2}	9.64×10^{5}	1.89×10^{6}	1.02×10^{-4}
C , A	$M^5.s^{-1}$	1.20×10^{22}	3.75×10^{9}	7.36×10^{9}	1.63×10^{12}
C , E_a	kJ. mol^{-1}	1.73×10^{3}	7.97×10^{2}	1.57×10^{3}	110.388
k_1 , A	$M^{-1}.s^{-1}$	2.25×10^{9}	1.04×10^{27}	2.05×10^{27}	1.10×10^{-18}
k_1 , E_a	kJ. mol^{-1}	1.80×10^{2}	1.28×10^{18}	2.52×10^{18}	7.15×10^{-17}
$k_{red,1,FeL}$, A	$M^{-1}.s^{-1}$	5.44×10^{11}	6.40×10^{29}	1.26×10^{30}	4.32×10^{-19}
$k_{red,1,FeL}$, E_a	kJ. mol^{-1}	1.60×10^{2}	3.19×10^{18}	6.26×10^{18}	2.55×10^{-17}
				Reference t-value	1.64795

References

[1] G. F. Hewitt and J. G. Collier, *Introduction to Nuclear Power*, Second Edition ed. CRC Press, 2000.

[2] M. Joyce, "The Fission Process," in *Nuclear Engineering, A Conceptual Introduction to Nuclear Power*: Butterworth-Heinemann, 2017, ch. 4.

[3] J. K. Jenkin, "Atomic Energy is ‘‘Moonshine’’: What did Rutherford *Really* Mean?," *Phys. Perspect.*, vol. 13, pp. 128-145, 2011, doi: 10.1007/s00016-010-0038-1.

[4] V. Nesvizhevsky and J. Villain, "The discovery of the neutron and its consequences (1930–1940)," *C. R. Physique*, vol. 18, no. 9-10, pp. 592-600, 2017, doi: 10.1016/j.crhy.2017.11.001.

[5] M. Joyce, "Fundamentals of Radioactivity," in *Nuclear Engineering, A Conceptual Introduction to Nuclear Power*: Butterworth-Heinemann, 2017, ch. 3.

[6] W. Bleam, "Element Abundance," in *Soil and Environmental Chemistry*, 2nd ed.: Elsevier Inc., 2017, ch. 1, pp. 1-38.

[7] O. Hahn and F. Strassmann, (in German), *Naturwiss.*, vol. 27, pp. 11-15, 1939.

[8] L. Meitner and O. R. Frisch, "Products of the Fission of the Uranium Nucleus," *Nature*, vol. 143, pp. 471-472, 1939, doi: 10.1038/143471a0.

[9] N. Bohr and J. A. Wheeler, "The Mechanism of Nuclear Fission," *Physical Review*, vol. 56, pp. 426-450, 1939, doi: 10.1103/PhysRev.56.426.

[10] I. Hore-Lacy, "Nuclear Power," in *Nuclear Energy in the 21st Century*: Academic Press, 2007, ch. 3, pp. 37 - 53.

[11] M. Joyce, "Fundamental Concepts," in *Nuclear Engineering, A Conceptual Introduction to Nuclear Power*: Butterworth-Heinemann, 2017, ch. 1.

[12] D. M. Brink, "Nuclear Fission and Fusion," in *Encyclopedia of Condensed Matter Physics*, F. Bassani, G. L. Liedl, and P. Wyder Eds., 2005, pp. 113-118.

[13] M. Joyce, "Advanced Reactors and Future Concepts," in *Nuclear Engineering, A Conceptual Introduction to Nuclear Power*: Butterworth-Heinemann, 2017, ch. 11.

[14] M. E. Ricotti, "Nuclear energy: Basics, present, future," *The European Physical Journal Conferences*, 2013, doi: 10.1051/epjconf/20135401005.

[15] OECD-NEA, "Technology Roadmap Update for Generation IV Nuclear Energy Systems," 2014, https://www.gen-4.org/gif/upload/docs/application/pdf/2014-03/gif-tru2014.pdf.

[16] M. Joyce, "Historical Context," in *Nuclear Engineering, A Conceptual Introduction to Nuclear Power*: Butterworth-Heinemann, 2017, ch. 2.

[17] S. M. Goldberg and R. Rosner, *Nuclear Reactors: Generation to Generation*. American Academy of Arts and Sciences, 2011, https://www.amacad.org/sites/default/files/academy/pdfs/nuclearReactors.pdf

[18] A. Boyle, "“Banishing the atom pile bogy”: Exhibiting Britain's first nuclear reactor," *Centaurus*, vol. 61, no. 1-2, pp. 14-32, 2020, doi: 10.1111/1600-0498.12220.

[19] J. Chater, "A history of nuclear power," https://courses.engr.illinois.edu/npre470/sp2018/web/readings/James_Chater_History_nuclear.pdf

[20] B. P. Commission, "THE FUTURE OF NUCLEAR ENERGY IN THE UK," The University of Birmingham, July 2012, https://www.birmingham.ac.uk/documents/news/nuclear-energy-summary-pdf.pdf.

[21] T. Roberts and H. Clark, "Nuclear electricity in the UK", [Online] Available: https://assets.publishing.service.gov.uk/media/5c9a5d37ed915d07b20fa2ba/Nuclear_electricity_in_the_UK.pdf.

[22] IAEA. "Country Nuclear Power Profiles, 2018 Edition: United Kingdom." https://www-pub.iaea.org/MTCD/Publications/PDF/cnpp2018/countryprofiles/UnitedKingdom/UnitedKingdom.htm.

[23] "Management of spent nuclear fuel and its waste: A Joint Research Centre and EASAC report." https://easac.eu/fileadmin/PDF_s/reports_statements/NFC_leaflet_finalFINAL.pdf

[24] NEA, "State-of-the-Art Report on the Progress of Nuclear Fuel Cycle Chemistry," 2018,OECD Publishing, Paris.

[25] A. Sherry, P. J. A. Howarth, P. Kearns, and N. Waterman, "A Review of the UK's Nuclear R&D Capability." 2010,

https://pure.manchester.ac.uk/ws/portalfiles/portal/32909497/FULL_TEXT.PDF

[26] "Office of Nuclear Energy: Strategic Vision," 2021, https://www.energy.gov/sites/prod/files/2021/01/f82/DOE-NE%20Strategic%20Vision%20-%2001.08.2021.pdf.

[27] NEA, "Strategies and Considerations for the Back End of the Fuel Cycle," NEA No. 7469, 2021, OECD Publishing, Paris.

[28] D. Hambley, "Storage of thermal reactor fuels – Implications for the back end of the fuel cycle in the UK," *EPJ Nuclear Sci. Technol.*, vol. 2, no. 21, 2016, doi: 10.1051/epjn/2016014.

[29] IAEA, "Nuclear Fuel Cycle Information System," 2009, IAEA-TECDOC-1613.

[30] J. Kyffin and A. Hillier, "Technological Development to Support a Change in the United Kingdom's Strategy for Management of Spent AGR Oxide Fuel," in *International Conference on Management of Spent Fuel from Nuclear Power Reactors*, Vienna International Centre, 2015. [Online]. Available: https://www-pub.iaea.org/iaeameetings/cn226p/Session7/ID37Kyffin.pdf

[31] NEA, "Nuclear Energy Data," NEA No. 7474, 2019, OECD Publishing, Paris.

[32] A. Paulenova, "Factors Controlling Redox Speciation of Plutonium and Neptunium in Extraction Separation Processes," 2012, DE-FC07-07ID14829.

[33] NEA, "Physics and Safety of Transmutation Systems: A Status Report", NEA No. 6090, 2006, OECD Publishing, Paris.

[34] M. Salvatores and G. Palmiotti, "Radioactive waste partitioning and transmutation within advanced fuel cycles: Achievements and challenges," *Progress in Particle and Nuclear Physics*, vol. 66, no. 1, pp. 144-166, 2011.

[35] E. Commission, "REPORT FROM THE COMMISSION TO THE COUNCIL AND THE EUROPEAN PARLIAMENT on progress of implementation of Council Directive 2011/70/EURATOM and an inventory of radioactive waste and spent fuel present in the Community's territory and the future prospects," 2019.

[36] M. Joyce, "Radioactive Waste Management and Disposal," in *Nuclear Engineering, A Conceptual Introduction to Nuclear Power*: Butterworth-Heinemann, 2017, ch. 15.

[37] J. E. Birkett *et al.*, "Recent developments in the purex process for nuclear fuel reprocessing: Complexant based stripping for uranium/plutonium separation,"

(in English), *Chimia*, Article vol. 59, no. 12, pp. 898-904, 2005, doi: 10.2533/000942905777675327.

[38] O. D. Fox *et al.*, "Advanced PUREX Flowsheets for Future Np and Pu Fuel Cycle Demands " in *Separations for the Nuclear Fuel Cycle in the 21st Century*, G. J. Lumetta, L. N. Kenneth, S. B. Clark, and J. I. Friese Eds., (ACS Symposium Series, no. 933), 2006, ch. 6, pp. 89-102.

[39] A. Doyle. "Nuclear reprocessing ends at Sellafield's Thorp plant." The Chemical Engineer. https://www.thechemicalengineer.com/news/nuclear-reprocessing-ends-at-sellafield-s-thorp-plant/ (accessed 2019).

[40] J.-P. Glatz, P. Soucek, and R. Malmbeck, *Reprocessing and Recycling of Spent Nuclear Fuel*. WoodHead publishing, 2015.

[41] IPFM, "Plutonium Separation in Nuclear Power Plants: Status, Problems, and Prospects of Civilian Reprocessing Around the World," 2015. [Online]. Available: http://fissilematerials.org/library/rr14.pdf

[42] A. Ramanujam, "An Introduction to the Purex Process," *IANCAS Bulletin*, pp. 11-26

[43] W. N. Association. "Processing of Used Nuclear Fuel." https://www.world-nuclear.org/information-library/nuclear-fuel-cycle/fuel-recycling/processing-of-used-nuclear-fuel.aspx (accessed 2019).

[44] NEA, "Advanced Nuclear Fuel Cycles and Radioactive Waste Management," NEA No. 5990, 2006, OCED Publishing, Paris.

[45] R. J. Taylor *et al.*, "The Applications of Formo- and Aceto-hydroxamic Acids in Nuclear Fuel Reprocessing," *Journal of Alloys and Compounds*, vol. 271-273, pp. 534-537, 1998, doi: 10.1016/S0925-8388(98)00146-7.

[46] W. Duan, M. Zhao, C. Wang, and S. Cao, "Recent Advances in the Development and Application of Annular Centrifugal Contactors in the Nuclear Industry," *Solvent Extraction and Ion Exchange*, vol. 32, no. 1, pp. 1-26, 2014, doi: 10.1080/07366299.2013.833741.

[47] R. Taylor *et al.*, "The EURO-GANEX Process: Current Status of Flowsheet Development and Process Safety Studies," *Procedia Chemistry*, vol. 21, pp. 524-529, 2016, doi: 10.1016/j.proche.2016.10.073.

[48] D. N. Graham, "Process Description of the EURO-GANEX Process," 2014, SACSESS - NNL13172 - R.3.1.1 - rev 1.

[49] C. Rhodes, R. Harris, and D. Graham, "Process Description report of Concept Euro- GANEX Plant," D8.1, 2018.

[50] R. Malmbeck *et al.*, "EURO-GANEX, a Process for the Co-separation of TRU," presented at the Sustainable Nuclear Energy Conference, Manchester, 9-11 April, 2014.

[51] A. Paulenova, P. Tkac, A. M. Brown, B. M. Matteson, J. E. Bruso, and M. A. Cleveland, "Plutonium Chemistry in the UREX+ Separation Processes."

[52] L. Nunez and G. F. Vandegrift, "Evaluation of Hydroxamic Acid in Uranium Extraction Process: Literature Review," Argonne National Laboratory, 2001.

[53] J. E. Birkett *et al.*, "Controlling Neptunium and Plutonium Within Single Cycle Solvent Extraction Flowsheets for Advanced Fuel Cycles," (in English), *Journal of Nuclear Science and Technology*, Article; Proceedings Paper vol. 44, no. 3, pp. 337-343, Mar 2007, doi: 10.3327/jnst.44.337.

[54] B. J. Colston, G. R. Choppin, and R. J. Taylor, "A preliminary study of the reduction of Np(VI) by formohydroxamic acid using stopped-flow near-infrared spectrophotometry," (in English), *Radiochimica Acta*, Article vol. 88, no. 6, pp. 329-334, 2000, doi: 10.1524/ract.2000.88.6.329.

[55] D. Y. Chung and E. H. Lee, "The Reduction of Np(VI) by Acetohydroxamic Acid in Nitric Acid Solution," *Bull. Korean Chem. Soc.*, vol. 26, no. 11, 2005.

[56] M. Chotkowski, "Redox interactions of technetium with neptunium in acid solutions," *J. Radioanal. Nucl. Chem.*, vol. 317, no. 1, pp. 527–533, 2018.

[57] F. P. L. Andrieux, C. Boxall, and R. J. Taylor, "Acetohydroxamatoiron(III) Complexes: Thermodynamics of Formation and Temperature Dependent Speciation," (in English), *Journal of Solution Chemistry*, Article vol. 37, no. 11, pp. 1511-1527, Nov 2008, doi: 10.1007/s10953-008-9327-6.

[58] S. Edwards, F. Andrieux, C. Boxall, R. Taylor, and D. Woodhead, "Neptunium(IV)-Hydroxamate Complexes: Their Speciation, and Kinetics and Mechanism of Hydrolysis," *Dalton Transactions*, vol. 48, no. 2, pp. 673-687, 2019, doi: 10.1039/C8DT02194E.

[59] S. Dhungana and A. L. Crumbliss, "Coordination chemistry and redox processes in siderophore-mediated iron transport," (in English), *Geomicrobiology Journal*, Article vol. 22, no. 3-4, pp. 87-98, Apr-Jun 2005, doi: 10.1080/01490450590945870.

[60] B. S. Matteson, "The Chemistry of Acetohydroxamic Acid Related to Nuclear Fuel Reprocessing," Doctor of Philosophy, Oregon State University, 2010.

[61] B. S. Matteson, P. Tkac, and A. Paulenova, "Complexation Chemistry of Zirconium(IV), Uranium(VI), and Iron(III) with Acetohydroxamic Acid," (in

English), *Separation Science and Technology*, Article; Proceedings Paper vol. 45, no. 12-13, pp. 1733-1742, 2010, doi: 10.1080/01496395.2010.493829.

[62] S. Sinkov and G. Choppin, "Acetohydroxamic Acid Complexes with Trivalent f-Block Metal Cations," *Journal of Nuclear Science and Technology*, vol. 39, 3, pp. 359-362, 2002, doi: 10.1080/00223131.2002.10875483.

[63] M. J. Carrott, O. D. Fox, C. J. Maher, C. Mason, and R. J. Taylor, "Solvent extraction behavior of plutonium (IV) ions in the presence of simple hydroxamic acids," (in English), *Solvent Extraction and Ion Exchange*, Article vol. 25, no. 6, pp. 723-745, 2007, doi: 10.1080/07366290701634560.

[64] R. J. Taylor, "Progress towards Understanding the Interactions between Hydroxamic Acids and Actinide Ions," *Journal of Nuclear Science and Technology*, vol. 39, 3, pp. 886-889, 2002, doi: 10.1080/00223131.2002.10875611.

[65] A. Paulenova, "An Overview of Actinide Chemistry," U. S. D. o. E. C. F. O. National Analytical Management Program (NAMP), Ed., ed.

[66] R. J. Taylor, I. S. Denniss, and A. L. Wallwork, "Neptunium control in an advanced Purex process," *Nuclear Energy*, vol. 36, no. 1, pp. 39-46, 1997.

[67] K. K. Ghosh, "Kinetic and mechanistic aspects of acid-catalysed hydrolysis of hydroxamic acids," (in English), *Indian Journal of Chemistry Section B-Organic Chemistry Including Medicinal Chemistry*, Review vol. 36, no. 12, pp. 1089-1102, Dec 1997.

[68] K. K. Ghosh, P. Tamrakar, and S. S. Thakur, "Kinetics and mechanism of the hydrolysis of hydroxamate siderophore," (in English), *Journal of the Indian Chemical Society*, Article vol. 78, no. 4, pp. 185-188, Apr 2001.

[69] D. Y. Chung and E. H. Lee, "Kinetics of the hydrolysis of acetohydroxamic acid in a nitric acid solution," (in English), *Journal of Industrial and Engineering Chemistry*, Article vol. 12, no. 6, pp. 962-966, Nov 2006.

[70] N. Choure and S. A. Bhoite, "Acid-catalyzed hydrolysis of N-phenylbenzohydroxamic acid," (in English), *Journal of the Indian Chemical Society*, Article vol. 87, no. 6, pp. 735-738, Jun 2010.

[71] J. Mollin and T. Kučerová, "Mechanism of acid catalysed hydrolysis of hydroxamic acids," *Collection of Czechoslovak Chemical Communications*, vol. 41, no. 10, pp. 2885-2894, 1976, doi: 10.1135/cccc19762885.

[72] K. K. Ghosh, S. K. Rajput, and K. K. Krishnani, "KINETIC-MODEL FOR ACID-CATALYZED HYDROLYSIS OF BENZOHYDROXAMIC ACID,"

(in English), *Journal of Physical Organic Chemistry,* Article vol. 5, no. 1, pp. 39-43, Jan 1992, doi: 10.1002/poc.610050106.

[73] D. C. Berndt and R. L. Fuller, "The Kinetics and Mechanism of the Hydrolysis of Benzohydroxamic Acid," *Journal of Organic Chemistry,* vol. 31, no. 10, pp. 3312–3314, 1966, doi: 10.1021/jo01348a048.

[74] M. J. Carrott *et al.*, "Oxidation-reduction reactions of simple hydroxamic acids and plutonium(IV) ions in nitric acid," (in English), *Radiochimica Acta,* Article vol. 96, no. 6, pp. 333-343, 2008, doi: 10.1524/ract.2008.1502.

[75] B. S. Mane and M. H. Jagdale, "Kinetics of the acid catalysed hydrolysis of hydroxamic acids," *Reaction Kinetics and Catalysis,* vol. 6, pp. 417-424, 1977.

[76] R. J. Taylor and I. May, "The reduction of actinide ions by hydroxamic acids," (in English), *Czechoslovak Journal of Physics,* Article; Proceedings Paper vol. 49, pp. 617-621, 1999, doi: 10.1007/s10582-999-1041-0.

[77] F. P. L. Andrieux, C. Boxall, and R. J. Taylor, "The Hydrolysis of Hydroxamic Acid Complexants in the Presence of Non-oxidizing Metal Ions 1: Ferric Ions," (in English), *Journal of Solution Chemistry,* Article vol. 36, no. 10, pp. 1201-1217, Oct 2007, doi: 10.1007/s10953-007-9183-9.

[78] R. J. Taylor, I. S. Denniss, and I. May, "Hydroxamic acids - novel reagents for Advanced Purex processes," presented at the Atalante 2000, Scientific research on the back-end of the fuel cycle for the 21st century, Avignon, 2000. [Online]. Available: <Go to WoS>://WOS:000170066500033.

[79] I. Sanchez-Garcia, L. J. Bonales, H. Galan, J. Manuel Perlado, and J. Cobos, "Advanced direct method to quantify the kinetics of acetohydroxamic acid (AHA) by Raman spectroscopy," *Spectrochimica Acta Part A: Molecular and Biomolecular Spectroscopy,* vol. 229, p. 117877, 2020.

[80] F. P. L. Andrieux, C. Boxall, I. May, and R. J. Taylor, "The Hydrolysis of Hydroxamic Acid Complexants in the Presence of Non-oxidizing Metal Ions 2: Neptunium (IV) Ions," (in English), *Journal of Solution Chemistry,* Article vol. 37, no. 2, pp. 215-232, Feb 2008, doi: 10.1007/s10953-007-9225-3.

[81] F. P. L. Andrieux, C. Boxall, and R. J. Taylor, "The hydrolysis kinetics of hydroxamic acid complexants in the presence of oxidising plutonium (IV) ions."

[82] F. P. L. Andrieux, C. Boxall, I. May, and R. J. Taylor, "A Preliminary Study of the Hydrolysis of Hydroxamic Acid Complexants in the Presence of Oxidising Metal Ions," in *Actinides Conference*, San Francisco, CA, Jul 12-17 2009, vol. 9, BRISTOL: Iop Publishing Ltd, in IOP Conference Series: Materials Science and Engineering, 2010, doi: 10.1088/1757-

899X/9/1/012081. [Online]. Available: <Go to WoS>://WOS:000285500700081

[83] F. P. L. Andrieux, C. Boxall, H. M. Steele, and R. J. Taylor, "The Hydrolysis of Hydroxamic Acid Complexants in the Presence of Non-oxidizing Metal Ions 3: Ferric Ions at Elevated Temperatures," (in English), *Journal of Solution Chemistry,* Article vol. 43, no. 3, pp. 608-622, Mar 2014, doi: 10.1007/s10953-014-0142-y.

[84] M. Alyapyshev, A. Paulenova, M. A. Cleveland, J. E. Bruso, and P. Tkac, "Hydrolysis of Acetohydroxamic Acid Uunder UREX+ Conditions," presented at the GLOBAL 2007: Advanced Nuclear Fuel Cycles and Systems, Boise, ID, USA, September 9-13, 2007. [Online]. Available: <Go to WoS>://WOS:A1994MW99000012.

[85] S. Edwards, F. Andrieux, C. Boxall, R. Taylor, and D. Woodhead, "Hydrolysis of Hydroxamic Acid Complexants in the Presence of Non-oxidizing Metal Ions," in *Material Challenges in Current and Future Nuclear Technologies*, 2012, vol. 1383: Materials Research Society, in MRS Proceedings, doi: 10.1557/opl.2012.210. [Online]. Available: http://journals.cambridge.org/article_S1946427412002102

[86] R. J. Taylor, S. I. Sinkov, G. R. Choppin, and I. May, "Solvent extraction behavior of neptunium (IV) ions between nitric acid and diluted 30% tri-butyl phosphate in the presence of simple hydroxamic acids," (in English), *Solvent Extraction and Ion Exchange,* Article vol. 26, no. 1, pp. 41-61, 2008, doi: 10.1080/07366290701784159.

[87] R. J. Lemire, OECD, Ed. *Chemical Thermodynamics of Neptunium and Plutonium*. Elsevier, 2001.

[88] P. Tkac and A. Paulenova, "The Effect of Acetohydroxamic Acid on Extraction and Speciation of Plutonium," *Separation Science and Technology*, vol. 43, pp. 2670–2683, 2008, doi: 10.1080/01496390802122238.

[89] M. N. Hughes and G. Stedman, "KINETICS AND MECHANISM OF REACTION BETWEEN NITROUS ACID AND HYDROXYLAMINE .1," (in English), *Journal of the Chemical Society,* Article no. MAY, pp. 2824-&, 1963, doi: 10.1039/jr9630002824.

[90] G. S. Barney, "The Reaction of Hydroxylamine with Nitrous Acid," Richland, Washington, 1971.

[91] M. R. Bennett, G. M. Brown, L. Maya, and F. A. Posey, "Oxidation of Hydroxylamine by Nitrous and Nitric Acids," *Inorg. Chem.*, vol. 21, pp. 2461-2468, 1982.

[92] J. R. Pembridge and G. Stedman, "KINETICS, MECHANISM, AND STOICHEIOMETRY OF THE OXIDATION OF HYDROXYLAMINE BY NITRIC-ACID," (in English), *Journal of the Chemical Society-Dalton Transactions,* Article no. 11, pp. 1657-1663, 1979, doi: 10.1039/dt9790001657.

[93] R. J. Gowland and G. Stedman, "Kinetic and Product Studies on the Decomposition of Hydroxylamine in Nitric Acid," *Journal of Inorganic Nuclear Chemistry,* vol. 43, no. 11, pp. 2859-2862, 1981.

[94] G. S. Barney and P. B. Duval, "Model for predicting hydroxylamine nitrate stability in plutonium process solutions," (in English), *Journal of Loss Prevention in the Process Industries,* Article vol. 24, no. 1, pp. 76-84, Jan 2011, doi: 10.1016/j.jlp.2010.10.004.

[95] G. S. Barney, "KINETIC STUDY OF REACTION OF PLUTONIUM(IV) WITH HYDROXYLAMINE," (in English), *Journal of Inorganic & Nuclear Chemistry,* Article vol. 38, no. 9, pp. 1677-1681, 1976.

[96] T. W. Newton, "Redox Reactions of Plutonium Ions in Aqueous Solutions," in *Advances in Plutonium Chemistry*, 1967-2000, ch. 3.

[97] V. S. Koltunov and G. I. Zhuravleva, *Radiokhimiya,* vol. 20, no. 5, pp. 661-669 (pp. 569-576 in English translation), 1978.

[98] S. L. Yarbro, S. B. Schreiber, E. M. Ortiz, and R. L. Ames, "Reducing Pu(IV) to Pu(III) with hydroxylamine in nitric acid solutions," *Journal of Radioanalytical and Nuclear Chemistry,* vol. 235, no. 1-2, pp. 21-24, 1998.

[99] G. Bengtsson, S. Fronaeus, and L. Bengtsson-Kloo, "The kinetics and mechanism of oxidation of hydroxylamine by iron(III)," (in English), *Journal of the Chemical Society-Dalton Transactions,* Article no. 12, pp. 2548-2552, 2002, doi: 10.1039/b201602h.

[100] Yang. Pei-Wen *et al.*, "Visible-absorption spectroscopy as a biomarker to predict treatment response and prognosis of surgically resected esophageal cancer," *Scientific Reports,* vol. 6, 2016, Art no. 33414, doi: 10.1038/srep33414.

[101] C. V. Raman and K. S. Krishnan, "A New Type of Secondary Radiation," *Nature,* vol. 121, pp. 501 – 502, 1928, doi: doi.org/10.1038/121501c0.

[102] H. Scientific. "The Theory of Raman Spectroscopy." http://www.horiba.com/uk/scientific/products/raman-spectroscopy/raman-academy/raman-tutorial/the-theory-of-raman-spectroscopy/ (accessed 2019).

[103] K. J. I. Ember *et al.*, "Raman spectroscopy and regenerative medicine: a review," *Regenerative Medicine,* vol. 2, no. 12, 2017, doi: 10.1038/s41536-017-0014-3.

[104] G. S. Bumbrah and R. M. Sharma, "Raman Spectroscopy - Basic principle, instrumentation and selected applications for the characterization of drugs of abuse," *Egyptian Journal of Forensic Sciences,* vol. 6, pp. 209-215, 2016.

[105] C. Yuen, W. Zheng, and Z. Huang, "Surface-enhanced raman scattering: Principles, nanostructures, fabrications, and biomedical applications," *Journal of Innovative Optical Health Sciences,* 2012.

[106] J. Langer *et al.*, "Present and Future of Surface-Enhanced Raman Scattering," *ACS Nano,* vol. 14, pp. 28-117, 2020.

[107] C. M. Teodorescu, "Image molecular dipoles in surface enhanced Raman scattering," *Physical Chemistry Chemical Physics,* vol. 17, p. 23102, 2015, doi: 10.1039/c4cp05082g.

[108] G. Xue and J. Dong, "Stable silver substrate prepared by the nitric acid etching method for a surface-enhanced Raman scattering study," *Anal. Chem,* vol. 63, no. 20, pp. 2393–2397, 1991.

[109] A. Alqudami and S. Annapoorni, "Fluorescence From Metallic Silver and Iron Nanoparticles Prepared by Exploding Wire Technique," *Plasmonics,* vol. 2, pp. 5-13, 2007, doi: 10.1007/s11468-006-9019-2.

[110] C. Eith, M. Kolb, A. Rumi, and A. Seubert, K. H. Viehweger, Ed. *Practical Ion Chromatography - An Introduction,* 2nd ed. Metrohm.

[111] H. Schafer, M. Laubli, and R. Dorig, *Ion Chromatography - Theory - Columns and Eluents*. Metrohm.

[112] H. Small, T. S. Stevens, and W. T. Bauman, "Novel ion exchange chromatographic method using conductimetric detection," *Anal. Chem.,* vol. 47, no. 11, pp. 1801-1809, 1975, doi: 10.1021/ac60361a017.

[113] SeQuant, "A Practical Guide to Ion Chromatography - An Introduction to Troubleshooting Manual," 2007.

[114] V. R. Meyer, *Practical High-Performance Liquid Chromatography*, Fifth ed. Wiley, 2010.

[115] D. Westerlund, P. Forssén, and T. Fornstedt, "Basic HPLC Theory and Definitions: Retention, Thermodynamics, Selectivity, Zone Spreading, Kinetics, and Resolution," in *Analytical Separation Science*: John Wiley and Sons, 2015, ch. 1.

[116] T. Brinkmann, C. H. Specht, and F. H. Frimmel, "Non-linear calibration functions in ion chromatography with suppressed conductivity detection using hydroxide eluents," *Journal of Chromatography A*, vol. 957, pp. 99-109, 2002.

[117] I. R. Epstein, K. Kustin, and L. J. Warshaw, "A kinetics study of the oxidation of iron(II) by nitric acid," *Journal of American Chemical Society*, vol. 102, no. 11, pp. 3751-3758, 1980, doi: 10.1021/ja00531a015.

[118] K. Naresh, "Applications of Fluorescence Spectroscopy," *Journal of Chemical and Pharmaceutical Sciences*, no. Special Issue 5, pp. 18-21.

[119] C. E. Housecroft and E. C. Constable, "Introduction to spectroscopy," in *Chemistry*, 4th ed., 2010, pp. 376-389.

[120] M. B. Shinn, "Colorimetric Method for Determination of Nitrite," *Ind. Eng. Chem. Anal. Ed.*, vol. 13, no. 1, pp. 33-35, 1941.

[121] H. Yu, R. Schmitt, A. Sapin, P. Chaimbault, and P. Leroy, "Comparison between two derivatization methods of nitrite ion labeled with 15 N applied to liquid chromatography-tandem mass spectrometry," *Anal. Methods*, vol. 10, no. 31, pp. 3830-3836, 2018.

[122] G. W. Trownson, "The High Temperature Corrosivity of Radiolysed Nitric Acid Solutions," PhD, School of Chemistry, Manchester, 2016.

[123] K. Bendschneider and j. Robinson, "A new spectrophotometric method for the determination of nitrite in seawater," University of Washington Oceanographic Laboratories, 1952.

[124] G. H. Jeffery, J. Bassett, J. Mendham, and R. C. Denney, *Vogel's Textbook of Quantitative Chemical Analysis*. Longman Scientific and Technical, 1989.

[125] J. Zhu, X. Yang, F. Fan, and Y. Li, "Factors affecting the determination of iron species in the presence of ferric iron," *Applied Water Science*, vol. 8, 2018, Art no. 228.

[126] V. M. Aksenenko, N. S. Murav'ev, and G. S. Taranenko, "Raman-scattering study of nitric-acid solutions," *J. Appl. Spectrosc.*, vol. 44, pp. 70-72, 1986.

[127] T. Nakabayashi, K. Kosugi , and N. Nobuyuki, "Liquid Structure of Acetic Acid Studied by Raman Spectroscopy and Ab Initio Molecular Orbital Calculations," *J. Phys. Chem. A.*, vol. 103, no. 43, pp. 8595-8603, 1999.

[128] R. E. Nightingale and E. L. Wagner, "The Vibrational Spectra and Structure of Solid Hydroxylamine and Deutero-Hydroxylamine," *J. Chem. Phys.*, vol. 22, no. 2, pp. 203-208, 1954.

[129] R. S. Krishnan and K. Balasubramanian, "Raman spectrum of hydroxylamine hydrochloride (NH3OH.Cl)," *Proceedings of the Indian Academy of Sciences - Section A,* vol. 59, pp. 285-291, 1964.

[130] J. McFarlane, L. H. Delmau, D. W. DePaoli, C. H. Mattus, C. E. Phelps, and B. D. Roach, "Hydroxylamine Nitrate Decomposition under Non-radiological Conditions," Oak Ridge National Laboratory, July 2015.

[131] J. L. Velada, Y. Liu, and M. B. Huglin, "Effect of pH on the swelling behaviour of hydrogels based on *N*-isopropylacrylamide with acidic comonomers," *Macromolecular Chemistry and Physics,* vol. 199, no. 6, pp. 1127-1134, 1998.

[132] S. Alavi and D. L. Thompson, "Hydrogen bonding and proton transfer in small hydroxylammonium nitrate clusters: A theoretical study," *J. Chem. Phys.,* vol. 119, no. 8, pp. 4274-4282, 2003.

[133] M. Kazanci, J. P. Schulte, C. Douglas, P. Fratzl, D. Pink, and T. Smith-Palmer, "Turning the Surface-Enhanced Raman Scattering Effect to Different Molecular Groups by Switching the Silver Colloid Solution pH," *Applied Spectroscopy,* vol. 63, no. 2, pp. 214-223, 2009.

[134] M. Xu, J. P. Larentzos, M. Roshdy, L. J. Criscenti, and H. C. Allen, "Aqueous divalent metal-nitrate interactions: hydration versus ion pairing," *Phys. Chem. Chem. Phys.,* vol. 10, pp. 4793-4801, 2008.

[135] M. Precek, A. Paulenova, and B. J. Mincher, "Reduction of Np(VI) in irradiated solutions of nitric acid," *Procedia Chemistry,* vol. 7, pp. 51-58, 2012, doi: 10.1016/j.proche.2012.10.010.

[136] G. A. Hope, R. Woods, G. K. Parker, A. N. Buckley, and J. McLean, "Spectroscopic characterisation of copper acetohydroxamate and copper n-octanohydroxamate," *Inorganica Chimica Acta,* vol. 365, pp. 65-70, 2011, doi: 10.1016/j.ica.2010.08.028.

[137] D. C. Edwards, S. B. Nielsen, A. A. Jarzecki, T. G. Spiro, and C. B. Myneni, "Experimental and theoretical vibrational spectroscopy studies of acetohydroxamic acid and desferrioxamine B in aqueous solution: Effects of pH and iron complexation," *Geochimica et Cosmochimica Acta,* vol. 69, no. 13, pp. 3237-3248, 2005, doi: 10.1016/j.gca.2005.01.030.

[138] O. Cozar *et al.,* "IR, Raman and surface-enhanced Raman study of desferrioxamine B and its Fe(III) complex, ferrioxamine B," *Journal of Molecular Structure,* vol. 788, no. 1-3, pp. 1-6, 2006, doi: 10.1016/j.molstruc.2005.04.035.

[139] T. k. Das, M. Couture, Y. Ouellet, M. Guertin, and D. L. Rousseau, "Simultaneous observation of the O—O and Fe—O2 stretching modes in

oxyhemoglobins," *Proc. Natl. Acad. Sci. USA*, vol. 98, no. 2, pp. 479-484, 2001, doi: 10.1073/pnas.98.2.479.

[140] J. I. Wirgau, I. Spasojevic, H. Boukhalfa, I. Batinic-Haberle, and A. L. Crumbliss, "Thermodynamics, kinetics, and mechanism of the stepwise dissociation and formation of tris(L-lysinehydroxamato)iron(III) in aqueous acid," (in English), *Inorganic Chemistry*, Article vol. 41, no. 6, pp. 1464-1473, Mar 2002, doi: 10.1021/ic0109795.

[141] I. Pernoll, U. Maier, R. Janoschek, and G. Zundel, "Interpretation of the Raman spectra of aqueous acid solutions in terms of the polarizability of hydrogen bonds. Part 1.—Aqueous HCl solutions," *J. Chem. Soc., Faraday Trans. 2*, vol. 71, pp. 201-206, 1975.

[142] J. Iwata and H. Koseki, "Decomposition of Hydroxylamine/Water Solution with Added Iron Ion," *Journal of Hazardous Materials*, vol. 104, pp. 39-49, 2003, doi: 10.1016/S0304-3894(03)00233-4

[143] Y. Iwata, H. Koseki, and H. F., "Study on Decomposition of Hydroxylamine/Water Solution," *Journal of Loss Prevention in the Process Industries*, vol. 16, pp. 41-53, 2003, doi: 10.1016/S0950-4230(02)00072-4.

[144] I. May, R. J. Taylor, I. S. Denniss, and A. L. Wallwork, "Actinide complexation in the PUREX process," (in English), *Czechoslovak Journal of Physics*, Article; Proceedings Paper vol. 49, pp. 597-601, 1999, doi: 10.1007/s10582-999-1038-8.

[145] M. Sampath, P. K. Sinha, S. Kumar, K. M. Mudali, and R. Natarajan, "New data on decomposition of nitric solutions of acetohydroxamic acid," *Journal of Radioanalytical and Nuclear Chemistry*, vol. 291, pp. 649-651, 2012.

[146] S. D. Chambreau, D. M. Popolan-Vaida, G. L. Vaghjiani, and S. R. Leone, "Catalytic Decomposition of Hydroxylammonium Nitrate Ionic Liquid: Enhancement of NO Formation," *J. Phys. Chem. Lett.*, vol. 8, no. 10, pp. 2126-2130, 2017, doi: 10.1021/acs.jpclett.7b00672.

[147] G. C. M. Bourke and G. Stedman, "Mechanism of the Acid Catalysed Pathway for the Nitrosation of Hydroxylamine," *J. Chem. Soc. Perkin Trans. 2*, pp. 161-162, 1992, doi: 10.1039/P29920000161.

[148] C. Wei, W. J. Rogers, and M. S. Mannan, "Thermal decomposition hazard evaluation of hydroxylamine nitrate," *Journal of Hazardous Materials*, vol. 130, no. 1-2, pp. 163-168, 2006, doi: 10.1016/j.jhazmat.2005.07.044.

[149] P. Tkac, M. Precek, and A. Paulenova, "Redox Reactions of Pu(IV) and Pu(III) in the Presence of Acetohydroxamic Acid in HNO3 Solutions," (in English),

Inorganic Chemistry, Article vol. 48, no. 24, pp. 11935-11944, Dec 2009, doi: 10.1021/ic901081j.

[150] M. Precek, "The Kinetic and Radiolytic Aspects of Control of the Redox Speciation of Neptunium in Solutions of Nitric Acid," PhD, Chemistry, Oregon State University, 2012.

[151] O. Gok, "Ferrous Oxidation Catalyzed by Oxy-Nitrogen Species (NO_x)," *Asian Journal of Chemistry,* vol. 24, no. 12, pp. 5485-5489, 2012.

[152] P. Bruno, M. Caselli, G. de Gennaro, P. Ielpo, and A. Traini, "Analysis of heavy metals in atmospheric particulate by ion chromatography," *Journal of Chromatography A,* vol. 888, no. 1-2, pp. 145-150, 2000, doi: 10.1016/S0021-9673(00)00503-3.

[153] L. Coury, "Conductance Measurements Part 1: Theory," in "Current Separations 18:3," 1999.

[154] J. C. Oxley and K. R. Brower, "Thermal Decomposition of Hydroxylamine Nitrate," in *SPIE*, 9 May 1988, vol. 0872, in Propulsion, pp. 63-70, doi: 10.1117/12.943754.

[155] P. Griess, "Bemerkungen zu der abhandlung der H.H. Weselsky und Benedikt "Ueber einige azoverbindungen."," *Chem. Ber.,* vol. 12, pp. 426-8, 1879.

[156] Y. Ziouane and G. Leturcq, "New Modelling of Nitric Acid Dissociation Function of Acidity and Temperature," *ACS Omega,* vol. 3, pp. 6566-6576, 2018, doi: 10.1021/acsomega.8b00302.

[157] L. A. Ridnour *et al.,* "A Spectrophotometric Method for the Direct Detection and Quantitation of Nitric Oxide, Nitrite, and Nitrate in Cell Culture Media " *Anal. Biochem.,* vol. 281, pp. 223-229, 2000, doi: 10.1006/abio.2000.458.

[158] H. McKenzie, J. McDonald-Taylor, F. McLachlan, R. Orr, and D. Woodhead, "Modelling of nitric and nitrous acid chemistry for solvent extraction purposes," *Procedia Chemistry,* vol. 21, pp. 481-486, 2016, doi: 10.1016/j.proche.2016.10.067.

[159] H. Komiyama and H. Inoue, "Reaction and Transport of Nitrogen Oxides in Nitrous Acid Solutions," *Journal of Chemical Engineering of Japan,* vol. 11, no. 1, 1978.

[160] E. Abel and H. Schmid, *Z. Phys. Chem.,* vol. 134, pp. 279-300, 1928.

[161] M. S. Rayson, J. C. Mackie, E. M. Kennedy, and B. Z. Dlugogorski, "Accurate Rate Constants for Decomposition of Aqueous Nitrous Acid," *Inorg. Chem.,* vol. 51, pp. 2178-2185, 2012.

[162] K. Burger, F. Gaizer, and E. Schulek, "Analytical uses of bromine monochloride: Determination of hydroxylamine. Contributions to the bromic acid-hydrochloric acid reaction," *Talanta,* vol. 5, no. 2, pp. 97-101, 1960.

[163] L. Adamcikova, T. Vranova, and I. Valent, "COMPLEX DYNAMICAL BEHAVIOR IN THE OXIDATION OF HYDROXYLAMINE BY BROMATE," (in English), *International Journal of Chemical Kinetics,* Article vol. 26, no. 3, pp. 347-353, Mar 1994.

[164] S. O. Idris, E. Sunday, M. O. Ibitomi, J. F. Iyun, and Y. Mohammed, "Mechanism of the Redox Reaction of Hydroxylamine and Bromate Ions in Aqueous Hydrochloric Acid Medium," *Arch. Appl. Sci. Res.,* vol. 2, no. 5, pp. 316-324, 2010.

[165] A. A. Naumov, N. D. Goletskii, B. Y. Zilberman, and A. A. Murzin, "Specific Features of Decomposition of Hydroxamic Acids in Two-Phase Nitric Acid Systems with Alcohols and TBP, as Applied to ^{99}Mo Stripping," *Radiochemistry,* vol. 59, no. 6, pp. 596-606, 2017, doi: 10.1134/S1066362217060078.

[166] K. Zhang and S. T. Thynell, "Thermal Decomposition Mechanism of Aqueous Hydroxylammonium Nitrate (HAN): Molecular Simulation and Kinetic Modeling," *Journal of Physical Chemistry A,* vol. 122, no. 41, pp. 8086-8100, 2018, doi: 10.1021/acs.jpca.8b05351.

[167] V. I. Marchenko, K. N. Dvoeglazov, O. A. Savilova, and V. I. Volk, "Reduction of Pu(IV) and Np(VI) with Hydroxylamine in Solutions of Low Acidity with High Uranium Content," *Radiochemistry,* vol. 54, no. 5, pp. 459-646, 2012.

[168] A. A. Silkov, "Electrical conductivity of aqueous solutions and the hydrolysis constant of hydroxylamine hydrochloride in the temperature range 0-50°C," *Russian Journal of Physical Chemistry,* vol. 74, no. 10, pp. 1786-1791, 2000.

[169] R. W. Ashcraft, S. Raman, and W. H. Green, "Predicted Reaction Rates of HxNyOz Intermediates in the Oxidation of Hydroxylamine by Aqueous Nitric Acid," *J. Phys. Chem. A,* vol. 112, pp. 7577-7593, 2008, doi: 10.1021/jp711401p.

[170] V. S. Koltunov and G. I. Zhuravleva, "Kinetics of actinide reduction by hydroxylamine. III. Plutonium(IV) reduction in nitric acid solution.," *Radiokhim.,* vol. 20, no. 94, 1978.

[171] v. s. Koltunov and G. I. Zhuravleva, "Kinetics of actinide reduction by hydroxylamine. IV. Plutonium(IV) reduction in perchloric acid solution.," *Radiokhim.*, vol. 20, no. 661, 1978.

[172] M. Totan, E. Antonescu, and F. G. Gligor, "Quantitative Spectrophotometric Determinations of Fe3+ in Iron Polymaltose Solution," *Indian Journal of Pharmaceutical Sciences*, vol. 80, no. 2, pp. 268-273, 2018.

[173] M. L. Moss and M. G. Mellon, "Colorimetric Determination of Iron with 2,2'-Bipyridyl and with 2,2',2'-Terpyridyl," *Ind. Eng. Chem. Anal. Ed*, vol. 14, no. 11, pp. 862-865, 1942.

[174] J. Woods and M. Mellon, "Thiocyanate Method for Iron: A Spectrophotometric Study," *Ind. Eng. Chem. Anal. Ed.*, vol. 13, no. 8, pp. 551-554, 1941.

[175] M. Hoshino, H. Yasui, H. Sakurai, T. Yamaguchi, and Y. Fujita, "Improved Spectrophotometric Determination of Total Iron and Iron(III) with *o*-hydroxyhydroquinonephthalein and Their Characterization," *The Pharmaceutical Society of Japan*, vol. 131, no. 7, 2011.

[176] H. Pyenson and P. H. Tracy, "A 1,10—Phenanthroline Method for the Determination of Iron in Powdered Milk," *Journal of Dairy Science*, vol. 28, no. 5, 1945.

[177] W. B. Fortune and M. G. Mellon, "Determination of Iron with o-Phenanthroline: A Spectrophotometric Study," *Ind. Eng. Chem. Anal. Ed.*, vol. 10, no. 2, pp. 60-64, 1938.

[178] L. Xu, H. Tian, H. Yao, and T. Shi, "New kinetic and mechanistic findings in the oxidation of hydroxylamine by Ce(IV) in perchloric acid media," *International Journal of Chemical Kinetics*, vol. 50, no. 12, pp. 856-962, 2018, doi: 10.1002/kin.21220.

[179] D. G. Karraker, T. S. Rudisill, and M. C. Thompson, "Studies of the effect of acetohydroxamic acid on plutonium and neptunium by 30 vol. % tributyl phosphate.," Westinghouse Savannah River Company. [Online]. Available: http://www.osti.gov/bridge/

[180] G. Bengtsson, "A Kinetic Study of the Reaction between Iron(III) and Hydroxylamine in Strongly Acid Perchlorate Solutions," *Acta Chemica Scandinavica*, vol. 27, pp. 1717-1724, 1973, doi: 10.3891/acta.chem.scand.27-1717.

[181] J. Lind and G. Merenyi, "Kinetic and Thermodynamic Properties of the Aminoxyl (NH_2O*) Radical," *J. Phys. Chem. A.*, vol. 110, pp. 192-197, 2006.

[182] A. J. Bard, R. Parsons, and J. Jordan, *Standard potentials in Aqueous Solution*, 1st Edition ed. Dekker, New York, 1985.

[183] W. A. Waters and I. R. Wilson, "Mechanism of the oxidation of hydroxylamine by ceric sulphate," *J. Chem. Soc. A*, pp. 534-536, 1966.

[184] L. Treindl and A. Viludova, "Kinetics and mechanism of a redox reaction of Ce^{4+} ions with hydroxylamine," *Collet Czech Chem Commun.*, vol. 39, pp. 3456-3462, 1974.

[185] S. B. Hanna, R. R. Kessler, A. Merbach, and S. Ruzicka, "Planning a Kinetic and Mechanistic Study with Cerium (IV)," *J. Chem. Educ.*, vol. 53, no. 8, pp. 524-527, 1976, doi: 10.1021/ed053p524.

[186] R. J. Taylor, C. Mason, R. Cooke, and C. Boxall, "The Reduction of Pu(IV) by Formohydroxamic Acid in Nitric Acid," *Journal of Nuclear Science and Technology*, Supplement 3, pp. 278-281, 2002.

[187] M. Hassan, S. Nisar, S. A. Kazmi, M. Qadri, S. Imad, and R. Naz, "Kinetics and Mechanism of Reduction of Fe(III)-Acetohydroxamic Acid by Hydroxylamine Hydrochloride at Acidic pH," *Pak. J. Chem.*, vol. 5, no. 1, pp. 8-13, 2015, doi: 10.15228/2015.v05.i01.p02.

[188] E. Farkas, E. A. Enyedy, L. Zekany, and G. Deak, "Interaction between iron(II) and hydroxamic acids: oxidation of iron(II) to iron(III) by Desferrioxamine B under anaerobic conditions," *Journal of Inorganic Biochemistry*, vol. 83, pp. 107-114, 2001.

[189] H. Boukhalfa, S. D. Reilly, and M. P. Neu, "Complexation of Pu(IV) with the Natural Siderophore Desferrioxamine B and the Redox Properties of Pu(IV)(siderophore) Complexes," (in English), *Inorg. Chem.*, Article vol. 46, no. 3, pp. 1018-1026, Feb 2007, doi: 10.1021/ic061544q.

[190] B. Monzyk and A. L. Crumbliss, "MECHANISM OF LIGAND SUBSTITUTION ON HIGH-SPIN IRON(III) BY HYDROXAMIC ACID CHELATORS - THERMODYNAMIC AND KINETIC STUDIES ON THE FORMATION AND DISSOCIATION OF A SERIES OF MONOHYDROXAMATOIRON(III) COMPLEXES," (in English), *Journal of the American Chemical Society*, Article vol. 101, no. 21, pp. 6203-6213, 1979, doi: 10.1021/ja00515a009.

[191] F. P. L. Andrieux, C. Boxall, and R. J. Taylor, "Determination of the Constants of Formation of Complexes of Iron(III) and Acetohydroxamic Acid," in *Application of Thermodynamics to Biological and Materials Science*, M. Tadashi Ed.: InTech, 2011, ch. 16, pp. 441-458.

[192] P. Xu and R. Hoffmann, "The Dimerization of H2NO," *J. Phys. Chem.,* vol. 120, pp. 1283-1296, 2016, doi: 10.1021/acs.jpca.5b12674.

[193] Z. Li, L. Wang, Y. Liu, Q. Zhao, and J. Ma, "Unraveling the interaction of hydroxylamine and Fe(III) in Fe(II)/Persulfate system: A kinetic and simulating study," *Water Research,* vol. 168, 115093, 2020.

[194] J. Billeter, G. Puxty, and K. Hungerbühler, "Hydroxylamine decomposition in the presence of iron studied by calorimetry, online mid-IR and UV-vis spectroscopy," presented at the 35th Inorganic Reaction Mechanisms Meeting (IRMM 2005), 2006.

[195] R. A. Robinson and V. E. Bower, *A. Phys. Chem.,* vol. 65, p. 1279, 1961.

[196] D. A. Bazylinski and T. C. Hollocher, "Evidence from the Reaction between Trioxodinitrate(II) and 15NO That Trioxodinitrate (II) Decomposes into Nitrosyl Hydride and Nitrite in Neutral Aqueous Solution," *Inorg. Chem.,* vol. 24, pp. 4285 – 4288, 1985.

[197] V. Shafirovich and S. V. Lymar, "Nitroxyl and its anion in aqueous solutions: Spin states, protic equilibria and reactivities toward oxygen and nitric oxide," *PNAS,* vol. 99, no. 11, pp. 7340-7345, May 28 2002, doi: 10.1073/pnas.112202099.

[198] V. A. Lorenz-Fonfria and E. Padros, "Method for the Estimation of the Mean Lorentzian Bandwidth in Spectra Composed of an Unknown Number of Highly Overlapped Bands," *Applied Spectroscopy,* vol. 62, no. 6, pp. 689-700, 2008.

[199] S. A. Kazmi and J. V. McArdle, "KINETICS OF FORMATION OF BIS-(ACETOHYDROXAMATO) AND TRIS(ACETOHYDROXAMATO)FE(III)," (in English), *Journal of Inorganic & Nuclear Chemistry,* Article vol. 43, no. 11, pp. 3031-3034, 1981.

[200] D. L. Wertz and M. L. Steele, "Coordination of Fe^{3+} in Concentrated Aqueous Solutions with Chloride Ligands," *Inorganic Chemistry,* vol. 19, no. 6, pp. 1652-1656, 1980, doi: 10.1021/ic50208a044.

[201] M. Magini and T. Radnai, "X-ray diffraction study of ferric chloride solutions and hydrated melt. Analysis of the iron(III)–chloride complexes formation," *The Journal of Chemical Physics,* vol. 71, no. 11, 2008, doi: 10.1063/1.438233.

[202] G. W. Brady, M. B. Robin, and J. Varimbi, "The Structure of Ferric Chloride in Neutral and Acid Solutions," *Inorganic Chemistry,* vol. 3, no. 8, pp. 1168–1173, 1964, doi: 10.1021/ic50018a023.

[203] I. Persson, "Ferric Chloride Complexes in Aqueous Solution: An EXAFS Study," *Journal of Solution Chemistry*, vol. 47, no. 5, pp. 797–805, 2018, doi: 10.1007/s10953-018-0756-6.

[204] Metrohm, "MagIC Net 2.1 Online Help,"